Cranfield University

T. D. Dunstan

Turbulent Premixed Flame Kernel Growth During The Early Stages Using Direct Numerical Simulation

School of Engineering

PhD

Cranfield University

School of Engineering

PhD

2008

T. D. Dunstan

Turbulent Premixed Flame Kernel Growth During The Early Stages Using Direct Numerical Simulation

Supervisor: Dr K. W. Jenkins

Academic Year 2006 to 2008

This thesis is submitted in partial fulfilment of the requirements for the degree of Doctor of Philosophy

ABSTRACT

In this thesis Direct Numerical Simulation (DNS) is used to investigate the development of turbulent premixed flame kernels during the early stages of growth typical of the period following spark ignition. Two distinct aspects of this phase are considered: the interaction of the expanding kernel with a field of decaying turbulence, and the chemical and thermo-diffusive response of the flame for different fresh-gas compositions. In the first part of the study, three-dimensional, repeated simulations with single-step chemistry are used to generate ensemble statistics of global flame growth. The surface-conditioned mean fluid-velocity magnitude is found to vary significantly across different isosurfaces of the reaction progress variable, and this is shown to lead to a bias in the distribution of the Surface Density Function (SDF) around the developing flame. Two-dimensional simulations in an extended domain indicate that this effect translates into a similar directional bias in the Flame Surface Density (FSD) at later stages in the kernel development. Properties of the fresh gas turbulence decay are assessed from an independent, non-reacting simulation database.

In the second part of this study, two-dimensional simulations with a detailed 68-step reaction mechanism are used to investigate the thermo-diffusive response of pure methane-air, and hydrogen-enriched methane-air flames. The changes in local and global behaviour due to the different laminar flame characteristics, and the response of the flames to strain and curvature are examined at different equivalence ratios and turbulence intensities. Mechanisms leading to flame quenching are discussed and the effect of mean flame curvature is assessed through comparison with an equivalent planar flame. The effects of hydrogen addition are found to be particularly pronounced in flame kernels due to the higher positive stretch rates and reduced thermo-diffusive stability of hydrogen-enriched flames.

Keywords: DNS, Spark Ignition, IC engine, Hydrogen addition, Displacement speed

ACKNOWLEDGEMENTS

For the constant guidance and support throughout the course of this work I would like to thank my supervisor Dr Karl Jenkins, whose enthusiasm, understanding and generosity contributed a great deal to the successful completion of this thesis, and to the quality of my time at Cranfield.

Special thanks also to Prof. Stewart Cant for his invaluable advice and encouragement, in particular on the use of the DNS codes SENGA and SENGA2.
Many other people have helped me in some way in completing this thesis, but in particular I would like to thank Drs Timos Kipouros and K.K.J. Ranga-Dinesh for all the interesting and fruitful discussions, and Dr Nilanjan Chakraborty for his useful and insightful comments.

The expertise and technical assistance of Dr Les Oswald and staff at the Cranfield University High Performance Computing Facility are also gratefully acknowledged.

Financial support was provided by the Engineering and Physical Sciences Research Council, UK (EPSRC). Additional resources were also provided by the Consortium On Computational Combustion For Engineering Applications (COCCFEA) in supplying access to the UK's HPCx and HECToR high-performance computing facilities.

To my parents

TABLE OF CONTENTS

TABLE OF FIGURES

TABLE OF TABLES

NOTATION

1. Symbols

1.1 Arabic

a	Speed of sound
a_T	Tangential strain rate
A	Flame surface area
A_L	Laminar flame surface area
B	Pre-exponential Arrhenius constant
c	Progress variable
$c*$	Progress variable value for surface conditioned quantities
c_k	Molar concentration of species k
C_n	Model constant
C_p	Specific heat capacity at constant pressure
C_v	Specific heat capacity at constant volume
D_k	Diffusivity of species k
Da	Damkohler number
E	Stagnation internal energy
$E(k)$	Energy spectrum function
$f_{k,i}$	i th component of the body force for species k
h_k	Enthalpy of species k
h_k^0	Reference enthalpy of formation of species k
I	Flame speed modification factor
k	Fourier space wavenumber / RANS turbulent kinetic energy
Ka	Karlovitz number
Ka_r	Karlovitz number based on reaction layer time scale

K_m	Local surface curvature / reaction rate of step m
l	Eddy length scale
l_0	Integral length scale
L	Flame isoline length
L_i	Characteristic wave amplitude variation
L_L	Laminar flame isoline length
Le	Lewis number
Ma	Markstein number
n_i	i th component of the flame normal vector
p	Pressure
P	Scalar projection of SDF position on kernel displacement vector
Pr	Prandtl number
q	Heat flux
q_r	Radiative heat transfer
Q	Unspecified quantity / heat source term
R^0	Universal gas constant
R	Mean kernel radius
R_{c*}	Mean radius of the progress variable isosurface at $c*$
R_{ij}	Velocity correlation tensor
Sc	Schmidt number
s_d	Flame surface displacement speed
s_L^0	Unstretched planar laminar flame speed
s_n	Normal diffusion component of displacement speed
s_r	Reaction component of displacement speed
s_t	Tangential diffusion component of displacement speed
s_T	Turbulent flame speed
t	time
T_0	Fresh gas /cold boundary temperature

T	Temperature / turbulent energy transfer rate
T_a	Activation temperature
T_{ad}	Adiabatic flame temperature
u'	Root mean square velocity fluctuation
u_0	Integral scale velocity
u_i	i th component of velocity
V	Volume
$V_{k,i}$	i th component of diffusion velocity for species k
W_k	Molecular weight of species k
x	Spatial position / co-ordinate direction
X_k	Mole fraction of species k
y	Co-ordinate direction
Y_k	Mass fraction of species k
Y_P	Product mass fraction
Y_R	Reactant mass fraction
z	Co-ordinate direction
Z_k	Chemical symbol of species k

1.2 Greek

α	Heat release parameter
β	Zel'dovich number
δ	Diffusive laminar flame thickness
δ_{ij}	Kronecker delta
δ_{th}	Thermal laminar flame thickness
Δ	Increment
γ	Isentropic index / ratio of specific heats
ε	Turbulence kinetic energy dissipation rate

η	Kolmogorov length scale
κ	Bulk viscosity
λ	Thermal diffusivity / conductivity
λ_i	Characteristic wave velocity
Λ	Burning velocity eigenvector
μ	Dynamic viscosity
μ_0	Fresh gas / reference dynamic viscosity
ν	Kinematic viscosity
Ξ	Wrinkling factor
Ξ_{gen}	Generalised wrinkling factor
ρ	Density
ρ_0	Fresh gas / reference density
σ	Surface density function
Σ	Flame surface density
Σ_{gen}	Generalised flame surface density
τ	Heat release parameter
τ_0	Integral time scale
τ_η	Kolmogorov time scale
τ_f	Characteristic flame time scale
ϕ	Equivalence ratio
ϕ_{ij}	Velocity spectrum tensor
χ	Scalar dissipation rate
$\dot{\omega}$	Reaction rate
$\dot{\omega}_k$	Reaction rate of species k

2. Acronyms

BML	Bray Moss Libby
CSP	Computational Singular Perturbation

DNS	Direct Numerical Simulation
EBU	Eddy Break Up
EGR	Exhaust gas recirculation
FSD	Flame Surface Density
FGM	Flamelet generated Manifold
FPI	Flame Prolongation of ILDM
IC	Internal Combustion
ITNFS	Intermittent Turbulent Net Flame Stretch
ILDM	Intrinsic Low Dimensional Manifold
LES	Large Eddy Simulation
LODI	Local One Dimensional Inviscid
NSCBC	Navier Stokes Characteristic Boundary Conditions
pdf	Probability Density Function
PE	Partial Equilibrium
PID	Proportional Integral Derivative
PLIF	Planar Laser Induced Fluorescence
QSS	Quasi Steady State
RANS	Reynolds Average Navier Stokes
SDF	Surface Density Function
SDR	Scalar Dissipation Rate
SI	Spark Ignition

1 INTRODUCTION

1.1 The Problem of Turbulent Premixed Combustion

Some of the complexity encountered in the study of premixed flame kernels can be appreciated by considering the range of processes that occur during successful ignition:

A spark, discharging into a turbulent field of premixed fuel and oxidiser creates a thin column of ionised gas with temperatures of ~$6x10^4$K and pressures approaching 200bar [1,2]. Over a time scale of ~10^{-3}s, this heat is rapidly transferred to the surrounding fluid, lowering the temperature in the channel core by an order of magnitude, and producing an approximately spherical, high-temperature region with a diameter ~10^{-3}m containing combustion products, unconsumed oxidiser, and high concentrations of dissociated radicals. These radicals diffuse out from the hot core into the fresh gas on time scales of the order 10^{-6}s, and through length scales of ~10^{-5}m [3]. On contact with the pre-heated reactants in the fresh gases, they induce breakdown reactions of the primary fuel molecules, producing lighter fuel species, additional radicals, and heat. The process continues through several thousand[1] individual steps involving several thousand chemical species undergoing chain branching, chain carrying and chain terminating reactions which span time scales from 10^{-8}s to 10s [4]. If sufficient chemical energy is released during this process to sustain the reaction, a flame kernel is formed by the outwardly propagating reaction wave.

As the flame kernel expands it begins to interact with the turbulence spectrum - from the smallest eddies, comparable in size to the flame thickness ~10^{-4}m, up to the largest, with sizes of the order of the chamber dimensions, and across time scales of an equally wide range. The kernel is transported globally by the larger eddies, while the smaller scales strain and curve the flame surface, increasing the flame area and causing local changes to the reactive-diffusive balance in the flame front. As the kernel encounters an

[1] The oxidation of cetane n-$C_{16}H_{34}$, a component in diesel and jet fuel, involves ~6000 reactions and ~2000 species. Lighter hydrocarbons such as methane are considerably simpler (§4.2.5.3).

increasingly broad portion of the turbulence spectrum, the expansion accelerates due to the enhanced rate of growth of flame area, until finally, the reactants are fully consumed and the process terminates.

The example given above illustrates some of the difficulties faced in turbulent combustion research. The physical processes underlying the global rate of heat release and flame behaviour, which are generally the quantities of interest, occupy scales spanning four decades in length, and seven in time. In addition, turbulent flows are inherently chaotic and unpredictable, and closely coupled to the reactive-diffusive behaviour of the flame, which, in turn, involves a very large number of interrelated chemical processes. While the details of the initial spark discharge phase are beyond the scope of the present work, it is clear that such systems still present many challenges – most of which are not specific to flame kernel initiation but apply to turbulent premixed combustion in general.

Premixed combustion systems, where the fuel and oxidiser form a homogenous mixture prior to ignition, are widely used in automotive, aeronautic, industrial and domestic applications. Compared to non-premixed combustion devices, they have the advantage of allowing close control over the composition of the reacting mixture, and so may be operated much closer to the lean limit whilst still providing reliable performance.

The technology has been in existence for many years, and during this time many advances have been made towards higher power densities, improved efficiency and reduced pollution. More recently, however, tightening emissions regulations, the rising cost of conventional fuels, and the need to explore new fuel types, add impetus to the need to understand and accurately model turbulent combustion systems. At present only the reaction mechanisms for light hydrocarbon species such as hydrogen and methane can be said to be well understood, and even here the behaviour of these flames in a turbulent environment is complex and not reducible to any simple, universal parameters. New fuel types such as hydrogen, syngas and bioethanol offer potentially sustainable sources of fuel for transportation and power generation, but the design of efficient and reliable devices capable of exploiting these fuels relies on the ability to accurately

predict their behaviour at a fundamental level. Similarly, techniques such as Exhaust Gas Recirculation (EGR) in internal combustion engines, or onboard fuel reforming and hydrogen addition, produce changes in flame characteristics which are not predictable in a reliable way from a purely theoretical stance. Numerical simulation and accurate experiment must therefore play key roles in the understanding of such systems.

In spark ignition devices, the early stages of growth of the flame kernel are crucial to the overall performance of the system. During this phase, the effects of turbulent straining tend to have a predominantly negative impact on the rate of heat release, due to the high mean curvature of the flame surface increasing the probability of locally reduced, and even negative, flame speeds. The global movement of the kernel is also important since the level of contact with the electrodes, and hence the associated heat loss through conduction, is known to be a leading cause of delayed heat release or even misfire in spark ignition engines. Understanding the fundamental processes present during these stages provides valuable insight into the causes of the observed cycle-to-cycle variations in such systems, and is therefore a prerequisite to developing more accurate models for use in engineering simulations and design.

1.2 The Scope of DNS

Direct Numerical Simulation (DNS), in general terms, refers to numerical simulations where all the scales of turbulence are resolved on the computational grid without the need for additional modelling. DNS in the context of combustion shares this same ideal – to fully resolve both the flow and chemistry without the need for modelling – but at present, for all but the simplest fuels, this remains only a theoretical notion. An approximation of the spatial resolution requirements for DNS illustrates some difficulties [5].

In a domain of size L, the flow must be resolved by a computational grid of N points in each coordinate direction. The range of turbulent length scales present[2] will include integral length scales l_0 of the order of the domain dimensions $l_0 \sim L$, down to the Kolmogorov scales η, which may be estimated from the turbulent Reynolds number as $\eta = l_0 / \mathrm{Re}_t^{3/4}$. The grid point separation must be less than this last length scale to ensure full resolution, therefore $L/N \sim l_0/N < \eta$, and the number of grid points required in each direction becomes $N > \mathrm{Re}_t^{3/4}$, or in three-dimensions: $N > \mathrm{Re}_t^{9/4}$.

This demonstrates the fundamental limitation of DNS in that the number of grid points required rises exponentially with the turbulence Reynolds number, and it is only relatively recently that the rapid increase in computing power has made DNS a feasible option for turbulence research. When considering DNS of combustion, however, it is almost always the case that resolution of the chemical scales places an even greater restriction on the practical domain size.

To resolve a flame of thickness δ, a minimum number of grid points Q spanning the flame front is required, where, in the present case $Q \sim 12$ and $Q \sim 20$ are found to be adequate for the single-step and complex chemical mechanisms respectively. The flame thickness can be estimated from $\delta = \nu / s_L^0 Sc$, where ν is the kinematic viscosity, s_L^0 is the flame speed, and Sc is the Schmidt number which is of order unity[3]. Given these conditions, the inequality $l_0/\delta < N/Q$ must be satisfied.

The relation between the chemical time scales τ_f, and the large-scale turbulent structures can be quantified through the ratio of their characteristic time scales, known as the Damkohler number, $Da = \tau_t / \tau_f = l_0 s_L^0 / u' \delta$, where u' is the velocity associated with integral scale eddies. Combining these relations gives

---

[2] Definitions of the various turbulence length and time scales used here are given in Section 2.3

[3] Laminar flame speed s_L^0, and Schmidt number are discussed in Sections 2.2 and 4.1.1 respectively

$$\mathrm{Re}_t \, Da = \frac{l_0 s_L^0}{\nu \delta} = \frac{l_0^2}{\delta^2} < \frac{N^2}{Q^2} \qquad \textbf{(1.1)}$$

The inequality in Eq. 1.1 implies that for a given Reynolds number and chemical mechanism, a limit exists on the achievable Damkohler number, or equivalently, that given a minimum acceptable Damkohler number, Eq. 1.1 defines the upper limit for the available Reynolds number. As a practical example, Reynolds and Damkohler numbers in internal combustion engines at moderate loads are estimated [6] to be in the range $100 < \mathrm{Re}_t < 1000$, and $Da \sim 100$, so taking even the lowest figures in this range, a three-dimensional DNS would require a total of $\sim 10^9$ grid points according to 1.1. This is, at present, an achievable but expensive and time-consuming computation, but demonstrates that DNS is just beginning to be capable of capturing flows of practical interest.

Spatial resolution is only part of the problem however; in the absence of reacting species, the time step of an explicit solver is limited by the passage of acoustic waves through any single computational cell according to the Courant Friedrichs Lewy (CFL) condition. In reacting flows however, a more restrictive criterion must be considered: the time scale of the fastest reacting species. In general, this limitation is characterised by the *stiffness* of the chemical mechanism, which is defined as the ratio of the longest to shortest kinetic time scales of the reaction mechanism, which, as noted in the opening passage, can be large.

In addition to these spatial and temporal resolution requirements, a separate transport equation must be solved for all N-1 chemical species present, with source terms evaluated for each reaction in the step list. The most comprehensive mechanism available for methane-air combustion at present, the GRI-Mech 3.0 [7], comprises 53 individual species and 325 reaction steps. For the heavier fuels more commonly used in practice, the size and complexity of the mechanisms is considerably greater.

It is clear from this that combustion DNS in the true sense is not a realistic prospect, and is unlikely to become so in the foreseeable future. In the more restricted, fluid-dynamic,

sense however, DNS is well established now as an extremely powerful tool for investigating the fundamental behaviour of turbulent flames. Through judicious simplifications to the domain geometry or chemical mechanism, the computational effort can be concentrated on a specific process, or set of processes, to provide high quality information on the quantities of interest.

1.3 Aims of This Study

The aim of the present work is to use DNS to study the development of turbulent flame kernels during the early stages of growth. In practical terms this refers to the period immediately following an ignition event where the volume of burnt gas is approximately spherical, and small compared to the turbulent scales in the surrounding flow. This situation occurs in many real-world settings, the most obvious being spark-ignition (SI) internal combustion engines. In fact, any ignition method involving a point source of energy will result in a flame kernel, but more generally, many of the results derived from the study of kernels may also be applied to any flame with a high mean curvature in relation to the flame thickness, and not just to flames with spherical symmetry.

In the context of SI engines, this period of kernel development is particularly important to the overall performance of the engine. After the spark discharge has ended, and before the kernel has developed into a fully turbulent flame, the kernel is at its most susceptible to the effects of turbulent straining and heat losses to the electrodes, which, if excessive, can lead to a delayed pressure rise, or ultimately to complete misfire. In simulations of the combustion cycle in SI engines it is generally not possible to fully resolve the flame kernel on the computational mesh during these early stages, and so models must be introduced to account for as much of the missing information as possible.

From a more fundamental perspective, spherical flames are interesting for a number of reasons. The presence of mean curvature changes the reactive-diffusive balance through

the flame front, and so the global response of the flame to strain and curvature can differ markedly from that of a planar flame, and particularly so for less thermo-diffusively stable fuels such as those containing high proportions of hydrogen.
The time-dependence of the kernel configuration is also important. Most computational studies are carried out on statistically planar flames, where statistical stationarity is assumed after a short period. Accordingly, data may be spatially averaged from a snapshot at a single point in time and taken to be representative of all planar flames under similar thermo-chemical and turbulent conditions. This differs fundamentally from the inherently time-dependent growth of a kernel; not only does the mean curvature of the flame surface reduce over time, but the relation of the surface to the turbulence spectrum also changes. Therefore, a similar method of analysis is not possible: the history of the system must be taken into account.

In recognition of the above comments on the scope of DNS, this study consists of two parts, each of which concentrates on different aspects of kernel growth during the early stages.

In the first part, the interaction of the kernel with a three-dimensional field of decaying, homogenous and isotropic turbulence is investigated. Chemistry is reduced to a simplified, one-step scheme to allow multiple realisations at each set of parameter values, which are then used to build ensemble statistics for the flame behaviour. A second, independent study is also carried out into the turbulence decay properties of the fresh gases.

Specifically, the aims of this part of the study are:

1. To investigate, through changes to the initial distribution of energy in the turbulence spectrum, the impact of the different scales of turbulence on the global growth of the kernel.
2. To investigate the effect of the different scales of turbulence at different positions through the flame front, and the change in these effects through time.

3. To make use of repeated simulations to generate ensemble-average statistical information on global-average flame properties, and also on the global distribution of certain key local quantities.
4. To illustrate the underlying causes of the observed effects by developing a phenomenological model - both to aid further understanding, and as a first step towards quantitative modelling.

The emphasis in this part of the study is therefore on the hydrodynamic interaction of the kernel with the turbulence, but at the expense of an accurate treatment of the chemistry. To the best of the author's knowledge the observations made regarding the impact of the turbulence at different positions through the flame front have not previously been noted, and constitute new information in this area. In addition, the technique of using ensemble statistics to investigate the global distribution of local quantities does not appear to have been used previously in this field.

The second part of this study concerns the effects of mixture composition and equivalence ratio on kernel growth and extinction. In contrast to the first part, the emphasis here is on an accurate representation of the chemistry, and the simulations are therefore restricted to single, two-dimensional realisations for each set of parameter values.

A detailed 68-step mechanism for methane-air is used, and in addition to varying the equivalence ratio and turbulence intensity, the effect of adding small quantities of molecular hydrogen to the reactants is also investigated.
Hydrogen doping in IC engines has been suggested as a method of achieving reliable combustion at much lower equivalence ratios than conventional fuel mixtures, whilst avoiding the containment and transportation issues surrounding the use of pure hydrogen as a fuel source [8]. Compared to pure methane, hydrogen has a higher laminar flame speed, increased reactivity, and a substantially lower lean equivalence ratio limit. Some of these properties become apparent in mixtures with as little as 10% hydrogen addition by volume, however the changes in flame properties are not straightforward, and cannot be predicted simply from the properties of the constituent

fuels. In particular, the high mobility of the H_2 molecule changes the response of the blended flame to strain and curvature away from that of a pure methane-air flame, and the impact of this change is more pronounced for developing flame kernels due to the presence of mean curvature. This study addresses some of these issues with the following specific aims:

1. To examine the thermo-diffusive response of developing flame kernel at different equivalence ratios, both with and without hydrogen addition.
2. To differentiate the effects of the changes in laminar flame characteristics from the changes in the thermo-diffusive stability due to hydrogen addition.
3. To compare the effects of hydrogen addition in statistically planar flames to the kernel configuration.
4. To examine the causes of extinction for flame kernels in general, and also the enhanced resistance to extinction exhibited by hydrogen enriched flames.

While a number of studies have been published previously on DNS of planar flames using detailed chemistry - and one such study [9] is explicitly used here for the comparison with planar H_2-enriched flames - no previously published work has been found on DNS of flame kernels using a detailed chemical mechanism, either for pure or blended fuels.

1.4 Thesis Outline

Chapter 2 begins with some of the theoretical background to the study of turbulent premixed flames, with the emphasis on fundamental behaviour and canonical results relevant to the discussions contained in the body of the thesis. In Chapter 3 a more specific review of the literature is provided, concentrating on the current state of knowledge in the fields of turbulent flames, flame kernel analysis, DNS, and related issues in areas such as RANS/LES modelling, IC engine simulation, and laminar flame studies of hydrogen-doped fuels. In Chapter 4 the governing equations and numerical implementation details for the two DNS codes, SENGA and SENGA2, are given. Some

results which validate the performance of the code and identify potential sources of error are also provided. In Chapter 5 results from the first part of the study concerning the turbulence / kernel interaction are presented, and Chapter 6 contains the results from the detailed chemistry simulations. Summaries are provided for each chapter, and in Chapter 7 the thesis is concluded and suggestions for future work are offered.

2 THEORETICAL BACKGROUND

2.1 Governing Equations

The full governing equations for multi-dimensional, multi-component, reacting, ideal gas flows are presented in this section. Derivations of these equations are available in a number of texts [10,11] and so are not repeated here. In practise many of the terms included in these equations are omitted in numerical codes since their contribution is either negligible or too computationally expensive to be retained in full. The specific assumptions and simplifications used in SENGA and SENGA2 are described in Sections 4.1 and 4.2 respectively.

All symbols have their usual meaning except where stated otherwise and summation is implied over directional indices i and j.

Conservation of Total Mass

$$\frac{\partial \rho}{\partial t} + \frac{\partial \rho u_i}{\partial x_i} = 0 \qquad \textbf{(2.1)}$$

Conservation of Momentum

$$\frac{\partial}{\partial t}\rho u_i + \frac{\partial}{\partial x_j}\rho u_j u_i = -\frac{\partial p}{\partial x_i} + \frac{\partial \tau_{ji}}{\partial x_j} + \rho \sum_{k=1}^{N} Y_k f_{k,i} \qquad \textbf{(2.2)}$$

For ideal gases, pressure p is calculated from the equation of state:

$$p = \rho R^0 T \sum_{k=1}^{N} \frac{Y_k}{W_k} \qquad \textbf{(2.3)}$$

where R^0 is the universal gas constant, Y_k and W_k the mass fraction and molecular weight respectively of species k.

The viscous stress tensor τ_{ij} for Newtonian fluids is

$$\tau_{ij} = \mu\left[\frac{\partial u_i}{\partial x_j} + \frac{\partial u_j}{\partial x_i}\right] + \left(\kappa - \frac{2}{3}\mu\right)\frac{\partial u_k}{\partial x_k}\delta_{ij} \qquad \textbf{(2.4)}$$

where the mixture coefficient of dynamic viscosity μ is independent of pressure but is composition and temperature dependent, with $\mu \propto T^{\alpha}$ for $1/2 \le \alpha \le 1$. κ is the bulk viscosity and δ_{ij} is the Kronecker delta. Kinetic theory provides a method of calculating the coefficients of dynamic viscosity μ_i based on binary molecular collisions in a single species i. A mixture coefficient can then be obtained through an appropriate averaging operation [12], or through a more rigorous reduction of the system of equations produced by kinetic theory [13]. A simpler and computationally faster alternative is to assume a constant Prandtl number, Pr, and evaluate the viscosity from the mixture coefficients of thermal conductivity λ, and specific heat capacity C_p:

$$\mu = \frac{\lambda}{C_p}\mathrm{Pr} \qquad \textbf{(2.5)}$$

Where the Prandtl number $\mathrm{Pr} = C_p\mu/\lambda$ is specified as a mixture average constant.

The final term in (2.2) accounts for the presence of body forces $f_{k,i}$ acting on species k in the ith direction, for example, due to gravitational or electromagnetic fields.

Conservation of Energy

$$\frac{\partial}{\partial t}\rho E + \frac{\partial}{\partial x_i}\rho u_i E = -\frac{\partial}{\partial x_i}pu_i + \frac{\partial}{\partial x_j}\tau_{ij}u_i - \frac{\partial}{\partial x_i}q_i - \dot{Q} + \rho\sum_{k=1}^{N} Y_k f_{k,i}\left(u_i + V_{k,i}\right) \qquad \textbf{(2.6)}$$

Stagnation internal energy E, is related to enthalpy h_k through the caloric equation of state

$$E = \sum_{k=1}^{N} Y_k h_k - \frac{p}{\rho} + \frac{1}{2} u_i u_i \qquad \textbf{(2.7)}$$

For species with enthalpy h_k^0 at reference temperature T_0, and temperature dependent specific heat capacity $C_{p,k}$

$$h_k = \int_{T_0}^{T} C_{p,k} dT + h_k^0 \qquad \textbf{(2.8)}$$

The term $\dot{Q}$ accounts for external sources such as heat input from a spark discharge.

The heat flux vector q_i is evaluated from

$$q_i = -\lambda \frac{\partial T}{\partial x_i} + \rho \sum_{p=1}^{N} h_p Y_p V_{pi} + R^0 T \sum_{p=1}^{N} \sum_{k=1}^{N} \left(\frac{X_k D_{T,p}}{W_i D_{pk}} \right) \left(V_p - V_k \right) + \dot{q}_r \qquad \textbf{(2.9)}$$

where the RHS terms represent, from left to right respectively, thermal conduction, heat transfer due to diffusion of species with different specific heat capacities, heat transfer due to concentration gradients (the Dufour effect), and heat transfer due to radiation $\dot{q}_r$. The Dufour effect is the reciprocal of the Soret effect which appears in the full form of the diffusion velocity equation (2.17), and accounts for species diffusion due to temperature gradients. Unlike the Soret effect however, the Dufour effect is much less significant and almost universally neglected in practise.

Full consideration of the radiative heat transfer term $\dot{q}_r$ requires solution of the following equation [11]

$$\dot{q}_r = \int_0^{\infty} \oiint I_v \Omega d\Omega dv \qquad \textbf{(2.10)}$$

where the spectral intensity $I_v(x,\Omega,t)$ is defined as the radiant energy per unit area, per unit time in the direction of unit vector Ω, per unit solid angle about that direction, per unit frequency range at frequency v, at position x and time t. Evaluation of I_v involves considering emission characteristics, losses due to absorption and scattering along the beam path, and gains due to interaction with other rays. It is therefore an exceedingly complex calculation, and computationally expensive to solve accurately. In gas phase combustion however, radiative heat flux is usually relatively small, and except where large particles such as soot are involved or heat transfer to device walls is significant, Eq. 2.10 can be simplified considerably without great loss of accuracy. For the present work these simplifications are outlined in more detail in Section 4.2.1.3.

Conservation of Species

$$\frac{\partial \rho Y_k}{\partial t} + \frac{\partial}{\partial x_i}\left(\rho Y_k \left(u_i + V_{k,i}\right)\right) = \dot{\omega}_k \qquad \textbf{(2.11)}$$

$\dot{\omega}_k$ is the rate of production or reaction rate of species k For a system of N reacting species of chemical symbol Z_k undergoing M reaction steps of the form

$$\sum_{k=1}^{N} \nu'_{k,m}\, \mathrm{Z}_k \leftrightarrow \sum_{k=1}^{N} \nu''_{k,m}\, \mathrm{Z}_k \qquad \text{For } m = 1,\ldots,M \qquad \textbf{(2.12)}$$

where $\nu'_{k,m}$ and $\nu''_{k,m}$ are the molar coefficients of concentration, an expression for the reaction rate is given by

$$\dot{\omega}_k = W_k \sum_{m=1}^{M} \left(\nu''_{k,m} - \nu'_{k,m}\right) K_m(T) \prod_{\beta=1}^{N} c_\beta^{\nu'_{\beta,m}} \qquad \textbf{(2.13)}$$

and is subject to compatibility condition

$$\sum_{k=1}^{N} \dot{\omega}_k = 0 \tag{2.14}$$

The concentration c_β is related to the species mass fraction through

$$c_\beta = \frac{\rho Y_\beta}{W_\beta} \tag{2.15}$$

A reaction rate $K_m(T)$ is then required for each reaction step. No theoretically derived expressions are available for these constants and their accurate determination remains a central issue in combustion modelling today. The general form of the reaction rate most often follows the empirically derived Arrhenius Law:

$$K_m(T) = B_m T^{n,m} \exp\left(-\frac{E_m}{R^0 T}\right) \tag{2.16}$$

Where B_m is a pre-exponential factor, n the temperature exponent, and E_m the activation energy, which must all be supplied as model constants. Reliable data on Arrhenius parameters are available for well understood mechanisms of simple fuels such as H_2 and CH_4, but for more complex fuels many uncertainties remain. Reduced, semi-global and global mechanisms and their associated parameters must be selected with care, and typically are only optimised across a specific and limited range of objectives for the flame behaviour. This area is perhaps the greatest potential source of inaccuracy in combustion modelling at present, and is the subject of much research activity. These issues are discussed more fully in Section 3.8.1.

The term $V_{k,i}$ in Eqs. 2.11 and 2.17 is the mass diffusion velocity vector of species k, and can be calculated from the following expression, given in terms of the mole fraction X_p:

$$\nabla X_p = \sum_{k=1}^{N} \frac{X_p X_k}{D_{pk}} \left(V_k - V_p\right) + \left(Y_p - X_p\right) \frac{\nabla p}{p} + \sum_{k=1}^{N} Y_p Y_k \left(f_p - f_k\right)$$
$$+ \sum_{k=1}^{N} \left[\left(\frac{X_p X_k}{\rho D_{pk}} \right) \left(\frac{D_{T,k}}{Y_k} - \frac{D_{T,p}}{Y_p} \right) \right] \frac{\nabla T}{T} \qquad \textbf{(2.17)}$$

The terms in Eq. 2.17 indicate, from left to right, diffusion due to: concentration gradients, pressure gradients, differential body forces between species, and finally diffusion due to temperature gradients, also known as the Soret effect. By far the dominant term in the majority of cases is the first, often referred to as Fickian diffusion[4], and is determined by the coefficient D_{pk}. The second and third terms become significant only in particular cases where strong pressure gradients and body forces are present and there is also a significant difference in molecular weights between species. The Soret effect is also often neglected but has been found to be significant [14,15] in the transport of relatively light species such as hydrogen, which play an important part in the flame response at high strain rates and in the onset of flame instabilities.

Solution of the full system of equations in Eq. 2.17 for multi-component, multi-dimensional flows puts a significant additional load on any computation, and various levels of simplification exist to overcome this. The first is the zeroth-order or Hirschfelder-Curtiss approximation, obtained by considering only the diagonal terms in the diffusion matrix and so not taking into account cross-diffusion, Soret or Dufour effects [16]. A further level of simplification is reached by using Fick's Law, where a single coefficient is defined for each species diffusing into the mixture. This simplification is justified in lean hydrocarbon-air flames on the grounds that mixture properties are largely determined by the dominating presence of the inert gas nitrogen. An alternative approach is to assume a constant Lewis number, $Le_k = \lambda / \left(\rho C_p D_k\right)$, and to estimate the diffusion coefficient from calculated values of C_p and λ.

[4] There is some ambiguity in the literature over the terms Fickian or Fick's Law, and they are often used in a more restricted sense to refer only to binary mixtures with equal diffusivities.

To ensure continuity of total mass, two additional compatibility conditions also apply:

$$\sum_{k=1}^{N} Y_k = 1 \qquad \text{and} \qquad \sum_{k=1}^{N} V_{k,i} Y_k = 0 \tag{2.18}$$

and for all the simplifications mention here (with the exception of Fick's Law in binary mixtures with unity Lewis numbers) overall conservation of mass is not ensured, and so in these cases a correction velocity is also required.

The equations presented here constitute the most complete description available for multi-component reacting flows where the continuum assumption can be applied. However, their inherent complexity and non-linear nature limits their predictive power for many practical situations. This intractability can in some ways be avoided by considering highly simplified configurations, and these are considered in the next section.

2.2 Laminar Flames

It is instructive to first of all consider the simplest configuration for a deflagration wave: the one-dimensional laminar flame. Not only does this idealized flame provide one of the few situations where, with some appropriate simplifying assumptions, analytical solutions for the governing equations can be found, but it also constitutes the basic phenomenological element, or building block, for many of the more complex combustion models. Recently, detailed experimental measurements of the structure and composition of such flames have become possible, and the simplified geometry allows DNS to be carried out with detailed molecular transport models and reaction mechanisms that would be computationally impossible for more complex configurations. The laminar flame is therefore both of interest in its own right, and also provides vital common ground on which the various disciplines in combustion research converge.

2.2.1 Asymptotic Flame Structure

Following Williams [11], by applying certain assumptions about the governing equations it is possible to arrive at an analytical solution for the laminar flame structure and flame speed; two of the most important characteristics of a premixed laminar flame. The assumptions used are summarized below:

- One-dimensional, steady, planar flow, with Mach number M << 1.
- The fluid is an ideal-gas binary mixture of reactants (R) and products (P) with equal and constant transport coefficients, and Lewis number Le = 1.
- The reaction proceeds in a single, irreversible step from R→P.
- Only Fickian diffusion is considered.
- The flame is adiabatic, and no external forces are present.

The system of equations can be simplified by introducing the non-dimensional variables:

$$\tau \equiv C_p\left(T - T_{ad}\right)/q \tag{2.19}$$

which represents the non-dimensional specific enthalpy or temperature, where q is the total heat released per unit mass of the mixture, and T_{ad} is the temperature at the upstream boundary, and

$$\xi \equiv \int_0^x \frac{mC_p}{\lambda} dx \tag{2.20}$$

where m is the mass burning velocity and x is the spatial coordinate, and represents a distance variable with an upstream boundary at $\xi = -\infty$ and downstream boundary at $\xi = \infty$.

If the reaction rate is assumed to have an Arrhenius form a further non-dimensional variable is obtained:

$$\omega \equiv (1-\tau)\exp\{-\beta(1-\tau)/[1-\alpha(1-\tau)]\} \qquad \textbf{(2.21)}$$

where $\alpha \equiv (T_{ad} - T_0)/T_{ad}$, and $\beta \equiv \alpha E_1 / R^0 T_{ad}$, and E_1 is the activation energy.

The original set of equations can now be restated as

$$\frac{d^2\tau}{d\xi^2} - \frac{d\tau}{d\xi} = -\Lambda\omega \qquad \textbf{(2.22)}$$

where Λ is the burning velocity eigenvector and the terms, from left to right, represent diffusion, convection and reaction respectively.

The asymptotic analysis relies on a strongly temperature dependent reaction rate such that ω is a sharply peaked function of temperature with a maximum that approaches the adiabatic flame temperature T_∞ as $\beta \to \infty$. The Arrhenius Law satisfies this condition, although it should be pointed out that any function that approximates this behaviour is acceptable. It can be seen that the Zel'dovich number β is an important flame parameter and for the asymptotic analysis to be valid must take on appropriately large values, while the non-dimensional heat release parameter α should remain close to unity. Values of β and α for real flames typically lie in the range $5 < \beta < 20$, and $0.6 < \alpha < 0.8$, so this is a reasonable assumption for most flames of interest, and indicates the range of validity for the asymptotic results.

Examination of Eq. 2.21 suggests that for values of $(1-\tau)$ close to unity, the reaction rate term is exponentially small, and so the diffusion and convection terms in Eq. 2.22 must be approximately in balance. This zone is referred to as the convective-diffusive zone and a solution to Eq. 2.22 can be found of the form

$$\tau_n = A_n e^{\xi} \qquad \text{for } n = 0, 1, 2, \ldots \qquad \textbf{(2.23)}$$

where A_n are constants.

It can be seen that since $0 < \tau < 1$, Eq. 2.23 fails for large values of ξ, and so a second zone must exist in the region where $1-\tau$ is of order β^{-1} where the reaction rate becomes non-negligible. In this reactive-diffusive zone the spatial scale is small compared to ξ; the convection term in Eq. 2.22 becomes negligible and a balance must therefore now exist between the diffusive and reactive terms.

The basic flame structure obtained by this analysis is shown in Figure 2.1.

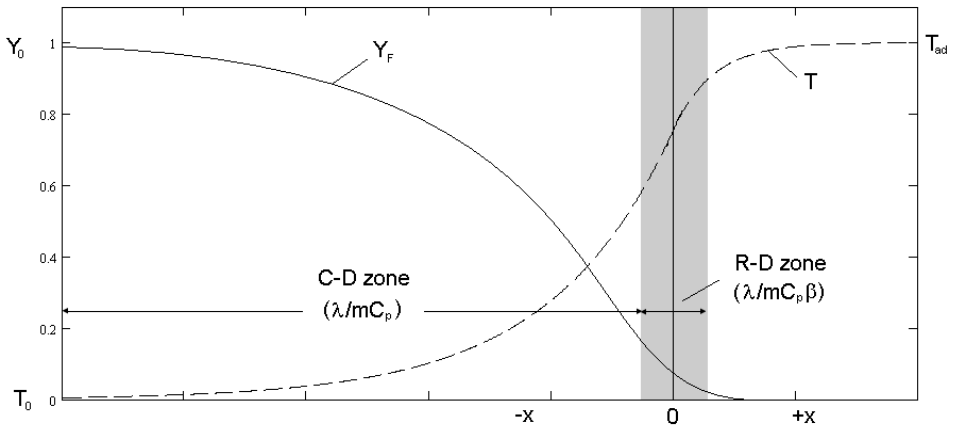

Figure 2.1 Schematic illustration of the asymptotic flame structure. C-D is the convective-diffusive zone, R-D is the reactive-diffusive zone, and Y_F is the normalised mass fraction of reactants.

By introducing an additional stretched variable for the reactive-diffusive zone and applying appropriate matching conditions at the interface, an expression for the burning rate eigenvalue is obtained, which in dimensional form is

$$s_L = \left(\frac{2\lambda\rho BT^n}{\beta^2\rho_0^2 C_p}\right)^{\frac{1}{2}}\left(1+\frac{1.344-3\alpha}{\beta}+O\left(\frac{1}{\beta^2}\right)\right)\exp\left(\frac{-E_1}{2R^0T_{ad}}\right) \qquad \textbf{(2.24)}$$

where O means terms of the order, and B is the pre-exponential factor appearing in the Arrhenius expression of Eq. 2.16.

The significance of the above analysis is that it reveals the key features and parameters that define the burning rate and approximate structure of any premixed flame given that the fuel has sufficiently high activation energy. These are:

- A convective-diffusive, or pre-heat zone with characteristic thickness $\delta = \lambda / mC_p$ where the reaction rate is negligible. The temperature increases exponentially through conduction, and the reactant mass fraction is depleted through diffusion with increasing x.
- A reactive-diffusive, or inner zone with characteristic thickness $\delta_r = \delta / \beta$, where convection is negligible, and where the reaction rate is a sharply peaked function of temperature with a maximum at $T_{\omega_{MAX}} \approx T_{ad}$. The reactant mass fraction is reduced by a factor β^{-1} from the value at the upstream boundary due to diffusion in the pre-heat zone.
- Strong flame-speed dependence on the thermo-fluidic parameters λ / C_p and p, and on the chemical-kinetic[5] parameters B, T_{ad}, and E_1.
- Secondary dependence on β, ρ_0, and α.

Despite the necessarily approximate results produced through this analysis, valuable insight is provided into the basic mechanisms that underlie many of the more subtle phenomena observed in real flames.

It should be noted that the flame speed dependence on pressure (inversely proportional) disappears when mass burning flux is considered rather than the absolute flame speed, and so in predicting fuel consumption and heat release rates it is not of primary importance.

For a particular fuel, where the transport properties and Arrhenius parameters are given, the most pronounced flame speed dependence is therefore the adiabatic flame temperature T_{ad}, which causes increased thermal gradients normal to the flame front and hence greater heat flux ahead of the reaction layer.

---

[5] Although these result from the Arrhenius assumption, similar dependencies should be expected from any appropriate expression for the reaction rate.

T_{ad} depends on both the exothermicity or heating value of the fuel, and also on the equivalence ratio ϕ of the premixed gases:

$$\phi = \frac{(Y_F / Y_O)}{(Y_F / Y_O)_{st}} \qquad \textbf{(2.25)}$$

where Y_F and Y_O are the total mass fractions of fuel and oxidiser respectively and the subscript st refers to stoichiometric conditions. Thus for stoichiometric flames ϕ = 1. For lean flames, ϕ < 1, an excess of oxidiser is present in the reactants and the adiabatic flame temperature is reduced from its maximum value (note that the maximum T_{ad} does not necessarily correspond to ϕ = 1 due to non-unity Lewis number effects). A fundamental limit for premixed flames is revealed here, since for a fuel with activation temperature T_a (related to the activation energy $E_1 = T_a R^0$), if the equivalence ratio is reduced such that $T_{ad} \leq T_a$ then the chain-branching reactions responsible for driving the combustion process will cease to be initiated and the flame will extinguish.

The effect of non-unity Lewis numbers is not revealed in the above analysis although has important consequences particularly for strained and curved flames as discussed in the next section. The assumption of Le = 1 is made for convenience rather than necessity here but is a reasonable assumption for moderately lean methane-air flames. For pure hydrogen-air flames however Le $\approx$ 0.3, reflecting the high mobility of both molecular and atomic hydrogen, and these flames respond very differently in unsteady flows.

Under the assumption of a one-dimensional flame, no consideration is given to any tangential gradients in the flow field or geometric variation of the flame surface, and it is assumed to be unstrained, planar and steady state. In extending the study of laminar flames into more than one dimension, taking this into account is therefore one of the first requirements.

2.2.2 Flame stretch

A propagating flame in a multi-dimensional flow may be both curved, due to the underlying geometry or distortion by turbulent eddies, and subject to steady or unsteady tangential straining. These act to increase or decrease the surface area of a local flame element depending on the flame configuration and flow conditions, and are referred to collectively as flame stretch. To discuss flame stretch some quantities are first needed to properly define the flame surface.

The reaction progress variable, c, represents the state of completion of the reaction, and varies from 0 in the reactants to 1 in the products. c can be defined according to any scalar field that varies monotonically through the flame front between two well defined values; most usually the normalised mass fraction of the deficient reactant or temperature are used:

$$c = \frac{Y_F - Y_{F0}}{Y_{F\infty} - Y_{F0}} \qquad \text{or} \qquad c = \frac{T - T_0}{T_\infty - T_0} \tag{2.26}$$

In the case of a one-step reaction with unity Lewis number these definitions are identical. For real flames, and simulations involving multi-component fuels, identifying an appropriate scalar becomes more problematic, and these issues are discussed further with respect to the flame speed in Section 6.3.1.

In general the progress variable $c(x,t)$ is a function of both space x and time t, and an isosurface is defined such that c = constant = c^*. For an elemental area A on the $c = c^*$ surface the stretch rate k is defined as the rate of change of area per unit area:

$$k = \frac{1}{A}\frac{dA}{dt} \tag{2.27}$$

Following Pope [17] k may also be expressed as a sum of the contributions due to: fluid velocity u_i, surface displacement speed s_d and curvature K_m[6], where the displacement speed of the surface is defined from the absolute surface velocity V_i as

$$s_d n_i = V_i - u_i \tag{2.28}$$

and the unit normal vector n_i of the surface is

$$n_i = -\frac{1}{|\nabla c|}\frac{\partial c}{\partial x_i} \tag{2.29}$$

where the negative sign reflects the convention that $\vec{n}$ points in the direction of the reactants.

The stretch rate can now be written

$$k = (\delta_{ij} - n_i n_j)\frac{\partial u_i}{\partial x_i} + s_d \frac{\partial n_i}{\partial x_i} = a_T + s_d K_m \tag{2.30}$$

from which the underlying sources of stretch become apparent. The first term represents the divergence of the fluid velocity in the tangent plane, or tangential strain rate a_T. The second term represents the product of the surface displacement speed with the curvature, which can also be expressed in terms of the principal radii of curvature R_1 and R_2:

$$K_m = \frac{\partial n_i}{\partial x_i} = \left(\frac{1}{R_1} + \frac{1}{R_2}\right) \tag{2.31}$$

---

[6] The subscript m refers to the mean of the local curvature, which for an isoline is identical to the single value of principal curvature. The m is retained here for notational clarity – in particular to avoid confusion with total stretch k.

Stretch affects the flame in two fundamental ways. The most important is the production (or destruction for negative stretch rates) of flame surface area leading to an increase (decrease) in overall fuel consumption. A secondary, though important, effect relates to the deviation of the displacement speed s_d from the planar, unstrained laminar value s_L^0. A positively stretched flame will have increased mass concentration and thermal gradients in the direction normal to the flame front, and so the diffusion of heat away from the flame and of unburnt reactants towards the flame will increase in proportions determined by the Lewis number.

For $Le < 1$, the diffusion of mass exceeds the diffusion of heat, so when subjected to positive stretch the concentration of reactants in the inner layer increases while diffusion of heat away from the inner layer increases by a lesser amount, leading to an overall increase in the burning intensity and therefore also s_d. As well as being important in predicting s_d, this also indicates a potential thermo-diffusive instability for some sub-unity Le flames – most notably lean hydrogen-air flames. At very low Lewis numbers ($Le < 0.6$) the increase in s_d due to positive stretch in positively curved regions (convex towards the reactants) causes the flame to accelerate into the fresh gases, while slowing down in negatively curved. This leads to enhanced wrinkling and an increase in flame surface area, combined with local extinctions in the negatively curved regions.

.For $Le > 1$, the converse is true; positive stretch leads to a reduction in s_d and the flame is thermo-diffusively stable.

In characterizing the influence of stretch on a flame it is useful to introduce a non-dimensional number that also takes into account the response time of the flame: the Karlovitz number Ka ;

$$Ka = \frac{t_c}{t_f} = \frac{k\delta}{s_L^0} \qquad \textbf{(2.32)}$$

t_c and t_f are the characteristic times associated with flame and flow respectively, and δ is the diffusive thickness of the flame, estimated as

$$\delta = \frac{\lambda}{\rho_0 C_p s_L^0} \tag{2.33}$$

Asymptotic analysis [11], corroborated by experimental evidence gathered over a wide range of fuels [18,19] shows that the flame speed varies linearly with stretch rate for small values of stretch, allowing use of the approximate relation

$$\frac{s_d}{s_L^0} = 1 - \frac{L_M}{s_L^0} k \tag{2.34}$$

The gradient L_M has the units of length and is often normalised by the diffusive flame thickness as $Ma = L_M / \delta$, where L_M and Ma are known as the Markstein length and Markstein number respectively. Combining Eq. 2.32 and Eq. 2.34 with the definition of the Markstein number it can also be seen that

$$\frac{s_d}{s_L^0} = 1 - MaKa \tag{2.35}$$

Values for the Markstein coefficients differ depending on the definition of the flame speed used. Displacement speeds are commonly used in laminar-flow experimental studies since this is most easily calculated from measurements of the fluid velocity and knowledge of the flow configuration, although identification of a suitable position in the flame from which to take measurements is not obvious and can lead to ambiguities when comparing results.

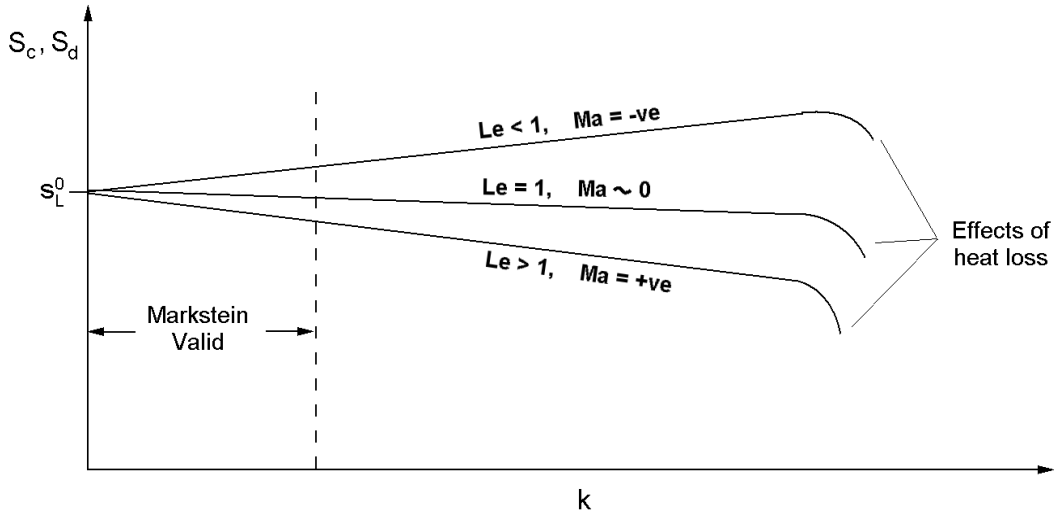

Figure 2.2 Schematic illustration of flame speed variation due to stretch.

The basic flame response for different Markstein numbers is illustrated in Fig 2.2 above. Several canonical experimental configurations exist for determining Markstein numbers; planar stagnation flow flames [18,19], and outwardly propagating spherical flames [20] being the most prevalent. Evaluating Markstein numbers, particularly for Lewis numbers close to unity is problematic and considerable scatter is found in the reported figures. Due to the close coupling of chemical and transport processes that lie behind flame-speed stretch effects, these flows also offer a challenge to numerical simulations. Accurate treatment of transport processes, heat loss and chemical mechanisms are all required in order to calculate Markstein numbers numerically with reasonable accuracy. Prediction of the non-linearity observed at high stretch rates, including the onset of the turning point shown in Fig 2.2 and flame quenching, are more challenging still, and so simplified, one-dimensional configurations are generally used [21,22].

It should also be noted that Markstein type (i.e. linear) behaviour is only observed for moderately unsteady stretch rates. Detailed one-dimensional simulations [23,24] have shown that for unsteady oscillations in the stretch rate the flame response is attenuated and shifted as the frequency increases, such that the flame can withstand much higher stretch rates than under steady state conditions.

2.3 Freely Decaying Homogeneous Isotropic Turbulence

The classical view of the turbulence cascade comes from research into meteorological flows by Richardson in 1922, later substantially refined by the work of Kolmogorov in 1941. Under Richardson's phenomenology, kinetic energy enters the system from large-scale shear flows or body forces that depend on the initial conditions or boundary geometry. These large scale structures then degenerate into more homogenous integral-scale or energy-containing eddies of characteristic length l_0, time τ_0 and velocity u_0.

These integral scale eddies 'break up' due to their inherent instability into successively smaller and smaller eddies; the process repeating itself to form an energy cascade until at the smallest scales the energy is dissipated by viscous forces.

The turbulence can be characterised through a turbulent Reynolds number based on the integral scale length and velocity:

$$\mathrm{Re}_t = (u' l_0)/\nu \tag{2.36}$$

where u' is the r.m.s. velocity fluctuation and is assumed to be $u' \approx u_0$.

A basic assumption of the cascade is that Re_t is large, such that the process of eddy break up and energy transfer to the smallest scales is essentially inviscid over a significant range of scales, and that the dissipation range simply adjusts to whatever is passed to it from larger scales eddies.

This basic phenomenology was refined considerably by Kolmogorov [25] who made a series of hypotheses about the statistical properties of the eddies at scales below the integral length scale. Under this view the integral length scales, containing the bulk of the kinetic energy, are non-isotropic and dependent on the mechanism of turbulence generation and boundary conditions. Sufficiently far below this scale ($l \approx l_0/6$ for example [26]) the statistical properties of the flow become homogeneous (invariant to translations in space) and isotropic (invariant to rotations and reflections), and are independent of the initial conditions. This Universal Equilibrium Range can be further

subdivided into the inertial range and dissipation range. The inertial range is controlled by inviscid processes and is therefore determined only by the rate of transfer of energy from the larger scales. The dissipation range, where viscous forces are significant, is determined by both the rate of transfer of energy from the larger scales and the viscosity ν.

The smallest scales of the flow, or Kolmogorov scales, are denoted η, τ_η, and u_η for length, time, and velocity respectively. By making some additional assumptions it is possible to relate the Kolmogorov scales to the energy containing integral range through scaling laws that depend only on the viscosity ν, and dissipation rate of kinetic energy ε.

The rate at which energy enters the cascade T can be estimated from the integral scales as

$$T \approx \frac{u_0^2}{(l_0/u_0)} \approx \frac{u_0^3}{l_0} \qquad \textbf{(2.37)}$$

By also assuming that this rate of energy transfer is approximately constant at all scales, then a balance must exist between this rate of transfer and the dissipation: $\varepsilon \approx T \approx u_0^3/l_0$.

The dissipation rate can be estimated from the rate of strain associated with Kolmogorov scale eddies, such that $\varepsilon \approx 1/\tau_\eta \approx u_\eta/\eta$:

$$\varepsilon \approx \nu u_\eta^2/\eta^2 \approx u_0^3/l_0 \qquad \textbf{(2.38)}$$

Finally, the Kolmogorov scales may be characterized by a Reynolds number of order unity since the inertial forces at this scale must be comparable to the viscous forces for dissipation to become significant. Therefore $u_\eta \eta \approx \nu$, and the following relations can be formed

$$\eta / l_0 \approx (u_0 l_0 / \nu)^{-\frac{3}{4}} = \mathrm{Re}_t^{-\frac{3}{4}} \quad \textbf{(2.39)}$$

$$u_\eta / u_0 \approx (u_0 l_0 / \nu)^{-\frac{1}{4}} = \mathrm{Re}_t^{-\frac{1}{4}} \quad \textbf{(2.40)}$$

$$\tau_\eta / \tau_0 \approx (u_0 l_0 / \nu)^{-\frac{1}{2}} = \mathrm{Re}_t^{-\frac{1}{2}} \quad \textbf{(2.41)}$$

And in the Inertial Subrange which is independent of ν,

$$u(l) \approx u_0 (l / l_0)^{\frac{1}{3}} \quad \textbf{(2.42)}$$

$$\tau(l) \approx \tau_0 (l / l_0)^{\frac{2}{3}} \quad \textbf{(2.43)}$$

The relations given in Eqs. 2.39 – 2.41 show that as the size and velocity of the integral scales, and therefore the turbulent Reynolds number, increases, the Kolmogorov scales decrease until a balance is achieved between the energy flux and the viscous dissipation.

2.3.1 The Energy Spectrum

Knowledge of the distribution of kinetic energy among the various scales present in the flow is important in understanding the dynamics of the cascade process and the decay of energy. From a DNS point of view, an initial velocity field must be specified that is a good approximation to the distribution expected in real flows with similar dimensions. Too large a deviation from this will result either in questionable data being extracted if no time is allowed for the turbulence to evolve, or unnecessary computation time while the spectrum adopts an appropriate form.

The Energy Spectrum function $E(k)$, defined in wavenumber space k, describes this distribution and is therefore of central importance. Transformations between wavenumber space and real space are achieved through the Fourier / inverse Fourier

transform, where for an arbitrary real space function $f(x)$ and its Fourier space equivalent $g(k)$ the transform pair is defined[7]

$$g(k) = Ft\{f(x)\} = \frac{1}{2\pi}\int_{-\infty}^{\infty} f(x)e^{-ikx}dx \quad \textbf{(2.44)}$$

$$f(x) = Ft^{-1}\{g(k)\} = \int_{-\infty}^{\infty} g(k)e^{ikx}dk \quad \textbf{(2.45)}$$

A real-space function that provides some information on the structure or level of coherence of the velocity fluctuations is first required, and this is provided by the two-point velocity correlation, or autocovariance tensor,

$$R_{ij}(\vec{r},t) = \left\langle u_i(x,t)u_j(x+\vec{r},t)\right\rangle \quad \textbf{(2.46)}$$

where $\vec{r}$ is the spatial separation of the points. In general R_{ij} is also a function of x but for homogeneous flows this dependence can be dropped.

Taking the transform (for each spatial dimension) of R_{ij} produces the velocity spectrum tensor ϕ_{ij}

$$\phi_{ij}(\vec{k},t) = Ft\{R_{ij}(\vec{r},t)\} \quad \textbf{(2.47)}$$

which when integrated through all wavenumber directions gives the energy spectrum as a function of the scalar wavenumber k

$$E(k) = \iiint \frac{1}{2}\phi_{ii}(\vec{k},t)\delta(|\vec{k}| - k)d\vec{k} \quad \textbf{(2.48)}$$

---

[7] Alternative definitions of the Fourier transform pair are used, but vary only in the position of the constant $1/2\pi$ and the negative sign in the exponent. The version here follows Pope [25].

$E(k)$ therefore represents the kinetic energy of wavenumbers in the range $k \to (k + dk)$ and has the property

$$KE = \frac{1}{2}\langle u_i u_i \rangle = \int_0^\infty E(k)dk \qquad \textbf{(2.49)}$$

The directional information contained in the velocity spectrum tensor ϕ_{ij} is lost in the integration of Eq. 2.48, however for isotropic flows this information is redundant, and under these conditions $E(k)$ can also be used to calculate additional quantities based on the velocity derivatives, including the dissipation rate ε

$$\varepsilon = \int_0^\infty 2\nu k^2 E(k)dk \qquad \textbf{(2.50)}$$

The integral length scale l_0 is defined by integrating the longitudinal velocity correlation function $f(r) = R_{11}(r\hat{e}_1)/u^2$ over r, and can be evaluated either from the real-space velocity correlation tensor

$$l_0 = \int_0^\infty f(r)dr = \frac{1}{u^2}\int_0^\infty R_{11}(r\hat{e}_1)dr \qquad \textbf{(2.51)}$$

or equivalently from the energy spectrum directly

$$l_0 = \frac{1}{u^2}\int_0^\infty \frac{1}{4k} E(k)dk \qquad \textbf{(2.52)}$$

Where the time dependence of l_0, f and R_{11} remains but has been omitted for clarity.

A convenient real-space interpretation of $E(k)$ is to associate it with the energy contained in eddies of size $l \approx 2\pi/k$. This is a reasonable approximation for l in the inertial range but becomes increasingly misleading for $l << l_0$ and $l \sim \eta$.

The form of the energy spectrum for high Reynolds number flows is illustrated schematically in Fig 2.3 on a log-log plot of $E(k)$ versus k. The existence of the region in the universal equilibrium range with a –5/3 exponential dependence on k was predicted by Kolmogorov and has been confirmed for many types of flow across a wide range of (relatively large) Reynolds numbers.

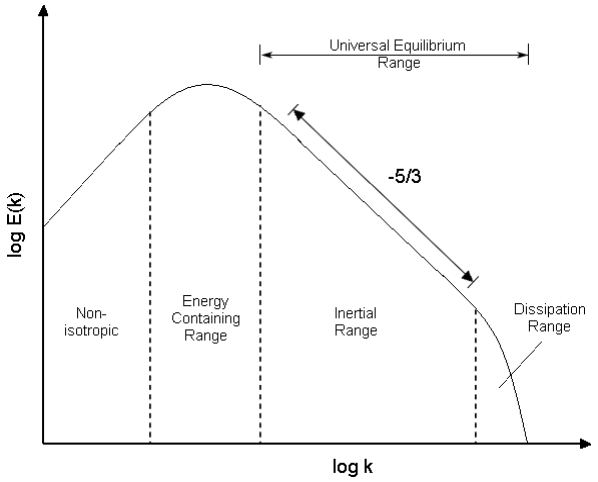

Figure 2.3 Schematic example of the energy spectrum for high Reynolds number turbulence on a log-log plot highlighting the –5/3 dependence in the inertial range.

The problem with this picture at the low Reynolds number flows of interest in this study is illustrated in Fig 2.4. It can be seen that as the turbulence bandwidth narrows, a considerable overlap exists between the energy-containing and dissipation ranges. In addition, simulations have shown [27] that far from being confined to Kolmogorov scale eddies, dissipation becomes significant at scales of the order $l \sim 30\eta$. Under these conditions Kolmogorov's second similarity hypothesis does not hold and there is no range of eddies with a structure independent of ν, and hence no appreciable inertial sub-range.

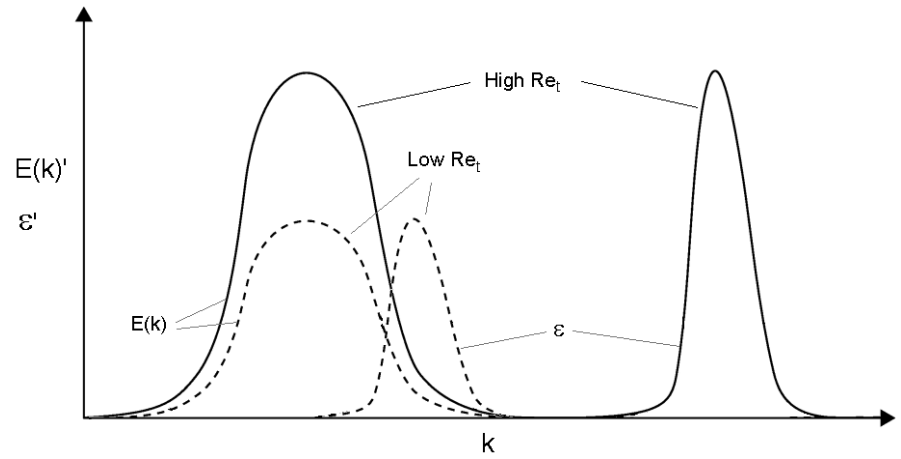

Figure 2.4 Schematic distribution of normalised energy E(k)' and dissipation ε' ranges for high and low Reynolds number flows.

2.3.2 The Final Period of Decay

Although the high-Reynolds-number assumption used in Kolmogorov's analysis is not explicitly defined, most combustion DNS is carried out at Reynolds numbers well below this level, and so it is useful to consider how the spectrum and its evolution differ under these conditions.

Batchelor and Townsend [28] identified conditions under which, for very low Reynolds numbers, the non-linear inertial terms in the Navier-Stokes equations became negligible. They refer to this as the Final Period of Decay.

From measurements taken in grid-generated turbulence, two important analytical results were shown to hold in this regime:

$$u^2 \propto t^{-5/2}, \qquad f(r,t) = e^{-r^2/8\nu t} \tag{2.53}$$

for sufficiently large t.

For turbulent Reynolds numbers approaching this final period, but where some inertial energy transfer is still present, Schumann and Patterson [29] numerically investigated two candidate spectra that are expected to evolve as Eq. 2.53

$$E(k) = 16\sqrt{\frac{2}{\pi}}u^2 \frac{k^4}{k_p^5} e^{-2\left(\frac{k}{k_p}\right)^2} \quad \textbf{(2.54)}$$

$$E(k) = u^2 \frac{k}{k_p^2} e^{\left(\frac{-k}{k_p}\right)} \quad \textbf{(2.55)}$$

Where u is the rms velocity fluctuation and k_p the peak wavenumber which identifies the wavenumber associated with the energy containing eddies. Both spectra were found to match experimental findings for two-point velocity correlations and energy decay reasonably well, but Eq. 2.55 fails to reproduce the expected inertial energy transfer as seen by tracking the skewness of the velocity derivative S through time,

$$S = \left\langle \left(\frac{\partial u_1}{\partial x_1} \right)^3 \right\rangle \Bigg/ \left\langle \left(\frac{\partial u_1}{\partial x_1} \right)^2 \right\rangle^{\frac{3}{2}} \quad \textbf{(2.56)}$$

which should be non-zero and approximately constant in freely decaying flows. A reduction in S over time indicates that the expected transfer of energy is being interrupted, typically by high wavenumber cut-off or inadequate resolution of the Kolmogorov scales.

2.3.3 Two-Dimensional Turbulence

While the study of two-dimensional turbulence does have some applications to real flows, such as in meteorology where the out-of-plane component of the flow on a large scale is negligible, for combustion DNS it is simply a matter of practicality. As mentioned previously the governing equations for a multi-component, three-dimensional, reacting flow remain unsolvable in their full form, so depending on the features of interest, omitting a spatial dimension can be the best option since it is often the case that accurate chemical kinetics are of greater importance than the correct turbulence dynamics.

An important finding from three dimensional combustion DNS is that the most probable shape of the flame is cylindrical [30], which to some extent supports the extrapolation of two-dimensional data to three-dimensional flames. Important differences exist between the two configurations however, principally with regard to time dependent behaviour such as the decay of energy, enstrophy, and the evolution of the energy spectrum. This is particularly important for intrinsically non-steady flames like the flame kernel where the history of the flow cannot properly be ignored.

To appreciate the differences between the two flows it is useful to consider the transport equation for vorticity $\vec{\omega} = \nabla \times \vec{u}$ in an incompressible fluid

$$\frac{\partial \vec{\omega}}{\partial t} + (\vec{u} \cdot \nabla)\vec{\omega} = (\vec{\omega} \cdot \nabla)\vec{u} + \nu \nabla^2 \vec{\omega} \qquad \textbf{(2.57)}$$

The first term on the RHS of Eq. 2.57 represents changes in ω due to 'stretching' or changes in the moment of inertia due to deformation, and the second is a diffusive term accounting for changes due to viscous forces. In three-dimensional turbulence the stretching term is fundamental to the cascade process; allowing the vorticity to intensify until a balance is achieved between inertial energy flux and viscous dissipation. By this mechanism, the decay of kinetic energy in 3D turbulence is governed by the rate of break up of the large scale eddies and is independent of ν.

In two-dimensional turbulence however, it can be seen that since $\omega_x = \omega_y = u_z = 0$ (if z is the out-of-plane dimension), this term no longer contributes and no stretching or intensification of vorticity is possible. The consequences of this are as follows

- Global kinetic energy is almost conserved in 2D turbulence for high Reynolds numbers. Vorticity is also almost conserved and behaves in a similar way to a passive scalar.
- In fully developed 2D turbulence the enstrophy, $\omega^2/2$, passes from larger to smaller scales, in some ways analogous to the cascade of energy in 3D.
- In complete contrast to 3D turbulence, an 'inverse cascade' of energy takes place in 2D, where kinetic energy accumulates in larger scale eddies which grow with time.

The exact mechanisms for the observed behaviour are not yet well established but the implications for two-dimensional DNS are clear. Statistics taken from fully developed fields of 2D and 3D turbulence with equivalent Reynolds numbers will be qualitatively different and this needs to be considered when making comparisons. For statistically non-steady flames the differences are even more marked, in particular the 'inverse cascade' of energy in 2D, which over longer time scales could significantly affect the development of a simulated turbulent flame.

3 Literature Review

3.1 Regimes of Turbulent Combustion

Turbulent combustion refers to a broad range of conditions under which unsteady combustion takes place. The complex interdependencies between the flow variables and the chemistry have so far prevented the development of a universal phenomenological framework to describe the various processes. It has therefore been necessary to divide the general process of turbulent combustion into identifiable regimes based on characteristic parameters of the flow and chemistry, within which a particular phenomenological model can be expected to remain valid. The exact number and type of these regimes as well as the positions of the regime boundaries remain active areas of debate. However, their existence allows progress to be made by developing the various turbulent combustion models along independent lines, which can then be applied *ad hoc* according to the expected regime(s) in any particular situation.

An important concept in turbulent combustion is that of the flamelet. Beginning with the ideas of Damkohler in the 1940s [31], and proposed by Williams in the context of turbulent diffusion flames [32], the turbulent flame can be regarded as a thin propagating surface suspended in a field of turbulence. Under this analysis the flame is thin and fast compared to the characteristic lengths and times of the surrounding eddies, and retains a quasi-laminar structure whilst being wrinkled and stretched by the turbulence.
The advantage of this approach is that it partially decouples the combustion process from the turbulence, allowing them to be handled separately in numerical codes, with the interaction reduced to some key parameters, the most important being flame stretch and the production of flame surface area by the turbulent eddies.

To characterise the interaction of the flame with the turbulence two non-dimensional numbers are commonly used: the Damkohler and Karlovitz numbers.

The Damkohler number, $Da = \tau_0 / \tau_f = l_0 / u' \tau_f$, relates the integral time scale, τ_0, to the flame time and characterises the interaction of the flame with the integral-scale turbulent eddies. Similarly, the Karlovitz number characterises the interaction of the flame with the Kolmogorov scales, $Ka = \tau_f / \tau_\eta$. A second Karlovitz number $Ka_r = \tau_{fr} / \tau_\eta$ is also useful since in a premixed flame the reaction occurs in a region considerably thinner than that characterised by the time scale τ_f , and the influence of eddies with this layer may be of greater importance, particularly for combustion near the regime boundaries. According to Peters [33] this reaction layer time scale can be estimated as $\tau_{fr} \approx 0.1 \tau_f$.

Classical regime diagrams, or Borghi diagrams, can be constructed for statistically planar turbulent flames using the non-dimensional length and velocity scale ratios l_0 / δ, and u' / s_L , where δ is typically taken to be the diffusive thickness of the flame δ. Plotted on a log-log scale to accommodate the full range of turbulence, different regimes can be identified, delimited by the values of the Damköhler and Karlovitz number that represent the limits of influence for eddies at the extremes of the turbulent spectrum.

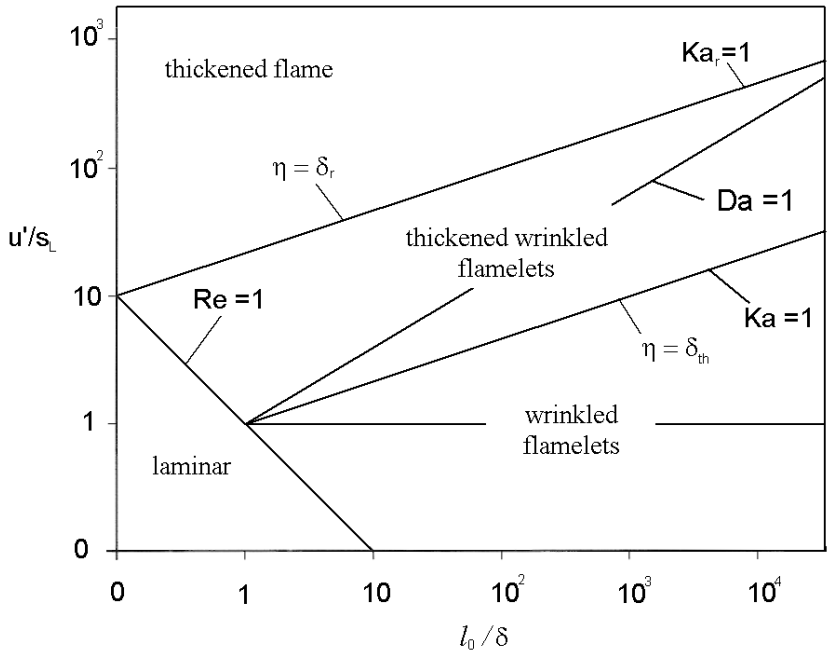

Figure 3.1 Modified regime diagram following Peters [3] **plotted on a log-log scale.**

The justification behind using the Damkohler and Karlovitz numbers to mark the regime boundaries is that away from unity ($Da >> 1$ and $Ka << 1$), a degree of scale separation exists that reduces the ability of the eddies to alter the flame structure. When $Da >> 1$ and $Ka << 1$ neither integral or Kolmogorov scale eddies are able to induce prolonged strain on the flame since the flame is able to respond on a shorter time scale and hence retain a laminar or quasi-laminar structure. In the wrinkled flamelets region as shown in Fig 3.1, where $Da \sim 1$ and $Ka << 1$, integral scale eddies are able to strain and wrinkle the flame front, thereby altering the mean rate of fuel consumption through increases in the total flame area and changes to the local flame speed due to stretch. Kolmogorov scales eddies remain unable to affect the quasi-laminar structure. For the region $Da \sim 1$, $Ka \sim 1$ and $Ka_r < 1$, marked the thickened-wrinkled flamelets region in Fig 3.1, small scale eddies are able to penetrate scales of the order of the diffusive flame thickness and so thicken the flame by enhancing the transport of heat and species in this zone. The reaction layer remains largely unperturbed however, and so flamelet like behaviour can still be assumed in this region. For higher turbulence intensities where $Da < 1$, $Ka > 1$ and $Ka_r \geq 1$, a flamelet like structure can no longer be assumed and the regime is characterised by a discontinuous flame front, significant thickening of the preheat zone by small scale eddies, and in the limit of very short turbulence time scales all wave-like behaviour is lost and combustion may continue in the homogeneous regime of a well-stirred reactor, where the mixing of reactants and products is assumed to be perfect.

The regions identified in this classical analysis are known to have only a very approximate validity when compared to observations of real flames, in particular, the onset of quenching for high Ka numbers has been found to be over predicted by the $Ka_r \geq 1$ criterion [34]. More generally, identifying a combustion process as a single point on the regime diagram excludes information about the full range of eddies acting on the flame and their effectiveness in quenching the flame, and does not take into account other important factors such as heat release or heat losses due to radiation.

As an intermediate configuration between the stretched laminar flame and the fully developed turbulent flame, many studies have focussed on the interaction of initially laminar flames with a single vortex or vortex pair, both numerically [5,35,36] and

experimentally [37]. The advantage of this configuration is that it combines well defined and repeatable initial conditions with a more realistic interaction between the flame and a turbulent eddy. Meneveau and Poinsot [38] use this approach to construct the ITNFS (Intermittent Turbulence Net Flame Stretch) model for the total stretch experienced by the flame from all scales of turbulence based on the effectiveness of eddies at each scale and velocity to distort the flame surface.

From these studies alternative regime diagrams have been constructed [5] which consider the full spectrum of eddies encountered by the flame, and these 'spectral diagrams' can, if required, be mapped onto the corresponding classical regime diagrams for comparison. Extensions to the classical regime diagram have also been suggested [39] which include numerical considerations such as the resolution or filter width, enabling the most appropriate combustion model to be selected based on both the expected combustion regime and the computational resources available.

In all the above examples, a fully developed, statistically planar flame is assumed, but for a developing flame kernel additional complications are introduced which prevent the direct application of the same criteria for regime identification. The presence of mean curvature alters both the unperturbed flame speed (dependent on the Lewis number of the mixture), the total stretch experienced by the flame surface, and also the geometrical configuration presented to the vortex or eddy. The velocity fluctuations are reduced from u' due to convection of the kernel by larger eddies and the entire system is evolving in time due to kernel growth and decaying turbulence.

Of particular relevance in this regard is recent work by Echekki and Kolera-Gokula [36] who have studied the interaction of an isolated vortex pair with initially laminar flame kernels of different radii, and which addresses some of the considerations mentioned above. By introducing the alternative non-dimensional scaling parameters $u_{\theta,\max}/s_L$ and R_v/R_f, where $u_{\theta,\max}$ is the maximum tangential velocity of the vortex and R_v and R_f are the vortex and flame radii respectively, a series of regimes were identified with similarities to the classical Borghi/Peters analysis:

- Laminar kernel regime: Little or no influence on the laminar flame propagation

- Wrinkled kernel regime: Significant straining of flame surface leading to increased flame area and burning rate. Flame front remains intact throughout.
- Breakthrough regime: Local extinction of the flame front occurs, recovery to continuous flame front or transition to global extinction dependent on vortex size and velocity.
- Global extinction regime.

These approximate regimes are shown in Fig 3.2 on a linear scale. Also indicated in Fig 3.2 are a series of suggested limit lines for the velocity and radii ratios respectively: (I) is the laminar kernel upper velocity limit $(u_{\theta,\max}/s_L)(\rho_b/\rho_u) \approx 1$, (II) is the breakthrough regime lower velocity limit $(u_{\theta,\max}/s_L)(\rho_b/\rho_u) \approx 2$, (III) is the size limit R_v/R_f << 1 below which no wrinkling is possible, and (IV) shows the limit $R_v/R_f \approx 1$ between the breakthrough regime and possible global extinction.

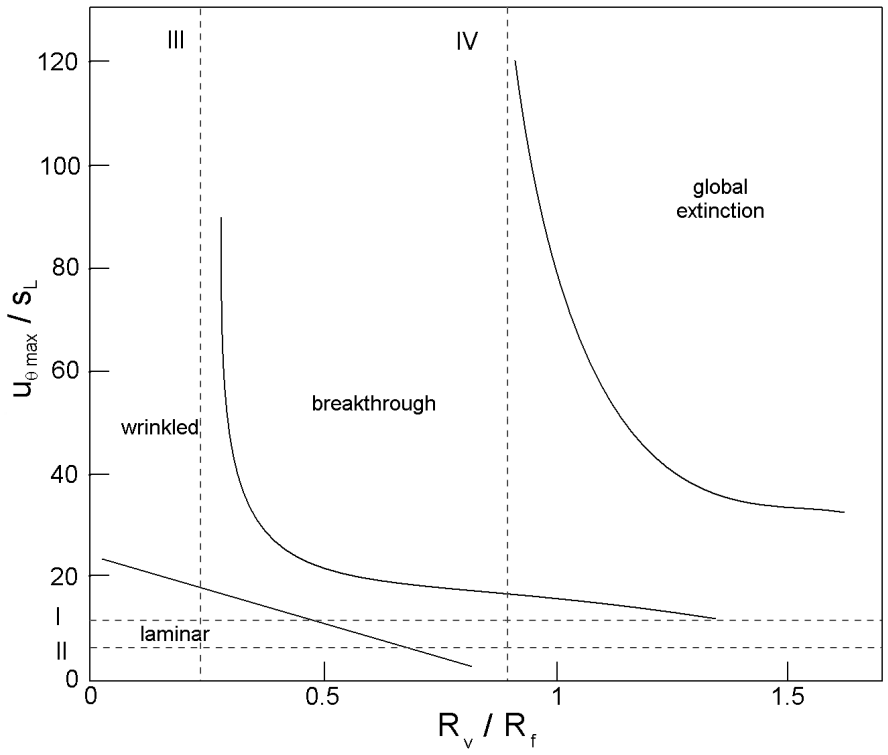

Figure 3.2 Kernel /vortex regime diagram from Echekki and Kolera-Gokula [36]**.**

3.2 Turbulent Flame Simulation and Modelling

Beyond the simplified configurations available to DNS, any attempt to simulate larger scale flows with more complex geometries requires that the computational effort be focused on resolving the largest structures present in the flow, since it is these that dominate the solution, and models must be used to account for the missing or unresolved information. This approach relies on the fact that, at the scales of interest, the small scale fluctuations will tend to have a universality that is independent of the mean flow, and therefore also a degree of statistical predictability that can be adequately captured by these models.

Strategies that have been developed to provide this modelling closure can be divided into three approximate categories: mixing-based models, one-point statistical models, and geometrical or flamelet based models. Under the first two of these, no assumptions are made *a priori* about the existence of a coherent flame surface. The mixing based approach (described further in §3.3.2) considers that, to leading order, the reaction progress variable behaves as a passive scalar, and that the rate of heat release is controlled principally by the rate of turbulent mixing between the reactants and products. Statistical models such as the pdf method (§3.3.3), whilst again avoiding the need to make any assumptions about the specific mode of combustion, explicitly take into account the chemistry by estimating one-point probability distributions for the species mass fractions, together with the non-reacting flow variables. Flamelet models on the other hand, differ from these last two in that a pre-existing, active flame surface is assumed from the outset, and the rate of combustion is evaluated from the geometric evolution of this surface due to propagation, and distortion by the turbulence.

While these models are developed from different phenomenological starting points, they are also in some sense equivalent since they aim to represent the same underlying physical processes, and this allows straightforward algebraic expressions to be derived [41] that relate the key quantities.

The precise implementation of any given model, however, depends also on the type of simulation being undertaken. The most prevalent of these at present, adapted originally from non-reacting flow solvers, are RANS, and more recently LES.

3.2.1 RANS

In Reynolds-Average Navier-Stokes Simulations (RANS), all quantities are split into mean and fluctuating components. When dealing with the large density variations associated with heat release in reacting flows it is most convenient to work with the Favre, or density-weighted mean and fluctuating components, where for an arbitrary quantity Q : $Q = \tilde{Q} + Q''$, where $\tilde{Q} = \overline{(\rho Q)} / \overline{\rho}$, and $\tilde{Q}'' = \overline{\left[\rho\left(Q - \tilde{Q}\right)\right]} / \overline{\rho} = 0$.

Applying this decomposition to the governing equations leads to additional terms representing the contribution of small scale fluctuations to the mean quantities. For example, the transport equation for species k becomes:

$$\frac{\partial \overline{\rho} \tilde{Y}_k}{\partial t} + \frac{\partial}{\partial x_i}\left(\overline{\rho} \tilde{u}_i \tilde{Y}_k\right) = -\frac{\partial}{\partial x_i}\left(\overline{V_{k,i} Y_k} + \overline{\rho} u_i'' Y_k''\right) + \overline{\dot{\omega}_k} \qquad \textbf{(3.1)}$$

Similar averaging of the full set of equations leads to additional unclosed terms that also require modelling – in particular the Reynolds stresses appearing in the momentum equation and turbulent enthalpy flux in the energy equation - but from a combustion point of view the three terms on the RHS of Eq. 3.1 represent the main quantities of interest. For large Reynolds numbers, the laminar diffusive fluxes, represented by $\overline{V_{k,i} Y_k}$, are usually small compared to the turbulent transport and so are often neglected in practice. The remaining RHS terms represent the turbulent flux and mean reaction rate respectively. Turbulent fluxes are most often modelled using a gradient assumption according to

$$\overline{\rho} u_i'' Y_k'' = -\frac{\mu_t}{Sc_{kt}} \frac{\partial \tilde{Y}_k}{\partial x_i} \qquad \textbf{(3.2)}$$

where μ_t is a turbulent viscosity and Sc_{kt} is a turbulent Schmidt number for species k. The gradient assumption is valid at high turbulence Reynolds numbers but has been found to fail under certain conditions where the pressure change across the flame front

is significant and can drive the turbulent flux in the opposite direction to that suggested by Eq. 3.2.

Accurate modelling of the mean reaction rate term $\overline{\dot{\omega}}$, is the most important consideration for accurate RANS solutions, and has been the focus of much research. However, a widely applicable closure strategy has, so far, proved elusive; many alternative approaches have been suggested, the most prominent of which are outlined later in this section.

3.2.2 LES

In some ways a compromise between the resolution of DNS and the scale and flexibility of RANS, Large Eddy Simulations (LES) aim to compute all unsteady flow features above a particular physical size, defined by the filter width. The inherent unsteadiness of the solution means it perhaps has more in common with DNS than with results typically obtained from RANS, although it should be noted that unsteadiness can also be accommodated in RANS provided sufficient separation of the time scales involved.

Similar to RANS the quantities of interest are split into resolved and un-resolved parts: $Q = \tilde{Q} + Q''$. In LES these represent the filtered and sub-grid components respectively. The filtering operation is, again, most conveniently done on Favre or density weighted quantities according to

$$\overline{\rho}\tilde{Q}(\vec{x}) = \int \rho Q(\vec{x}^*) F\left(\vec{x} - \vec{x}^*\right) d\vec{x}^* \qquad \textbf{(3.3)}$$

were the filter $F(\vec{x})$ may be defined in spectral or physical space for filter width Δ. The most commonly used types of filter are: a spectral cut-off filter

$$\overline{F}(k) = \begin{cases} 1 & \text{if } k \leq \pi/\Delta \\ 0 & \text{otherwise} \end{cases} \qquad \textbf{(3.4)}$$

a physical-space box filter

$$F(\vec{x}) = \begin{cases} 1/\Delta^3 & \text{if } |x_i| \leq \Delta/2 \\ 0 & \text{otherwise} \end{cases} \quad \textbf{(3.5)}$$

and a physical-space Gaussian filter

$$F(\vec{x}) = \left(\frac{6}{\pi\Delta^2}\right)^{\frac{3}{2}} e^{\left(-\frac{6x_i^2}{\Delta^2}\right)} \quad \textbf{(3.6)}$$

Applying one of the above filters to the governing equations results in unclosed terms which are formally similar to the equivalent produced in RANS, and also require modelling to close the equations. Compared to RANS, a considerably higher level of detail is available for modelling of the sub-grid terms in LES due to the resolved part of the spectrum, however, these models are derived from the same underlying phenomenological arguments.

3.2.3 Flamelet Modelling Approaches

From the relation between the premixed flame structure and the turbulence spectrum as schematised in the combustion regime diagrams of Section 3.1, it can be seen that for a wide range of flow conditions relevant to practical combustion devices, combustion occurs within a thin and fast layer relative to the surrounding flow. This observation, originating in the work of Damköhler in 1940 [31], forms the phenomenological starting point for many turbulent combustion models in use today.

Damkohler's original hypothesis states that the increase in turbulent flame speed over the laminar equivalent s_T / s_L^0 is determined principally by the increase in the amount of active flame area A

$$\frac{s_T}{s_L^0} = \frac{A}{A_L} \tag{3.7}$$

For low to moderate levels of turbulence the increase in area is linked to the turbulence intensity and integral and Kolmogorov length scales, but at higher turbulence intensities ($u'/s_L^0 > 6$) this relation weakens and evidence suggests that alterations to the flame structure by the small scales becomes important [42,43]. The precise range of validity of the flamelet assumption remains an open question. Meneveau and Poinsot [38] suggest two possible definitions. The first states that the flame front must be everywhere continuous such that any line passing from the fresh to the burnt gases must cross at least one active flame surface. This is too restrictive for practical purposes since local extinction will not necessarily have a significant impact on the global flame behaviour, and so a looser definition – that the flamelet regime exists if the '[local quenching does not] ...inhibit the growth of the active flame surface', is suggested instead.
[44,45]
Within this general framework the broad class of approaches known collectively as flamelet models have been developed, which make use of the fact that the local structure of the flame can be approximated by that of a laminar flame under similar thermochemical and hydrodynamic conditions. Some of the more widely used formulations are outlined in this section.

3.2.3.1 The Bray-Moss-Libby (BML) Model

The BML model combines the flamelet approach with assumptions on the probability distribution of the progress variable, c, in high Damkohler number flows. Since its introduction in 1977 [46], it has been widely studied and extended, and is used both as a modelling closure strategy, and as an analytical tool capable of revealing some quite subtle phenomena in turbulent flames.

A one-step irreversible reaction with unity Lewis number is assumed, and the reaction progress variable c is introduced to represent the state of the reaction. For a given location and time, the probability distribution of c may be written

$$\overline{P}(c,\vec{x},t) = \alpha(\vec{x},t)\delta(c) + \gamma(\vec{x},t) f(c,\vec{x},t) + \beta(\vec{x},t)\delta(1-c) \tag{3.8}$$

where δ is the Dirac delta function, and α, γ, and β are the probabilities of finding unburnt ($c = 0$), partially burnt ($0 < c < 1$), and fully burnt ($c = 1$) gases respectively. Under the assumptions of the single-step, unity Lewis number flame, the reaction rate may be expressed solely as a function of c, and therefore the mean reaction rate can be written

$$\overline{\dot{\omega}}(\vec{x},t) = \int_0^1 \dot{\omega}(c)\overline{P}(c,\vec{x},t)dc \tag{3.9}$$

and since $\dot{\omega}(0) = \dot{\omega}(1) = 0$, it follows that

$$\overline{\dot{\omega}}(\vec{x},t) = \gamma(\vec{x},t)\int_0^1 \dot{\omega}(c) f(c,\vec{x},t)dc \tag{3.10}$$

Under this analysis the original problem has been reframed in terms of determining the probabilities α, γ, and β, and the distribution $f(c,\vec{x},t)$. By assuming high Damkohler and Reynolds numbers such that $\gamma \approx 0$ expressions for α and β are readily obtained [41,47]

$$\alpha = \frac{1-\tilde{c}}{1+\tau\tilde{c}} \qquad \text{and} \qquad \beta = \frac{\tilde{c}(1+\tau)}{1+\tau\tilde{c}} \tag{3.11}$$

where the heat release factor $\tau = (T_b - T_u)/T_u$ is introduced.

The assumption that $\gamma \approx 0$ takes the flamelet concept to its logical limit by implying an infinitely thin flame, which clearly cannot be valid when considering the mean reaction rate. An expression may be derived (Eq. 3.12) from manipulation of the transport

equation for c that relates the mean reaction rate to the scalar dissipation rate (SDR), $\overline{\rho}\tilde{\chi} = \overline{\rho D \nabla c \cdot \nabla c}$, a key quantity in turbulent combustion modelling.

$$\overline{\dot{\omega}} = \frac{2\overline{\rho\chi}}{2c_m - 1} \tag{3.12}$$

where c_m is a parameter defined as $c_m = \left(\int_0^1 c\dot{\omega}f(c)dc\right) \Big/ \left(\int_0^1 \dot{\omega}f(c)dc\right)$, and the distribution $f(c)$ can be assumed approximately constant within the integral limits.

Alternatively, the mean reaction rate may also be estimated from the flamelet crossing frequency [48] according to

$$\overline{\dot{\omega}} = 2\dot{\omega}_c \frac{1+\tau}{\left(1+\tau\tilde{c}\right)^2} \frac{c(1-c)}{\hat{T}} \tag{3.13}$$

where $\hat{T}$ is the flame crossing frequency, and $\dot{\omega}_c$ is a reaction rate per flame crossing, both of which must be modelled according to appropriate time scale estimates of the turbulence and flame transit times respectively.

Equation. 3.13 results from an assumed binary, or telegraphic progress variable signal, which is relatively easy to extract from a real flame, and so by formulating the mean reaction rate in this way it provides a convenient link between experiment and model. The equivalence of the two methods of deducing the mean reaction rate expressed in Eqs. 3.12 and 3.13, with one based on turbulent mixing through the SDR and one on a geometrical flamelet analysis, also highlights the connections that exist between the various approaches.

From a modelling perspective, the BML formalism offers a simple but effective framework on which to base closure strategies, however, it also provides considerable insight as an analytical tool, and can been used to predict the occurrence of counter-gradient turbulent diffusion and flame generated turbulence.

3.2.4 Flame Surface Density

The flame surface density (FSD) Σ is defined as the flame surface area per unit volume. An expression for the mean reaction rate in terms of this quantity can therefore be written

$$\overline{\dot{\omega}} = \rho_0 \langle s_c \rangle_s \Sigma \tag{3.14}$$

where s_c is a representative flame speed in the local flame normal direction, and $\langle \ldots \rangle_s$ denotes a surface averaging operation over a suitable scalar isosurface.

The advantage of the FSD approach can be seen in that it partially decouples the effects of thermochemistry and the effects of turbulence through the terms s_c, and Σ respectively, allowing a wide range of implementations according to how these quantities are determined.

A first approximation for s_c may be obtained by setting it equal to the unstretched, planar laminar flame speed s_L^0. This is generally too crude however, since the local flame speed can change significantly due to unsteady effects, and so some of the coupling must be reintroduced through modifying the flame speed according to the strain and curvature of the isosurface.

One method of taking this into account, valid only for low levels of stretch and therefore weak turbulence, is provided by the linear stretch theory introduced in §2.2.2 where the flame speeds can be related through the Markstein and Karlovitz numbers as

$$s_c = s_L^0 (1 - MaKa) \tag{3.15}$$

although, while Ma can be determined to a reasonable level of accuracy for a particular fuel through experiment or computation, the unsteady stretch rate represented by Ka

must be estimated from the resolved quantities, thereby introducing an additional source of uncertainty.

A greater level of accuracy for flame response may be achieved by referencing a flamelet library, where values for flame speeds are tabulated against any number of parameters such as stretch and fresh gas composition. These methods are discussed more in the context of mechanism reduction in §3.8. An assessment of the agreement between various methods of evaluating the strained laminar flame speed and those found in an unsteady flame can be found in Hawkes and Chen [49].

The FSD Σ may be determined either from an algebraic expression or by solving a balance equation with suitable closure for the unresolved terms.
Bray et al. [48] propose an algebraic closure under the BML framework, based on the flamelet crossing frequency, of the form $\Sigma = n/\sigma$, where n is the number of crossings per unit length of mean flame surface, and σ is the flame orientation factor - equal to the mean cosine of the angle between the mean and instantaneous flame fronts. Similarly to the BML expression for mean reaction rate (Eq. 3.13), this may be expressed as

$$\Sigma = \left(\frac{g}{\sigma}\right)\frac{1+\tau}{\left(1+\tau\tilde{c}\right)^2}\frac{c(1-c)}{L} \qquad \textbf{(3.16)}$$

where g is a model constant, and L is the wrinkling length derived from an estimate of the integral length scale.

Fractal methods, based on arguments on the scale similarity of turbulence in the inertial subrange, have also been proposed [50,51], leading to

$$\Sigma = \frac{1}{L_a}\left(\frac{L_a}{L_b}\right)^{D-2} \qquad \textbf{(3.17)}$$

where L_a and L_b are the outer and inner cut-off length scales respectively, and D is the fractal dimension. Outer and inner cut-off scales may be estimated from the integral and Kolmogorov lengths respectively, but the effects of turbulence intensity, mixture composition, and pressure, amongst others, are all contained within the fractal dimension D, which therefore requires careful modelling.

A transport equation for the FSD was first proposed by Marble and Broadwell [52] and later given firmer mathematical footing through more thorough statistical and geometric arguments [17]. Under this last derivation the FSD is associated with a specific isosurface of the progress variable corresponding to $c = c^*$, and the instantaneous value is written

$$\Sigma(c^*) = \left(\overline{\left|\nabla c\right|_{c=c^*}}\right)\overline{P}(c^*) \qquad \textbf{(3.18)}$$

where $\overline{P}(c^*)$ is the probability of finding a $c = c^*$ surface at that position.

An important quantity in premixed flame analysis is introduced in Eq. 3.18: the conditional progress variable gradient magnitude $\sigma_{c^*} = \left|\nabla c\right|_{c=c^*}$, also know as the Surface Density Function (SDF). The SDF can be viewed as a measure of the inverse of the local flame thickness, and, apart from its close relation to the FSD as indicated in Eq. 3.18, it also appears in the expression for the diffusive components of the surface displacement speed, and so plays a key role in determining the flame-turbulence interaction.

From the balance equation for the progress variable, combined with the relation in Eq. 3.18, the FSD transport equation may be expressed in terms of a classical reactive-diffusive balance, or alternatively in kinematic form as a propagating surface with displacement speed normal to the flame surface [53,54]. The latter form is chosen here since it provides the greatest physical insight into the problem.

$$\frac{\partial \Sigma}{\partial t}+\frac{\partial}{\partial x_i}\left(\langle u_i \rangle_s \Sigma\right)+\frac{\partial}{\partial x_i}\left(\langle s_d n_i \rangle_s \Sigma\right)=\left\langle \left(\delta_{ij}-n_i n_j\right)\frac{\partial u_i}{\partial x_i}\right\rangle_s \Sigma+\left\langle s_d \frac{\partial n_i}{\partial x_i}\right\rangle_s \Sigma \qquad \textbf{(3.19)}$$

where the surface average operator for any quantity Q is defined

$$\langle Q \rangle_s = \overline{Q|\nabla c|\|_{c=c^*}} \Big/ \overline{|\nabla c\|_{c=c^*}} \qquad \textbf{(3.20)}$$

s_d is the displacement speed of the surface relative to the fluid velocity in the flame normal direction, δ_{ij} is the Dirac delta function, and n_i is the unit vector normal to the flame surface.

The terms on the LHS of Eq. 3.19 represent, from left to right respectively: unsteadiness, convection by the mean flow, and propagation of the surface normal to itself. The terms on the RHS represent sink or source terms for Σ due to tangential strain rate, and the combined effects of propagation and curvature respectively.
The two RHS terms are often referred to collectively as the total stretch k (§2.2.2), which may then be used to parameterise the flame response to the combined effects of strain and propagation-curvature without explicit knowledge of the individual terms.

Identifying the flame surface with a single value of the progress variable leads to some difficulties when the flame thickness is non-negligible, as in the case of a fully resolved DNS flame, and particularly when the flame is highly curved such that the difference between the areas of the isosurfaces becomes significant. This may be overcome by instead considering a generalised FSD Σ_{gen} as proposed by Boger et al. [55]

$$\Sigma_{gen} = \int_0^1 \Sigma dc^* = \int_0^1 \left(\overline{|\nabla c\|_{c=c^*}}\right) dc^* = \overline{|\nabla c|} \qquad \textbf{(3.21)}$$

where the balance equation for Σ_{gen} is formally identical to 3.19, and the surface average operator becomes $\langle Q \rangle_s = \overline{Q|\nabla c|} \big/ \overline{|\nabla c|}$.

An important point here is that, according the definition in Eq. 3.21, for a fully resolved flame the transport equations for the generalised FSD Σ_{gen}, and the Surface Density Function SDF σ are also formally identical, and so under these conditions the SDF may be viewed as the local value of the generalised FSD.

Following RANS or LES decomposition of Equation 3.19 into resolved and unresolved components, additional terms are created which require modelling, where typically, these terms account for straining by the mean or resolved flow, straining by the turbulent or sub-grid fluctuations, and a destruction term to account for flame annihilation due to interactions, and to prevent infinite growth of the FSD. Several models have been proposed for these terms, see for example Cant et al. [54], or Duclos et al. [56] for a general review.

3.2.5 Flame Wrinkling Factor

Closely related to the Flame Surface Density is the Flame Wrinkling Factor Ξ, which describes the total flame surface area A per unit area of the projected mean flame surface A_p in the direction of propagation:

$$\Xi(c^*) = \frac{A}{A_p} = \frac{\overline{\left|\nabla c\right\|_{c=c^*}}}{\left|\overline{\nabla c\right|_{c=c^*}}} \qquad \textbf{(3.22)}$$

A generalised wrinkling factor analogous to Eq. 3.21 may also be used: $\Xi_{gen} = \overline{|\nabla c|} \big/ |\nabla \bar{c}|$.

As for the FSD, Ξ may be estimated from an algebraic expression or found from the closed form of the balance equation, however, while a useful concept for describing the degree of wrinkling experienced by the surface, the wrinkling factor is rarely used directly in turbulent flame simulations, perhaps due to the relative complexity of the balance equation compared to the FSD.

3.2.6 G-Equation

The G-Equation or level-set approach was proposed initially by Williams [57], and has subsequently been developed by Peters [3]. The basic concept relies on associating the flame front with a particular value, or level, of a scalar field, G, where the scalar field only has a physical meaning for the isosurface $G = G_0$ representing the flame front. A transport equation for G may be written

$$\frac{\partial G}{\partial t} + u_i \frac{\partial G}{\partial x_i} = s_d \left| \nabla G \right| \qquad \textbf{(3.23)}$$

The G-equation approach is attractive from a computational point of view because only the scalar G-field must be resolved on the computational grid, thereby avoiding the much more demanding task of resolving the flame front. One difficulty, however, is that for variable density flows, the displacement speed term must also take into account the effects of heat release. A second problem is the coupling between the G-field and the temperature or energy fields, for which the relations are not straightforward, and in this regard model formulations based directly on the progress variable are at an advantage.

3.2.7 Surface Displacement Speed

As seen from the G-equation (Eq. 3.23) and the kinematic form of the FSD transport equation (Eq. 3.19), particular emphasis is placed on the displacement speed s_d, which through its response to changes in strain and curvature can substantially affect the rate of production or destruction of flame surface or FSD. Further insight can be gained into the behaviour of s_d by considering the physical processes that underlie it.

Following Echekki and Chen [58], the transport equation for the reaction progress variable c, expressed in kinematic form, is

$$\left.\frac{\partial c}{\partial t}\right|_{c=c^*} + u_i \left.\frac{\partial c}{\partial x_i}\right|_{c=c^*} = s_d \left|\nabla c\right|_{c=c^*} \tag{3.24}$$

which may be combined with the classic reactive-diffusive formulation (Eq. 4.4), to provide an expression for s_d in terms of a reactive-diffusive balance:

$$s_d = \left.\frac{\dot{\omega} + \nabla \cdot (\rho D \nabla c)}{\rho |\nabla c|}\right|_{c=c^*} \tag{3.25}$$

This may be further divided into components due to reaction s_r, normal diffusion s_n, and tangential diffusion s_t:

$$s_r = \frac{\dot{\omega}_k}{\rho |\nabla c|} \qquad s_n = \frac{\vec{n} \cdot \nabla (\rho D \vec{n} \nabla c)}{\rho |\nabla c|} \qquad s_t = -D \nabla \cdot \vec{n} \tag{3.26}$$

where $s_d = s_r + s_n + s_t$.

A number of important features are revealed by expressing s_d in this way. Firstly, that a simple, linear, negative relation exists between the tangential diffusion component and the curvature in proportion to the diffusivity of the progress variable D. This shows that in regions of positive curvature the displacement speed will always be reduced by this term, indicating the principal mechanism leading to thermo-diffusively stable behaviour. A second observation is the presence of the SDF term in the denominator of both the reactive and normal diffusive components, which once again highlights the importance of this term in the FSD formulation and the complex coupling between thermo-chemistry and the flame surface geometry.

The displacement speed evaluated near the reaction layer, has been shown to be the most reliable flame speed to use in unsteady computations [49,59]. Alternative quantities such as the consumption speed can be used and are well defined for laminar flames, but become difficult to evaluate accurately as wrinkling increases (§6.3.1).

3.3 Other approaches

Flamelet based methods have the principal disadvantage that they presuppose the existence of a quasi-laminar, continuous flame front, and are unable to explicitly handle any potentially large deviations from this quasi-laminar behaviour, such as might occur during ignition, local extinction or flame interactions. They are best suited therefore to situations where something is known *a priori* about the combustion regime, and flamelet type combustion is expected, which is the case for many practical combustion devices. A number of alternative approaches are available which derive from entirely different phenomenological starting points, and therefore avoid the difficulties associated with the flamelet assumptions.

3.3.1 Probability Density Functions

At any given point and time in the domain, the state of the reaction can be completely described by joint pdfs of the scalar variables: $P\left(Y_1^*...Y_N^*;\vec{x},t\right)\Delta Y_1...\Delta Y_N$, within the range $-Y_N\Delta/2 \le Y_N* \le Y_N\Delta/2$, where Y_N^* can be species mass fraction, temperature, or even velocity components. From knowledge of these joint pdfs, mean quantities such as the reaction rates, together with all higher order moments, are easily obtained from

$$\overline{Q}(\vec{x},t) = \int_{Y_1...Y_N} Q\left(Y_1^*...Y_N^*\right)P\left(Y_1^*...Y_N^*;\vec{x},t\right)dY_1^*...dY_N^* \qquad \textbf{(3.27)}$$

The problem now becomes one of determining the pdfs. Two approaches are commonly used for this: a presumed form for the pdf, or the solution of a balance equation. In presumed pdfs methods an analytical function, typically a β-function, is assumed for the pdfs at each point, and a balance equation must be solved for the variance. Modelling is then required in this balance equation for the terms representing turbulent transport, production, dissipation and reaction.

Alternatively, an exact balance equation for the pdfs may be derived [41,60]. When the joint velocity-composition pdfs are used, terms for convection, reaction, and mean pressure gradients are exact and do not require modelling, therefore this approach is attractive when complex chemical mechanisms involving large numbers of scalars are involved.

A difficulty remains in evaluating terms involving spatial gradients however since only single point statistics are considered, and in addition, the solution of the full set of equations is computationally very demanding, and most often Monte Carlo methods are used to obtain approximate solutions at a reasonable cost. For these reasons pdf methods are not as widely used as others, but this may change as computing costs reduce.

3.3.2 Mixing Controlled Models

For high Damkohler number flows, where $Da = \tau_0 / \tau_f \gg 1$, the mean reaction rate may be assumed to be dominated by turbulent mixing over the precise thermo-chemical state of the flame. One of the first models to make use of this assumption is the Eddy Break-Up model (EBU) proposed by Spalding [61], in which the mean reaction rate is expressed as proportional to the standard deviation of the product mass fraction or progress variable, and inversely proportional to the turbulent mixing time, often approximated as $\tau_t = k/\varepsilon$

$$\dot{\omega} = C_{EBU} \overline{\rho} \frac{\sqrt{c''^2}}{\tau_t} \tag{3.28}$$

where C_{EBU} is a model constant. The progress variable fluctuations may then be estimated from a model or derived from the full balance equation for the variance:

$$\frac{\partial \overline{\rho} c''^2}{\partial t} + \nabla \cdot \left(\overline{\rho} \tilde{u} c''^2 \right) + \nabla \cdot \left(\overline{\rho} u'' c''^2 \right) = \nabla \cdot \left(\overline{\rho D \nabla c''^2} \right) + \overline{2c'' \nabla \cdot \left(\rho D \nabla \tilde{c} \right)} - 2\overline{\rho} u'' c'' \cdot \nabla \tilde{c} - \overline{2\rho D \nabla c'' \cdot \nabla c''} + 2\overline{\dot{\omega} c''} \tag{3.29}$$

The last two terms on the RHS are the most significant for high Damkohler number flows, and represent the dissipation and source for the scalar variance respectively. This again highlights the importance of the scalar dissipation rate χ, which in this case describes the rate of decay of inhomogeneities between reactants and products, and can be though of as the effect of micro-mixing through turbulent fluctuations. The importance of χ in turbulent combustion modelling increases as the turbulence length and time scales increase, although even at the scales available to DNS the scalar dissipation rate is an important characteristic of the flow.

EBU type models have the advantages of being simple to implement, with a low computational overhead and so are often used in commercial codes, however they have known deficiencies, particularly in anisotropic flows, and their accuracy decreases further as the chemical time scales become significant.

3.4 Flamelet Analysis using DNS

Since, in general, DNS makes no *a priori* assumptions about the structure of the flame or even the existence of flamelets, it provides an ideal platform from which to analyse flamelet models. Data obtained from DNS can be interrogated directly to reveal the underlying behaviour of the quantities of interest in flamelet models at a level of detail well beyond that available to experiment. The data may also be post-processed to provide LES or RANS decompositions so that particular models can be assessed for accuracy against the exact, or at least fully resolved, solutions.

A large number of studies have focussed on the behaviour of the displacement speed and its components, and on the distributions of the quantities affecting it such as the local curvature, tangential strain rate, and dilatation.

A well known result from several studies involving 3D simulation with simplified chemistry [30,62,63], non-unity Lewis numbers [62,64] and detailed H_2-O_2 chemistry in two-dimensions [63] is of the preferential alignment of the flame with extensive

tangential strain rates. Baum et al. [63] note that this leads to a thinning of the local flame front due the bringing together of isosurfaces in the flame normal direction, thereby causing a net production of scalar gradients by the turbulence. More recently, Chakraborty and Swaminathan [65] investigated this alignment for different values of the Damkohler number and found that preferential alignment of the scalar gradients with the most compressive strain rate only occurs for low Damkohler number flames. At higher values of Da, the dilatation due to heat release along the flame front can overcome this tendency, and so cause the alignment of the scalar gradients with the most extensive strain rate – thus leading to dissipation of scalar gradients by the turbulence. It is also noted that despite this change in alignment the mean tangential strain rate remains positive, and so turbulence is still a net source for flame area generation.

The sensitivity of the displacement speed to the each of the components of the stretch rate – the tangential strain rate a_T and propagation-curvature $s_d K_m$ terms, has been found to be dependent mainly on the mean strain rate for planar flames. While the greatest local variation in s_d is caused by tangential diffusion due to curvature, pdfs of curvature [30,63,64] show a near zero mean for planar flames and so the effects tend to cancel out.

Chen et al. [59,66] used detailed methane-air and hydrogen-air mechanisms in two-dimensions at different equivalence ratios to investigate Lewis number effects. For unity Lewis number flames, tangential straining was found to be the dominant term if only moderately curved flame elements were included (over 90% of flame elements for a planar flame in this case). A similar result was found by Chakraborty and Cant [67]: using simplified chemistry in 3D, s_d conditioned on regions of near zero curvature showed a negative correlation with stretch, but otherwise a weak positive correlation due to the relation of strain with curvature. In the same study it was shown that at a critical value of a_T, compressive normal strain rates occur which act to bring together isosurfaces and increase the SDF. This causes a net reduction in the combined $s_n + s_r$ term which leads to a negative correlation between s_d and a_T. For sub-unity Lewis

number flames, while the response of s_d to curvature is still dominated by the tangential diffusion term s_t, a secondary effect on the combined $s_n + s_r$ terms is observed [68] due to the relation of SDF to curvature, where for $Le < 1$ a weakly positive correlation exists between SDF and curvature and for $Le \approx 1$, a weak negative correlation is found.

The linear stretch dependence (Markstein) assumption has been found to be valid over a wider range of stretch than predicted from theory [66] with an approximately linear range for $-1 < \mathrm{Ka} < 1$, but at higher turbulent frequencies the flame is unable to react and an attenuation in the response is seen. This has also been noted in one-dimensional complex chemistry simulations [23]. Hawkes and Chen [69] found that even in low Damkohler number flows the curvature-propagation term showed significant variation, indicating alterations to the local thermo-diffusive balance and should be taken into account in any modelling of the effect.

The global flame behaviour has also been investigated using DNS: Bell et al. [70] have carried out three-dimensional simulations with detailed chemistry for lean methane-air flames at different turbulence intensities. It was found that the increased turbulent flame speed s_T at higher turbulence intensities could not be accounted for only by the increase in flame surface area. An increase in s_T due to flame area by 23% and 64% was reported, and by an additional 9.8% and 12.8% due to chemistry for low $1.7\, s_L^0$ and high $4.3\, s_L^0$ intensity turbulence respectively. The chemical-kinetic effects were linked to the residence time of certain intermediate species due to variations in the flame normal fluid velocity with curvature.

3.5 Flame Kernel Analysis

DNS analyses of flame kernels are relatively less common than those on statistically planar flames in spite of the prevalence of kernels in practical situations – both in experimental and engineering applications. However, some important differences exist

between planar and spherical flames; Not only is the local thermo-diffusive balance altered by the mean curvature during the early stages, but the effects of mean curvature appear to be significant even for large kernel radii [71]. In addition, the thermal expansion due to confinement of the burnt gases causes higher mean stretch rates compared to planar flames, and as mentioned in the introduction, during the early stages the kernel will be exposed to a limited but constantly broadening band of the turbulence spectrum, until it reaches a comparable size to the integral length scales.

Statistics of the local reactive-diffusive balance have been investigated by Jenkins et al [72] using one-step 3D simulations. The main differences between the kernel and planar configurations were noted as 1) s_t is predominantly negative for kernels due to the mean positive curvature, whereas $\rho(s_r + s_n)$ stays close to ρs_L^0 even in regions of locally high curvature, and. 2) SDF is negatively correlated with curvature, which is attributed to the negative correlation of tangential strain with curvature – i.e. SDF is mainly strain dependent. This finding is confirmed in studies by Chakraborty et al. [73] and Klein et al. [74] who examined kernels at different points in their development, and note a positive correlation between $s_r + s_n$ and stretch which increases for smaller kernel radii, and which can again be attributed to the negative correlation between tangential strain and curvature leading to a negative correlation between SDF and curvature, which also becomes stronger as the kernel radius decreases. This negative tangential strain-curvature correlation has also been confirmed experimentally by Renou et al. [75] for various Lewis numbers.

Comparisons of experimental kernel data using 2D OH PLIF (Planar Laser Induced Fluorescence of the OH radical) with single-step, 3D DNS results have been made [75-78]. Statistics of curvature and FSD show good qualitative agreement for equivalently processed (2D) data - validating the qualitative results for single-step DNS for unity Lewis numbers, and demonstrating the feasibility of such comparisons.

Complex chemistry in the kernel configuration has been considered by Van Oijen et. al. [79] who examined expanding kernels numerically using a simplified one-dimensional FGM method (§3.8) to describe the chemical structure of the flame. They found that the

global mass burning rate can only be properly predicted by taking into account the full stretch and surface area profiles through the flame front. Approximating these quantities from only a single isosurface, such as at the inner reaction layer, resulted in large errors even at low turbulence intensities.

Thevenin [80], carried out three-dimensional DNS of methane-air flames using unity Lewis number and low-Mach number assumptions with a method of tabulated flamelet libraries known as Flame Prolongation of ILDM (FPI) (§3.8). The database was analysed for the global flame properties of flame surface area, global stretch rate, mean curvature and thickness. It was observed that the initial increase in flame surface area for all turbulent cases was actually lower than that of an equivalent laminar kernel, and this was attributed to the presence of velocity fluctuations acting on the flame surface in the direction of the burnt gases following initialisation, and only after these have dissipated does wrinkling take effect and the fully turbulent flame begins to develop.
Mean flame thickness, based on the thermal gradient on an isosurface of CO_2 mass fraction (and closely related to the inverse of the SDF, $1/|\nabla c|$), showed no significant variation with turbulence intensity, however an approximately linear positive correlation was found between flame thickness and curvature for both positive and negative values of curvature, which supports the findings of Klein et al. [74] for flames with high mean curvature.
It was also noted that there was significant variation in the statistics collected from nominally identical simulations (in terms of turbulence and flame parameters), and the need to take this into account when comparing data was stressed.

Tanoue et al. [81] experimentally investigated lean methane-air flames at equivalence ratios between the lean limit and stoichiometric ratio, noting an almost linear increase in the Markstein number for laminar flames with increasing equivalence ratio. This trend was reflected in observations of turbulent kernels which showed that the enhancement of the burning velocity with turbulence increased as the equivalence ratio was reduced, until the lean limit was reached. Production of surface area due to stretch was assumed to be a function only of turbulence intensity u'/s_L, so the difference in global burning rate was attributed to a relative increase in the laminar flame speed.

Some now classical experimental results on the turbulent burning velocity of expanding spherical flames across a range of turbulent Reynolds numbers were carried out by Abdel-Gayed et. al. [82,83]. According to their analysis a reduction in the apparent turbulence intensity experienced by small kernels, attributed to convection by the larger eddies has an exponential time dependence of the form

$$\frac{s_T^{'}(t)}{s_T} = \left[1 - \exp\left(-0.2(t/\tau_t)^{0.75}\right)\right]^{0.5} \qquad \textbf{(3.30)}$$

where $s_T^{'}(t)$ is the instantaneous turbulent flame speed and s_T the fully developed value. The fully developed value was found to depend principally on the turbulence intensity and integral length scale for low values of the turbulent Reynolds number. At higher Reynolds numbers, turbulent straining, characterised by a global Karlovitz number $Ka = (u'/\lambda)(\delta/s_L^0)$, and the Lewis number must be taken into account to capture the 'bending' or fall-off of the increase in s_T with u'.

More recently Lipatnikov and Chomaik [84] developed an analytical expression for the reduction in the global burning rate observed in flame kernels compared to planar flames by considering the global stretch effects due to the mean curvature. For the early stages of kernel growth where the ratio of the flame thickness to flame radius is close to unity, a non-linear expression for the expansion rate of the kernel was found to give good agreement with the experimental data obtained by Bradley et. al. [85]. When the ratio of the mean flame thickness to flame radius is much less than unity, a linear expression could be used with reasonable accuracy, and the particular, composition-dependent behaviour can be taken into account through the specification of a turbulent Markstein number.

This analysis suggests that the reduction in curvature-induced stretch as the kernel expands is the principal explanation for the observed [85] increase in turbulent flame speed. However, the increasing exposure of the kernel to the turbulent spectrum as it expands is not explored, even though this is taken into account in the growth of the mean flame brush thickness, and cited in the original work as the main explanation of

the effect. It should be noted that the flame radius data presented by Bradley et al. and subsequent analysis by Lipatnikov and Chomaik are based on kernel sizes beyond those found in the early stages as defined in the present study, due to limitations on the imaging resolution.

The movement of the kernel centre is addressed theoretically by Pope and Cheng [86] who estimate the initial kernel centre velocity to be equal to the turbulence rms velocity u' at $t = 0$, so that the velocity variance 'seen' by the kernel rises exponentially from zero to the integral length scale as the radius increases. Beretta et al. [87] analysed images of kernel growth from an optical access engine to track the kernel centres and found a similar exponential increase in the centre displacement. The final displacement was found to be relatively independent of the turbulence intensity since higher intensities caused more rapid growth of the kernel surface to counteract the greater initial displacement velocity.

3.6 Two vs. Three Dimensional Statistics

The relations between data obtained from two and three dimensional simulations, and two dimensional data extracted from three dimensional simulations are important considerations. In addition to the qualitative differences observed in the behaviour of two dimensional turbulence, as described in Section 2.3.3, the range of surface shapes represented in two dimensional simulations is obviously limited to variation of a single principle curvature. The shape of a surface element in a three dimensional flow can be described by the shape factor θ, given by the ratio of the smallest to largest values of the two principle curvatures: $\theta = k_s / k_l$. Shape factors of 1, 0, and –1 represent spherical, cylindrical and pseudo-spherical (or spherical saddle points) respectively. DNS of non-reacting flows [88] has shown that the pdf of θ is sharply peaked around 0, suggesting that for material (non-propagating) surfaces, cylindrical elements predominate, and it is also noted that the expectation of cylindrical elements increases with the magnitude of the mean curvature.

This finding has been extended to reacting flows by the analysis of Cant et al. [30]. Although heat release was not taken into account, the findings show that in addition to cylindrical elements being most probable, spherical elements are essentially non-existent, and saddle points occur only with very low probability. Also noted in this study is the relation between curvature and tangential strain rate, showing that high values of curvature are only found in areas of low and negative tangential strain rates, suggesting that positive strain acts to reduce, or draw-out the curvature.

These findings lend support to the use of two-dimensional simulations in examining turbulent flames. More recent three dimensional DNS using detailed hydrogen-air and methane-air mechanisms carried out by Tanahashi et al. [89,90] agrees with the previous findings on the distribution of the shape factor, but also emphasises the existence of inherently three-dimensional fine-scale turbulent structures acting on the flame fronts. For high turbulence intensities, fine scale eddies with axes aligned perpendicular to the flame front are shown to cause a local increase in heat release rate of up to 120% of the laminar flame value, although the overall contribution of these events, particularly at lower Reynolds numbers, is reported to be small.

The above investigations were carried out for statistically planar flames. For statistically spherical / cylindrical flames Thevenin et al. [91] has compared statistics of curvature, mean kernel radius and global stretch rate for equivalent two and three-dimensional DNS with unity Lewis numbers. A reduction in mean radius growth was observed for the three-dimensional case, and a higher value of the maximum stretch rate and mean curvature was also found compared to two-dimensions. It was noted, however, that only one realisation of the three-dimensional case was used whilst the two-dimensional cases were repeated and ensemble-averaged, and so the differences may partly be explained by the low sample size.

Using the same code, an analysis of two-dimensional slices taken from a three-dimensional DNS [80] found discrepancies of between 70%-80% from the three-dimensional values for the mean, standard deviation and skewness of curvature, owing to large tails in the two-dimensional sample pdf. By excluding large deviations from the

mean and taking ensemble averages over a number of slices, this error was reduced, but only to between 10%-30%.
The same analysis technique of comparing two dimensional data taken from three dimensional simulations was carried out by Hult et al. [78] for statistics of FSD and Gashi et al. for curvature and wrinkling [77] who found similar, qualitative discrepancies between the two.

The emerging picture from these studies is that while two dimensional simulations seem able to capture the essential physics of the flame–turbulence interaction, and are therefore valid for qualitative, parametric analyses, care must be taken in making direct comparisons with three dimensional data, whether from three dimensional DNS or two dimensional data taken from experiments.

3.7 Flame Kernel development in SI Engines

For efficient operation of a spark ignition (SI) engine combustion must be as rapid as possible, whilst avoiding the occurrence of pre-ignition or knock. Complete consumption of the fuel during the cycle is necessary to avoid inefficiency and unburned fuel emissions. Faster combustion also allows the pressure increase to be more accurately placed at the most optimal point during the combustion stroke, thereby potentially providing greater power output per cycle.

High rates of heat release can be achieved simply by increasing the turbulence intensity, which enhances the turbulent flame speed through an increase in the flame surface density. It is a convenient fact that the turbulence intensity in a piston engine closely correlates with piston speed during the compression stroke, so that as the engine speed increases, the turbulence intensity and rate of heat release also increase. This means that to leading order the mean effective pressure in the cylinder can be approximated as a function of crank angle only [1].
During the ignition phase however, before the fully turbulent flame is established, the developing kernel is very sensitive to turbulent straining, and too high a turbulence

intensity can lead to retarded kernel development or even quenching. The operating range defined by these two conflicting requirements is further narrowed by the need to use mixtures as close as practically possible to their lean limit in order to maximise efficiency and reduce engine-out emissions.

Accurate simulations of flame kernel development throughout the combustion phase are therefore essential in understanding the processes leading to undesirable cycle-to-cycle variations. As noted in the introduction, the processes occurring at various points in the combustion phase span a very wide range of length and time scales, and it has not been possible to accommodate all of these within a single, multi-dimensional modelling framework. Most approaches therefore divide the process into three distinct parts: 1) spark ignition. 2) quasi-laminar kernel growth 3) fully-developed turbulent flame.
The spark ignition phase, according to Maly and Vogel [92], can be further divided into sub-stages of breakdown, arc, and glow discharge, which have a combined duration of the order of 1ms. The initial breakdown phase, with a time scale in the region of 1ns, produces a thin column of plasma with peak temperatures and pressures approaching ~60000K and ~200bar respectively. This produces a strong, outwardly-propagating shock wave and dissociation and ionisation of the gases in the column. During the subsequent arc and glow discharge phases the plasma column expands outwards driven by thermal expansion, with decaying radial velocities of the order ~100ms^{-1}. The temperature drops rapidly due to conduction and re-association of the gases to an equilibrium value still well above the adiabatic flame temperature of ~3000K.

Following this ignition phase, a quasi-laminar kernel with a radius ~0.5mm begins to propagate radially outwards, and is strained and convected by the turbulent velocity field. The transition from the ignition phase to the kernel phase is marked by the point at which chemical heat release becomes the dominant cause of thermal expansion. As noted in a number of studies [1,93], this phase of flame kernel development is crucial to the overall rate of heat release, since the rate of expansion of the kernel passes through a minimum at this point and the kernel is therefore particularly susceptible to the effects of turbulent straining and heat loss to the electrodes. For this reason it is also the most difficult phase to simulate, since to accurately account for these effects requires

information the specific geometry and flow conditions surrounding the electrodes, which is generally well beyond the level of resolution available in a multi-dimensional, full-cycle simulation.
Successful growth during this phase leads to increased flame surface wrinkling as the kernel experiences a greater portion of the turbulence spectrum, and eventual transition to a fully-developed turbulent flame.

Cycle-resolved, unsteady simulations of IC engines typically take a piece-wise approach to modelling each of these phases. Starting with a zero or one-dimensional model to account for the spark ignition process; a second model is then used for the quasi-laminar kernel expansion and transition to turbulent flame, the results of which are then used to initialise a fully-developed turbulent flame model once the kernel can be adequately resolved on the computational grid. Examples of this approach can be found in Fan et al. [94-96] who developed the Discrete Particle Ignition Kernel (DPIK) model, which attempts to overcome the problem of resolving the small initial kernel by using Lagrangian particles to represent the kernel flame surface. Particles are initialised along the spark channel and the spherical growth of the kernel is tracked by the position of the particles as they travel radially outwards according to an estimated energy balance within the kernel. After a critical radius is reached, the number density of these particles in any given computational cell is then used to initialise a flamelet model based on the G-equation.
A slightly different, but related, approach is taken by Duclos et al. [97] whose Ark and Kernel Tracking Ignition Model (AKTIM) uses Lagrangian particles to track the gravity centres of a large number of hypothetical kernels, each with a statistical weighting. The spark plug geometry is also represented by a collection of static particles, thereby avoiding the need for mesh refinement.

In both of these models, the kernel is assumed to be spherical during its initial phase of growth, although, under both turbulent and laminar conditions, it has been found [2,98] that a non-spherical kernels can occur due to shock induced flow along the electrodes. And while convection of the kernel and its effect on heat losses to the electrodes is

taken into account by the AKTIM model, no turbulence-induced changes in the flame structure are considered in either case.

It is useful to consider a model for the turbulent flame speed developed by Herweg and Maly [99] which has shown good agreement with experimental data and is used in a number flamelet based IC engine models [100]. It explicitly takes into account the size dependent interaction of the kernel with the flow field and reveals the important physical processes occurring during this phase.

For a given fresh gas composition with laminar flame speed s_L^0, and assuming an infinitely thin flame front, the mean propagation speed of the flame surface s_t is expressed

$$\frac{s_t}{s_L^0} = I_0 + I_0^{1/2}\left(\frac{u'}{u'+s_L^0}\right)^{1/2}\left[1-\exp(-R/L)\right]^{1/2}\left[1-\exp(-t/\tau_L)\right]^{1/2}\left(u'/s_L^0\right)^{5/6} \qquad \textbf{(3.31)}$$

where the individual terms represent:

1) $I_0 + I_0^{1/2}$ Strain. Where I_0 is close to unity, and for flames with $Le \sim 1$ the strain rate tends to decrease s_t, and is particularly important at small kernel radii.

2) $\left(\frac{u'}{u'+s_L^0}\right)^{1/2}$ Effective turbulence factor. Accounts for the fact that the movement of the kernel will change the apparent magnitude of turbulent velocity fluctuations.

3) $\left[1-\exp(-R/L)\right]^{1/2}$ Size dependent integral length scale. For kernel radius R and length scale L, this recognises that turbulence length scales much greater than the kernel radius are not experienced by the flame surface.

4) $\left[1-\exp\left(-t/\tau_L\right)\right]^{1/2}$ Time dependent integral time scale. Similarly to term 3, recognises time scale variation, where the characteristic time $\tau_L = L/\left(u'+s_L^0\right)$.

5) $\left(u'/s_L^0\right)^{5/6}$ Fully-developed flame. Approximates the value of s_t as the size and time dependent terms approach unity.

This analysis highlights the fact that the effects of turbulence are felt by the kernel from the earliest stages following spark ignition, even where a quasi-laminar flame structure is assumed. The time and length scale dependence of the kernel-spectrum interaction is also made clear and demonstrates the importance of taking this into account.

3.8 Chemical Mechanism Reduction

The complexity of the reactions for even a relatively simple fuel such as methane oxidising in air means that it quickly becomes necessary to make some simplifications before a multi-dimensional simulation can be carried out. Some methods for achieving this are outlined here, although it should be noted that none of the approaches described here will necessarily provide the best results in any given situation, and so other factors such as the numerical implementation, objectives of the work, and availability of resources may be at least as important in choosing a mechanism.

Many species present in the full reaction mechanisms of hydrocarbon-air flames act over very short time scales compared with those of the major species, and so are relatively isolated from perturbations on the time scale of the surrounding turbulence. This fact allows the Quasi Steady-State (QSS) and Partial Equilibrium (PE) assumptions to be used, which form the basis of all attempts at reducing the full mechanisms to a more tractable size suitable for multi-dimensional DNS. The QSS assumption says that the overall rate of change of species mass fraction Y_i is negligible and so can be considered constant. Similarly, PE is applied to an individual reaction step when it can be assumed to be in equilibrium.

For simple fuels such as methane, semi-global or small multi-step mechanisms can be generated through judicious choice of the most important species and reactions with knowledge of the time scales and dependencies of the individual species and reactions [3]. For larger mechanisms this becomes difficult and time-consuming, and more systematic approaches are required.

One such method is sensitivity analysis, whereby a flame property of interest A is selected (for example laminar flame speed $A = s_L$), and its response to a small variation of the rate constants ε (pre-exponential factor or activation energy) for each reaction step is recorded. The resulting sensitivity $\partial A/\partial \varepsilon$ can then be plotted for all reaction steps, across any number of different initial thermochemical conditions such as equivalence ratio or pressure, and the least (and most) important reactions can be easily identified.

Elimination of entire species is more beneficial from a computational point of view, and a graphical method for analysing the relations among species has also been suggested [10]. Known as a Directed Relation Graph (DRG), the interrelations of each species are represented schematically and a measure of dependency is calculated from the estimated error introduced by the removal of a species based on the stoichiometric coefficients in each reaction. From the resulting graph it is possible to identify dependency groupings among the species and so select species or groups of species that can be removed from the mechanism whilst limiting unintended effects on the remaining reactions.

Computational Singular Perturbation (CSP) analysis, and the related Intrinsic Low Dimensional Manifolds (ILDM) [101] take a more rigorous mathematical approach to identifying the species and reactions suitable for QSS and PE assumptions to be applied. In both CSP and ILDM simplified reacting systems are considered by neglecting convection and diffusion and assuming isobaric, adiabatic and homogenous conditions. Taking the Jacobian of the simplified system of governing equations, the response of the system to some small perturbation in composition space can be estimated by assuming it to be locally linear. Analysis of the characteristic time scales (eigenvalues) and directions (eigenvectors) of the system provides information that can be used to apply

QSS and PE to particular species and reactions. At this point ILDM, in contrast to CSP, goes further by considering the trajectories of the system in composition space from different initial positions, with the aim of identifying reduced-dimension manifolds from which the system can be described. It is found that these 'attracting manifolds' are characterised by the slowest evolving species. Compositions in the vicinity of the manifold approach it on short time scales and long before the equilibrium composition is reached. This is a very useful result for complex chemistry DNS since it provides a well founded justification for the use of reduced mechanisms. For an n dimensional manifold, only n species conservation equations must be solved, and the remaining species can be found from a look-up table as a function of the resolved species concentrations.

One deficiency of ILDM is that only chemical kinetic information is used in the analysis, and so convection, diffusion and non-adiabatic processes are not taken into account, but which are known to have a strong influence on the flame behaviour. The alternative approach of Flamelet Generated Manifolds (FGM) [102,103] avoids these limitations by solving a series of one-dimensional (spatial) flamelet equations that can include terms to account for convection, diffusion, stretch, and curvature. Manifolds can then be generated as functions of controlling variables such as the mass fraction of a slowly evolving species, stretch rates, or a suitably defined progress variable.

The accuracy of such methods can be improved by simply increasing the dimension of the manifold, however, for higher dimensions the computational effort required to generate these manifolds and perform the look-up operations can defeat their original purpose, and so it has been suggested to create the table entries for a given manifold as required during the simulation. In–Situ Adaptive Tabulation (ISAT) [104] takes advantage of the fact that only a small region of the composition manifold is actually visited during a simulation, and so although slow during the initial stages when many new table entries are being generated, overall, speedup factors of $O(1\times10^3)$ have been reported for chemistry calculations in a methane-air mechanism.

The main limitation of FGM and the related Flame Prolongation of ILDM (FPI) [105], is that a flamelet structure is presupposed in the manifold construction. Deviations from flamelet behaviour and non-flamelet behaviour therefore cannot be explored with these

techniques and so their validity in flows where the regime is not known *a priori* is questionable, and therefore remains limited to relatively low turbulence intensities.

3.9 Hydrogen Addition to CH_4-Air Flames

The use of pure hydrogen as a fuel in IC engines is superficially attractive from the point of view of emissions reduction, since if combustion is complete, engine-out emissions are near zero. Pure hydrogen's low lean flammability limit combined with its high molecular mobility and resistance to strain potentially allows for ultra-lean combustion. Technical problems remain however. Power output is restricted due to the occurrence of preignition and knock, which combined with the low energy density of pure hydrogen compared with conventional hydrocarbon fuels means that advances in turbo charging and direct injection techniques are necessary before reasonable performance is achieved [106].

Some of the same benefits of hydrogen are seen when it is added in small quantities to heavier - and more energy dense - hydrocarbons such as methane. Experimental investigations into the behaviour of hydrogen doped flames indicate an increased turbulent flame speed through enhanced wrinkling [107], greater resistance to strain-induced quenching, and a lower lean flammability limit.

The ability of hydrogen doped flames to resist higher unsteady stain rates is only partly due to an increase in the unstrained laminar flames speed. Di Sarli and Di Benedetto [108] note that the laminar flame speed is always well below that calculated from a linear combination of pure H_2 and CH_4 at the same equivalence ratio. Using sensitivity analysis they show that for lean flames and low H_2 mole fractions ($\alpha < 0.5$), the reaction remains dominated by the initial breakdown of CH_4. The following principle reactions are identified:

$$H + O_2 + H_2O \leftrightarrow HO_2 + H_2O \qquad (1)$$

$$H + O_2 \leftrightarrow O + OH \qquad (2)$$

$$OH + CO \leftrightarrow H + CO_2 \quad (3)$$

$$OH + CH_4 \leftrightarrow CH_3 + H_2O \quad (4)$$

$$H + CH_3 + M \leftrightarrow CH_4 + M \quad (5)$$

In particular, CH_4 oxidation proceeds mainly through reaction 4 involving the hydroxyl radical OH, which has also been confirmed in experimental studies [109], and so the production of OH through the main chain branching reaction 2 is crucial.

It is also noted that increased H radical concentrations due to H_2 addition do not lead directly to an increased burning intensity since there is also competition for the H radical from the dominant chain-terminating reaction 1.

The observed net effect, both from experiment [110,111] and computation [20,21] is that, for lean methane-air flames, hydrogen addition results in

- Higher laminar flame speed, where the increase is more pronounced at lower equivalence ratios.
- Reduced laminar flame thickness.
- Reduced sensitivity to steady strain rates (higher –ve Markstein number)
- Reduced sensitivity to unsteady strain rates (faster response time).
- Increased FSD and turbulent flame speed s_T.
- Lower lean flammability limit.
- Higher extinction strain rates.

These properties have been shown to translate to real IC engines situations [112], however, it was also noted that the spark timing must be adjusted from the pure fuel position to account for the increased flame speed, otherwise the thermal efficiency decreases and NOx emissions rise.

3.10 Summary

A considerable body of literature exists on DNS of statistically planar turbulent flames both with and without complex chemistry for simple hydrocarbon-air flames in both two

and three dimensions. For this configuration the statistics of the flame geometry and diffusive-reactive behaviour are now reasonably well understood.
Flamelet based models for premixed flames, and in particular the FSD and G-equation approaches appear to be the most promising techniques for predicting many flows of practical interest, and the focus of DNS studies has therefore been on improving understanding of the key quantities in these models: the flame surface displacement speed and its response to strain and curvature.

Turbulent flame kernels have been studied extensively through experiment, due in part to their important practical application in spark ignition engines.
From the research into kernel formation and growth in SI engines it is well recognised that the early stages of growth following ignition constitute one of the most crucial phases of the combustion cycle, and an improved understanding of this phase is therefore essential in predicting cycle-to-cycle variations in engine performance.
Alternative fuels, in particular hydrogen, are increasingly being considered as an important next step in IC engine development, and hydrogen addition – either to natural gas (mainly methane) or conventionally fuelled engines shows potential as a bridging technology: to reduce emissions and improve engine efficiency without requiring the radical changes to infrastructure that alternative fuels demand.

DNS of the early stages of kernel development has predominantly been carried out in three-dimensions and with single-step chemistry. Complex chemistry in 3D has only been achieved by employing reduction methods that make *a priori* assumptions about the flame structure, and so are not able to capture the full range of flame phenomena. As far as the author is aware no flame kernel simulations have so far been carried out where the full transport equations are solved for a detailed chemical mechanism.

4 NUMERICAL IMPLEMENTATION

All simulations in this study were carried out using the SENGA and SENGA2 DNS codes developed by R. S. Cant at the University of Cambridge. The two codes share the same basic architecture: both solve three-dimensional, compressible reacting Navier-Stokes equations using explicit higher-order spatial discretisation and low-storage Runge-Kutta time advancement schemes. However, several important differences exist between the codes, which are summarised below for SENGA vs. SENGA2 respectively:

- Single step vs. multi-step, multi-species reaction mechanisms.
- Constant vs. temperature and composition dependent thermodynamic properties.
- Adiabatic vs. optically thin radiation model.
- Third-order vs. fourth-order Runge-Kutta time advancement.
- Non-dimensional vs. dimensional forms of the governing equations.
- Standard NSCBC implementation on boundaries vs. improved NSCBC with inclusion of chemical source terms.
- Fixed time step vs. (optional) embedded PID adaptive time stepping.

In the following sections the governing equations and numerical formulations used in each code are presented. The theoretical background to the numerical methods that are common to both codes, such as the spatial discretisation, time advancement, turbulence generation, and boundary conditions are described fully in Section 4.1, and for brevity in the sections relating to SENGA2, only the relevant differences in implementation from the original configuration will be given.

4.1 SENGA

4.1.1 Governing Equations

The governing equations in non-dimensional form are;

mass:

$$\frac{\partial \rho}{\partial t} + \frac{\partial (\rho u_k)}{\partial x_k} = 0 \tag{4.1}$$

momentum:

$$\frac{\partial (\rho u_i)}{\partial t} + \frac{\partial (\rho u_k u_i)}{\partial x_k} = \frac{\partial P}{\partial x_i} + \frac{1}{\mathrm{Re}} \frac{\partial (\tau_{ki})}{\partial x_k} \tag{4.2}$$

energy:

$$\frac{\partial (\rho E)}{\partial t} + \frac{\partial (\rho u_k E)}{\partial x_k} = -(\gamma - 1) M^2 \frac{\partial (P u_k)}{\partial x_k} + \frac{1}{\mathrm{Re}} (\gamma - 1) M^2 \frac{\partial (\tau_{ki} u_i)}{\partial x_k} + \frac{\tau}{\mathrm{Re}\,\mathrm{Pr}} \frac{\partial}{\partial x_k} \left[\lambda \frac{\partial T}{\partial x_k} \right] - \frac{\tau}{\mathrm{Re}\, Sc} \frac{\partial}{\partial x_k} \left[\rho D \frac{\partial c}{\partial x_k} \right] \tag{4.3}$$

and reaction progress variable c:

$$\frac{\partial (\rho c)}{\partial t} + \frac{\partial (\rho u_k c)}{\partial x_k} = \dot{\omega} + \frac{1}{\mathrm{Re}\, Sc} \frac{\partial}{\partial x_k} \left[\rho D \frac{\partial c}{\partial x_k} \right] \tag{4.4}$$

γ is the ratio of specific heats and the Reynolds, Prandtl, Schmidt and Mach numbers appearing in the above equations are respectively

$$\mathrm{Re} = \frac{\rho_0 u_0 l_0}{\mu_0}, \quad \mathrm{Pr} = \frac{\mu_0 C_{P0}}{\lambda_0}, \quad Sc = \frac{\mu_0}{\rho_0 D_0}, \quad M = \frac{u_0}{a_0} \tag{4.5}$$

The non-dimensional reference values are: domain size $l_0 = L$, laminar flame speed $u_0 = s_L$, and time $t_0 = l_0/u_0$. Other quantities are normalised by fresh gas reference values of density ρ_0, pressure P_0, temperature T_0, thermal conductivity λ_0, molecular diffusivity D_0, and dynamic viscosity μ_0 respectively.

The speed of sound a_0, in the fresh gases is

$$a_0 = \sqrt{\gamma R T_0} \tag{4.6}$$

A heat release factor τ is defined

$$\tau = \frac{T_{ad} - T_0}{T_0} \tag{4.7}$$

and the viscous shear stress tensor is given by

$$\tau_{ij} = \mu\left[\frac{\partial u_i}{\partial x_j} + \frac{\partial u_j}{\partial x_i} - \frac{2}{3}\frac{\partial u_k}{\partial x_k}\delta_{ij}\right] \tag{4.8}$$

Finally, the system of equations is closed with the thermal (Eq. 4.9) and caloric (Eq. 4.10) equations of state:

$$P = \frac{1}{\gamma M^2}\rho(1+\tau T) \tag{4.9}$$

$$E = \frac{1}{\gamma}(1+\tau T) + \frac{1}{2}(\gamma - 1)M^2 u_k u_k + \tau(1-c) \tag{4.10}$$

4.1.2 One-step Chemistry

A one-step, irreversible reaction between reactants R and products P of the form $R \rightarrow P$ is assumed. The state of the reaction is represented by the progress variable c, defined here as the normalised mass fraction of products:

$$c = \frac{Y_p - Y_{p0}}{Y_\infty - Y_{p0}} \tag{4.11}$$

and which varies from 0 in the fresh gases to 1 in the fully burnt products.

The reaction rate $\dot{\omega}$ is determined from an Arrhenius relation (Eq. 4.12), using a non-dimensional pre-exponential factor B^* (Eq. 4.13)

$$\dot{\omega} = B^* \rho (1-c) \exp\left[-\frac{\beta(1-T)}{1-\alpha(1-T)} \right] \tag{4.12}$$

$$B^* = \frac{B l_0}{\rho_0 u_0} \exp\left[-\frac{\beta}{\alpha} \right] \tag{4.13}$$

The heat release parameter α, and the Zel'dovich number β, are constants defined for a particular fuel by

$$\alpha = \frac{\tau}{1+\tau} = \frac{T_{ad} - T_0}{T_{ad}} \quad \text{and} \quad \beta = \frac{E(T_{ad} - T_0)}{R T_{ad}^2} \tag{4.14}$$

where T_{ad} is the adiabatic flame temperature, E is the activation energy, and R is the universal gas constant.

4.1.3 Spatial Discretisation and Time Advancement

All first and second derivatives on the interior grid points are discretised using an explicit, 10^{th} order central differencing scheme. While potentially more accurate spectral schemes are available for non-reacting flows where periodic boundaries may be used, the explicit central difference scheme used here provides comparable accuracy to

these other methods whilst allowing greater flexibility over boundary conditions, and also facilitating parallel processing techniques using domain partitioning.
The full 10^{th} order scheme requires a stencil width of 5 grid points in each coordinate direction and is therefore only achievable sufficiently far from the boundary. Grid points approaching a boundary use 8^{th}, 6^{th}, 4^{th}, 2^{nd} ordered central difference schemes respectively and a 2^{nd} order one-sided scheme is used on the boundary point itself.

Coefficients for the interior scheme are obtained by rearranging a Taylor's series expansion around points on the stencil for terms up to h^{10}, where h is the grid point separation. As the boundary is approached the coefficients are obtained similarly from the associated reduced stencils.

To advance the solution in time, a third-order, low storage Runge-Kutta scheme developed by Wray [113] is used. Three sub steps are taken for each time increment and at any point in the process only two storage locations are required: one for the dependent variable and one for the derivative.

4.1.4 Boundary Conditions

The specification of accurate boundary conditions for compressible reacting flows remains an active area of research in the DNS community. The use of high resolution, non-dissipative numerical methods capable of accurately reproducing acoustic activity means that acoustic waves must be carefully handled on the boundaries. Failure to do this can lead to potentially unphysical interactions of reflected waves with the flame, and the possible onset of instabilities due to the close coupling of heat release with acoustic perturbations.

As mentioned previously, the assumption of periodicity, as often applied to non-reacting flows in cubic domains, is not appropriate in reacting flows due to the strong inhomogeneity and anisotropy of the flow. Alternatively, the application of Dirichlet, Neumann or mixed / Robin type conditions lead to large boundary errors and acoustic

wave reflections, which due to the non-dissipative nature of the numerical schemes, persist in the solution and can lead to highly non-physical results.

In the present code, the Navier-Stokes Characteristic Boundary Conditions (NSCBC), developed by Poinsot and Lele [114], are used. Based on characteristic analysis of the governing equations and an assumption of locally one-dimensional, inviscid flow on the boundary, NSCBC are able to provide a number of boundary types including subsonic or supersonic, non-reflecting or partially reflecting inflows and outflows, and adiabatic or isothermal, no-slip or slip walls amongst others. Compared to alternative schemes they significantly reduce errors and acoustic reflections on the boundaries and appear to be stable over long simulation times. A more complete description can be found in Poinsot and Lele [114] or Poinsot and Veynante [5]. The basic methodology is summarised in the following section.

4.1.4.1 Navier-Stokes Characteristic Boundary Conditions

By considering a point on the right hand boundary at $x_1 = L$, as illustrated in Fig 4.1, the governing equations (in dimensional form as presented in Chapter 2) may be re-written in terms of waves propagating normal to the boundary for mass, momentum, energy (where e_s is the sensible energy), and species k respectively:

$$\frac{\partial \rho}{\partial t} + d_1 + \frac{\partial}{\partial x_2}(\rho u_2) + \frac{\partial}{\partial x_3}(\rho u_3) = 0 \qquad \textbf{(4.15)}$$

$$\frac{\partial}{\partial t}(\rho u_1) + u_1 d_1 + \rho d_3 + \frac{\partial}{\partial x_2}(\rho u_2 u_1) + \frac{\partial}{\partial x_3}(\rho u_3 u_1) = \frac{\partial \tau_{1j}}{\partial x_j} \qquad \textbf{(4.16)}$$

$$\frac{\partial}{\partial t}(\rho u_2) + u_2 d_1 + \rho d_4 + \frac{\partial}{\partial x_2}(\rho u_2 u_2) + \frac{\partial}{\partial x_3}(\rho u_3 u_2) + \frac{\partial P}{\partial x_2} = \frac{\partial \tau_{2j}}{\partial x_j} \qquad \textbf{(4.17)}$$

$$\frac{\partial}{\partial t}(\rho u_3)+u_3 d_1+\rho d_5+\frac{\partial}{\partial x_2}(\rho u_2 u_3)+\frac{\partial}{\partial x_3}(\rho u_3 u_3)+\frac{\partial P}{\partial x_3}=\frac{\partial \tau_{3j}}{\partial x_j} \tag{4.18}$$

$$\begin{aligned}&\frac{\partial}{\partial t}(\rho E)+\frac{1}{2}\sum_{k=1}^{3}u_k^2 d_1+\frac{d_5}{\gamma-1}+\rho u_1 d_3+\rho u_2 d_4+\rho u_3 d_5\\&+\frac{\partial}{\partial x_2}\left[u_2(\rho e_s+P)\right]+\frac{\partial}{\partial x_3}\left[u_3(\rho e_s+P)\right]=\frac{\partial}{\partial x_i}\left(\lambda\frac{\partial T}{\partial x_i}\right)+\frac{\partial}{\partial x_j}(u_i\tau_{ij})+\dot{\omega}_T\end{aligned} \tag{4.19}$$

$$\frac{\partial}{\partial t}(\rho Y_k)+Y_k d_1+\rho d_{5+k}+\frac{\partial}{\partial x_2}(\rho u_2 Y_k)+\frac{\partial}{\partial x_3}(\rho u_3 Y_k)=\frac{\partial}{\partial x_j}\left(\rho D_k\frac{\partial Y_k}{\partial x_j}\right)-\dot{\omega}_k \tag{4.20}$$

From characteristic analysis of the Euler equations [115], the d_i terms in Eqs. 4.15-4.20 may be expressed as a linear combination of the wave amplitude variations L_i

$$d_1=\frac{1}{a^2}\left[L_2+\frac{1}{2}(L_5+L_1)\right] \tag{4.21}$$

$$d_2=\frac{1}{2}(L_5+L_1) \tag{4.22}$$

$$d_3=\frac{1}{2\rho a}(L_5-L_1) \tag{4.23}$$

$$d_4=L_3 \tag{4.24}$$

$$d_5=L_4 \tag{4.25}$$

$$d_{5+k}=L_{5+k} \tag{4.26}$$

Which in turn may be expressed as functions of the characteristic velocities λ_i and spatial gradients of the primitive variables:

$$L_1=\lambda_1\left(\frac{\partial P}{\partial x_1}-\rho a\frac{\partial u_1}{\partial x_1}\right) \tag{4.27}$$

$$L_2 = \lambda_2 \left(a^2 \frac{\partial \rho}{\partial x_1} - \frac{\partial P}{\partial x_1} \right) \tag{4.28}$$

$$L_3 = \lambda_3 \frac{\partial u_2}{\partial x_1} \tag{4.29}$$

$$L_4 = \lambda_4 \frac{\partial u_3}{\partial x_1} \tag{4.30}$$

$$L_5 = \lambda_5 \left(\frac{\partial P}{\partial x_1} + \rho a \frac{\partial u_1}{\partial x_1} \right) \tag{4.31}$$

$$L_{5+k} = \lambda_{5+k} \frac{\partial Y_k}{\partial x_1} \tag{4.32}$$

where the characteristic wave velocities λ_i are given by

$$\lambda_1 = u_1 - a\,, \qquad \lambda_5 = u_1 + a\,, \qquad \lambda_2 = \lambda_3 = \lambda_4 = \lambda_{5+k} = u_1 \tag{4.33}$$

The characteristic wave amplitudes and velocities appearing in Eqs. 4.27 – 4.33 may be associated with various physical waves traversing the boundary plane in the normal direction. L_1 and L_5 represent the left and right going acoustic waves respectively, L_2 and L_{5+k} correspond to the normal convection of entropy and species k respectively, and L_3 and L_4 to the convection of the transverse velocity components. These are illustrated schematically in Fig 4.1.

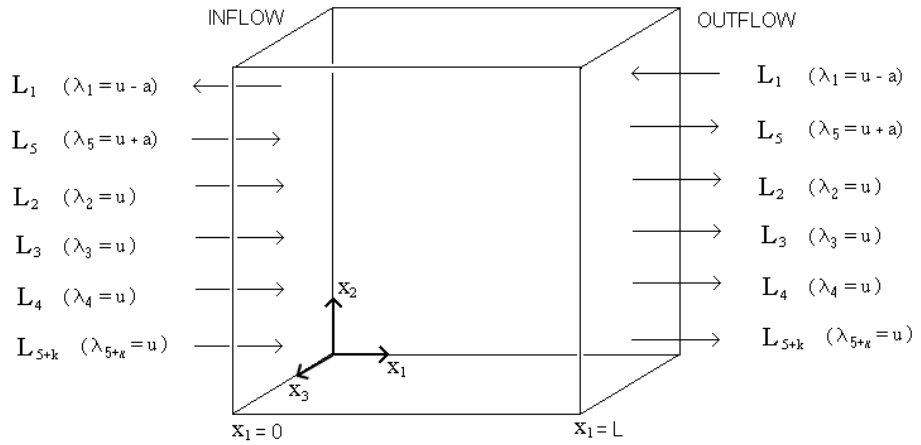

Figure 4.1. Characteristic wave amplitude directions and velocities for subsonic inflows and outflows in the Navier-Stokes Characteristic Boundary Conditions.

Under this formalism the conserved variables may be specified on the boundaries in terms of L_i and λ_i, which therefore also requires knowledge of the spatial derivatives appearing in Eqs. 4.27 - 4.32. Considering again the right hand boundary at $x_1 = L$, for the outgoing waves $L_2 - L_{5+k}$ these gradients may be calculated from the interior grid points in the region of the boundary. Accepting the reduced accuracy of the one-sided finite difference scheme on the boundary, the system remains stable since it is based on an upwind approximation. For the left-going wave L_5 however, using a similar treatment would involve a downwind one-sided approximation which is known to lead to numerical instabilities, and so an alternative method of specifying the incoming wave amplitudes must be used.

This alternative method comes in the form of the Local One-Dimensional Inviscid (LODI) relations. By disregarding the viscous and transverse terms in Eqs. 4.15 - 4.20. (and in this case reaction terms also), it then becomes possible to solve the resulting system of one-dimensional Euler equations to provide expressions for the incoming wave amplitudes L_i. In terms of the primitive variables these are

$$\frac{\partial \rho}{\partial t} + \frac{1}{a^2}\left[L_2 + \frac{1}{2}(L_5 + L_1)\right] = 0 \qquad \textbf{(4.34)}$$

$$\frac{\partial P}{\partial t} + \frac{1}{2}(L_5 + L_1) = 0 \qquad \textbf{(4.35)}$$

$$\frac{\partial u_1}{\partial t} + \frac{1}{2\rho a}\left(L_5 - L_1\right) = 0 \quad \textbf{(4.36)}$$

$$\frac{\partial u_2}{\partial t} + L_3 = 0 \quad \textbf{(4.37)}$$

$$\frac{\partial u_3}{\partial t} + L_4 = 0 \quad \textbf{(4.38)}$$

$$\frac{\partial Y_k}{\partial t} + L_{5+k} = 0 \quad \textbf{(4.39)}$$

For inviscid, non-reacting flows the above equations fully specify the primitive variables on the boundary, however, additional conditions are needed for the reacting Navier-Stokes equations for the viscous and species source terms. An obvious requirement of these additional terms is that as the viscosity and reaction rate go to zero, the system of equations relaxes to the original inviscid, non-reacting solution. The precise form of these conditions depends on the required boundary behaviour and will be discussed in the following section.

4.1.4.2 Non-Reflecting Outflow / Inflow

A spherically expanding kernel initialised near the centre of the computational domain will produce net outflow velocities on all boundaries, so for laminar and low turbulence intensity flows it is reasonable to specify non-reflecting outflow type boundaries on all faces on the assumption that any errors due to local flow reversal will be small. As the turbulence intensity is increased however, local inflow velocities at the boundaries are able to overcome the net expansion velocity, thereby preventing the boundary errors from being convected away from the interior solution.

Under these conditions it has been found that better numerical stability can be achieved by using a mixed scheme that allows the boundary type to be locally determined from the velocity normal at the boundary.

For a non-reflecting outflow, as illustrated in Fig. 4.1, wave amplitudes L_2 to L_{5+k} are all leaving the domain and so may be calculated from the interior grid point values. It then only remains to specify L_1 (For a left-hand boundary L_5 must be specified and L_1 calculated from interior points).

From the LODI relation 4.35, and assuming a constant pressure on the boundary, a reasonable choice for L_1 might be $L_1 = -L_5$. However, fixing the pressure in this way leads to complete reflection of acoustic waves, and so is not a practical choice for the present configuration. Conversely, failing to specify any pressure information on the boundary, while this minimises wave reflection, has been found to lead to a mean pressure drift over the course of the simulation that is equally problematic.

The approach taken is therefore to specify a target pressure in such a way the instantaneous pressure on the boundary is allowed to vary within a limited range, thereby providing a mechanism for information on the far-field pressure to reach the boundary whilst still allowing acoustic waves to leave the domain. To achieve this L_1 is set according to the relation

$$L_1 = \frac{\sigma}{aL}\left(1 - M^2\right)\left(P - P_\infty\right) \qquad \textbf{(4.40)}$$

where P_∞ is the far-field pressure, M^2 is the maximum Mach number of the flow, L is the domain length, and σ is a model constant. Low values of σ cause minimal acoustic reflections, whereas higher values constrain the pressure variation to an increasingly limited range around the far-field value. In practice, a value of $\sigma \sim 0.28$ is found to give the most satisfactory results.

For inflow conditions it can be seen from Fig 4.1 that all but the outgoing pressure wave amplitude variations (L_5 or L_1 for right and left boundaries respectively) must be specified. Imposing fixed velocities, where these are known, in addition to the temperature is one possible means of acquiring the necessary values of the incoming

L_i s. Although this method once again leads to wave reflections due to the creation of a velocity node on the boundary, as long as at least one non-reflecting boundary is present in the domain, the accumulated errors do not generally reach significant levels.

In the present work, however, a different approach is taken. Since the incoming velocities are not know, imposing a fixed, and essentially arbitrary value of the velocity could produce sharp discontinuities along the boundary where the flow changed from a locally determined inflow to local outflow. To prevent this an approach similar to the non-reflecting outflow is adopted where target values of the relevant variables are specified and boundary point values are brought towards these target values whilst still allowing some transient variation to occur. For a right hand boundary the L_i s are therefore specified as follows

$$L_1 \text{ or } L_5 = \frac{\sigma}{aL}\left(1-M^2\right)\left(P-P_\infty\right) \tag{4.41}$$

$$L_2 = \sigma_2\left(T-T_\infty\right) \tag{4.42}$$

$$L_3 = \sigma_3\left(v-v_\infty\right) \tag{4.43}$$

$$L_4 = \sigma_4\left(w-w_\infty\right) \tag{4.44}$$

$$L_{5+k} = \sigma_{5+k}\left(Y_k - Y_{k,\infty}\right) \tag{4.45}$$

where target values of $v_\infty = w_\infty = 0$, $Y_{k,\infty} = 0$, $T_\infty = T_{init}$, and $P_\infty = P_{init}$ are used together with constants $\sigma_2 = 0.1$, $\sigma_3 = \sigma_4 = 100.0$, $\sigma_{5+k} = 0.1$, and $\sigma = 0.28$ as before.

It should be noted that the constants used in 4.41-4.45 are not derived from theoretical considerations but have been chosen simply through trial and error to provide stability and to minimise any observed boundary generated disturbances.

Finally, additional conditions are needed to extend these inviscid relations to the full Navier-Stokes equations. For the case of a non-reflecting inflow, Poinsot and Lele [114] suggest that the normal stress gradients be set to zero:

$$\frac{\partial \tau_{11}}{\partial x_1} = 0 \tag{4.46}$$

whereas for a non-reflecting outflow the same condition is applied to the tangential stress and normal heat flux terms:

$$\frac{\partial \tau_{12}}{\partial x_1} = \frac{\partial \tau_{13}}{\partial x_1} = \frac{\partial q}{\partial x_1} = 0 \tag{4.47}$$

These viscous conditions differ slightly from the others in that they are not applied at the characteristic level in terms of wave amplitude variation, but directly on the primitive variables in Equations 4.15 - 4.20.

It is recognised that, while the well-posedness of characteristic boundary conditions for the Euler equations has been demonstrated, the same cannot be said of their extension to the Navier Stokes equations as described above. However, their use is justified on practical grounds by their proven effectiveness over alternative methods, and they provide a stable method of advancing the solution on the boundaries, without inducing excessive errors throughout the interior of the domain.

4.1.5 Initial Turbulence Generation

Initial turbulent velocity fields in both SENGA and SENGA2 are generated using the spectral method of Orszag [116], later refined by Rogallo [117]. The method has become an accepted standard technique for producing a homogeneous, isotropic, and initially solenoidal turbulence field. Any number of random initial fields may be generated, where the statistical properties are maintained by ensuring that the energy content of each Fourier mode conforms to a pre-specified energy spectrum.

Starting from the velocity spectrum tensor ϕ_{ij} (§2.3.1), under the conditions of homogeneity, isotropy and continuity, and recognising that the real-space velocity components cannot have imaginary parts, the spectrum tensor may be written

$$\phi_{ij}(k) = \overline{\hat{u}_i^*(k)\hat{u}_j(k)} \tag{4.48}$$

where k is the linear wavenumber vector, * denotes the complex conjugate, and the overbar represents a time, space or ensemble average value.

In an incompressible flow the there is no component of the velocity in the direction of the wavenumber vector, and so the velocity vector may be written as the sum of only the orthogonal wavenumber components:

$$\hat{u}(k) = \alpha(k)e_1 + \beta(k)e_2 \tag{4.49}$$

where e_1 and e_2 are unit basis vectors with e_3 aligned with the wavenumber k. The complex functions α and β must therefore be found, and from the relation between the velocity spectrum tensor and energy spectrum (Eq. 2.48, §2.3.1), the expression

$$\phi_{ii}(k) = \frac{E(k)}{2\pi k^2} = \alpha\alpha^* + \beta\beta^* \tag{4.50}$$

can be used, where the averaging condition used in 4.48 is removed to ensure that each Fourier mode has a specified energy content. This last step is important, particularly in DNS where the sample size of large eddies is small, and so large deviations from the specified energy spectrum at these wavenumbers is possible if the condition is only imposed on average quantities.

Solutions for α and β, compatible with Eq. 4.50, are:

$$\alpha = \sqrt{\frac{E(k)}{2\pi k^2} e^{i\theta_1}} \cos\phi \tag{4.51}$$

$$\beta = \sqrt{\frac{E(k)}{2\pi k^2} e^{i\theta_2}} \sin\phi \tag{4.52}$$

where θ_1 and θ_2 are phase angles and ϕ is the azimuthal angle of the e_1 basis vector, all of which have randomly assigned, uniform distributed values between 0 and 2π radians.

The Fourier space basis vectors e_1 - e_3 may be aligned with the computational grid by setting the e_{13} component to 0, yielding

$$e_1 = \left(\frac{k_2}{M}, -\frac{k_1}{M}, 0 \right) \tag{4.53}$$

$$e_2 = \left(\frac{k_1 k_3}{kM}, \frac{k_2 k_3}{kM}, -\frac{k_1^2 + k_2^2}{kM} \right) \tag{4.54}$$

$$e_3 = \left(\frac{k_1}{k}, \frac{k_2}{k}, \frac{k_3}{k} \right) \tag{4.55}$$

where $M = \sqrt{k_1^2 + k_2^2}$.

Applying this to Eq. 4.49 provides the Fourier space velocity components

$$\hat{u}_1(k) = \frac{\alpha k k_2 + \beta k_1 k_3}{kM} \tag{4.56}$$

$$\hat{u}_2(k) = \frac{-\alpha k k_1 + \beta k_2 k_3}{kM} \tag{4.57}$$

$$\hat{u}_3(k) = \frac{\beta(k_1^2 + k_2^2)}{kM} \tag{4.58}$$

4.1.5.1 Implementation

In implementing this method, an additional constrained of symmetry must be imposed to ensure that the physical space velocity components are real. This requirement also means that it is only necessary to provide Fourier space velocity components over half the computational domain since the remaining real-space values follow from the complex component of the Fourier space velocities and the symmetry condition.

The full three-dimensional inverse transform of the velocity vector may be written

$$u_i(x_1, x_2, x_3) = \int \hat{u}_i^{(1,2)}(x_1, x_2, k_3) e^{-i2\pi k_3 x_3} dk_3 \tag{4.59}$$

where $\hat{u}_i^{(1,2)}$ represents the partial transform of the $\hat{u}_i$ vector in the x_1 and x_2 directions. The symmetry condition can now be imposed in the remaining x_3 direction such that

$$\hat{u}_i^{(1,2)}(x_1, x_2, -k_3) = \hat{u}_i^{*(1,2)}(x_1, x_2, k_3) \tag{4.60}$$

The procedure used in SENGA is firstly to populate grid points over half the domain in the range $0 \le k_3 \le N_z/2$, where the wavenumber origin 0 is located in the centre of the domain, and N_z is the node number in the x_3-direction. Following this, symmetry is imposed along lines in x_3 according to Eq. 4.60, thereby populating the remaining grid points in the range $-N_z/2 \le k_3 \le 0$. A final one-dimensional inverse transform is then carried out in the remaining x_3 direction to complete the process.

It should be noted that although the choice of x_3 as a special direction to impose symmetry is arbitrary, this must be taken into account when producing initial fields for

two-dimensional turbulence. In the present work, all 2D initial fields are generated in the x-z planes for this reason, and subsequently transformed as necessary prior to computation.

A second feature of this method is that the initial fields are constructed assuming periodicity, and an incompressible fluid. When transferred to a domain employing NSCBC, or any other approximate boundary treatment, with a fully compressible formulation, the initial errors generated on the boundaries after the first time step lead to unavoidable initial pressure transients traversing the domain during the early stages of the simulation. It is therefore desirable to let the initial solution evolve for a short time to allow these transients to decay. This is not always possible, however, and these issues are discussed in more detail in Section 5.1.2.

4.2 SENGA 2

The principal differences between SENGA and SENGA2 are outlined at the beginning of this chapter. While the general formulation remains similar, the addition of multi-species chemistry and transport complicates the implementation considerably, and several additional numerical routines are required to evaluate all the quantities at each time step. In contrast to SENGA, SENGA2 is written entirely in dimensional form using standard S.I. units. This affords more straightforward compatibility with pre-existing thermo-chemical databases and reaction mechanisms - in particular those written in the well-established CHEMKIN format, for which a dedicated pre-processing routine is also supplied to convert these files for use in SENGA2.

In the following sections, the core numerical procedures - where they differ from those described previously for SENGA - are presented. The outline given here follows a more complete description given in a user manual accompanying the code, by R. S. Cant.

Equations are solved for the conservation of mass, momentum, internal energy and the mass fractions for N-1 reactive species as presented in Section 2.1. Body forces, bulk

viscosity and the Soret and Dufour effects are neglected. Modelling of the heat loss due to radiation is described in Section 4.2.2.

4.2.1 Thermodynamic Quantities

The mass specific heat capacity for species k has a temperature dependence that is approximated by a 5th-order polynomial of the form

$$C_{pk} = \sum_{i=1}^{5} a_{k,i}^{(l)} T^{i-1} \tag{4.61}$$

following the well established CHEMKIN data format. Polynomial coefficients $a_{ki}^{(l)}$ are taken from two intervals of temperature (l) of 0K < T <1000K and 1000K < T <3000K.

Similarly, the mass specific enthalpy and entropy may be found from

$$h_k = \sum_{i=1}^{5} \frac{a_{k,i}^{(l)}}{i} T^i + a_{k,i+1}^{(l)} \tag{4.62}$$

$$s_k = a_{k,1}^{(l)} \ln T + \sum_{i=1}^{5} \frac{a_{k,i}^{(l)}}{i-1} T^{i-1} + a_{k,i+2}^{(l)} \tag{4.63}$$

respectively, where appropriate coefficients are taken from a pre-defined thermo-chemical data file.

Combining Eq. 4.62 with the caloric equation of state, the total internal energy may be written

$$E = \sum_{k=1}^{N} Y_k \left(\sum_{i=1}^{5} \frac{a_{k,i}^{(l)}}{i} T^i + a_{k,i+1}^{(l)} \right) - R_m T + \frac{1}{2} u_k u_k \tag{4.64}$$

where the mixture specific gas constant is found from $R_k = \sum_{k=1}^{N} Y_k R_0$.

Equation 4.64 may then be rearranged in ascending powers of T to form the expression

$$f(T) = \left(\frac{1}{2}u_k u_k - E\right) + \sum_{k=1}^{N} Y_k a_{k,i+1}^{(l)} + \left[\sum_{k=1}^{N} Y_k \left(a_{k,1}^{(l)} - R_k\right)\right]T + \sum_{i-2}^{5}\left(\sum_{k=1}^{N} Y_k \frac{a_{k,i}^{(l)}}{i}\right)T^i \qquad \textbf{(4.65)}$$

which is solved for $f(T) = 0$ during run-time to any desired level of accuracy using Newton-Raphson iteration.

Thermal conductivity for the mixture has a temperature dependence of the form

$$\frac{\lambda}{C_p} = A_\lambda \left(\frac{T}{T_0}\right)^r \qquad \textbf{(4.66)}$$

where C_p is the effective mass specific heat for the mixture, and in this case the values used for constants A_λ and r are $4.78\text{x}10^{-7}$ and 0.7 respectively.

Dynamic viscosity is then related to the thermal conductivity by assuming a constant Prandtl number for all species of $\Pr = 0.7$:

$$\mu = \frac{\lambda}{C_p}\Pr \qquad \textbf{(4.67)}$$

The diffusive flux for each species is found by applying Fick's law in the relation

$$\rho V_{k,i} Y_k = -\rho D_k \frac{\partial Y_k}{\partial x_i} + \rho V_i^{(c)} Y_k \qquad \textbf{(4.68)}$$

where the diffusion coefficient D_k is found from

$$D_k = \frac{\lambda}{\rho C_p Le_k} \tag{4.69}$$

in which a constant effective Lewis number, Le_k, is assumed for each species. The last term on the RHS of Eq. 4.68 represents a correction velocity term that must be included to ensure that continuity is preserved. Applying the compatibility condition (Eq. 2.18), the correction velocity may be calculated from

$$\rho V_i^{(c)} = \sum_{k=1}^{N} \frac{\partial}{\partial x_i} \rho D_k \frac{\partial Y_k}{\partial x_i} \tag{4.70}$$

4.2.2 Chemistry

In general, for a reaction mechanism involving M steps of the form given in Eq. 2.12, the molar rate of production for each species at each reaction step m is given by

$$\overline{\omega}_{k,m} = \left(\nu''_{k,m} - \nu'_{k,m}\right)\left[k_{f,m}(T)\prod_{\beta=1}^{N} c_\beta^{\nu'_{\beta m}} - k_{b,m}(T)\prod_{\beta=1}^{N} c_\beta^{\nu''_{\beta m}}\right] \tag{4.71}$$

where the overbar denotes molar quantities. Equation 4.71 expresses the net rate of production of species k at each step considering both forward and backwards reaction rates through the coefficients $k_{f,m}(T)$ and $k_{b,m}(T)$ respectively, where $c_\beta^{\nu_{\beta,m}}$ is the equilibrium molar concentration.

The forward reaction rate is evaluated from an Arrhenius expression (Eq. 2.16) where the step constants are obtained from the supplied mechanism data file.

For an irreversible reaction the reaction rate evaluation is complete at this point, however, where the reaction step involves both forward and backward reactions, a backward rate coefficient must also be found.

Where this is the case the backward rate $k_{b,m}$ is related to the forward rate $k_{f,m}$ through the following expression

$$\ln k_{b,m} = \ln k_{f,m} + \sum_{k=1}^{N} \left(\nu''_{k,m} - \nu'_{k,m}\right)\left(\frac{\overline{g}_k}{R^0 T} + \ln\frac{P^0}{R^0} - \ln T\right) \tag{4.72}$$

where $\overline{g}_k$ is the molar Gibbs free energy for species k given by $\overline{g}_k = \overline{h}_k - T\overline{s}_k$.

For reaction steps involving a third body, M, of the form

$$\sum_{k=1}^{N} \nu'_{k,m} Z_k + M \rightarrow \sum_{k=1}^{N} \nu''_{k,m} Z_k + M \tag{4.73}$$

the molar reaction rate may be calculated from

$$\overline{\omega}_{k,m} = \left(\nu''_{k,m} - \nu'_{k,m}\right) k_m(T) \left(\sum_{k=1}^{N} \eta_{k,M} c_k\right) \prod_{\beta=1}^{N} c_\beta^{\nu'_{\beta m}} \tag{4.74}$$

where the third body efficiencies $\eta_{k,M}$ are again taken from the supplied reaction mechanism data file.

4.2.3 Radiative Heat Transfer

In the present code an optically-thin radiation model has been included to account for radiative losses in the flame for multi-step chemistry simulations. The optically-thin assumption is widely used in gas phase combustion simulations where scattering and reabsorption are known to be negligibly small [118].

The heat loss term $\dot{q}_r$ in Eq. 2.9 is evaluated according to

$$\dot{q}_r = -4\sigma K_p \left(T^4 - T_\infty^4\right) \tag{4.75}$$

where σ is the Stefan-Boltzmann constant, T_∞ is the far-field temperature, and K_p is the Planck mean absorption coefficient for the mixture.

Four radiating species are considered: CH_4, CO, CO_2, and H_2O, and so the effective mixture Planck mean absorption coefficient may be calculated from

$$K_p = P_{CH_4} K_{CH_4} + P_{CO} K_{CO} + P_{CO_2} K_{CO_2} + P_{H_2O} K_{H_2O} \tag{4.76}$$

where P_k and K_k are the partial pressure and Planck mean absorption coefficients respectively for species k.

The temperature dependence of the species Planck mean absorption coefficients is approximated in the present model by a fifth-order polynomial fit with coefficients $A_{i,k}$, obtained by Ju et al [119] from the experimental data of Tien [120], where

$$K_k = \sum_{i=1}^{5} A_{i,k} T^i \tag{4.77}$$

The validity of this model in the present implementation is assessed in Section 4.2.5.4.

4.2.4 Spatial Discretisation and Time Advancement

Spatial derivatives for the interior points are evaluated from a 10^{th} order explicit central difference scheme, similar to that described in Section 4.1 for SENGA. Approaching the boundary a slightly higher order is retained: 8^{th}, 6^{th} , and 4^{th} order central differences, followed by 4^{th} order mixed and finally 4^{th} order one-sided on the boundary.

Time advancement is achieved with a low storage Runge-Kutta scheme with embedded error control, the full details of which can be found in [121]. The scheme is fourth order accurate and requires five sub-steps at each time increment.

As described previously, only two registers are used during the main procedure: one for dependent variable and one for the derivative, meaning that the information normally required for error estimation is overwritten at each sub step. To overcome this limitation, but at the expense of a slightly increased memory requirement, a third order embedded error estimation scheme is included.

Where adaptive time stepping is desired, the estimated maximum error norm may then be used in conjunction with a proportional-integral-derivative (PID) type control algorithm to determine the subsequent time step size.

4.2.5 Boundary Conditions

Navier-Stokes characteristic boundary conditions as formulated by Sutherland and Kennedy [122] are used in SENGA2. While fundamentally similar to those described previously (§4.1.4.1) for SENGA, in the present formulation the source terms in the species transport equations are retained in the characteristic analysis, and incorporated into the boundary conditions at the characteristic level through the wave amplitude variation terms.

In the absence of body forces, the primitive variable source terms in the momentum equations go to zero, and the characteristic-level source terms can therefore be written

$$s_1' = \frac{1}{2} s_p \tag{4.78}$$

$$s_2' = -\frac{1}{a^2} s_p \tag{4.79}$$

$$s_3' = 0 \tag{4.80}$$

$$s_4' = 0 \tag{4.81}$$

$$s_5' = \frac{1}{2} s_p \tag{4.82}$$

$$s_{5+k}' = s_{Y_k} \tag{4.83}$$

where $s_p = (1-\gamma)\sum_{k=1}^{N-1}\left(\breve{h}_k - \breve{h}_N\right)\omega_k$, and $s_{Y_k} = \omega_k / \rho$.

$\breve{h}_k$ is the reduced enthalpy of species k: $\breve{h}_k = h_k - C_p T R^0 / R$, and ω_k is the mass-based reaction rate.

Wave amplitude variations for incoming waves are specified as described previously for non-reflecting, mixed inflow/outflow boundary types, supplemented by the additional source terms according to

$$L_1 \text{ or } L_5 = s_{1/5}' + \frac{\sigma}{aL}\left(1 - M^2\right)\left(P - P_\infty\right) \tag{4.84}$$

$$L_2 = s_2' + \sigma_2\left(T - T_\infty\right) \tag{4.85}$$

$$L_3 = \sigma_3\left(v - v_\infty\right) \tag{4.86}$$

$$L_4 = \sigma_4\left(w - w_\infty\right) \tag{4.87}$$

$$L_{5+k} = s_{5+k}' + \sigma_{5+k}\left(Y_k - Y_{k,\infty}\right) \tag{4.88}$$

The additional viscous and heat flux terms, as before, are given by Equations 4.46 and 4.47 for an inflow and outflow respectively.

4.2.6 Parallelisation

Both SENGA and SENGA2 were constructed with large-scale parallel execution in mind, although in the present work only SENGA2 is used in this mode.

Parallelisation is achieved through straightforward domain partition (sometimes referred to as domain decomposition), using the Message Passing Interface (MPI) protocol for inter-processor communications. Under this scheme the global numerical domain may be divided into any number of sub-domains corresponding to physical partitions of the simulated global volume, and the solution is then advanced independently at each time step on each processor for each of these sub-domains. Variables from grid points on neighbouring processors that are required for the calculation of spatial derivatives are communicated through MPI messages at the beginning of each time step. For the 10^{th} order scheme implemented in the present code this entails a five-point data halo for all the conserved variables in each coordinate direction, assuming that no global boundary (other than periodic or a plane of symmetry) has been specified.

During initialisation a single processor is used exclusively for generating the initial turbulent field and to format and distribute the initial thermo-chemical and control data. Following this stage, however, the load balancing among processors is close to ideal due to the inherent load symmetry of the domain partition methodology, and so efficient large-scale parallelisation is readily achieved. So far, the code has been deployed on several large-scale parallel platforms, and near linear parallel speed-up has been observed for up to 128 processors. Details of the computational requirements for each of the databases used in this study are outlined in the relevant sections.

4.2.7 Code Validation

Many of the core numerical procedures used in SENGA2 such as the calculation of first and second spatial derivatives, and the Runge-Kutta time advancement routine, are either identical to, or are only slight modifications to those used previously in SENGA.

The accuracy and stability of these methods is well established, and so they are not re-evaluated here. On the other hand, molecular transport modelling, radiative heat transfer, the inclusion of a chemical source term in the NSC boundary conditions, and the application of locally determined inflow/outflow boundary conditions are implemented together in SENGA2 for the first time. Although these methods have been validated independently and used successfully in similar DNS codes, their use in combination, and in the present configuration remains unvalidated. It is therefore useful to examine their performance and also their potential as sources of inaccuracy.

4.2.7.1 Turbulence Decay with Inflow / Outflow Boundaries

As described in Section 4.1.4, under the mixed inflow / outflow NSCBC formalism, specification of incoming and outgoing characteristic wave amplitudes is determined by the local value of the boundary-normal velocity component. For an outflow, only a single wave amplitude, L_5 or L_1, is required, whereas for an inflow, values of the L_2, L_3, L_4, and $L_{Y,i}$ must be specified. As implemented in SENGA, the effect this has on non-reacting, decaying three-dimensional turbulence is examined in detail in Section 5.1.3

In addition to the above conditions, in SENGA2 viscous conditions are also dependent on the local boundary normal velocity, where on a non-reflecting outflow boundary the tangential flux gradients are set to zero:

$$\left(\nabla_\gamma \tau_{\beta\alpha}\right)\hat{n}_\gamma \hat{n}_\beta \hat{t}_{1,\alpha} = 0 \qquad \textbf{(4.89)}$$

and for a non-reflecting inflow this is applied to the normal stresses:

$$\left(\nabla_\gamma \tau_{\beta\alpha}\right)\hat{n}_\gamma \hat{n}_\beta \hat{n}_\alpha = 0 \qquad \textbf{(4.90)}$$

Given the already well recognised differences between two and three dimensional turbulence, it is useful to asses the effect of these boundary conditions on the properties of 2D decaying turbulence in the present configuration.

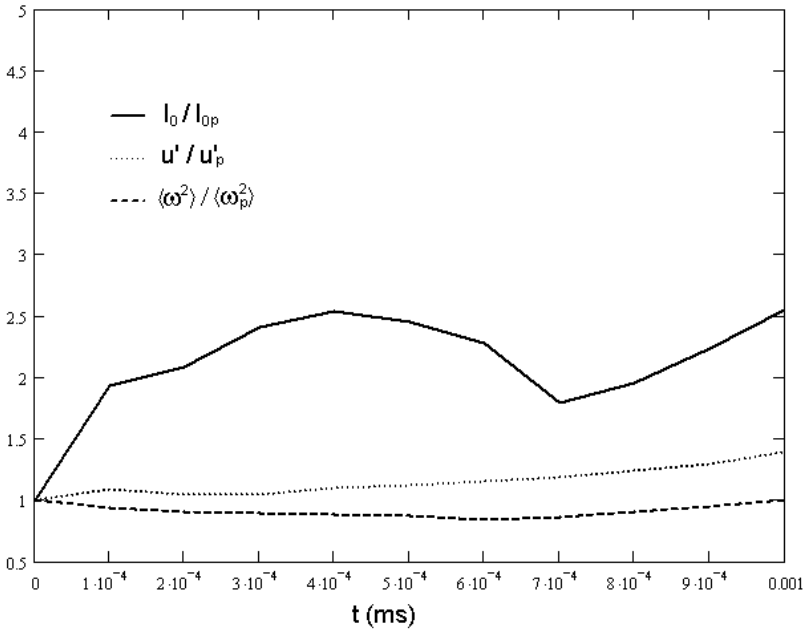

Figure 4.2 Evolution of integral length scale l_0, rms turbulent velocity u', and mean square enstrophy $\langle\omega^2\rangle$ normalised by values taken from an equivalent simulation with periodic boundaries. Initial values are l_0 = 1.34mm, u' = 1.65 ms^{-1}, and $\langle\omega^2\rangle$ = 1.21x10^7 s^{-2}. The domain is square with $N_x = N_y$ = 512 grid points and $L_x = L_y$ = 18mm.

In Figure 4.2 turbulence properties in a domain with mixed inflow/outflow boundaries are compared with those of the periodically bounded domain for initially identical velocity fields. It can be seen that u' and $\langle\omega^2\rangle$ remain close to the periodic solution throughout the simulation time (it is assumed that the use of periodic boundaries does not itself introduce any numerical errors into the solution), whereas the integral length scale shows an initially steep increase to approximately twice the periodic value, and fluctuates around this value for the remaining simulation time. Although not unphysical, this exaggerated growth in the integral scales is unfortunate since it is a further departure from three-dimensional turbulence decay. It should be noted that some of the discrepancy may be due to the lower sample size used in the calculation of l_0 in two-dimensions: turbulent velocity and vorticity are local quantities and so may be evaluated at each grid point, whereas l_0 is calculated by integrating the longitudinal velocity

correlation function across half the domain for each coordinate direction (only half the domain can be used due to periodicity), and so the sample size is reduced by more than two orders of magnitude.

Larger integral length scales will reduce the available simulation time due to enhanced global convection of the kernel towards the boundaries, but the effect is not expected to significantly alter any findings from analysis of flame kernel data since growth of the integral length scale is already a well recognised feature of two-dimensional turbulence.

4.2.7.2 Flame Passage Across a Boundary

The Navier-Stokes Characteristic Boundary Conditions as proposed by Poinsot and Lele [114] are not explicitly formulated for reacting flows, and while their accuracy and stability is quite satisfactory while the flame is far from the boundary, as the reaction rate becomes non-negligible on the boundary large pressure transients are generated, ultimately leading to flow reversal and entirely non-physical results.

By including the source term in the derivation of the NSCBC equations, Sutherland and Kennedy's [122] modified boundary conditions offer a considerable improvement over the original formulation. However, even here the flame - boundary interaction is far from ideal and for a multi-dimensional flame crossing a non-reflecting outflow, boundary generated pressure perturbations and local flow acceleration has been observed.

The effect is illustrated in Figs 4.3a–d. A single-step, laminar, circular flame is initiated at the lower left corner of the domain. Symmetry conditions are imposed on the left and bottom faces and mixed inflow / outflow NSCBC using Sutherland and Kennedy's formulation on the top and right.

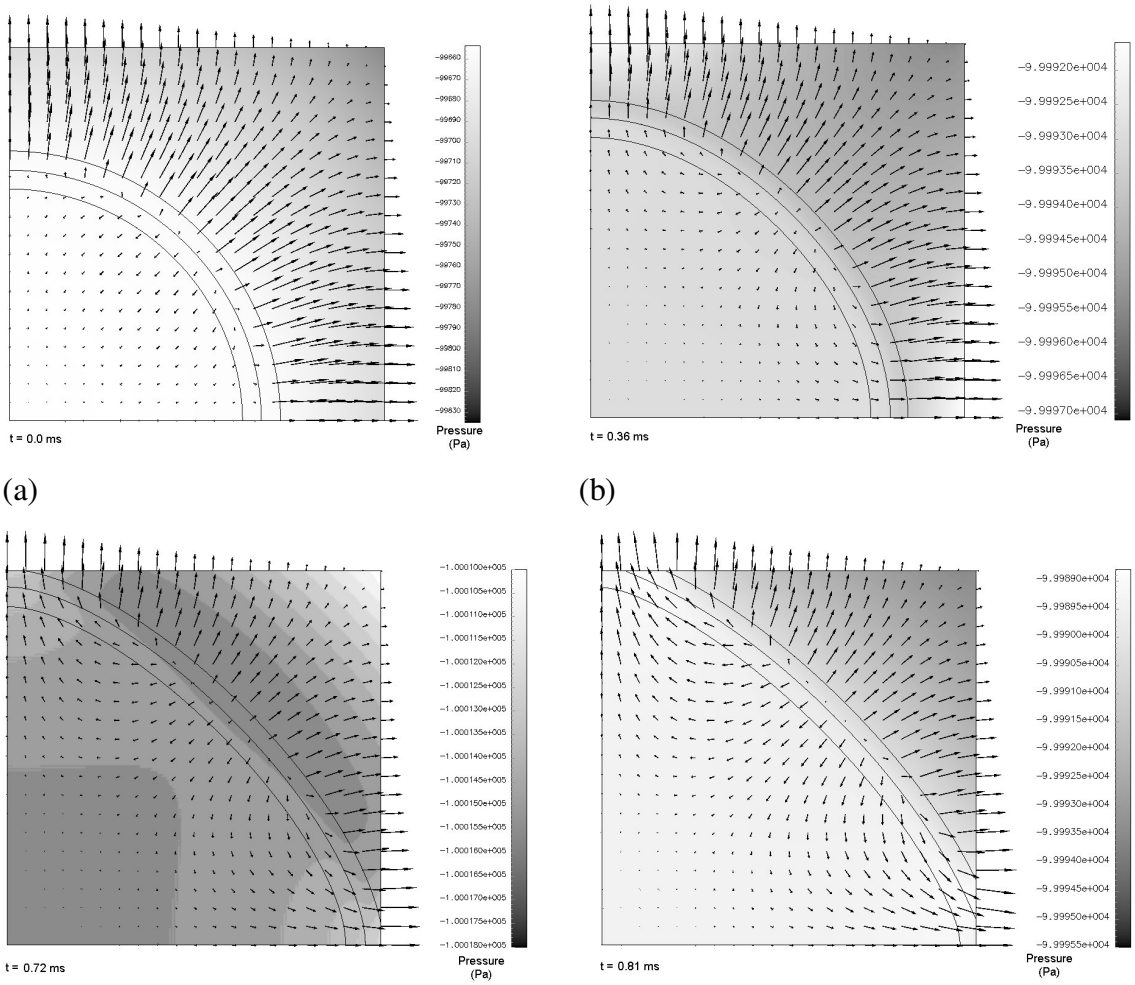

Figure 4.3 Expanding circular flame crossing non-reflecting outflow boundaries. Symmetry conditions imposed at left and bottom faces. Isolines of progress variable shown at c = 0.1, 0.8, and 1.0. Pressure field displayed as greyscale shading and velocity by vector arrows. (Note: t = 0 ms does not indicate the beginning of the simulation - the flame is in fact well established by this point).

It can be see from the velocity vectors that at all positions along the boundaries the local velocity normal points outside the domain, and so the boundaries here are acting identically to a standard non-reflecting outflow as prescribed in [122].

In Fig 4.3b the initial effects of the boundary can be seen in the slight loss of radial symmetry caused by a pressure differential parallel to the boundary. The flow pattern near the flame front remains largely unaffected. As the leading edge of the flame (c = 0.1 isoline) reaches the boundary this pressure differential becomes exaggerated and flow acceleration normal to the flame front is seen at the interface. Away from the flame

– boundary interface a tangential flow is induced at the flame front (tangential to the flame surface) which, due to the flame symmetry causes some tangential straining of the flame in that region. As the flame continues to pass across the boundary these anomalies persist but no further deterioration is apparent.

The effects of flame–boundary interaction remain negligibly small until the c = 0.1 isoline reaches a distance of approximately δ_{th} from the boundary. Within this distance and as the flame crosses the boundary, the flow anomalies remain relatively localised, and flame straining due to symmetry will not be present in a unsteady simulation. Given the above observations a prudent approach would therefore be to reject flame surface data or global statistics where any region of the flame is within a distance δ_{th} of the domain boundary. Since the effects remain localised it seems reasonable that flame data away from any flame-boundary interactions may still be used with reasonable confidence.

4.2.7.3 68-step Mechanism

The 68-step reduced mechanism used in the present study, developed by Warnatz [4], is based on a subset of C_1 kinetic data taken from a detailed methane-air mechanism which in full form consists of aggregated data for all species up to C_2. Species, thermochemical parameters and reaction rate data for the 68-step mechanism are given in Appendix 1.

For pure methane combustion simpler mechanisms are available that would produce comparable accuracy for the major species in a turbulent flame. However, for methane / hydrogen blends, chain initiating reactions for the breakdown of H_2 (reactions 2 and 3) must be included, which precludes applying a steady state assumption to the oxygen radical.

Several DNS studies have previously been published using the present mechanism [59,123], however to validate both the mechanism and code in its current formulation it is useful to compare the steady state profiles for transported species with an independently obtained solution for the same flame. For this purpose steady state mass

fractions for a stoichiometric methane-air flame generated using COSILAB® software [124] are used. The COSILAB profiles are calculated using detailed molecular transport modelling and GRI-Mech 3.0 [7], which at the present time represents the most comprehensive and extensively tested methane-air mechanism available, comprising 53 species and 325 reactions.

As Figures 4.4 a-c show, the agreement for the major species CH_4, O_2, CO_2, H_2O, and CO is reasonably good particularly in the preheat and reaction zones which are the most important in determining the overall rate of fuel consumption [7]. In the upstream regions of the flame the O, H and OH radicals play a critical role in the initial breakdown of CH_4 and H_2 through hydrogen abstraction, and again as shown in Fig 4.4b their concentrations are captured reasonably well (note the scale change from Fig 4.4a). Molecular hydrogen H_2 appears to be slightly over predicted in the upstream region, and this is most probably due to the differences in diffusive transport modelling used in each code. In particular, SENGA2 neglects thermal-diffusion (Soret) effects which have the tendency to drive light species such as H_2 towards hotter regions of the flow, and which may explain some of the discrepancy in this case. It is also worth noting that where H_2 has been added to the premixed gases, concentration gradients will be reduced in the preheat zone so that the diffusive flux, and any errors associated with its modelling, will also be reduced.

Profiles for many of the remaining intermediate species show considerable departures from the detailed calculations (although the absolute error is exaggerated by the scale change). However, their actual concentrations are not of direct interest in the present work, only their overall roles in the chain branching and chain carrying reactions of the more important species, which as noted, appear to be adequately captured.

It is also important to note that under unsteady conditions the need for accurate predictions of species concentrations and diffusive flux becomes progressively less important. The steady state calculated here must therefore be regarded as a worst-case situation, and in this context the performance of the mechanism appears quite adequate.

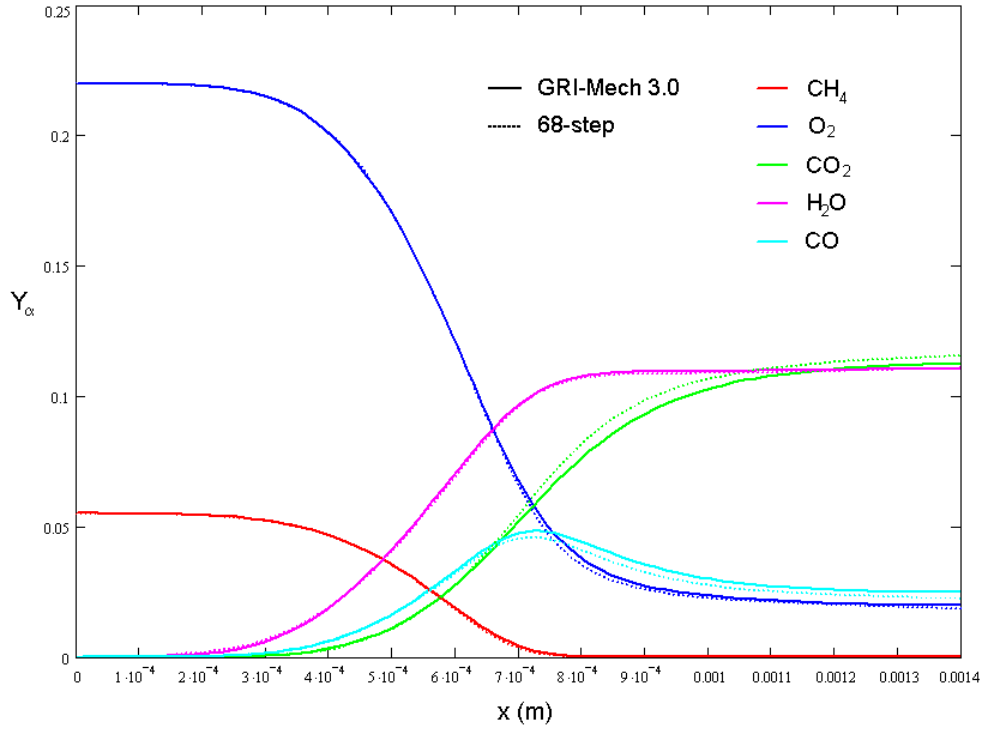

(a)

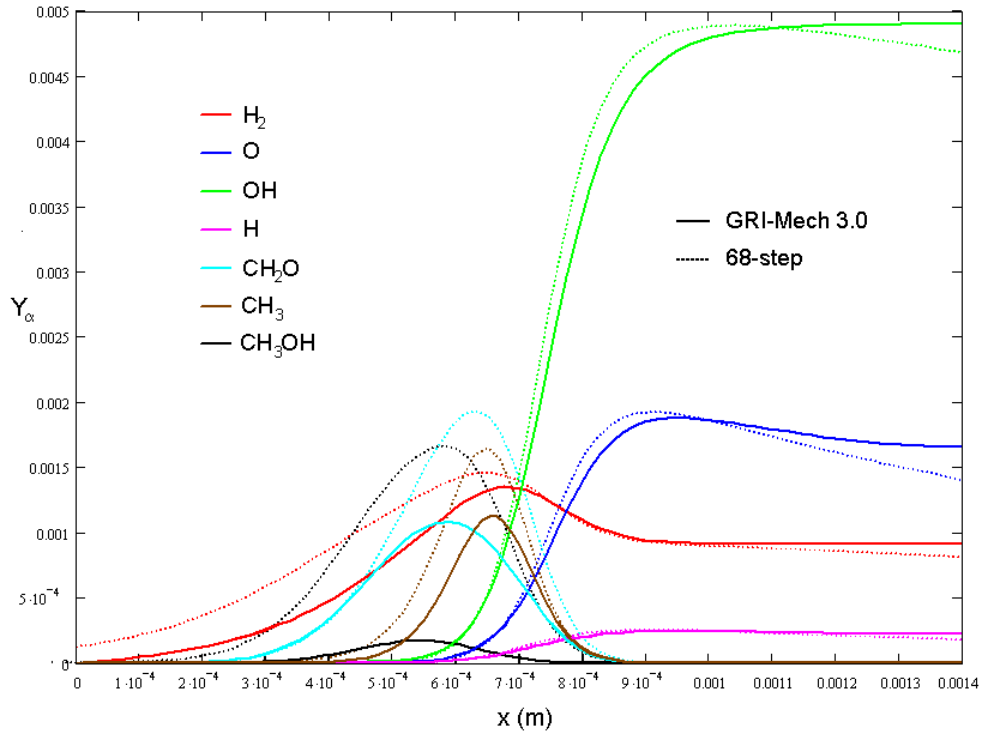

(b)

Figure 4.4 a-c Species mass-fraction profiles for steady-state stoichiometric laminar methane-air flame. GRI-Mech 3.0 (solid), and 68-step reduced mechanism (dots).

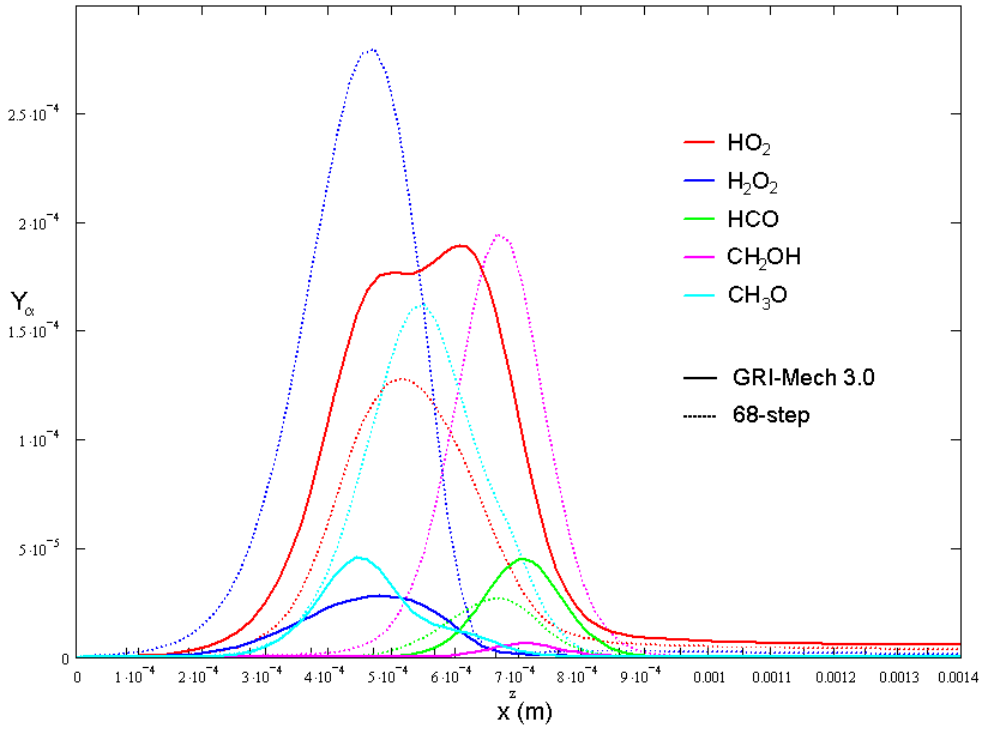

(c)

Figure 4.4 Continued.

4.2.7.4 Radiative Heat Loss Model

As shown in the previous section the species considered in the radiative heat loss model; CH_4, CO, CO_2, and H_2O are well predicted in the steady state limit. Figure 4.5 illustrates the effect of including the model on the steady state temperature profiles for pure methane-air flames at the various stoichiometries used in the present study.

The results are in agreement with previous findings [44,118], and also demonstrate the important observation that radiative losses increase considerably for lean flames close to the flammability limit. Guo et al [44,45] note the existence of a second flammability limit for lean flames at low stretch rates due purely to radiative losses: as the flame thickness increases it undergoes greater volumetric heat losses, which sets up a positive feedback loop of lower flame temperatures and increasing thickness, ultimately leading to extinction. It is clear therefore that for the ultra-lean flames of interest in the present study radiative losses are important even in unsteady flows.

In addition to the increased flame thickness a reduction in the laminar flame speed is also observed for the non-adiabatic flames of 0.26%, 1.37%, and 4.46% respectively for decreasing values of ϕ corresponding to Fig 4.5.

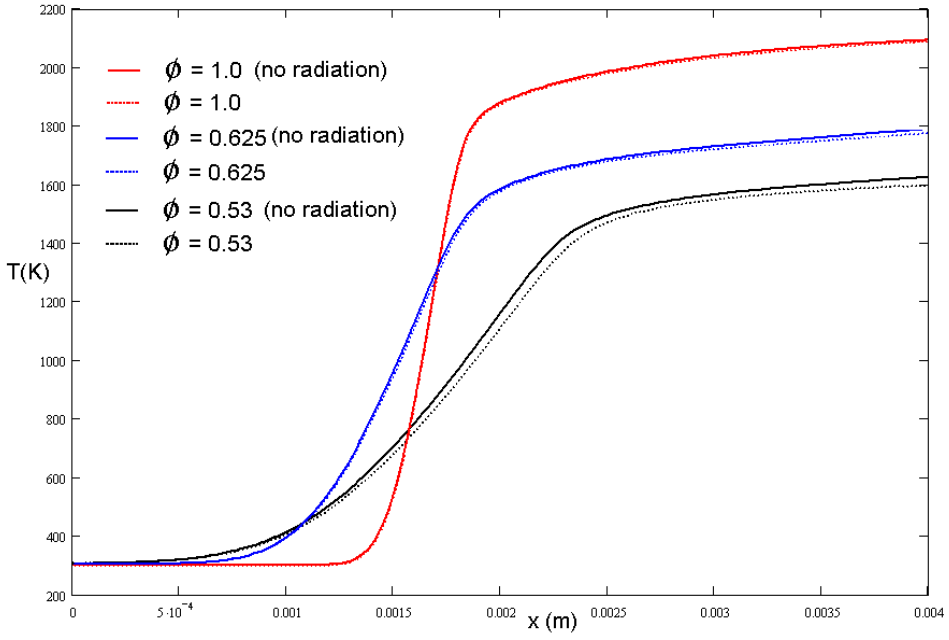

Figure 4.5 Steady State temperature profiles with and without radiative heat loss.

5 GLOBAL TURBULENCE EFFECTS WITH SIMPLIFIED CHEMISTRY

In this chapter results are presented on the interaction of the kernel with a field of decaying turbulence from a principally geometric point of view. Three-dimensional data on the kernel evolution were generated using the SENGA code for four different sets of initial turbulence parameters. Additional results were also obtained from SENGA2 in an extended two-dimensional domain to examine the findings over longer time scales.

An assessment of the combustion regime is provided, and the global effects of the turbulence are considered in Sections 5.1.4.1 and 5.1.4.2 respectively. The main focus of this chapter, however, is on the differential mean velocity magnitudes experienced by individual isosurfaces of the progress variable, and the possible causes and consequence of this observation.

Section 5.1.4.3 presents the data relating to this effect and demonstrates the existence of bias in the distribution of the surface density function around the kernel. A phenomenological model of the effect is put forward in Section 5.1.5.1, and finally, an additional two-dimensional database is used in Section 5.2 to investigate the effect in an extended domain for more developed flame kernels.

5.1 Three-Dimensional Simulations

5.1.1 Database Parameters

Initial turbulence parameters were selected, firstly with the aim of matching as closely as possible the conditions experienced by kernels in a typical IC engine, and secondly to produce data across a reasonable range of turbulence parameters so that a comparative analysis could be made into the influence of the different scales of the flow.

While the first of these objectives is met to a reasonable degree in Case A, extending the study to include smaller initial integral length scales and higher turbulence intensities lead to rates of dissipation of kinetic energy that are not very representative of real flows. Nevertheless they are not unphysical, in the sense that it is only the lack of supply of energy from the large scales that makes them unrealistic, and so useful qualitative information can still be gained from their analysis.

With this last point in mind, and considering the inherently time-dependent nature of the interaction of the turbulence with an expanding kernel, a parallel, non-reacting flow study is carried out into the decay properties of the fresh-gas turbulence across the same set of initial turbulence parameters listed in Table 5.1. By having a good understanding of the changes in length and time scales in the fresh gases, whether representative of real turbulence or otherwise, these changes may be taken into account in the analysis of the flame kernel development.

For each parameter set in the database - summarised in Table 5.1, a series of 6 repeated simulations were carried out with different, randomly generated initial turbulence fields. The initial fields were created using the spectral method of Orszag [116], as outlined in Section 4.1.5. Seed numbers supplied to the random number generator are unique to each individual simulation in order to minimise any possibility of spurious correlations between cases. Including the parallel cold-flow study, this constitutes a database of 48 individual simulations.

Computations were carried out on single 64-bit AMD Opteron 2.4HGz processors with 8GB shared RAM per dual-core node. A non-dimensional time step of $\Delta t/\tau_f = 3.0\text{x}10^5$ was used and simulations were continued until the c = 0.1 isosurface had reached a domain boundary - or in the case of the non-reacting flow database an equivalent elapsed time. Wall clock times were typically in the region of 110hrs for each of the flame kernel simulations, and 85hrs for the non-reacting flows.

Case	$l_{0,init}/\delta_{th}$	u'_{init}/s_L^0	$Re_{t\,(init)}$	Common parameters
A	2.93	4.0	151	Le =1 .0 Grid points (164^3)
B	1.66	2.0	43	Pr = 0.7 Domain size $L_{x,y,z} \approx 16\delta_{th}$
C	1.66	4.0	86	Sc = 0.7 Laminar flame speed $s_L^0 = 1.0$
D	1.08	4.0	56	$\beta = 6.0$ Initial kernel radius $R_{init} = 1.12\delta_{th}$
				$\rho_u/\rho_b = 4$

Table 5.1 Flame kernel database parameters. Le, Pr, Sc are the Lewis, Prandtl, and Schmidt numbers respectively. β is the Zel'dovich number, and $Re_{t(init)} = l_0u'/\nu$ is the initial turbulent Reynolds number.

All results are normalised by the unstretched laminar flame speed s_L^0, flame thermal thickness $\delta_{th} = (T_{ad} - T_0)/MAX|\partial T/\partial n|$, and flame time $\tau_f = \delta_{th}/s_L^0$, where T_{ad} is the adiabatic flame temperature, T_0 is the fresh gas temperature and n is the distance through the flame normal.

It should be noted that, unless otherwise stated, all quantities used in the following discussions refer to the ensemble average values of the six repetitions carried out for each case.

Surface conditioned variables such as position, velocity and SDF were evaluated at 10 isolevels of the progress variable (c = 0.1, 0.2,..., 1.0) by linear interpolation in the computational cell where a surface crossing was found. Validation of this method was carried out on a laminar kernel test case initialised with a constant, uniform drift velocity, where the error was found to be < 2% for mean values on any isosurface.

The potential loss of accuracy of this method compared with more complex methods is considered acceptable since it enabled evaluations to be carried out efficiently during run-time, and on multiple isosurfaces, so providing time-resolved information on these quantities throughout the flame structure.

5.1.2 Initialisation

The initial turbulent field conforms to the Schumann and Patterson energy spectrum [29] (Eq. 5.1), which is described in more detail in Section 2.3.2. The integral length scale and rms turbulent velocity are defined in wavenumber space through Eq. 5.1 by specifying the peak wavenumber k_p and rms velocity u respectively.

$$E(k) = 16\sqrt{\frac{2}{\pi}}u^2 \frac{k^4}{k_p^5} e^{-2\left(\frac{k}{k_p}\right)^2} \quad \textbf{(5.1)}$$

Superimposed onto this are the temperature, density and progress-variable fields from a precomputed laminar flame kernel with initial radius $R_{init} \approx 1.12\delta_{th}$. From preliminary tests it was found that, whilst the longest simulation time could be achieved by using the smallest initial kernel, a kernel that would otherwise propagate successfully under laminar conditions, could be quenched in the presence of turbulence.

This quenching is caused principally by turbulence induced strain and curvature, as discussed later, but during the early stages it was also found that some transient effects caused by the initialisation routine were contributing to this, and which are now briefly described.

5.1.2.1 Initial Transients

No pressure field information is produced during the initialisation of the turbulence – the flow is assumed to be incompressible, so resolution of this pressure field after the first time step produces large pressure gradients on and near the boundaries were the order of spatial derivatives is reduced and NSCBC approximations are applied. These errors are realised as acoustic waves which traverse the domain from the boundaries, pass through the initial kernel, and are then partially reflected from the opposing faces.
A second, unrelated effect occurs because the initial turbulence in the fully-burnt region of the kernel has not had time to adjust to the higher dynamic viscosity in the hot gasses,

and so has a greater ability to disrupt the flame structure than at later times when some of the energy has dissipated.

To overcome these issues whilst still allowing the maximum simulation time, the pre-exponential factor in the Arrhenius expression is initialised at 50% above its normal value and relaxed linearly back to its correct value by $t/\tau_f \approx$ 0.1. This has the effect of lowering the turbulence intensity during this period by increasing the laminar flame speed, and since the presence of initial transients described above precludes any quantitative information being extracted during these early stages, this approach allows the maximum useful information to be gained for the purposes of this study. It should also be noted that much more considerable transients are created from the spark ignition process in real IC engines, and no attempt is made to recreate these conditions here since it is the subsequent, relative effects of turbulence that are of interest.

5.1.3 Fresh Gas Turbulence Decay

Figures 5.1 - 5.4 present the evolutions of the mean and 95% confidence interval limits for the integral length scale, turbulence intensity, Damkohler number, and reaction-layer Karlovitz numbers respectively.

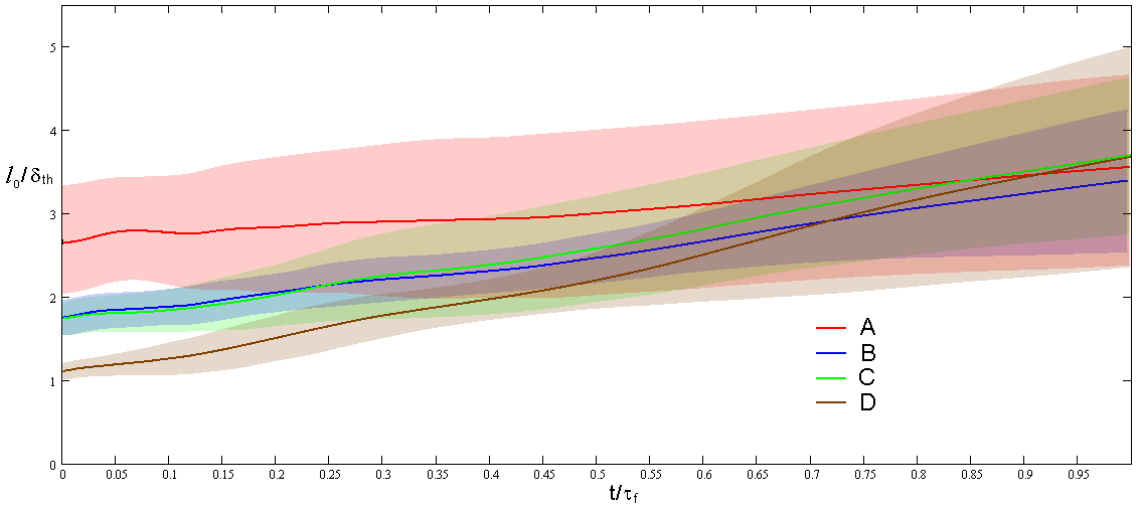

Figure 5.1 Evolution of the mean integral length scale l_0/δ_{th} (solid lines) with 95% confidence intervals (coloured bands) based on a t-distribution with 5 degrees of freedom.

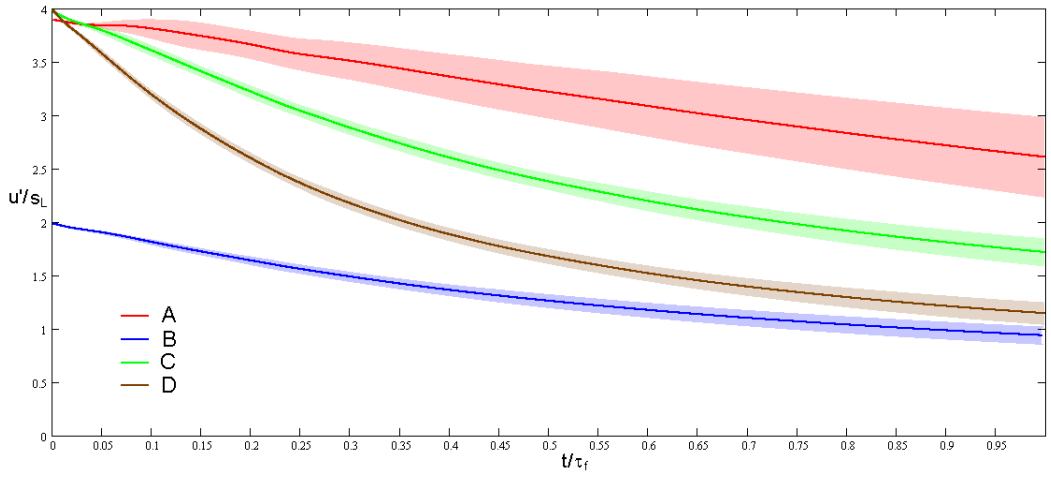

Figure 5.2 Evolution of the turbulence intensity u'/s_L (solid lines) with 95% confidence intervals (coloured bands).

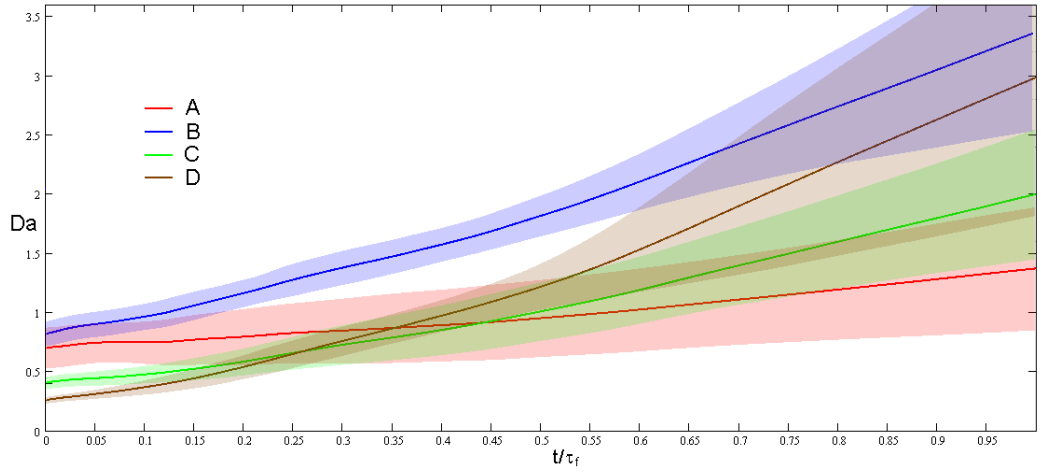

Figure 5.3 Evolution of the Damkohler number Da (solid lines) with 95% confidence intervals (coloured bands).

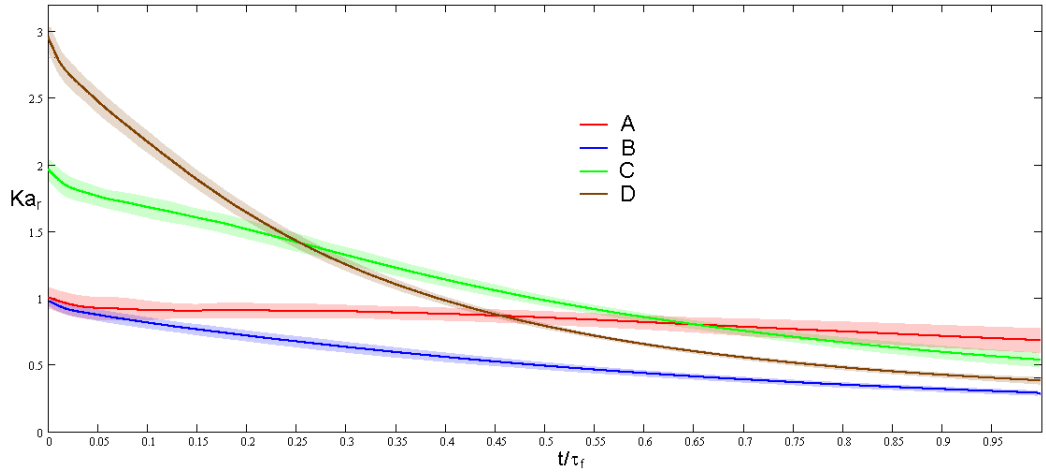

Figure 5.4 Evolution of the reaction-layer Karlovitz number Ka_r (solid lines) with 95% confidence intervals (coloured bands).

The Kolmogorov time scale used to evaluate the Karlovitz number used here is estimated from the dissipation rate of the turbulent kinetic energy ε , and the viscosity ν, according to the relation $\tau_\eta = (\nu/\varepsilon)^{1/2}$. It should be noted that this relation for τ_η is based on cascade arguments in fully developed turbulence, as described in §2.3.1, and so may not be quantatively accurate at the lower Reynolds numbers used here.

The time scale associated with the inner reaction layer of the flame τ_{fr}, is assumed to be approximately an order of magnitude lower than the time scale based on the thermal thickness, or more precisely $\tau_{fr} = \tau_f / \beta$, according to asymptotic analysis where β is the Zel'dovich number. This shorter time scale is used here since disruption to the inner reaction layer by small scale eddies is the most important indicator in determining the combustion regime at higher levels of turbulence intensity.

For high Damkohler numbers (Da >> 1) and low Karlovitz numbers (Ka_r << 1) a degree of scale separation is implied between the flame and the largest and smallest scales of turbulence respectively. From Figs 5.3 and 5.4 it can be seen that this separation of scales cannot be assumed for any of the flames in the present database. Initial Da values are 0.7, 0.8, 0.4, and 0.3 for cases A-D respectively, with corresponding initial Ka_r numbers 1.0, 0.9, 1.9, and 2.9. However, despite these initial figures, the disruption to

the flame structure that they suggest does not occur, and the reasons for this can be seen by examining Figs 5.1 and 5.2.

The rapid dissipation of kinetic energy, evident in cases B, C and particularly D, due to the high energy content of the small scale eddies, rapidly diminishes the ability of the Kolmogorov scales to disrupt the reaction layer of the flame, and in addition, the dissipation of vorticity caused by the increase in dynamic viscosity in the preheat zone will further reduce their power.

The growth of the integral length scales will also cause the integral time scales to increase over the course of the simulations, thereby decreasing the ability of these eddies to alter the larger scale flame structure.

Another important feature, illustrated in Fig 5.1, is the large variation of the integral length scales among individual simulations, and their convergence at approximately $t/\tau_f \approx 0.5$. This observation suggests that any meaningful distinction between integral length scales cannot be made after this time. However, at early times clear differences exist, and the influence of these scales before $t/\tau_f \approx 0.5$ is written into the geometry and structure of the kernels and remains throughout the simulations.

Turbulent Reynolds numbers $\mathrm{Re}_t = l_0 u'/\nu$ for all cases, as listed in Table 5.1, stay approximately constant due to the counterbalancing effects of dissipation and growth of the integral length scales.

5.1.4 Flame Kernel Results

When using repeated simulations, the length of time over which ensemble statistics may be extracted is dictated by the shortest simulation in the set. For the present database, the end point was determined in each case by when one of the c = 0.1 isosurfaces reached a boundary, and this occurred at $t/\tau_f = 0.35$, 0.54, and 0.75 for cases A, C, and D respectively, and not at all for Case B.

For all the figures presented in this section, where the statistics are strongly dependent on the number of samples in the set, data has been truncated at these points. In cases where the reduced set is still able to illustrate the important trends, the data is continued

to the end of the longest simulation time, but it should be remembered that the reliability of these trends is reduced after this point.

In Figure 5.5 time-series snapshots of the progress variable and vorticity magnitude for a typical simulation in Case A are presented. It is apparent that, contrary to the indications of the Damkohler and Karlovitz numbers, the inner reaction layer of the flame retains its structure throughout despite the significant straining and wrinkling evident in the preheat zone.

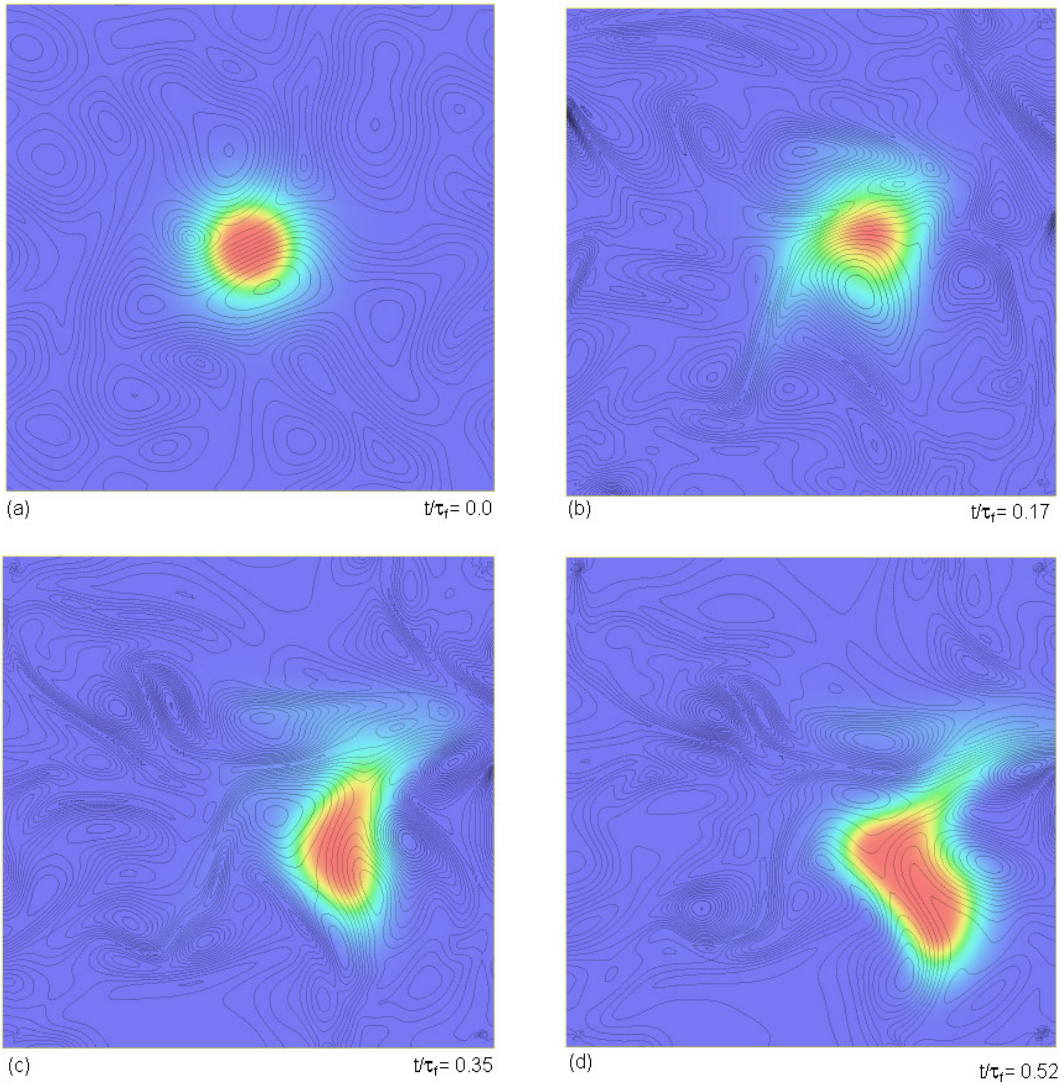

Figure 5.5 a-e. Snapshots of progress variable (colour) and vorticity magnitude (black contours) taken through a central x-y plane for a typical simulation in Case A ($l_{0,init}/\delta_{th}$ = 2.93, u'_{init}/s_L = 4).

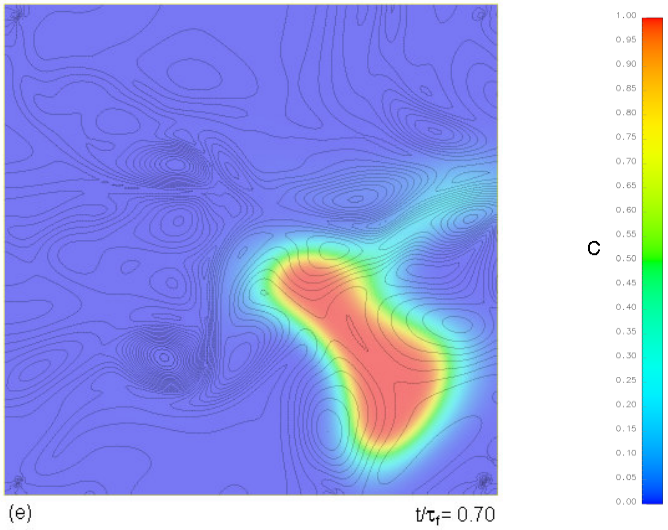

Figure 5.5 continued.

5.1.4.1 Regimes of Combustion

For all cases it is found that the flame structure remains in the wrinkled and thickened-wrinkled regimes according to the modified regime diagram of Peters [3]. There are two reasons for this: as noted previously, the larger eddies (of the order of the kernel diameter and above) convect the entire kernel without inducing significant strain on the flame surface. Secondly, when the initial integral length scale is small (irrespective of kernel size) the dissipation is very high, and eddies loose energy in the preheat zone before being able to disrupt the reaction layer. This is particularly true for Case D where Ka_r reaches unity after t/τ_f ~ 0.22 despite its high initial value of 2.9.

It is interesting to locate the current database on the regime diagram developed specifically for the kernel configuration by Echekki and Kolera-Gokula [36]. This uses the alternative length scale R_v/R_f, where R_v and R_f are the vortex and flame radii respectively, in place of the more usual l_0/δ_{th} used for planar flames. The diagram is constructed from kernel interactions with a single vortex, and so only an approximate comparison is possible, but by taking u' as the equivalent vortex velocity and $l_0/2$ as the vortex radius, flames in the current database (for all cases) lie close to the laminar / wrinkled-kernel boundary. This is perhaps a more accurate assessment of the regime

compared to the classical regime diagram, although for these very early stages of kernel growth a correction to the effective turbulence intensity to account for global kernel convection appears necessary when the value of R_v/R_f is large.

5.1.4.2 Global Flame Growth

The rate of growth of the kernels can be linked to a representative turbulent flame speed s_t through the relation $s_t = Is_L^0 A_T / A_L$, where A_T is the surface area of the turbulent flame and A_L the surface area of an equivalent laminar flame. The quantity A_T / A_L is the wrinkling factor, Ξ. I is a constant that accounts for changes in the value of the flame speed away from the unstretched laminar value s_L^0 due to the effects of unsteady strain and curvature.

In Figures 5.6a and b the wrinkling factor is presented together with the normalised global fuel consumption rate ω_V / ω_{VL}, which is the volume-integrated rate of reactant consumption, normalised by the equivalent laminar kernel value at the same point in time, and is therefore equivalent to the normalised global consumption speed of the flame.

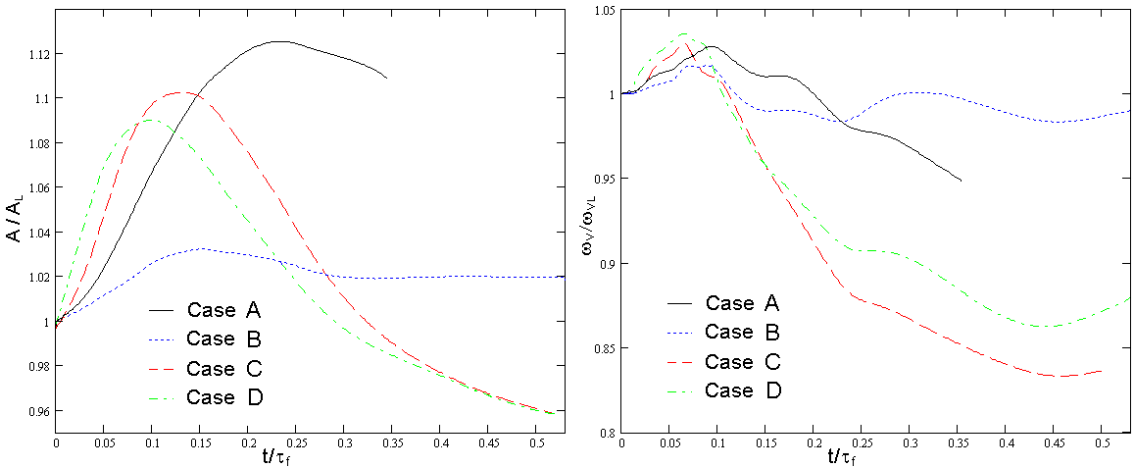

(a) (b)

Figure 5.6 a and b. Wrinkling factor (a) and global integrated reaction rate normalised by the equivalent laminar kernel value (b).

Flame surface areas conditioned on single values of the progress variable produce similar qualitative trends to those displayed in Fig 5.6a. However, in this case an average value is used based on the sum of all areas evaluated on the c isosurfaces (for c = 0.1, 0.2,..., 1.0), normalised by the equivalent sum from the laminar kernel. In this way the wrinkling at all isolevels through the flame brush is taken into account.

In all cases it is found that the effect of the turbulence is to decrease the global fuel consumption rate despite an increase in the surface area available for reaction. This is in contrast to a fully developed turbulent flame where any reduction in surface displacement speed due to turbulent strain and curvature is more than compensated for by the increased flame area available for reaction.

From Fig 5.6a it can be seen that the wrinkling factor is primarily a function of turbulence intensity, but also shows a noticeable dependence on integral length scales with the larger initial values of l_0 producing higher rates of surface area production.

High strain rates, as suggested by the initial Damkohler and Karlovitz numbers, clearly have a predominantly negative effect on the overall growth, and this is particularly evident in Cases C and D which have the highest initial Ka_r numbers.

For the unity Lewis number flames considered here, the lower global burning rate compared to the laminar flame suggests that the reductions in local flame speed due to tangential diffusion in areas of high curvature have a greater effect overall than any increase in flame area. The relations between the flame speeds, strain and curvature are examined in detail in Chapter 6.

In Fig. 5.6a the peak increase in surface area is seen to occur later as the initial integral length scale is increased, demonstrating again the reduction in effective turbulence due to the greater global convection of the kernel by the larger eddies.

Across all cases an initial increase in the burning rate can also be seen, and this is partly due to the elevated reaction rate during the initial stages, $t/\tau_f < 0.065$, which has the effect of reducing the turbulence intensity (u'/s_L^0) during this period by increasing s_L^0.

It appears that while flame wrinkling, which is enhanced by the presence of larger integral length scales, acts to increase the turbulent flame speed, the smaller integral

length scales, in contrast, are more likely to produce regions of high positive curvature, thereby effectively reducing the value of the constant I, and causing a comparatively greater reduction in the turbulent flame speed s_t.

It should be noted that the reduction of the global fuel consumption or turbulent flame speed shown here does not indicate global quenching of the flame, but only that the heat release is delayed with respect to the equivalent laminar kernel.

5.1.4.3 Differential Isosurface Velocities

In Figures 5.7a-h the surface conditioned mean velocity and displacement magnitudes are presented for all cases. The grey shaded areas indicate where at least one of the simulations in each case has reached a boundary. Data beyond this point are subject to increasing levels of distortion from boundary effects, in particular the apparent deceleration and bunching of the velocities towards the end of the simulation time which is the result of data points on the leading side of the surfaces being lost at the boundaries. The full data are retained here simply to aid comparison between cases.

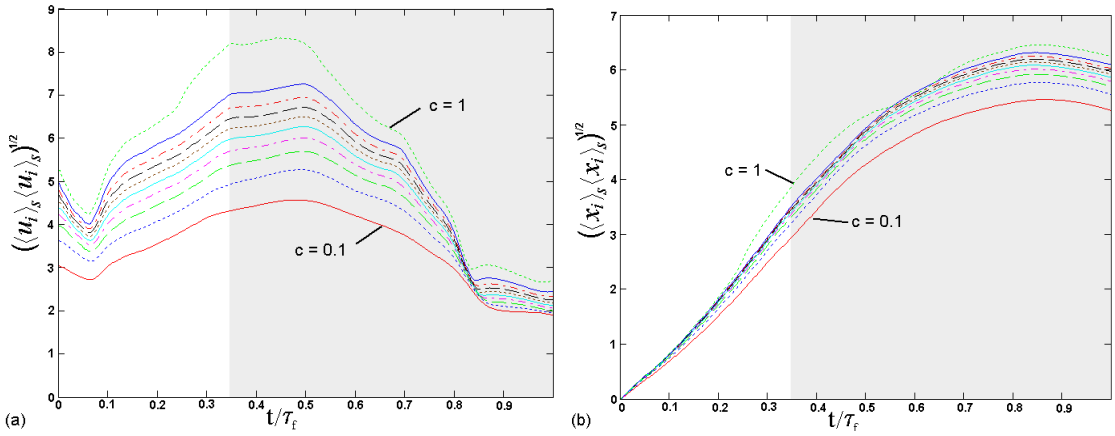

Figure 5.7. Surface-conditioned mean fluid velocity magnitudes (left), and surface-conditioned mean displacement magnitude from initial position (right) for cases A (a and b), B (c and d), C (e and f) and D (g and h). Grey areas indicate where at least one simulation has reached the boundary.

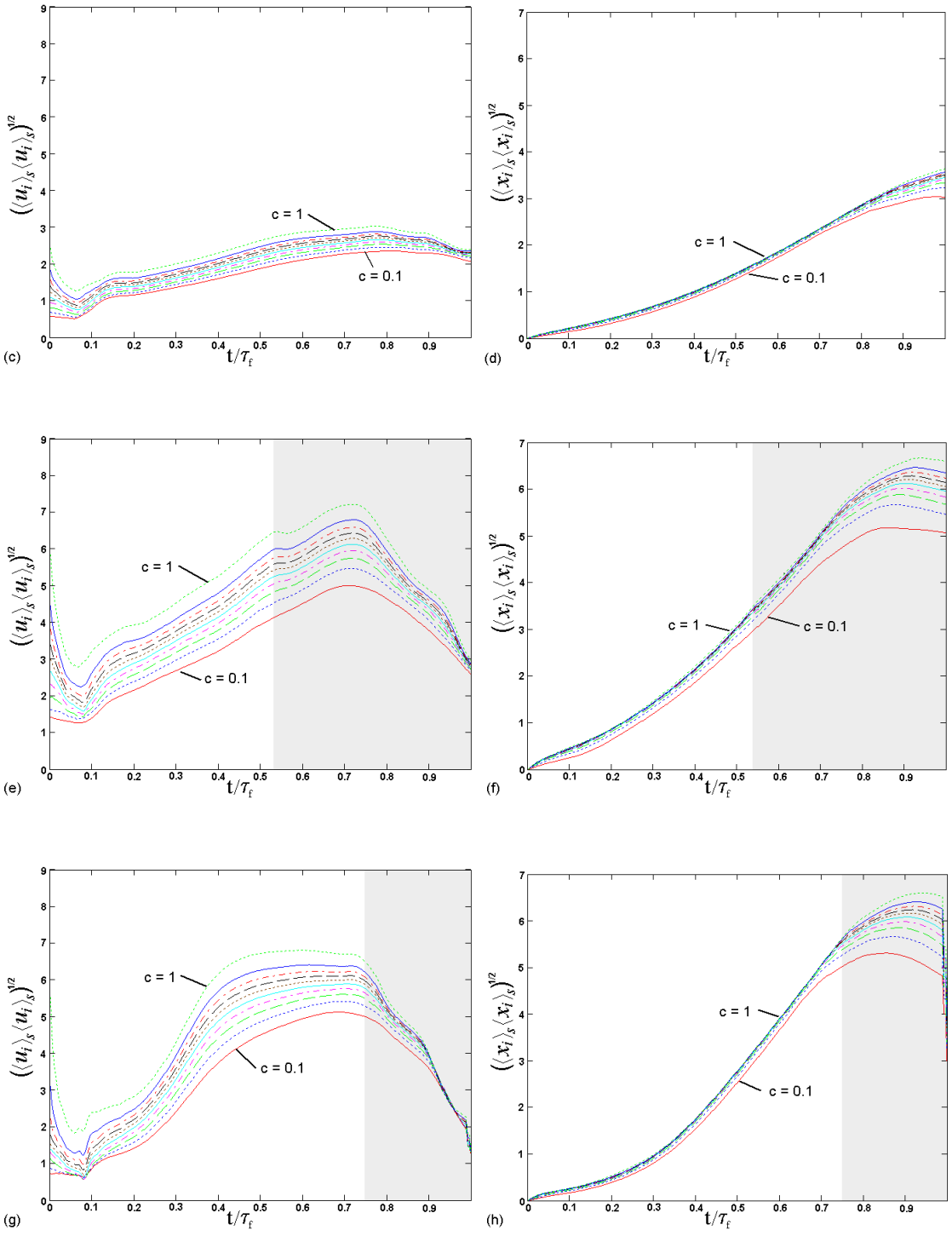

Figure 5.7 continued.

Comparing the surface conditioned mean fluid velocity magnitudes across all isolevels of the progress variable an interesting feature is revealed.

For all cases the surface-conditioned mean fluid velocity is significantly higher for increasing values of the progress variable, and this is reflected in the magnitude of the displacement of each isosurface centroid, where the displacement of the smaller isosurfaces (corresponding to higher values of progress variable) are greater than those of the larger isosurfaces.

Before discussing the reasons for this, a number of initial transient effects are evident in Figs 5.7a-h, and which are now briefly addressed. Eddies initialised within the region of burnt gases are the reason for the large initial velocity differentials which can be seen between the inner and outer isosurfaces at $t/\tau_f = 0$. These decay rapidly during the period $0 < t/\tau_f < 0.08$, with the rate of decay closely related to the proximity of the isosurface to the fully burnt gases due to the higher dynamic viscosity in this region.
Also visible at $t/\tau_f = 0.09$ is a dip in the velocity magnitudes across all isosurfaces, corresponding to the passage of initial acoustic transients from the boundaries. As stated before, this initial period is not of direct interest. Acoustically induced vorticity has been found to be negligible for turbulent flames [125], and in addition the transient effects noted here are common to all cases, and so any subsequent information remains qualitatively unaffected for the purposes of comparative analysis.

The cause of the differential velocity magnitudes experienced by different isosurfaces is a consequence of the fact that, in general, a kernel interacting with eddies larger than the kernel diameter will tend to be convected as a unit rather than experience any straining of the flame surface. At the global level this effect has been widely observed in experiments and incorporated into models of flame kernel development used in IC engine simulations. The results shown in Fig. 5.7 suggest that under certain conditions this same effect is present for different levels of the progress variable in flames with a high mean curvature - causing the smaller (higher valued) isosurfaces to experience a greater degree of coherence from the velocity perturbations acting over its surface.

A second important observation is that the surface mean velocity acts in approximately the same direction across all isosurfaces since, despite the difference in magnitude, a large proportion of the turbulence spectrum is shared by all isosurfaces. This has the

implication that, on average, isosurfaces will tend to be brought together on one side of the kernel - corresponding to the direction of convection – and isosurfaces on the opposite side will tend to be separated.

This isosurface proximity is quantified locally by the SDF. For the fully resolved flame, the locally evaluated flame surface density Σ' is equivalent to the surface density function $\sigma_{c=c^*} = |\nabla c|_{c=c^*}$ conditioned on a particular c* isosurface. A generalised SDF can also be used which does not depend on a the particular isosurface chosen [55], and which in the fully resolved limit becomes simply the magnitude of the local progress variable gradient $\sigma = |\nabla c|$.

The potential significance of differential isosurface mean velocities can therefore can be seen by considering the transport equation for Σ or Σ_{gen}:

$$\frac{\partial \Sigma}{\partial t} + \frac{\partial}{\partial x_i}\left(\langle u_i \rangle_s \Sigma\right) + \frac{\partial}{\partial x_i}\left(\langle s_d n_i \rangle_s \Sigma\right) = \langle k \rangle_s \Sigma \qquad \textbf{(5.2)}$$

where $\langle ... \rangle_s$ denotes a surface mean value.

The terms on the LHS in Eq. 5.2 represent respectively, unsteady effects, convection, and propagation in the direction of the flame normal; the term on the RHS contains the combined effects of strain and curvature. It is the second term on the LHS of Eq. 5.2 that is of interest here and represents the convection of Σ or σ by the surface conditioned mean velocity.

Since it has been shown above that the magnitude of the mean fluid velocity is dependent on the chosen isosurface for small kernel radii, the distribution of σ should be expected to be biased in the direction of this velocity – given that the direction is approximately uniform across the isosurfaces.

The importance of the displacement speed s_d, is also highlighted by Eq. 5.2, which is itself a function of the SDF. The absolute velocity of any point on an isosurface is a sum of the local fluid velocity and the displacement speed in the direction normal to the

isosurface: $s_i = u_i + s_d n_i$. To a first approximation s_d can be assumed to be equal to the density weighted laminar flame speed $\rho_0 s_L^0 / \rho$, and so for a statistically spherical kernel the term $s_d n_i$, when averaged over the entire isosurface, should be expected to be small compared to the fluid velocity, and particularly so as the turbulence intensity increases. The distribution of s_d and its relation with the SDF are addressed in more detail in Section 5.2.2

5.1.5 SDF Distribution Bias

To test the prediction of a bias in the SDF distribution a correlation coefficient can be calculated between the local SDF σ and its projection P along a vector aligned with the instantaneous direction of the mean surface velocity. Given the existence of a bias in the SDF distribution as described above, a positive correlation should be expected between σ and P for all the cases in this study.

Alternatively, the correlation between the SDF and centroid displacement vector can also be used, and is found to give quantatively similar but more consistent results since it takes into account the hysteresis of the system. Theoretically, the vector used in the correlation should be some function of both the displacement and surface-mean velocity, but for the present purposes, where the overall displacement of the kernel is limited by the domain size, it is sufficient to use only one of these. The relevant quantities are illustrated schematically in Fig 5.8

s is the position vector of the surface point relative to the centroid of a reference isosurface, **û** is the unit vector of the displacement of the isosurface centroid from its initial position, and P is the scalar projection of the position vector **s** onto the unit vector **û:** $P = \mathbf{s} \cdot \hat{\mathbf{u}}$

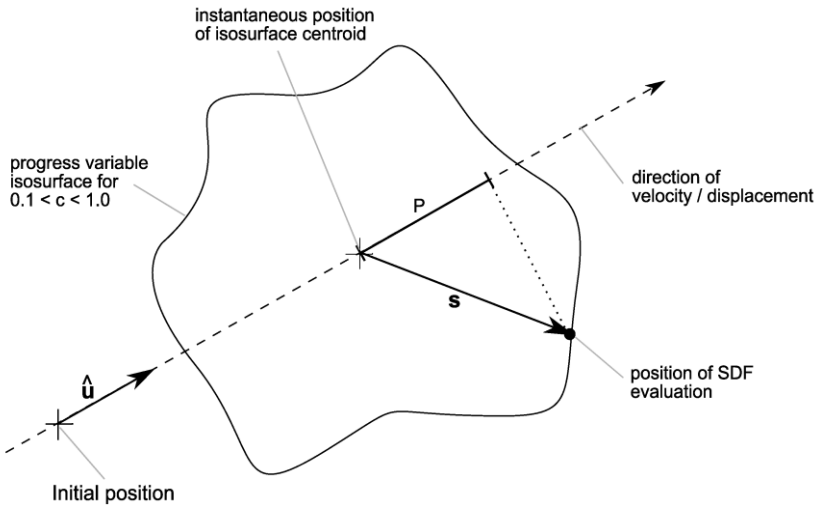

Figure 5.8 Schematic illustration of quantities used in the SDF-surface position correlation.

As noted before, the centroid displacement directions and mean velocity directions for each isosurface show relatively little variation through the flame brush, so the calculation of P is not sensitive to the choice of reference isosurface. The displacement unit vector of the c = 0.8 isosurface is therefore used here. The quantities P and σ are calculated for all values of the progress variable bounded by the c = 0.1 and c =1.0 isosurfaces. Excluding data beyond these limits precludes any potential skewing of the correlation due to the position of the kernel in the domain.

Figure 5.9 shows the evolution of the P-σ correlation for all cases with the associated 75% confidence intervals.

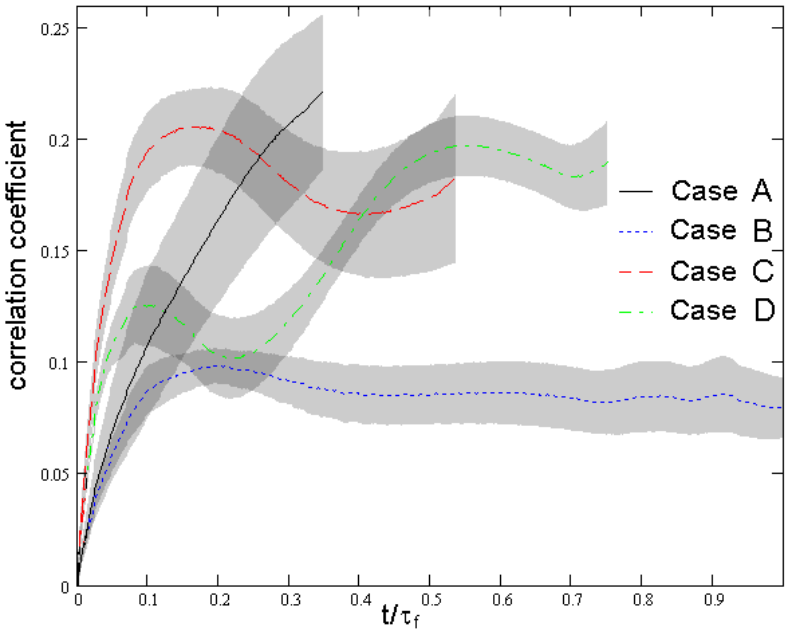

Figure 5.9 Correlation of σ with P for the c=0.8 isosurface. Grey bands indicate 75% confidence intervals; data ends indicate where an outer isosurface has reached the boundary in any individual simulation.

To estimate the combined effects of any errors introduced by the initial transients or boundary conditions, the P-σ correlation was calculated in a laminar flame test case for comparison. Using an identical computational domain to the main database, an initial uniform velocity $u'_{init}/s_L^0 = 4$ was imposed at $t/\tau_f = 0$ in a single coordinate direction, comparable in magnitude to the mean kernel velocity in Case A. The P-σ correlation in this case showed an initial minimum of –0.01 at $t/\tau_f \approx 0.09$, corresponding to the passage of acoustic pressure transients from the boundaries, and a subsequent maximum of 0.05 at $t/\tau_f \approx 0.35$ (cf. 0.22 for Case A at $t/\tau_f = 0.35$). So although present, these errors do not affect any of the qualitative conclusions drawn from these results.

The wide variation found between individual simulations is reflected in the relatively low (75%) confidence intervals, and highlights the need to consider ensemble statistics when examining this effect.

The initial steep rise in the correlation can be attributed partly to the artificially high vorticity within the fully burned region following initialisation. However, higher initial values for vorticity and u' are also expected in the fresh gases, and for all the cases, surface mean velocity differentials of comparable magnitude persist throughout the simulation, as illustrated in Figs 5.7a-h.

For the lowest turbulence intensity, Case B, where the longest simulation time is achieved, an approximately steady state is reached after $t/\tau_f \approx 0.3$ where an initially steep rise in the correlation is sustained by the persistent velocity differential through the isosurfaces. This suggests that a similar state may be achieved for the more realistic integral length scales, such as in Case A, given a sufficiently large domain.
The magnitude of the coefficient in each case, over the period where a comparison can be made, corresponds qualitatively to the turbulent Reynolds number, which stays approximately constant throughout the simulations.

The relative influence of the integral length scales, compared to the turbulence intensity, on the correlation is not very clear from this study due to the short simulation times in some of the cases. In fully developed, high Reynolds number turbulence, the statistics of the eddies at the scales of interest here should depend only on the dissipation rate, ε, and viscosity, ν, according to Kolmogorov's similarity hypotheses. Under these conditions the turbulent Reynolds number alone should be sufficient to parameterise the effect (for a given kernel geometry). From the present data, however, it can be seen that some sensitivity to l_0 and u' still exists - since Cases B and D have similar values of Re_t but different l_0, although it is difficult to extract more refined dependencies since steady states are not reached.
As noted previously from the cold-flow data, integral length scales in the fresh gases for all cases converge by $t/\tau_f \approx 0.5$, indicating that any subsequent changes in the correlations are principally due to u'.

The extent to which the σ - P correlation persists as the ratio l_0/R decreases over time under more realistic flow conditions cannot be determined from these data. The

requirement to repeat the simulations in order to get ensemble data places considerable restrictions on the practicable domain size and hence simulation time. However, from the trends in Fig. 5.9 it is reasonable to expect that for higher turbulence Reynolds numbers and over longer time scales, a peak correlation should be seen to occur sometime later than for all cases here, due to the presence of larger integral-scale eddies, and after reaching an approximately steady value should decay to zero as $l_0/R \to 0$.

5.1.5.1 Phenomenological Model

Following the hypothesis suggested in the previous section that the cause of the differential mean surface velocities is essentially geometric-probabilistic, a phenomenological model is now described which provides some useful additional insight into the results obtained through DNS.

The problem is most easily understood in spectral space, where an approximate relation between real-space length scales l and wavenumber k can be taken as $l = 2\pi/k$. A simplified, two-dimensional situation is considered, where each isosurface is treated as a material surface with area A_f embedded in a field of discrete eddies, each with length scale l and characteristic area $A_e = l^2$. This is shown schematically in Fig 5.10

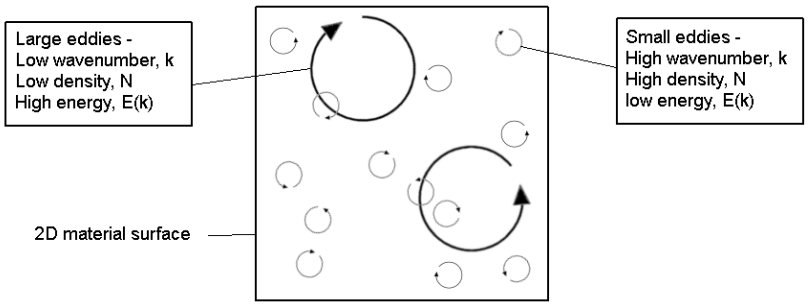

Figure 5.10 Schematic representation of an isosurface embedded in a two-dimensional field of discrete eddies.

It is assumed that the differences in surface mean velocity seen on each isosurface are a result of the greater degree of coherence of the velocity perturbations acting on the

smaller isosurfaces. Equivalently, this can be stated as that there is an increased probability that the velocity contributions on larger isosurfaces will sum to zero.

An estimate of this probability for each isosurface is then required. Since it is only the differences in probabilities between isosurfaces that cause the effect, it is not necessary to estimate the absolute probability of this occurring on each isosurface - only the differences in probability.

Assuming a sufficiently large domain, the velocity fluctuations of eddies at all wavenumbers can be considered normally distributed with mean $\mu = 0$ and standard deviation σ. However, the embedded isosurface will experience only a subset of this distribution, where the sample size N_k represents the number of eddies at wavenumber k acting on the surface at any given instant. The mean velocity contribution from eddies of wavenumber k in this subset, $\bar{u}_k$, will therefore be non-zero and with a standard deviation that is related to the sample size by $\sigma_{\bar{u},k} = \sigma / \sqrt{N_k}$, according to the central limit theorem.

The probability of the sample mean velocity at wavenumber k not summing to zero, $P(\bar{u}_k \neq 0)$, can therefore be assumed to be proportional to the sample standard deviation

$$P(\bar{u}_k \neq 0) \propto \sigma_{\bar{u},k} = C_1 / \sqrt{N_k} \qquad \textbf{(5.3)}$$

where the normal standard deviation σ, which is unknown, is replaced by a model constant C_1. Thus, the probability of a zero sum approaches unity as the number of eddies N_k approaches the total number present in the domain at that wavenumber[8].

[8] This condition is actually strictly imposed during the generation of the initial turbulence (§4.1.5)

The sample number N_k can be estimated from the geometry of the flame surface by assuming that eddies at each length scale are space-filling, such that

$$N_k = A_f / A_e = R_c^2 / l_k^2 = (R_c k / 2\pi)^2 \quad \textbf{(5.4)}$$

where R_c is the mean radius of the c* isosurface.

The ability of the eddies at wavenumber k to contribute to the surface mean velocity can be related to their kinetic energy, which may be evaluated from the energy spectrum function $E(k)$:

$$v_k = C_2 \sqrt{E(k)} \quad \textbf{(5.5)}$$

where v_k is the velocity contribution potential, and C_2 is a constant of proportionality.

Combining Eqs. 5.3 - 5.5, the total contribution to the isosurface mean velocity magnitude from all eddies at wavenumber k, $\langle |u_{c,k}| \rangle_s$, can then be considered proportional to the velocity contribution potential of eddies at each wavenumber, v_k, multiplied by the probability of those velocity contributions not summing to zero $P(\overline{u}_k \neq 0)$:

$$\langle |u_{c,k}| \rangle_s = C_0 \sqrt{E(k)} / R_c k \quad \textbf{(5.6)}$$

where C_0 is an amalgamated model constant. The total surface mean velocity magnitude $\langle |u_c| \rangle_s$ can then be found by integrating Eq. 5.6 across all wavenumbers:

$$\langle |u_c| \rangle_s = C_0 \int_0^\infty \left(\sqrt{E(k)} / R_c k \right) dk \quad \textbf{(5.7)}$$

and the resulting displacement magnitude $\langle |x_c| \rangle_s$ is obtained from a second integration through time

$$\langle |x_c| \rangle_s = C_0 \int_0^T \int_0^\infty \left(\sqrt{E(k)} / R_c k \right) dk dt \qquad \textbf{(5.8)}$$

It is important to note here that the displacement calculated this way can only account for movement of the kernel centroids by turbulent convection, and several other factors contribute to the actual displacement. These are discussed later in this section and in §5.2.2.

Evaluating Eqs. 5.7 and 5.8 therefore requires information on the time-dependent energy spectrum $E(k,t)$ and mean isosurface radius $R_c(t)$. Approximations to these could be made from assumptions about the form of the energy spectrum and the decay of turbulence intensity, and from analytical models that describe the mean growth rate of the kernel. In this case however, more accurate data is available directly from the simulations themselves.

While the time dependent mean isosurface radius data is easily obtained, information on the turbulent length scales and intensities is only available from the cold-flow database, since evaluating these quantities in the presence of heat release includes effects due to dilatation and thermal expansion that makes their interpretation uncertain.

The energy spectrum is therefore assumed, in the first instance, to have a Schumann and Patterson form (Eq. 5.1), where the time-dependent turbulence intensity u' is taken directly from the cold-flow data, and the peak wavenumber k_p is related to the integral length scales in the cold-flow data by $k_p(t) = l_0^{init} k_p^{init} / l_0(t)$.

The final forms of the velocity and displacement magnitude equations are therefore

$$\left\langle \left| u_c \right| \right\rangle_s = C_0 \int_0^\infty \left[\left(16\sqrt{\frac{2}{\pi}} u_{(t)}^2 \frac{k^4}{k_{p(t)}^5} e^{-2\left(\frac{k}{k_{p(t)}}\right)^2} \right)^{1/2} \Big/ R_{c(t)} k \right] dk \qquad \textbf{(5.9)}$$

$$\left\langle \left| x_c \right| \right\rangle_s = C_0 \int_{t=0}^{t=T} \int_0^\infty \left[\left(16\sqrt{\frac{2}{\pi}} u_{(t)}^2 \frac{k^4}{k_{p(t)}^5} e^{-2\left(\frac{k}{k_{p(t)}}\right)^2} \right)^{1/2} \Big/ R_{c(t)} k \right] dk dt \qquad \textbf{(5.10)}$$

While the quantity $\left\langle \left| u_c \right| \right\rangle_s$ in Eq. 5.9 can be viewed as equivalent to the mean fluid velocity magnitude on an isosurface, the quantity $\left\langle \left| x_c \right| \right\rangle_s$ from Eq. 5.10 does not represent the expected displacement magnitude of the isosurface centre, as noted above. The actual displacement of each isosurface centre will depend on its absolute velocity, which also contains information on the local displacement speed s_d of the surface with respect to the flow in the surface normal direction, and also on the distribution of flame surface density (FSD) around the kernel.

The effect s_d has on the actual isosurface displacement magnitude becomes more noticeable as the simulations progress since it will tend to reduce the differences in displacement between isosurfaces because of its lower value in areas of higher SDF. Equivalently, this can be thought of as the tendency for the flame to retain a flamelet-like structure, which restricts the range of flame thicknesses that are possible.

Equations 5.9 and 5.10 are evaluated using the time-dependent data on R_c, u', and l_0 taken from the DNS data as described, and with an arbitrary scaling factor C_0 for qualitative comparison. Case A is chosen since it represents the most realistic turbulent Reynolds number, and also because any effect of s_d on the isosurface displacement becomes less significant at higher turbulence intensities.

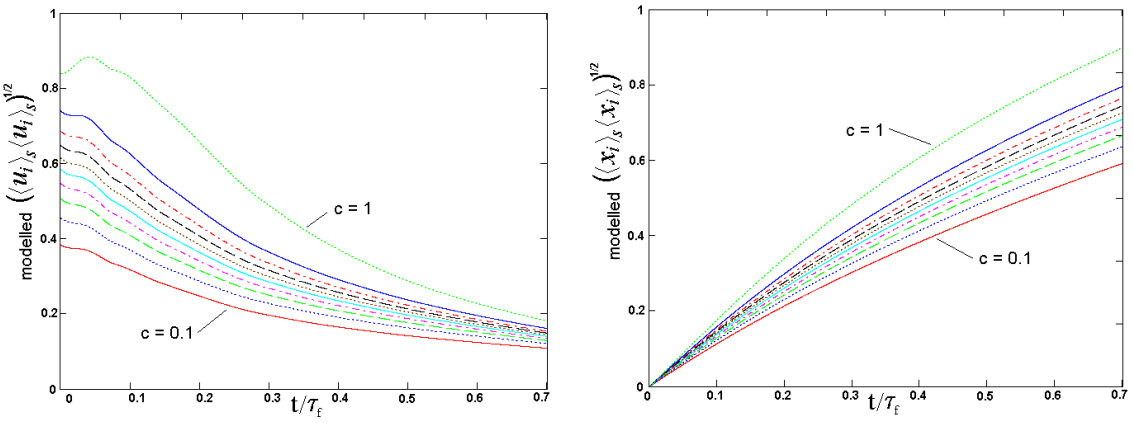

(a) (b)

Figure 5.11 Modelled isosurface mean velocity (a) and displacement (b) magnitudes against time. Arbitrary scaling applied to y-axes.

Comparison with the DNS results presented in Figs 5.7a and b reveals some important differences. Firstly, while the initial mean velocity differential seen in the DNS data is reproduced reasonably well by the model, the increase in magnitude over time for all isosurfaces has not been captured. Similarly for the displacement magnitude: while the qualitative differences are adequately captured by the model, the positive 'bending' of the DNS displacements, reflecting the slight acceleration of the kernel centres, contrasts with the global deceleration predicted by the model.

Further insight into these discrepancies can be seen by considering the model predictions of kernel displacement for all cases, compared with the DNS data, for a single representative isosurface at c = 0.8, as shown in Fig 5.12.

The model constant C_0 was adjusted to match the final values of Case A, and then left unchanged for the other cases. While an approximate match is also obtained for Case B, the discrepancies are seen to be greatest for Case C, and particularly Case D.

From the cold-flow data presented in Section 5.1.3 a possible explanation is suggested by the rate of change of the integral length scales and turbulence intensities for these two cases. The dissipation of kinetic energy and growth of the integral scales is greater in both these cases, and particularly for Case D where a greater proportion of the energy is initialised in the smaller, more dissipative scales compared with the other cases.

While the intention was to take this into account to some degree by incorporating the cold-flow data into the model, it appears that changes in the distribution of energy across the spectrum are much more marked in the presence of heat release. The reasons for these differences are the additional effects of flow acceleration through the flame front and a higher kinematic viscosity in the burnt gases.

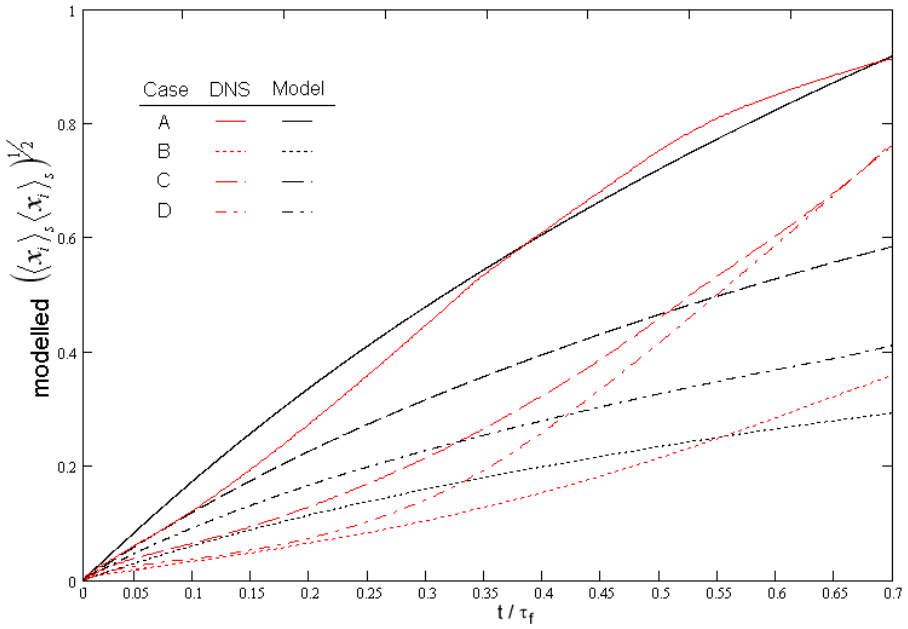

Figure 5.12 Modelled and DNS data for mean surface displacement magnitudes of the c = 0.8 isosurface for all cases. Model data scaled to match final value of Case A.

In support of this explanation, a recalculation of the model data is presented in Fig 5.13, using a modified form of the energy spectrum function (Eq. 5.11), where the pre-exponential peak-wavenumber exponent has been increased from 5 to 15.

$$E(k) = 16\sqrt{\frac{2}{\pi}} u_{(t)}^2 \frac{k^4}{k_{p(t)}^{15}} e^{-2\left(\frac{k}{k_{p(t)}}\right)^2} \qquad \textbf{(5.11)}$$

By making this change, the initial distribution remains unchanged from the original formulation (if the scaling factor C_0 is adjusted accordingly), but the sensitivity to changes in k_p over time is increased.

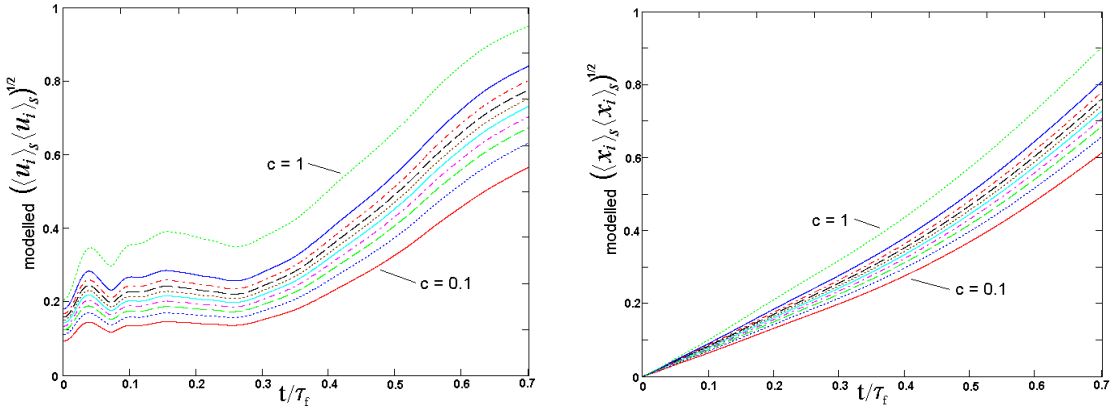

(a) (b)

Figure 5.13 Modelled isosurface mean velocity (a) and displacement (b) magnitudes against time for the modified spectrum model. Arbitrary scaling applied to y-axes.

The qualitative trends in both the velocity magnitudes and, over short times, the displacement magnitudes are now reasonably well captured by the modified model. If the initialisation effects present in the DNS data are disregarded, both the velocity differential of each isosurface, and the global acceleration of all isosurfaces over time is qualitatively reproduced.

The change to the spectrum sensitivity introduced by increasing the k_p exponent suggests that energy is transferred to the large scales at a much faster rate in the presence of heat release compared to the cold-flow data, which causes the energy spectrum to become increasingly peaked around the (decreasing) peak wavenumber. However, while this is plausible, considering the effects of heat release already mentioned, the significance of this is perhaps questionable. The peak wavenumber has been calculated from the integral length scale according to an order-of-magnitude estimate - $k_p(t) = l_0^{init} k_p^{init} / l_0(t)$, and so the change in the k_p exponent may in part simply correct for the inadequacy of this approximation. More generally it may also reflect the departure of the energy spectrum from anything resembling the initial Schumann and Patterson form, rather than simply a subtle redistribution of energy.

It is also noted that by changing only the pre-exponential k_p exponent, the dimensional consistency of the energy spectrum function is lost, and therefore also its generality. This is noticeable in the fact that the modified model does not produce good results when applied unaltered to the other cases in the database, but must be adjusted *ad hoc* to obtain a good fit.
Nevertheless, the intention with this model was not to develop a predictive tool, which would require much more extensive validation against data at higher Reynolds numbers than are available here, but as a heuristic device to provide insight into the mechanism behind the observed differential mean surface velocities.

From this point of view, the model demonstrates that the effect can be well captured by considering only geometrical and probabilistic arguments about the relation of an isosurface to the turbulence spectrum. And it lends support to the explanation of the phenomenon as an extension of the same process that causes an increase in the range of turbulent scales experienced by expanding kernels at higher Reynolds numbers.

The inherent sensitivity of the effect to the distribution of energy throughout the range of scales is also highlighted, and suggest that an alternative, perhaps more empirical, approach may be more suitable in the development of any predictive model, particularly where predictions of SDF bias are desired.

5.2 Two-Dimensional Simulations in an Extended Domain

To better understand the effects of the velocity differential on the isosurfaces at later times in the kernel development, the previous DNS analysis is repeated in an extended, two-dimensional domain under similar initial conditions of turbulence intensity and integral length scale. It should be expected that two-dimensional turbulence will not produce quantatively similar results due to the fundamentally different behaviour of two and three dimensional turbulence, and this is particularly true in view of the findings on the sensitivity of the differential surface velocity effect to changes in the turbulence energy spectrum.

However, since the basic mechanism appears to be geometrical, a similar effect should exist, and a two-dimensional study offers the possibility of investigating certain aspects, qualitatively, at higher Reynolds numbers and over longer time scales, since much larger domains are feasible.

In addition, a different code – SENGA2 is used in this study, which is implemented in fully dimensional form and features improvements to the Runge-Kutta time-advancement scheme and boundary conditions as outlined in Section 4.2. The possibility of code-specific anomalies that might otherwise affect the findings is therefore reduced.

5.2.1 Database Parameters

A single turbulence intensity and length scale are used, chosen to be comparable to Case A from the three-dimensional database, and, similarly to the previous study, simulations were repeated six times to provide ensemble statistics for analysis. These ensemble values are used in all following discussions unless otherwise stated. The simulation parameters are summarised in Table 5.2.

u' (ms^{-1})	l_0 (mm)	s_L^0 (ms^{-1})	δ_{th} (mm)	u'/s_L^0	l_0/δ_{th}	R_{init} (c = 0.8) (mm)	ρ_u/ρ_b	L_x , L_y (mm)
1.65 (1.60)	1.31 (3.47)	0.39	0.45	4.25 (4.12)	2.91 (7.57)	0.673	7.54	18.0

Table 5.2 Simulation parameters for 2D experiment sweep. Ensemble-average initial and estimated fresh-gas final (...) values.

Single-step chemistry representative of an atmospheric, stoichiometric methane-air flame are used. The domain is square with 512 grid points in each direction, providing 18mm side lengths and $\sim$12 grid points through the laminar flame thickness. The initial

fresh-gas turbulent Reynolds number is $Re_{t,init} \approx 143$, but in contrast to the three-dimensional behaviour the final values are considerably higher - $Re_{t,fin} \approx 367$, due to the 'inverse' cascade of energy, and growth of the integral scale eddies as described in Section 2.3.3. Another important difference between this study and the previous one is the higher density ratio of the 2D flame, $\rho_u/\rho_b = 7.45$ compared with 4.0 previously. This leads to an increased rate of growth of the kernel radius that, to some extent, counteracts the effects of an increasing integral length scale with regard to the range of turbulence scales experienced by the flame surface at the global level. The effects of this on the flame structure, and particularly the velocity differential at the isosurfaces, are addressed in the following sections.

The Schumann and Patterson energy spectrum [29] (Eq. 5.1) is again used to initialise the fresh gas turbulence, and the kernel initialisation procedure remains unchanged.
Reaction rate parameters remain constant throughout the simulations, but a slightly larger initial kernel radius is used ($R_{init} = 1.50\delta_{th}$ compared to $R_{init} = 1.12\delta_{th}$ previously) to ensure successful kernel development beyond the initial transients.

5.2.2 Results and Discussion

Inspection of Figure 5.14 reveals some important differences between the three-dimensional results and the current data. The higher density ratio causes more rapid expansion of the isosurfaces, such that the simulation time before the flame reaches the domain boundaries is only slightly increased from the three-dimensional studies. However, the period of growth of interest to this study is adequately covered.

The enhanced expansion also has direct consequences for the differential mean isosurface velocity and displacement, as predicted by Eqs. 5.9 and 5.10, owing to the more rapid increase in isosurface mean radius. On this point, it is worth noting that according to the phenomenological model (Eq. 5.4), in two dimensions the dependence should follow $R_c^{1/2}$ and $k^{1/2}$ in Eqs. 5.9 and 5.10 to maintain dimensional consistency.

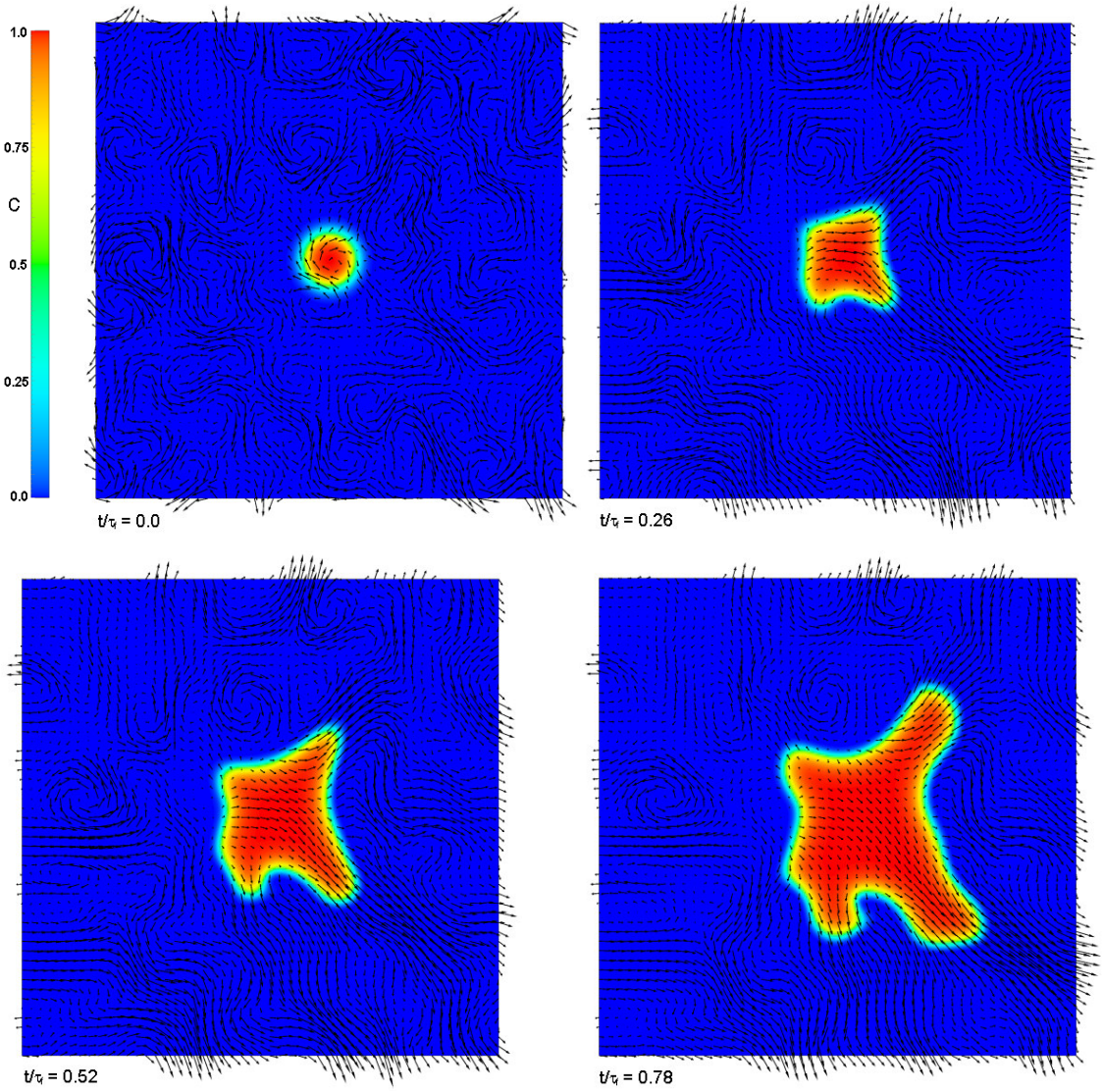

Figure 5.14 Snapshots of progress variable (colour) and velocity (vector arrows) for a typical simulation from the dataset. Domain dimensions $L_x = L_y = 18$mm

A second significant difference is the lack of small scale turbulence entering into the preheat layer, which is present in Case A in Fig 5.5 and predicted by the initial Damkohler and Karlovitz numbers. Estimated initial and final Damkohler numbers for the present kernels are 2.9 and 7.7 respectively, which are of the same order as for the three-dimensional data. A comparable Karlovitz number is not available however since the energy cascade arguments used to estimate the Kolmogorov scales do not apply in two-dimensional turbulence. The lack of small scale turbulence is a consequence of there being no vortex-stretching mechanism that would otherwise transfer energy

through the scales in three-dimensional turbulence, and so there is no equivalent to the dissipation range in the two-dimensional case.

The presence of small scale eddies entering into the preheat layer, although not essential for the differential velocity effect in question, is clearly important, and the fact that it does not occur in two-dimensions suggests caution in the interpretation of any two-dimensional data relating to this effect.

In spite of these observations a differential velocity effect is still seen to occur, as shown in Fig 5.15 a and b.

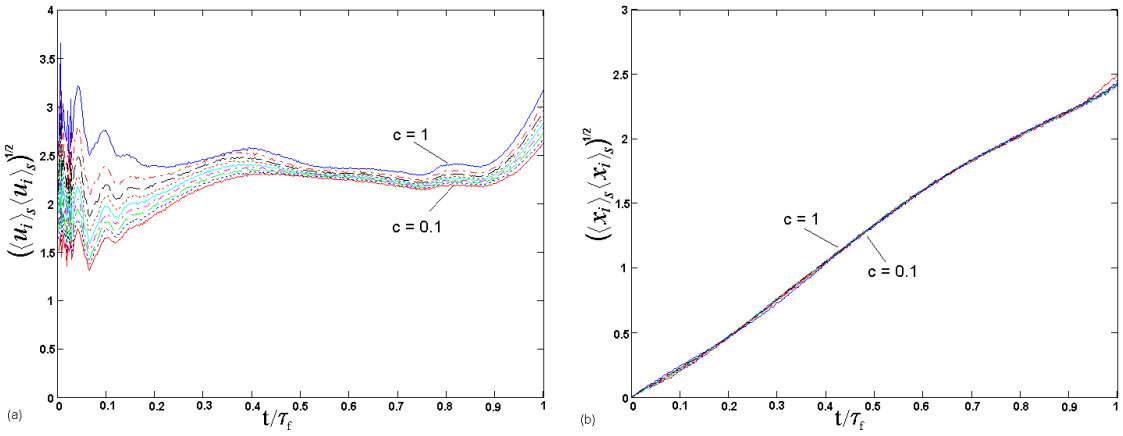

Figure 5.15 a and b. Surface-conditioned mean fluid velocity magnitudes normalised by laminar flame speed s_L^0 (a), and surface-conditioned mean displacement magnitude from initial position, normalised by flame thermal thickness δ_{th} (b). All tracked isosurfaces remain within the domain over the period presented.

After the period dominated by initialisation transients ($t/\tau_f < 0.1$), a similar trend to the three-dimensional DNS is seen in the isosurface mean velocities. A rising trend across all isosurfaces can be observed between $0.1 < t/\tau_f < 0.4$, followed by an approximately steady period between $0.4 < t/\tau_f < 0.9$ until the proximity of the boundary in one or more simulations causes an acceleration of the flow in the direction of the boundary (see Section 4.2.5). Before this point, a gradual reduction in the difference in velocities can be seen, which is in agreement with the model prediction over longer time scales.

The cumulative effect of these velocity histories is barely discernable in the difference in displacement magnitudes shown in Fig 5.15b, which more closely resemble the those of the lowest intensity Case B in the three-dimensional study. This is perhaps not surprising considering that the actual magnitude of the velocities experienced by the isosurfaces in this case are also of the same order as in Case B, despite the fresh-gas turbulence intensity being closer to cases A, C and D. The explanation for this lies partly in the slightly larger initial kernel radius used in the present work, and partly in the more rapid expansion of the isosurfaces due to the higher density ratio, both of which will tend to increase the probability of velocities summing to zero on any isosurface.

Figure 5.16 shows the correlation coefficient between the SDF and the projection P onto the vector aligned with the direction of displacement, as introduced in Section 5.1.5. In line with the three-dimensional results, a positive correlation is found, but with a peak value reduced from that seen in Case B (0.058 and 0.1 respectively). Also notable is the greater variation across the simulations, as reflected in the wide confidence interval band at the 75% level. The predicted steady state does not occur as seen in Case B, which is possibly a consequence of there being no cascade process supplying energy to the small scales in the two-dimensional case.

Another potential cause for the lower σ- P correlation is to do with difficulties evaluating the appropriate alignment vector for P. In the larger domain the displacement vector used to evaluate P will be increasingly influenced by the global movement the kernel, and so will not be as closely related to the mean velocities of the eddies directly affecting the kernel surfaces. This could potentially be resolved by identifying the global component of the velocity or displacement vector on all isosurfaces and subtracting it from the alignment vector prior to the calculation of P.

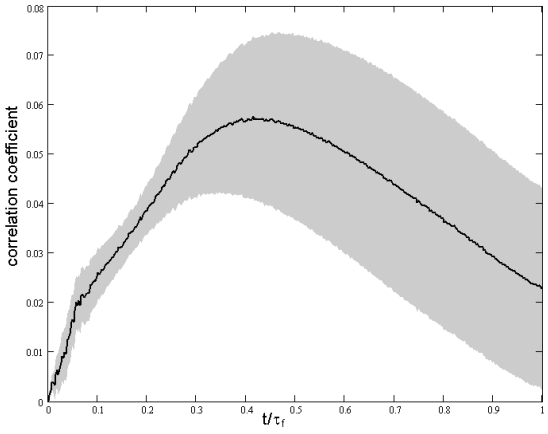

Figure 5.16 Correlation of σ with P for the c=0.8 isosurface. Grey band indicates 75% confidence interval.

Alternatively, it may be possible to evaluate it directly from the local surface quantities - equivalent to identifying an eigenvector for the SDF distribution on an isosurface. A potential complication of this method is whether the bias obtained in this way could be entirely attributed to the differential velocity mechanism suggested here since the connection between the bias and the mean velocity would be lost. From a modelling point of view it would then be a necessary to relate the bias to known quantities such as the sub-grid turbulence variables in RANS, or, where more detailed directional information is available such as in LES, the filtered velocity components.

It is interesting to examine the conditional probability density functions of some key surface quantities relating to the displacement speed s_d taken at t/τ_f = 0.4, as shown in Figs 5.17-5.19. The conditioning is applied to surface points depending on the sign of the scalar projection P, such that 'leading' (positive P) and 'trailing' (negative P) statistical semicircles for the surface quantities are extracted. Three isosurfaces are chosen, c = 0.1, 0.5 and 0.8, which represent: the outer edge of the preheat zone, the approximate position of maximum SDF, and the inner reaction layer respectively.

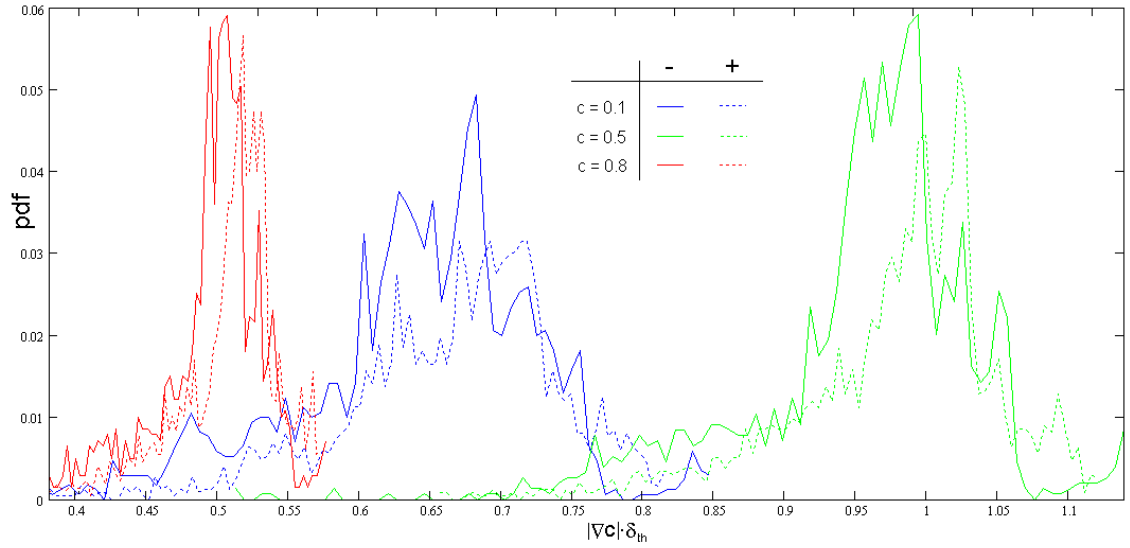

Figure 5.17 Probability density function of SDF at t/τ_f = 0.4, normalised by the flame thermal thickness δ_{th}, for isosurfaces at c = 0.1, 0.5 and 0.8, conditioned on leading (positive P) and trailing (negative P) sections of the kernel. Ensemble-averages values are used.

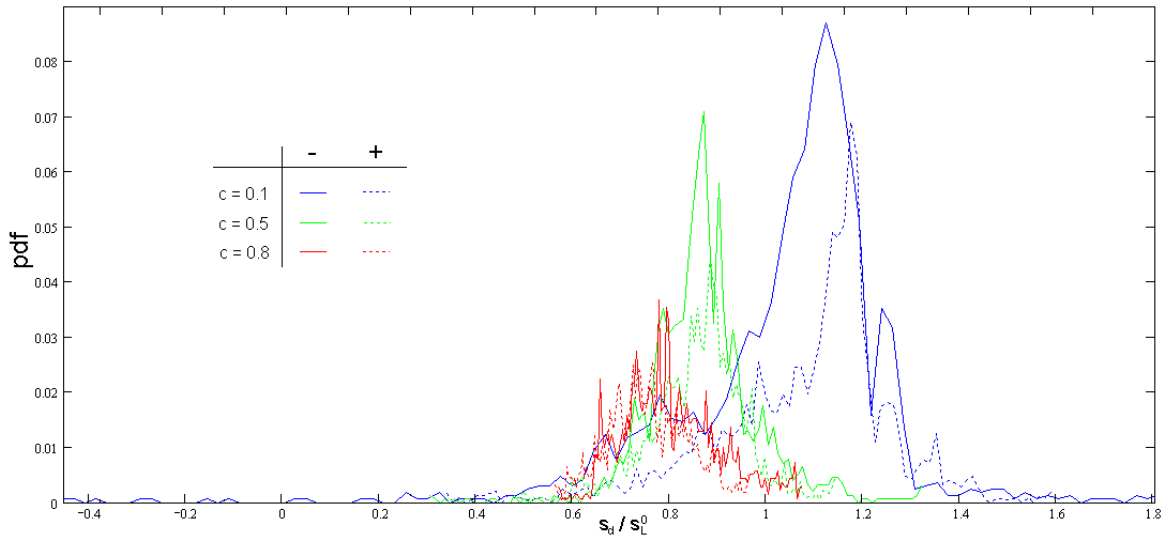

Figure 5.18 Probability density function of displacement speed s_d at t/τ_f = 0.4, normalised by s_L^0, for isosurfaces at c = 0.1, 0.5 and 0.8, conditioned on leading (positive P) and trailing (negative P) sections of the kernel. Ensemble-averages values are used.

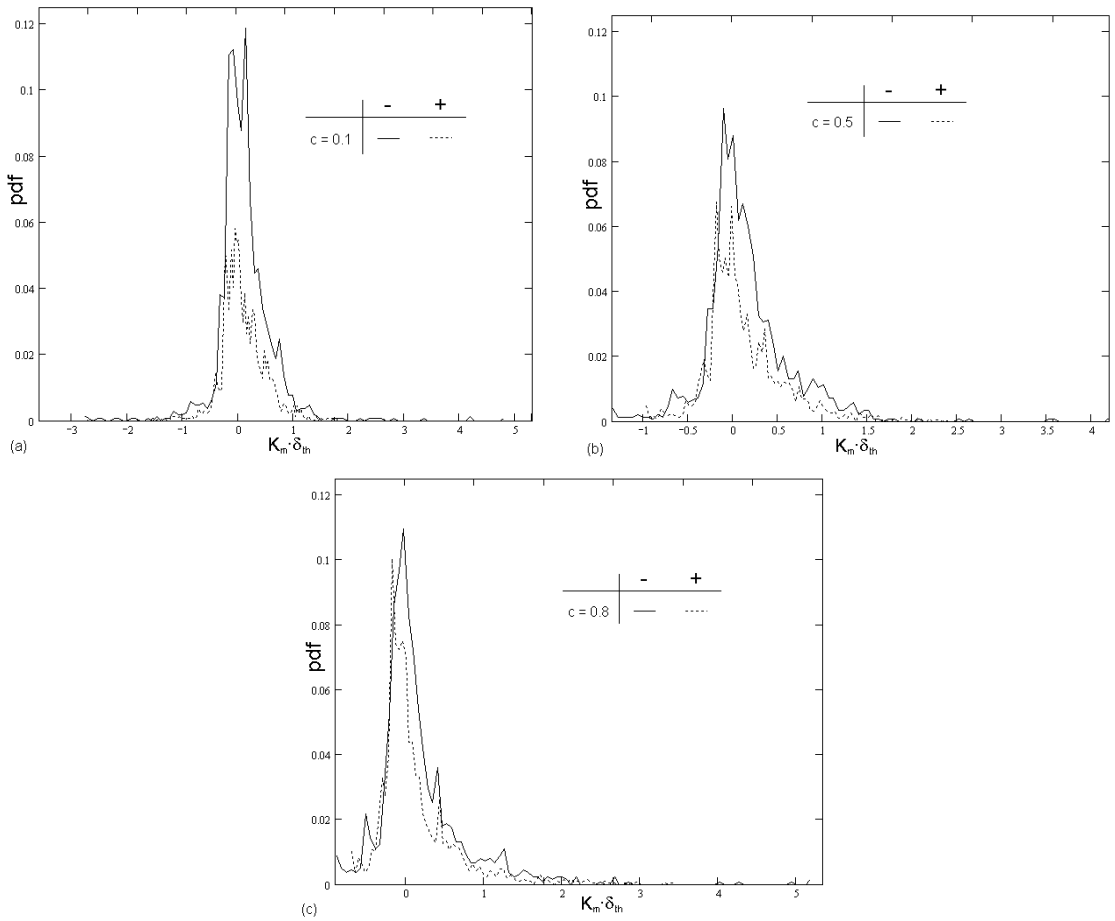

Figure 5.19a-c. Probability density functions of curvature K_m at $t/\tau_f = 0.4$, normalised by the flame thermal thickness δ_{th}, for isosurfaces at c = 0.1, 0.5 and 0.8, conditioned on leading (positive P) and trailing (negative P) sections of the kernel. Ensemble-averages values are used.

From Fig 5.17 a shift in the peak of the SDF towards higher values on the leading side can clearly be seen for all isosurfaces. Mean values are only slightly higher on the leading sides: by factors of 1.05, 1.02, and 1.03 for c = 0.1, 0.5 and 0.8 respectively, but a much more considerable difference is seen in the variances, which are greater on the leading sides by factors of 1.55, 2.18, and 2.84 respectively. This perhaps unexpectedly large difference is also reflected in the distributions of other quantities.

The variance of the local displacement speed s_d is increased by approximately the same factor of 1.5 for all isosurfaces on the leading side, whereas, similarly to the SDF, mean values of s_d are almost equal on both sides, with an increase of 1.04 on the c = 0.1 surface, but decreases of 0.98, and 0.94 on the c = 0.5 and c = 0.8 surfaces respectively.

In contrast, mean values of curvature on the leading side are reduced by factors of 0.84, 0.79, and 0.72 respectively for the c = 0.1, 0.5 and 0.8 isosurfaces, with corresponding increases in variance by factors of 1.01, 1.68 and 2.51. This signifies a marked increase in the wrinkling factor Ξ, and therefore also the flame surface density Σ, on the leading side of the kernels, along with a reduction in the mean curvature. A comparison of the conditional surface areas (isoline lengths) of each side confirms this - they are found to be greater on the leading side by a factor of approximately 1.5 for all isosurfaces.

The similarity of the leading and trailing values for both the SDF and s_d is perhaps quite surprising given the large variation in the magnitude of the fluctuations acting on each hemisphere, as indicated by the differences in variance. This suggests that, under the conditions used in these simulations, the response of s_d and the SDF to unsteady fluctuations is approximately linear, which is in agreement with theoretical predictions at low stretch rates (§2.2.2). It must also be the case that, considering the large differences in the distribution of curvature, the changes to displacement speed and SDF due to mean curvature are relatively small by this point in the kernel development.

An important consideration from these observations, is that the increase in wrinkling and surface area on one side of the kernel would - in itself – contribute to the movement of the kernel centroid. And since the conditioning is carried out using a vector aligned with this displacement, the difference in wrinkling is not surprising. However, wrinkling is only one factor in the movement of the centroid, and the link between the mean surface fluid velocity, the wrinkling, and the displacement of the isosurface centroid is not straightforward.

It was noted in the previous section that the unit vectors of displacement and velocity stay closely aligned during the simulations, and this is also found to be true in the present case. The ensemble-mean value of the cosine of the angle between the two vectors is 0.962 at t/τ_f = 0.4, where a value of 1 indicates perfect alignment, and 0

indicates orthogonality, and this close agreement between the two quantities remains throughout the simulations.

A question is therefore whether the mean surface velocity is also somehow determined by the distributions of wrinkling and surface area around the kernel. A plausible explanation of how this might occur would be due to the acceleration or dilatation of the flow at the flame front due to thermal expansion. Since this will contribute to the fluid velocity on the surface, a greater flame surface area on one side of the kernel could increase the contribution to the mean velocity in this direction.

In fact, from inspection of the histories of the surface velocities, and of the relation between the unit vectors of velocity and displacement, it appears that this cannot be the principal cause of the coupling.

Firstly, it is clear from the velocity plots in Figs 5.7 and 5.15 that a non-zero mean velocity is present on the isosurfaces from $t/\tau_f = 0$, before any significant wrinkling has occurred, which demonstrates that, at least at these early times, turbulent fluctuations provide the dominant contribution to the surface mean velocity.

A second, more interesting observation, is seen from the histories of the unit vectors, where without exception, changes in the unit displacement vectors are *preceded* by changes in the velocity vectors, with a delay in response of the order 0.1ms ($0.085\tau_f$).

For the velocity and displacement directions to be determined by the distribution of flame surface, as suggested above, the changes would need to be simultaneous, or possibly with a short delay in the change of the velocity vector. In these simulations, however, changes in the centroid displacement are always precipitated by changes in the mean surface velocity.

It is still possible that the increased wrinkling/FSD contributes to the mean surface velocity in the way described above, and in fact this could help explain the observed acceleration of the kernel centres, and the growth of the integral length scales as discussed in Section 5.1.5.1.

A better understanding of the mechanisms that leads to increased wrinkling in the direction of the mean surface velocity, and the role of the observed differences in

isosurface velocities requires a more targeted study, and so must remain the subject of future work. It might be speculated, however, that the greater mean velocity acting on the inner isosurfaces causes a mild increase in the instability of the flame on the leading side of the kernel, which in turn leads to increased flame surface area and wrinkling. This would be in some ways analogous to a buoyancy induced instability experienced by an upwardly propagating flame in a gravitational field or accelerating flow, which would have a similar tendency to 'push' the burnt gases preferentially in the direction of propagation.

5.3 Summary

In this section results were presented on the interaction of the developing kernel with a field of decaying, homogenous and isotropic turbulence. In the first part, a three-dimensional flame kernel database was used for the main analysis, together with a parallel cold-flow database to estimate the turbulence decay properties of the fresh gases. Four cases were considered: three different values of the initial integral length scale, and one at a reduced turbulence intensity.

An assessment of the combustion regime showed that in spite of the estimated Damkohler and Karlovitz numbers, combustion for all cases took place in the wrinkled / thickened wrinkled regime according Peters [3] and the wrinkled kernel regime according to the kernel-specific diagram of Echekki and Kolera-Gokula [36].

The effect of turbulence on the global rate of growth of the kernels was found to be negative for all cases despite an increase in flame surface area due to turbulent straining. This was attributed to lower mean surface displacement speeds resulting from an increased occurrence of regions of high positive curvature.

The surface-conditioned mean fluid velocity magnitude and position of the surface centroid was tracked for ten isosurfaces of the progress variable throughout the simulations. It was found that these quantities were not constant across the isosurfaces

but depended on the isosurface chosen, with higher velocities and displacements observed for smaller surfaces. By calculating the correlation between the SDF and its position along the kernel displacement vector, a positive bias was shown to exist in the SDF distribution in the direction of this vector.

The observation of differential isosurface velocities was explained by the tendency for smaller surfaces to be globally convected by the turbulence rather than undergo straining and wrinkling. A phenomenological model was constructed based on probabilistic-geometric arguments that was able to reproduce some of the basic features observed, and revealed the sensitivity of the effect to changes in the distribution of energy in the turbulence spectrum.

Finally, a second two-dimensional database was created to investigate the effect over longer time scales using an alternative DNS code. A similar bias in the SDF was observed but with a reduced magnitude compared to the first database. Pdfs were presented for the SDF, displacement speed and local curvature, conditioned on leading and trailing sides of the kernel. These revealed relatively small changes in the conditional mean values of s_d and SDF but a marked increase in wrinkling on the leading sides of the kernels, together with a reduction in the mean curvature.
A tentative explanation for this was suggested as due to an instability induced by the velocity differential of the isosurfaces, but it was emphasised that a more thorough investigation was not possible with the current data.

6 DETAILED CHEMISTRY COMPUTATIONS

The focus of this chapter is on the detailed thermo-chemical behaviour of lean methane-air and hydrogen-enriched methane-air flame kernels during the early stages of growth. Database parameters and numerical details are introduced in Sections 6.1 and 6.2, and an assessment of different flame speed definitions and the turbulence decay properties is made in Sections 6.3.1 and 6.3.2.

Analysis of the turbulent flame kernel simulations begins with a description of general results for the pure methane kernels in §6.3.3. The effects of hydrogen addition are introduced in §6.3.5 through a comparison of three cases that allows for a separation of the effects due to: laminar flame characteristics, thermo-diffusive stability, and turbulence-kernel interaction. Mechanisms leading to extinction and quenching are also discussed.

A comparison is made with previously published data on hydrogen-enriched planar flames in §6.3.6, and finally, the effects of turbulence intensity are presented in Section 6.3.7.

6.1 Database Parameters

Thermo-chemical and turbulence parameters for the cases considered in this section are summarised in Tables 6.1 and 6.2. Apart from the broad aim of producing a validated flame kernel database suitable for future analysis, the range of parameters was chosen with the following specific objectives in mind:

- To investigate the response of the kernel during the early stages of growth to the unsteady straining typically found in SI engines.
- To examine the mechanisms by which global and local quenching might occur under these conditions.
- To study the change in effectiveness of H_2 addition at different equivalence ratios and turbulence intensities.

- To investigate mean curvature effects in H_2 enriched flames by allowing a direct comparison with previously published DNS results of statistically planar lean CH_4/H_2 – air flames of Hawkes and Chen [9].

The equivalence ratio ϕ and H_2 mole fraction α used in cases A and B were selected principally to achieve the last of these objectives, however the interest in using an equivalence ratio of 0.53 is that it is recognised as being close to the lean ignition limit for methane-air flames [8], and therefore provides a logical starting point of particular relevance to the growth of flame kernels. The higher equivalence ratio of 0.625 used in C1 and D1 has been found to be closer to a practical minimum that would ensure stable combustion [8], but also facilitates the separation of certain effects present in the kernel growth, as explained in Section 6.3.5.

Turbulence length and time scales are typical of those found in internal combustion engines at moderate ($\sim$1500 rpm) engine speeds [1]. However, for the low pressure, ultra-lean flames studied here the thermal flame thickness δ_{th} and flame transit times τ_f are greater than the typical in-cylinder flame by as much as factor of $\sim$10, leading to substantially lower Damkohler numbers.

An initial kernel radius of ~1mm (to the c = 0.8 isoline) was chosen as typical of the kernel size in SI engines after the initial spark transients have decayed and the quasi-laminar phase of growth begins [126]. As noted previously, the actual conditions in a SI engine shortly after spark discharge are a great deal more complex than it is possible to recreate here, and a direct quantitative comparison is not the aim of the present study. The initial kernel radius used here is sufficient to ensure self sustained combustion in the absence of turbulent straining for all flames in the database.

Case	ϕ	α	s_L^0 (cms^{-1})	δ_{th} (mm)	τ_f (ms)	T_{ad} (K)	ρ_b/ρ_u	$R_{init,0.8}$ (mm)
A1, A2	0.53	0.0	7.11	1.46	20.53	1562	0.1960	0.95
B1, B2	0.53	0.3	10.11	1.06	10.48	1580	0.1920	0.97
C1	0.625	0.0	13.42	0.87	6.48	1710	0.1783	0.97
D1	0.625	0.3	18.21	0.68	3.73	1738	0.1737	1.01

Table 6.1. Flame parameters. Equivalence ratio ϕ, hydrogen mole fraction α, unstretched laminar flame speed s_L^0, flame thermal thickness δ_{th}, flame transit time $\tau_f = \delta_{th}/s_L^0$, adiabatic flame temperature T_{ad}, and burnt to unburnt gas density ratio ρ_b/ρ_u. Values taken from 1D steady-state calculations using SENGA2.

Case	u' (ms^{-1})	u'/s_L^0	l_0 (mm)	l_0/δ_{th}	τ_t (ms)	Re_t	Da
A1	1.51 (1.39)	21.24 (19.55)	1.30 (2.03)	0.89 (1.39)	0.861 (1.46)	149 (214)	0.042 (0.071)
A2	2.26 (3.35)	31.79 (47.12)	1.56 (2.75)	1.07 (1.88)	0.690 (0.821)	267 (698)	0.034 (0.040)
B1	1.51 (1.39)	14.93 (13.75)	1.30 (2.03)	1.23 (1.92)	0.861 (1.46)	149 (214)	0.082 (0.139)
B2	2.26 (3.35)	22.35 (33.14)	1.56 (2.75)	1.47 (2.59)	0.690 (0.821)	267 (698)	0.066 (0.078)
C1	1.51 (1.39)	11.25 (10.36)	1.30 (2.03)	1.49 (2.33)	0.861 (1.46)	149 (214)	0.133 (0.225)
D1	1.51 (1.39)	8.29 (7.63)	1.30 (2.03)	1.91 (2.99)	0.861 (1.46)	149 (214)	0.231 (0.391)

Table 6.2. Turbulence parameters. Initial values and estimated final values (...). Final values taken at t = 1.5ms for u'_{init} =1.51ms^{-1}, and t = 1.0ms for u'_{init} = 2.26ms^{-1}. Integral time scale $\tau_t = l_0/u'$, turbulent Reynolds number $Re_t = u' l_0/\nu$, and Damkohler number $Da = \tau_t/\tau_f$.

Alternative methods of calculating ϕ and α are used by some authors [18,22], but in this case the mixture equivalence ratio is defined as

$$\phi = \frac{\left(X_{CH4} + X_{H2}\right)/X_{AIR}}{\left(\left(X_{CH4} + X_{H2}\right)/X_{AIR}\right)_{st}} \quad \textbf{(6.1)}$$

and hydrogen fraction

$$\alpha = \frac{X_{H2}}{X_{CH4} + X_{H2}} \quad \textbf{(6.2)}$$

where X_i is the mole fraction of species i and $(...)_{st}$ denotes stoichiometric conditions.

Details of the 68-step chemical mechanism can be found in Section 4.2.5 and in Appendix 1. The 17 solved-for species are: CH_4, O_2, CO_2, H_2O, H_2, O, OH, H, HO_2, H_2O_2, CO, CH_2O, HCO, CH_2OH, CH_3OH, CH_3, CH_3O, and N_2.

6.2 Numerical Details

6.2.1 Resolution

Since the spatial and temporal resolution of DNS is governed by the chemical time and length scales, to determine the optimum values for the present mechanism a preliminary series of test calculations was carried out in a one-dimensional, steady-state, inflow-outflow configuration. A stoichiometric flame was used to maximise the magnitude of the scalar gradients, and with the physical domain length fixed the grid resolution was varied across the range of viable values. An estimate of the error associated with each level of resolution was obtained directly from the embedded PID error control used in SENGA2 for adaptive time stepping (§4.2.2). Under this system the size of the time step is controlled by the principal error norms of the explicit Runge-Kutta scheme [121], and

so serve as a useful proxy for the overall error of the system. A steady state solution is then sought where the time step is at a maximum over the range of spatial resolutions considered.

Using this method the steady-state time step was found to peak for a grid resolution $\Delta x = 2\text{x}10^{-5}$ m, which in two and three dimensions translates to $\Delta x = (\sqrt{2})\ \text{x}10^{-5}$m and $\Delta x = (2/\sqrt{3})\ \text{x}10^{-5}$m respectively. This level of resolution ensures at least 20 grid points within the thermal thickness for a stoichiometric flame. And although it is recognised that under high strain rates the flame thickness can be reduced considerably, it should also be noted that the laminar thickness of the lean flames used in the present study are several times that of a stoichiometric flame, so adequate resolution is still ensured.

All simulations were carried out in a square domain of $N_x = N_y = 1024$ grid points, allowing a domain length of $L_x = L_y = 14.48$mm. Having determined the necessary spatial resolution with adaptive time stepping, it was found subsequently that the time step could be increased slightly and fixed at $1\text{x}10^{-8}$s without loss of accuracy or stability. Computations were carried out in parallel across 64 Intel 5160 Xeon 3.0GHz dual-core processors using MPI as described in Section 4.2.4. 8Gb of shared memory was available per node, providing 2Gb RAM per core and a further 4Mb cache shared between each processor. The execution time for the lower turbulence intensity cases was in the region of 100hrs, and for the higher intensity cases, approximately 75hrs.

6.2.2 Initialisation

Initialising the flow variables necessarily involves making approximations about certain quantities, and on the structure of the flame in particular, which can lead to initial transient perturbations during the simulation as the flow adjusts to the correct solution. For some flow configurations, such as the statistically steady planar flame, this problem can be overcome by allowing the solution to evolve for long enough for these transient phenomena to dissipate. For intrinsically unsteady configurations such as the flame kernel this is not possible, and more effort is therefore required to produce an accurate

first guess in order to minimise the impact of these unwanted numerical effects on the solution. The initialisation procedure used here involved several steps, which are now briefly described.

An initial, incompressible turbulent field was generated using the spectral method described in §4.1.5. This produces steep pressure gradients as the pressure field is resolved and approximations are applied at the boundaries after the first time step. These lead to unwanted acoustic waves traversing the domain that are partially reflected from the boundaries producing noticeable perturbations of the flame front. To avoid this, the initial turbulent field was allowed to evolve for a short time until the pressure field was properly resolved and initial pressure transients had disappeared. This evolved data was then stored to be combined later with the initial flame data.

Generating the initial flame kernels involved several stages:

1. A 1D flame profile for the progress variable c, is generated analytically following a complementary error function profile. Mass fractions for the major species and temperature are then calculated as a function of the progress variable according to their equilibrium values for a given equivalence ratio and hydrogen mole fraction.

   The adiabatic flame temperature for each composition is found using Gaseq software [127].

   Following Halter et al. [110] the equilibrium molar composition is found from

$$\begin{aligned}&(1-\alpha)CH_4 + \alpha H_2 + (2-3\alpha/2+x)(O_2 + 3.76N_2)\\ \rightarrow\ &(1-\alpha)CO_2 + (2-\alpha)H_2O + x(O_2 + 3.76N_2) + 3.76(2-3\alpha/2)N_2\end{aligned} \qquad \textbf{(6.3)}$$

   where x is the excess air parameter:

$$x = (2-3\alpha/2)/\phi + 3\alpha/2 + 2 \qquad \textbf{(6.4)}$$

   Intermediate species and radicals are then added following a Gaussian profile with positions and order-of-magnitude quantities taken from a pre-calculated steady, stoichiometric solution.

2. This analytical profile is then used to initialise a 1D back-to-back planar flame with a separation distance slightly below the desired initial kernel diameter. The solution is then allowed to evolve until the separation equals the desired initial kernel diameter, by which time initial velocity, pressure, and mass fraction transients have decayed to negligible levels.

3. These 1D profiles are then used to define a 2D kernel as a function of radial distance from the kernel centre. The velocity components are corrected to account for divergence of the streamlines in the curved flame, so that the velocity magnitude decreases towards the boundary in proportion to the square of the radial distance.

The velocity and pressure fields obtained from both the turbulence and thermo-chemical initialisation procedures are then superimposed, and the density and internal energy are calculated from the specified variables to complete the process.

Using the above procedure, initial transients are reduced to a level where they are no longer evident in any of the quantities of interest. In particular the disturbance to the mean surface position and velocity from the pressure transients, seen in previous simulations, is significantly reduced.

6.2.3 Surface Conditioned Output

All surface conditioned quantities are calculated using linear interpolation in the computational cell where a surface crossing of the progress variable c is found, similar to the results presented in Chapter 5. With complex chemistry and a multi-component fuel, however, the method of determining c must be decided, and can in theory be associated with any scalar that varies monotonically through the flame normal. For the present, the methane mass fraction is used (Eq. 6.5), firstly, since it allows for a more reliable comparison with previously published work, and also, as shown in §6.3.1,

because the density weighted displacement speed based on the CH_4 mass fraction is more consistent and closer to other flame speed measurements when compared to one based on the H_2 mass fraction.

$$c = 1 - Y_{CH4} / Y^{u}_{CH4} \tag{6.5}$$

As found previously the error associated with using linear interpolation was < 2% in a laminar test case for any of the surface quantities, even for the smallest (most highly curved) surfaces. In the present case the grid resolution is approximately two times that used in the single step simulations, so the method was considered sufficient for the present purposes.

Global quantities such as mean kernel radius R_{c^*}, mean isoline length L_{m,c^*}, and total isoline length L_{c^*} are calculated during run-time at regular intervals (1.0μs) to provide time-resolved data. To calculate the global stretch rate dL_{c^*}/dt the derivative of a 5th order polynomial curve-fit to the time-resolved total isoline length was used, in order to overcome numerical noise in the raw data.

6.3 Results and Discussion

Due to the wide range of length and time scales between the flames in the database, results are presented here in absolute values with SI units rather than normalising by the respective characteristic flame scales, as often found in the literature. In this way it is felt that a more meaningful comparison can be made between the cases. It is also important to note that the use of τ_f as a reference scale, when applied to lean flames with long characteristic times (20.00ms for A1,2), has uncertain relevance in the context of IC engines. Even at lower engine speeds – 1200rpm for example, this represents the equivalent of nearly 180^{o} crank-angle degrees, whereas typically the combustion phase is completed in half this time.

6.3.1 Flame Speeds

Several methods exist in the literature to calculate the speed of the flame in multi-component fuels, and the choice of this definition can have a qualitative impact on derived quantities such as the Markstein length. For unstretched, steady-state laminar flames, these flame speeds, either relative to the burned or fresh gases, should be equal and constant. It is therefore useful to compare these differently defined flame speeds in the 1D configuration to asses their reliability for use in unsteady simulations.

The fuel consumption speed, s_c, has the advantage of being well defined and independent of the choice of isosurface and so is ideal for use in numerical laminar flame calculations where precise information on reaction rates through the flame front is readily available. Since it is an integral quantity, its use in curved and strained flames is more problematic. The integral path is defined by the local flame normal, which may curve and intersect with any number of other flame elements before passing into equilibrium compositions, and so care is required in its application to flows with a high turbulence intensity [49,59].

The consumption speed can be evaluated from any combination of species reaction rates. In the simplest case of a single species it is defined as

$$s_c = \frac{\int \dot{\omega}_k \, dn}{\rho_u \left(Y_k^b - Y_k^u \right)} \tag{6.6}$$

where $\dot{\omega}_k$ is the rate of mass production for species k, ρ_u is the fresh gas density, Y_k is the species mass fraction and superscripts u and b indicate unburnt and burnt values respectively. n is the flame normal path along which the integration is carried out.

Since the different diffusivities of the components in the fuel can lead to inconsistencies between the values of s_c for different species , an alternative definition is proposed by Sankaran and Im [128], who use a weighted sum of the reaction rates of the principal

fuel components, with the weighting determined by the heating value of each species. For CH_4 /H_2 flames where q_{CH4} and q_{H2} are the heating values of the respective fuels, the consumption speed becomes

$$s_c = \frac{\int \left(q_{CH4}\dot{\omega}_{CH4} + q_{H2}\dot{\omega}_{H2}\right)dn}{\rho_u\left[q_{CH4}\left(Y^b_{CH4} - Y^u_{CH4}\right) + q_{H2}\left(Y^b_{H2} - Y^u_{H2}\right)\right]} \qquad \textbf{(6.7)}$$

A more general extension to this weighted sum approach is suggested by Chen and Im [66] where the rate of heat release for all species is considered

$$s_c = \frac{\int\left(\sum_{k=1}^{N}\dot{\omega}_k h^0_k\right)dn}{\rho_u\left[\sum_{k=1}^{N} h^0_k\left(Y^b_k - Y^u_k\right)\right]} \qquad \textbf{(6.8)}$$

where h^0_k is the enthalpy of formation of species k and the sum is performed over all N species.

Figure 6.1a compares the four differently defined consumption speeds for a one dimensional laminar flame with fresh gas composition corresponding to Case F1 (ϕ = 0.625, α = 0.3). The approach to a steady-state for consumption speeds of pure CH_4 ($s_c^{(a)}$), pure H_2 ($s_c^{(b)}$), and the weighted sums according to Eqs. 6.7 ($s_c^{(c)}$) and 6.8 ($s_c^{(d)}$) are presented. In addition, in Fig 6.1b the steady state values are compared to the calculations of the density weighted displacement speed s_d, evaluated at all points through the flame front for both CH_4 and H_2.

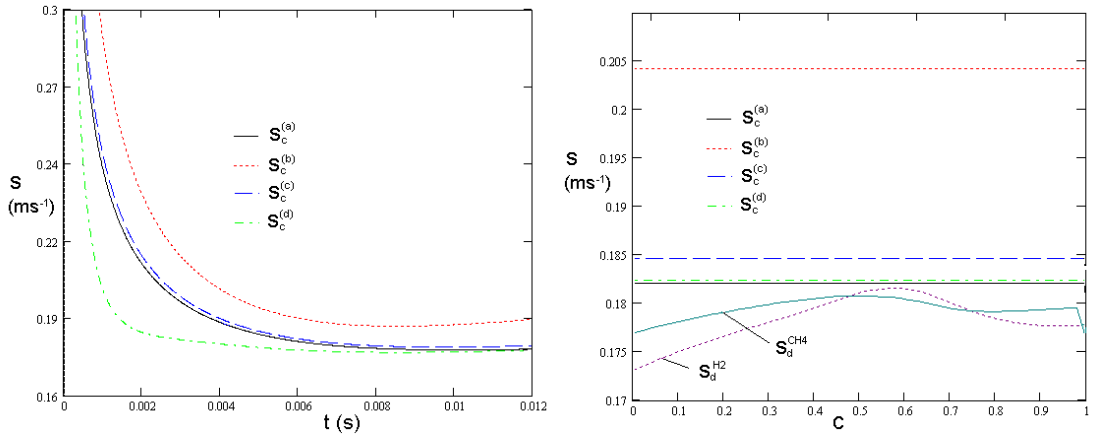

(a) (b)

Figure 6.1 (a) Approach to steady state for consumption speeds calculated according to Eqs. 6.6 – 6.8. $s_c^{(a)}$ = CH_4 only, $s_c^{(b)}$ = H_2 only, $s_c^{(c)}$ = (CH_4 +H_2) weighted sum , and $s_c^{(d)}$ = global weighted sum. (b) displacement speed profiles s_d for CH_4 and H_2 against progress variable c, and steady state values of consumption speed.

It can be seen from Fig 6.1a that reasonable agreement is achieved in the steady state limit with the exception of $s_c^{(b)}$ based only on H_2 consumption. This discrepancy has been noted before for steady stretched flames [22] and is thought to be due to high diffusivity of H_2 compared to the other major species. $s_c^{(d)}$, based on the global rate of heat release according to Eq. 6.8 is clearly the preferred method in this case, since it reaches a steady value considerably faster than the alternatives, and is also in good agreement with the final values of $s_c^{(a)}$, and $s_c^{(c)}$.

The density weighted displacement speed profiles s_d^{CH4}, and s_d^{H2} given in Fig 6.1b show some variation through the flame front, but on the whole the agreement is good (note the expanded scale in Fig 6.1b), particularly for isosurfaces in the higher temperature region of the flame ($c > 0.5$). It is also noted that s_d^{CH4} shows greater consistency through the flame than s_d^{H2}, and therefore appears to be a better choice for extracting displacement speed data in the enriched flame.

6.3.2 Fresh Gas Turbulence

In Section 4.2.7.1 the general influence of the boundary conditions on the decay of two-dimensional turbulence was addressed. For the present work, two specific initial fields are used in all simulations; one for each level of turbulence intensity, and so it is useful to examine the decay of these fields without heat release to assess the potential changes in turbulent strain rates experienced by the kernels.

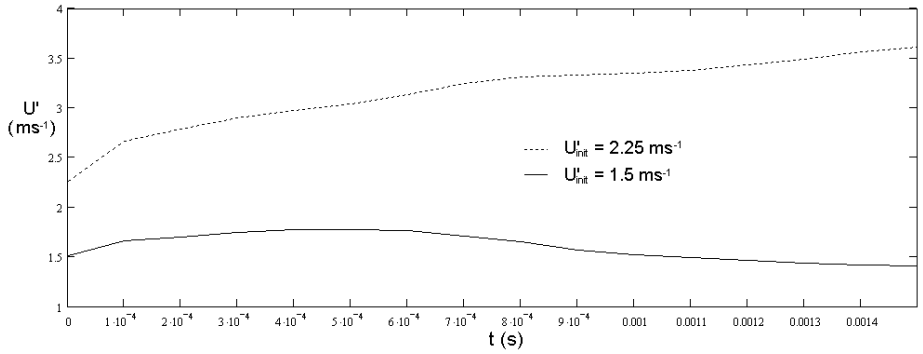

Figure 6.2 Cold-flow turbulent velocity for low (Cases A1, B1, C1, D1) and high (Cases A2, B2) turbulence intensity fields vs. simulation time.

An initial rise in u' is seen in both cases which is due to the influence of the boundary conditions, and in the high intensity case the increase is sustained through out the simulation. It should be noted that Cases A2 and B2 were terminated at t = 1ms as opposed to t = 1.5ms for the lower intensity cases due to the more rapid convection of the kernels towards the boundaries.

This increase in u' must be taken into account when comparing the effects of turbulence intensity on the global kernel growth, particularly since quenching of the kernel is observed at the higher intensities, which in part must be due to the flame experiencing increasingly high strain rates as it evolves – beyond those that would be expected in practice.

Further information is found by examining the change in directional and mean integral length scales as shown in Figs 6.3 and 6.4.

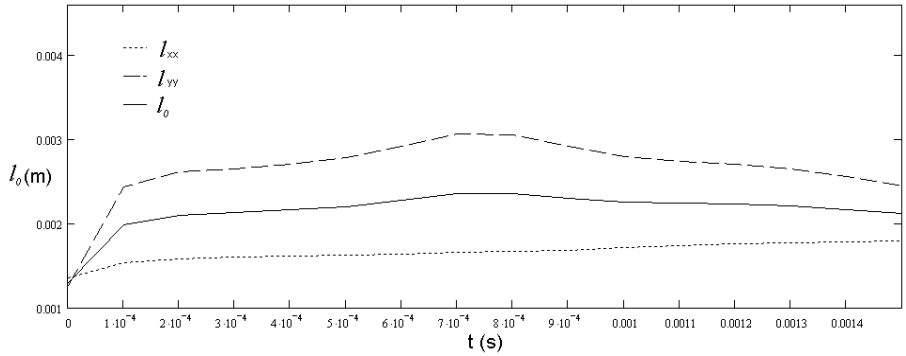

Figure 6.3 Integral length scales for u'_{init} = 1.5 ms^{-1}. Evaluated from the integrated two-point velocity correlation across half the domain for each coordinate direction.

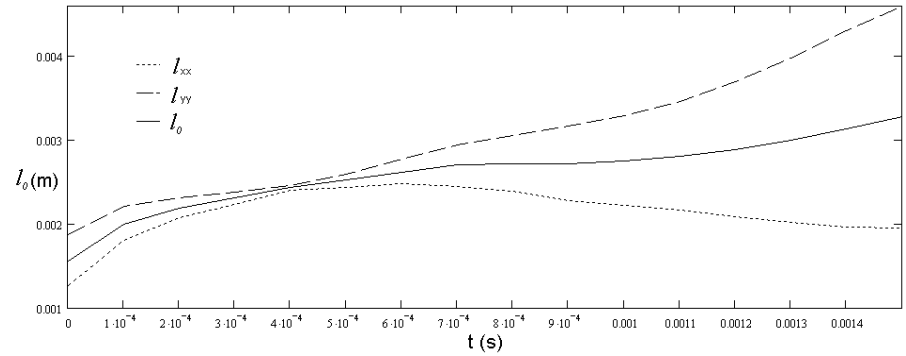

Figure 6.4 Integral length scales for u'_{init} = 2.25 ms^{-1}. Evaluated as above.

For the lower intensity case u'_{init} = 1.5 ms^{-1}, shown in Fig 6.3, after an initial rise in l_{yy} the values remain approximately constant, with the difference in l_{xx} and l_{yy} indicating a departure from isotropy. From Fig 6.4 it can be seen that a more marked increase in l_0 occurs at the higher turbulence intensity although isotropy is only lost towards the end of the simulation time. An increase in l_0 is expected in decaying 2D and 3D turbulence, as noted previously, and so it is not expected to introduce spurious effects into the kernel growth.

From the above information it is useful to locate the DNS results on the turbulent combustion regime diagrams as outlined in §3.1. According to the modified Peters diagram [3] at t = 0 all flames in the database are in the thickened-wrinkled flamelets regime, close to the boundary with the thickened flame regime. By the end of the

simulation time the lower intensity cases remain in this region while the higher intensity cases are more clearly identified as having moved to the thickened flame regime.

Placement on the Echekki and Kolera-Gokula regime [36] derived from kernel-vortex interactions is done by assuming the characteristic vortex radius to be half the integral length scale, which, taking into account the approximate kernel growth gives R_v/R_f ranges of 0.65-0.38, and 0.77-0.91 for the lower and higher turbulence intensities respectively. In this case the placement seems to underestimate the effect of the turbulence at the higher intensities. All lower intensity cases are in the wrinkled kernel regime with Case A1 close to the breakthrough regime boundary, and both higher intensity cases are placed in the middle of the breakthrough regime. From visual inspection of the results (Section 6.3.3) it appears the transition from wrinkled to breakthrough is reasonably well predicted but that global quenching is found to occur at considerably lower turbulence intensities, perhaps reflecting the fact that the small scales of turbulence are not taken into account in the analysis of [36].

6.3.3 General Description of Kernel Development

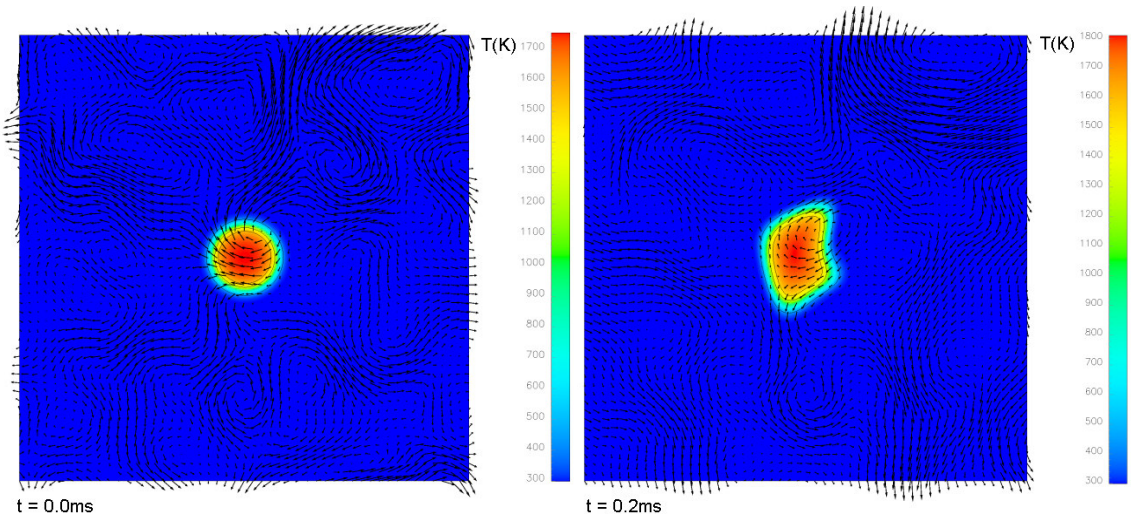

Figure 6.5 Case B1 (ϕ = 0.53, α = 0.3, u' = 1.5ms^{-1}). Temperature (colour), velocity fields (vector arrows). Domain dimensions: 14.48mm x 14.48mm.

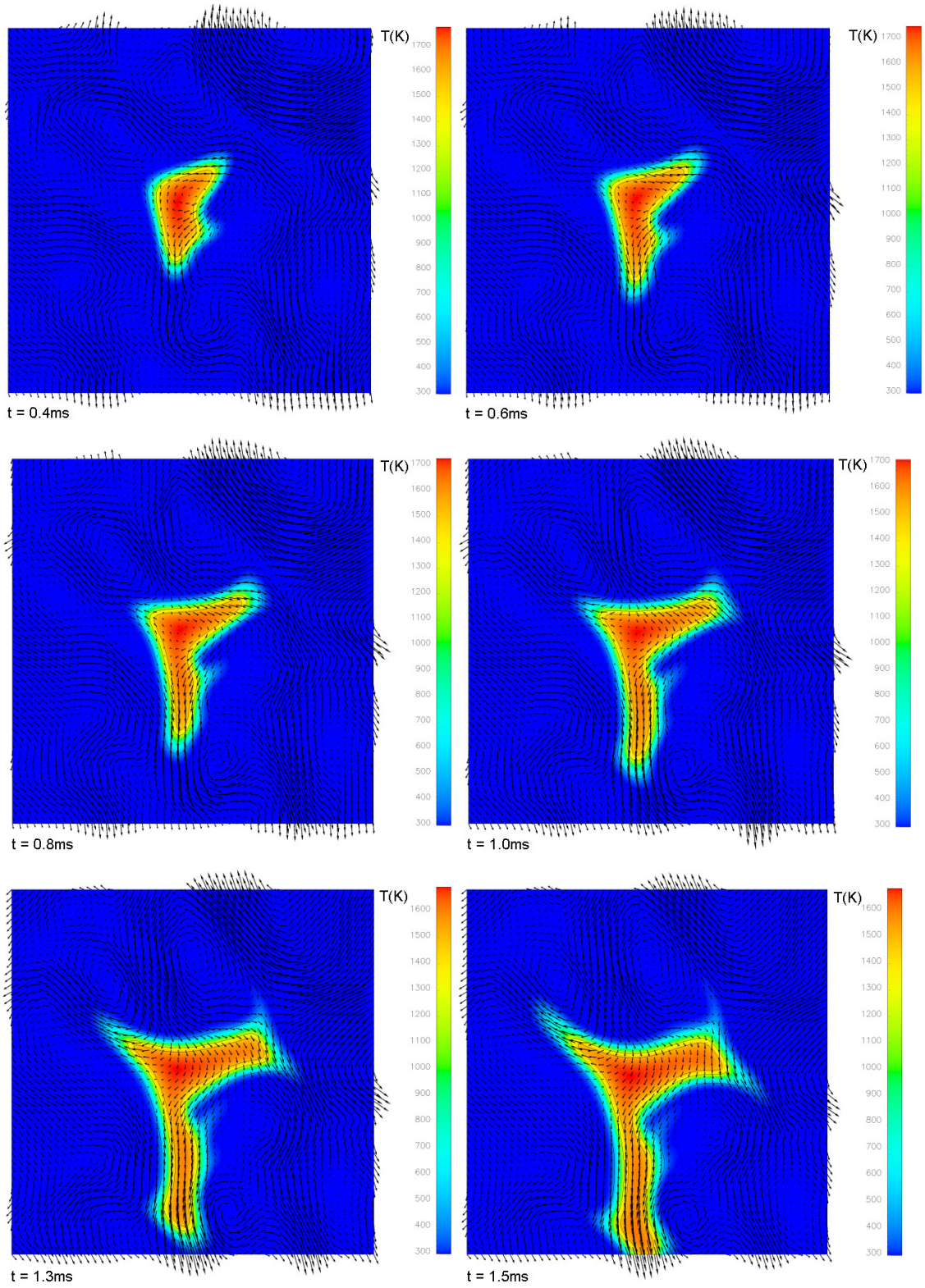

Figure 6.5 continued.

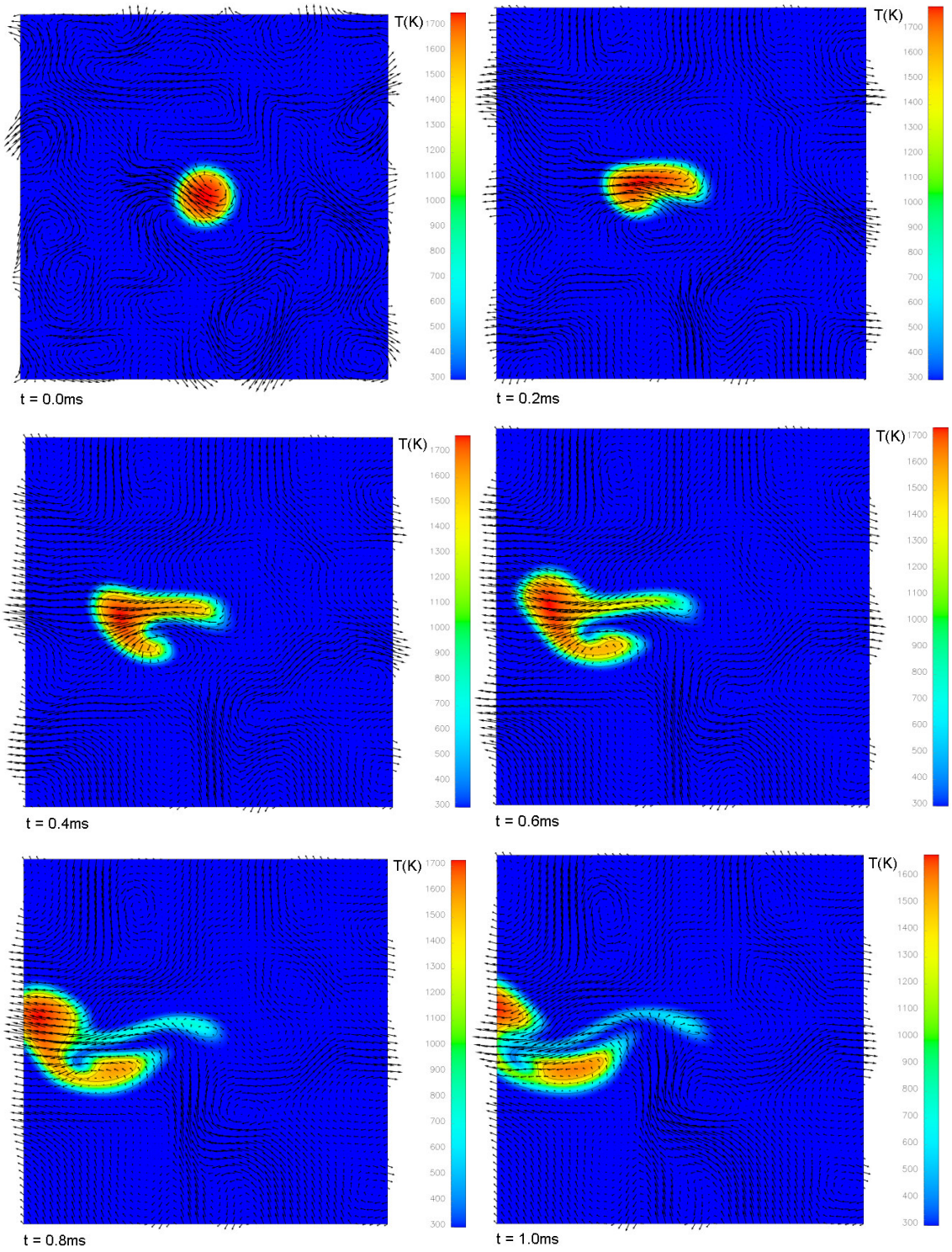

Figure 6.6 Case B2 (ϕ = 0.53, α = 0.3, u' = 2.25ms^{-1}). Temperature (colour), velocity fields (vector arrows). Domain dimensions: 14.48mm x 14.48mm.

Figures 6.5 and 6.6 show representative features for all flames with the same initial turbulence. For the lower intensity cases it can be see that the flame-turbulence

interaction is in agreement with the predictions of the combustion regimes discussed in §6.3.2. An initial, quasi-laminar phase of growth exists for t < 0.3ms followed by increased wrinkling of the flame front as the expanding kernel experiences a greater range of turbulent scales. Despite being highly curved and strained by the flow, the flame appears to remain intact and retains a flamelet like structure throughout, with isolines of the progress variable remaining approximately parallel locally. It is also noticeable that the curvature is very unevenly distributed around the kernel with a small number of highly curved and clearly identifiable regions, separated by regions of much lower curvature. This is discussed further in later sections with reference to the interrelations of surface properties.

For the higher turbulence intensity case shown in Fig 6.6 a similar period of quasi-laminar growth exists for t < 0.3 after which the flame is strongly strained and distorted by the flow, ultimately leading to two regions of local extinction and pinch-off.

Overall, extinction or the onset of quenching was observed in three of the flames in database. The results are summarised in Table 6.3.

Case	Outcome
A1	Global extinction (quenching onset at t ≈ 0.86ms)
A2	Global extinction (quenching onset at t ≈ 0.44ms)
B1	Successful transition to turbulent flame
B2	Local extinction (recovery / probable transition to turbulent flame)
C1	Successful transition to turbulent flame
D1	Successful transition to turbulent flame

Table 6.3 Summary of outcomes for the flame database.

The time of onset of quenching is assumed to occur when a turning point is seen in the growth of the c = 0.8 isoline, which can be associated with the inner reaction layer. This does not in itself indicate global extinction however since local extinction and pinch-off will cause a reduction in flame surface area, after which the kernel fragments may continue to propagate in isolation and transition to fully developed flames, as appears to be the case for Flame B2. The criterion used to determine global extinction, therefore, is

when the length of the c = 0.8 isoline, having reached a turning point in its growth, continues to decline monotonically to below its initial value.

Figure 6.7 shows the growth of the c = 0.8 isoline length for all cases, where the basic, qualitative differences between the cases can be seen, and the turning points mentioned above can be clearly identified.

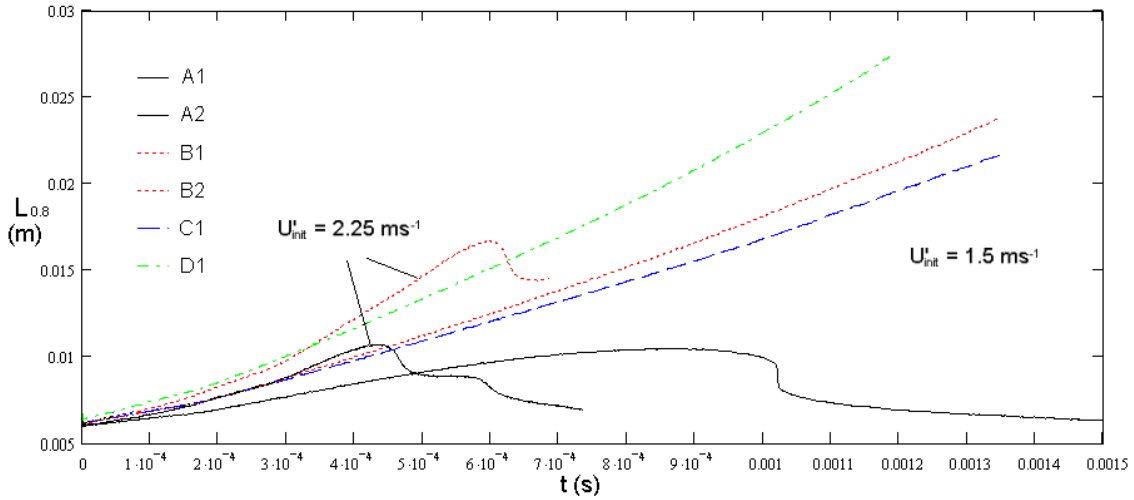

Figure 6.7 Growth in length of the c =0.8 isolines. Data ends when isolines reach the boundary or the simulation is terminated.

A first observation from Fig 6.7 is that all three H_2 doped flames, regardless of equivalence ratio, grow more rapidly than the pure CH_4 flames. This is particularly notable when comparing the B1 and C1 flames, where the C1 flame not only has a higher equivalence ratio, but also a higher laminar flame speed, and higher density ratio between the unburnt and burnt gases, all of which would otherwise suggest a greater kernel growth rate. A second immediate observation is the global extinction seen in flame A1, when it has been found in previous studies [9] that a statistically planar flame under comparable thermo-chemical and turbulent conditions exhibits self sustained combustion.

Finally, the resistance to extinction and quenching evident in the H_2 doped flames is more pronounced than expected, where even at the higher turbulence intensity the kernel in B2 appears to recover from a local extinction / pinch-off to continue

propagating. A more detailed examination and analysis of these phenomena are presented in the following sections.

6.3.4 Surface Conditioned Quantities for the Pure CH_4 Kernel

In this section the distribution of the surface based quantities s_d, a_T, K_m, σ, k, as introduced in Sections 2.2.2 and 3.2.7, are presented for the pure methane kernel case C1. These quantities are not only of particular importance to flamelet based modelling approaches, but provide valuable insight into the local flame dynamics and interrelation between the flow field and the chemistry.

The pure methane kernel (Case C1, ϕ = 0.625 α = 0.0, u' = 1.5ms^{-1}) is examined first since many of the qualitative trends and correlations common to all the cases can be introduced here without the potential added complications of preferential diffusion effects or local extinctions. And secondly, for the purposes of comparison and validation of the results against previously published data on pure CH_4 flames.

The density-weighted displacement speed $s_d^* = \rho s_d / \rho_0$ is used in all of the following unless otherwise stated, and will be referred to simply as the displacement speed s_d. The components of reaction s_r, normal diffusion s_n, and tangential diffusion s_t are defined on an isoline of methane mass fraction Y_{CH4}

$$s_r = \frac{-\dot{\omega}_k}{\rho_0 |\nabla Y_{CH4}|} \tag{6.9}$$

$$s_n = \frac{\vec{n} \cdot \nabla (\rho D_{CH4} \vec{n} \nabla Y_{CH4})}{\rho_0 |\nabla Y_{CH4}|} \tag{6.10}$$

$$s_t = -\frac{\rho D_{CH4}}{\rho_0} (\nabla \cdot \vec{n}). \tag{6.11}$$

where the progress variable is defined from $c = \left(Y_{CH4} - Y_{CH4,0}\right) / \left(Y_{CH4,\infty} - Y_{CH4,0}\right)$, and the term $\left|\nabla Y_{CH4}\right|$ appearing in the denominator of Eqs. 6.9 and 6.10 represents the gradient magnitude of the methane mass fraction, or surface density function (SDF) σ.

Considering first the distribution of these surface quantities from a snapshot taken near the end of the simulation, t = 1.1ms, when the kernel is at its most fully developed state, Fig 6.8 shows the profiles of the surface averaged components of displacement speed as a function of progress variable.

The results are in close qualitative agreement with previous DNS studies in three dimensions using a single-step global reaction [72,74,129]. It can be seen that the mean contribution from tangential diffusion, which is directly related to the mean curvature, is small at this stage of kernel development, suggesting that for the purposes of modelling the surface mean quantities, the mean curvature is not significant at this stage of growth. Locally, however, the curvature plays an important role in the diffusive-reactive balance in the flame front.

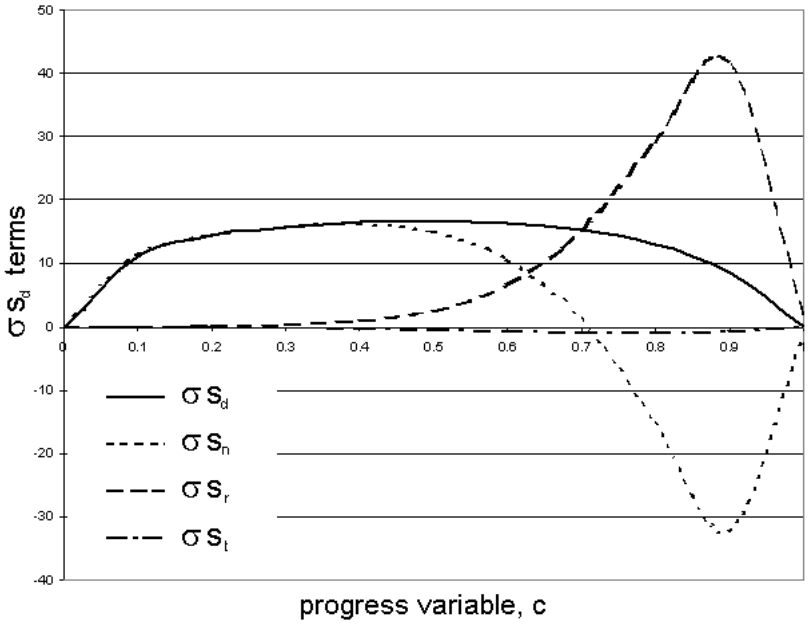

Figure 6.8 Profiles of surface-mean displacement speed and its components multiplied by the SDF σ, for Case C1 at t = 1.1ms

To understand the distribution of the local displacement speed about the mean, pdfs of the components are presented in Figs 6.9a-c for three isolines of the progress variable. The c = 0.8 isoline is chosen to represent the inner reaction layer. It has been found that the majority of the heat release occurs in the region 0.7 < c < 0.95, and that in this zone the variation of s_d due to strain and curvature is at a minimum [59]. In addition, isolines at c = 0.5 and c = 0.1 are shown in order to highlight the change in distribution through the flame front. The c = 0.5 isoline represents the approximate position of maximum scalar gradients, and the c = 0.1 line represents the outermost isolevel still undergoing significant flame-turbulence interaction. It has also been identified as an appropriate isosurface on which to evaluate the global turbulent burning velocity for flame kernels [71], which is explored further in Section 6.3.6.

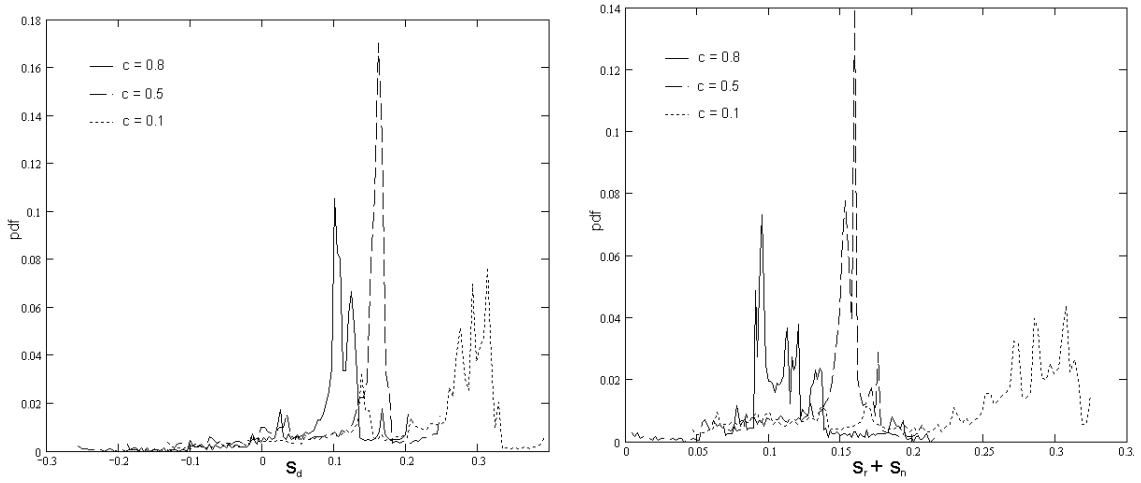

(a) (b)

Figure 6.9a-c PDFs of displacement speed and components for isolines at c = 0.8, 0.5, and 0.1 for Case C1 at t = 1.1ms. (a) s_d (b) $s_r + s_n$ (d) s_t.

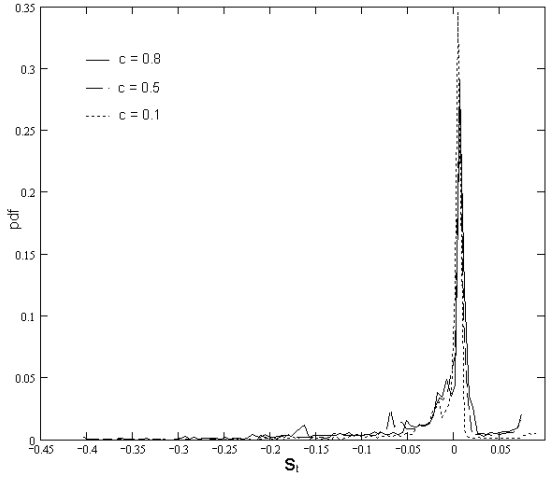

(c)

Figure 6.9 continued.

In Fig 6.9b the reactive and normal-diffusive components of the displacement speed are combined since it is of greater interest to consider the balance of these quantities to gain an understanding of the response of the flame to unsteady effects. The mean, variance and skewness for the above PDFs are summarised in Table 6.4.

	s_d (0.8)	s_d (0.5)	s_d (0.1)	$s_r + s_n$ (0.8)	$s_r + s_n$ (0.5)	$s_r + s_n$ (0.1)	s_t (0.8)	s_t (0.5	s_t (0.1)
mean	0.0928	0.1215	0.2209	0.1155	0.1383	0.2292	-0.0227	-0.0168	-0.0082
var	0.00385	0.00698	0.01216	0.00079	0.00132	0.00648	0.00534	0.00302	0.00158
skew	-1.652	-1.734	-1.179	1.305	-1.413	-0.765	-2.267	-2.496	-2.500

Table 6.4 Mean, variance and skewness of displacement speed and components for isolines at c = 0.8, 0.5, and 0.1 for Case C1 at t = 1.1ms

Examining Table 6.4 it is clear that s_d is not constant across the flame brush but varies from below the laminar flame speed ($0.134 ms^{-1}$) on the c = 0.8 isoline to above it on the c = 0.1 isoline. An assumption often used in modelling closures based on (density weighted) s_d is that it remains approximately constant through the flame. This appears to be a reasonable approximation for statistically planar flames but is not valid for the

curved, developing flames studied here. This finding is consistent with previous work on flame kernels using three-dimensional DNS with single-step chemistry [72].

It can also be seen that the combined $s_r + s_n$ contribution is always positive, whereas s_d is diminished by the predominantly negative contribution of s_t, so that while s_d has a positive mean value, negative displacement speeds also exist in regions where s_t is strongly negative. From Eq. (6.11) it is clear that high negative values of s_t are a direct consequence of high positive values of curvature, and so the distribution of s_t also directly reflects the distribution of curvature on the isoline. The negative skewness of the s_t distribution demonstrates the increased probability of finding high positive values of curvature. This is perhaps to be expected for a flame kernel which has an inherent mean positive curvature, and can be seen intuitively from inspection of the snapshot images in Fig 6.5.

The transition from $s_d / s_L^0 < 1$ on the c = 0.8 isoline to $s_d / s_L^0 > 1$ on the c = 0.1 isoline can be explained by considering the mean and variance of $s_r + s_n$ and s_t at each level. Towards the fresh gases the reaction component of $s_r + s_n$ is negligible and so s_d is determined solely by the diffusive balance in this zone. s_n is enhanced by turbulent transport in this region which acts to increase the mean scalar dissipation, and is reflected by the higher variance of $s_r + s_n$ compared with the inner reaction zone. In addition, the mean value of s_t has a lower magnitude here due to the lower mean curvature of the larger isoline. In the inner reaction zone the enhancement of s_n by turbulent transport is reduced due to the attenuation of the turbulent fluctuations in the pre-heat zone. In contrast the mean magnitude of s_t is increased since the mean curvature for the c = 0.8 isoline is greater. The result is a net decrease in s_d on the c = 0.8 isoline compared with c = 0.1.

To gain better insight into the flame response to strain and curvature it is useful to examine the correlations between the displacement speed and these quantities directly.

In Fig 6.10 plots of the displacement speed components against curvature are shown for all values on the c = 0.8 isoline. The results are in qualitative agreement with previous two-dimensional DNS studies within the comparable range of curvatures [40].
[23,118]

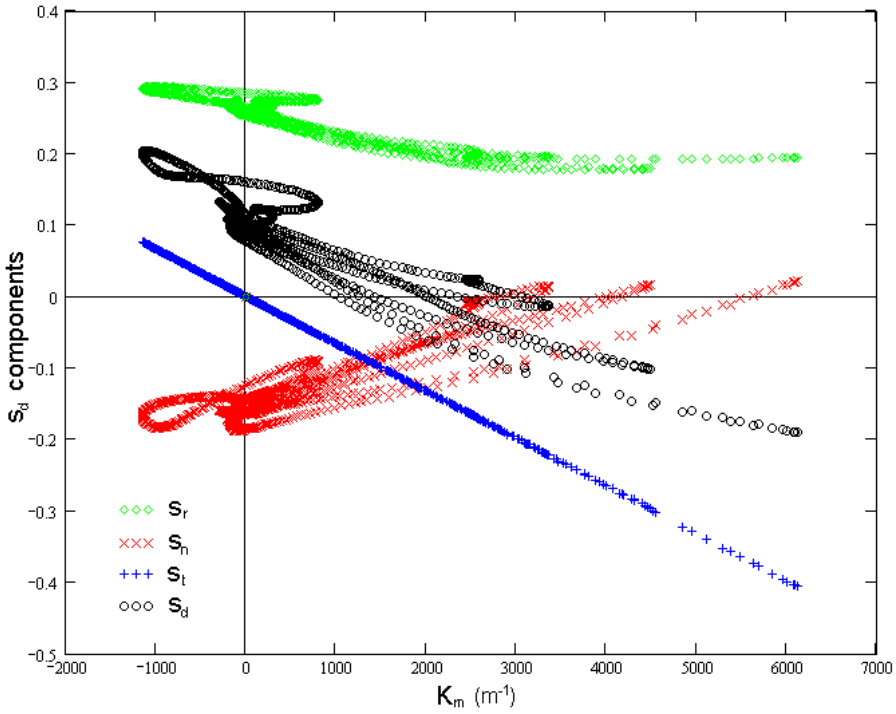

Figure 6.10 Displacement speed components vs. curvature K_m, for Case C1 on the c = 0.8 isoline at t = 1.1ms. Correlation coefficients: s_r-K_m = -0.910, s_n-K_m = 0.893, s_t-K_m = -0.999, s_d-K_m = -0.926.

Comparing the components of s_d to curvature in Fig 6.10 the linear relation of s_t to curvature is clear, and is the principal cause of the negative correlation between s_d and curvature.

The relations of s_r and s_n to curvature involve additional relations between the surface density function, tangential strain rate a_T and curvature. From Eqs. 6.9 and 6.10 it can be seen that a decrease in SDF, which appears in the denominator of both expressions, will tend to cause an increase in their respective magnitudes. A strong negative correlation is found between SDF and curvature – an effect that can be seen qualitatively in the flame thickening at positively curved regions in Fig 6.5 (for Case

B1). This negative correlation has been explained by Chakraborty and Cant [68] by the relation between curvature and the strain field. High values of tangential strain are associated with compressive normal strains assuming the dilatation is small, which acts to bring isolines together in these regions. Conversely, negative tangential strain rates, as found in regions of high positive curvature, cause extensive normal straining which tends to separate the isolines, thereby decreasing the SDF. From Eqs. 6.9 and 6.10 it can be seen that this reduction in SDF suggests an increases in the magnitudes of s_r and s_n for high positive curvature, whereas, as seen in Fig 6.10 this is not the case.

The decreasing magnitude of s_n is explained by the presence of the second derivative of the mass fraction gradient in Eq. 6.9, which reduces more rapidly with curvature than the gradient magnitude in the denominator. The reduction in reaction rate is more subtle, and can be attributed to secondary effects due to the sub-unity effective Lewis numbers of lean methane-air flames.

Although, by definition, the CH_4 mass fraction remains constant on an isoline, under positive tangential strain the preferential diffusion of species over heat into the reaction layer leads to an increase in the overall burning intensity and temperature. For regions of high positive curvature this effect is no longer present due to the correlation of positive curvature with negative tangential strain, thereby producing a net negative correlation between s_r and K_m.

Figures 6.11a, showing curvature against strain rate, and 6.11b showing temperature against strain rate demonstrate these relations. The $K_m - a_T$ correlation coefficient is –0.598, and the $T - a_T$ coefficient is 0.452, which although not strong has a large effect due to the highly non-linear temperature dependence of the reaction rate.

It should also be noted that a contribution to the heat loss is expected due to radiative heat losses from the flame thickening in these regions, but this is unlikely to be a major factor.

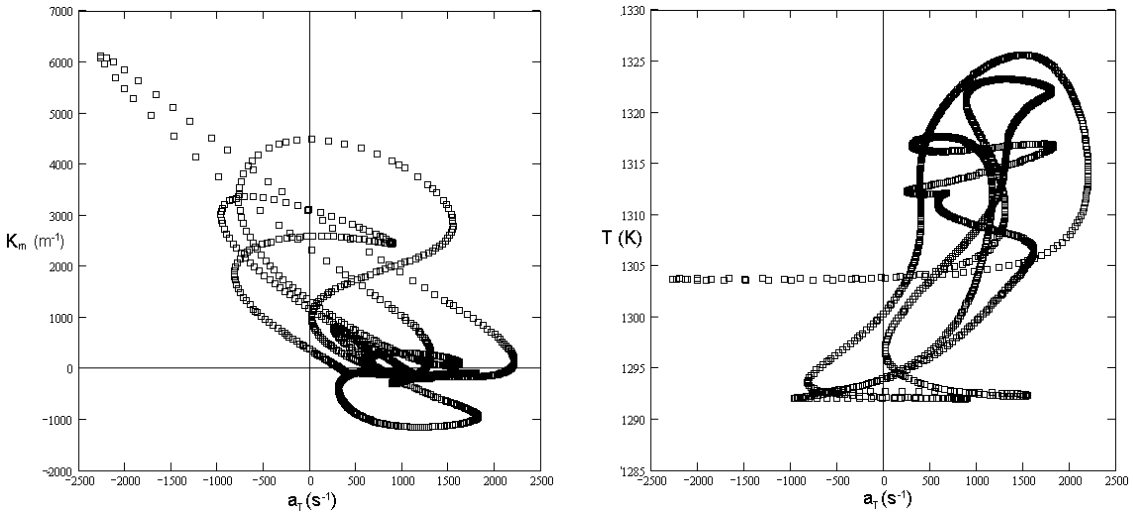

(a) (b)

Figure 6.11 Curvature K_m (a) and temperature T (b) against tangential strain rate a_T for Case C1 on the c = 0.8 isoline at t = 1.1ms.

The overall trends presented in this case are in good qualitative agreement with previous statistics collected from two and three dimensional studies using both single-step, unity Lewis number assumptions, and also with complex chemical simulations. The differences are most pronounced in the regions of high positive curvature which are both more probable than for a statistically planar flame, and sensitive to the differential diffusion of species that cannot be reproduced by simplified chemical schemes.

These factors are clearly both important in understanding the behaviour of both hydrogen-doped and pure methane kernels during the early stages of growth, particularly near the lean limit where the mechanisms leading to local extinction and flame quenching need to be better understood in order to improve our predictive capacity.

6.3.5 Hydrogen Addition

In general, the effect of adding small quantities of hydrogen to the reactants in a turbulent flame changes the behaviour in two basic ways. Through changes to the laminar flame speed and structure - an increase in laminar flame speed and reduction in

thickness of the planar, unstretched laminar flame, and also through thermo-diffusive effects which change the response of the flame to strain and curvature.

The first of these effects are easily quantified and for the present database are summarised in Table 6.1. Thermo-diffusive effects are more complex, and particularly so for flame kernels due the mean curvature: not only do thermo-diffusive effects alter the mean flame behaviour due to the presence of mean curvature, but for small kernels the mean curvature changes significantly through the flame front, which thereby alters the mean flame structure, in a time dependent manner, away from that of the planar laminar flame.

To investigate these effects a comparison can be made between cases B1 (ϕ = 0. 53, α = 0.3, u' = 1.5ms^{-1}), C1 (ϕ = 0.625, α = 0.0, u' = 1.5ms^{-1}) and D1 (ϕ = 0.625, α = 0.3, u' = 1.5ms^{-1}). Snapshots of the cases at t = 1.1ms are shown in Fig 6.12.

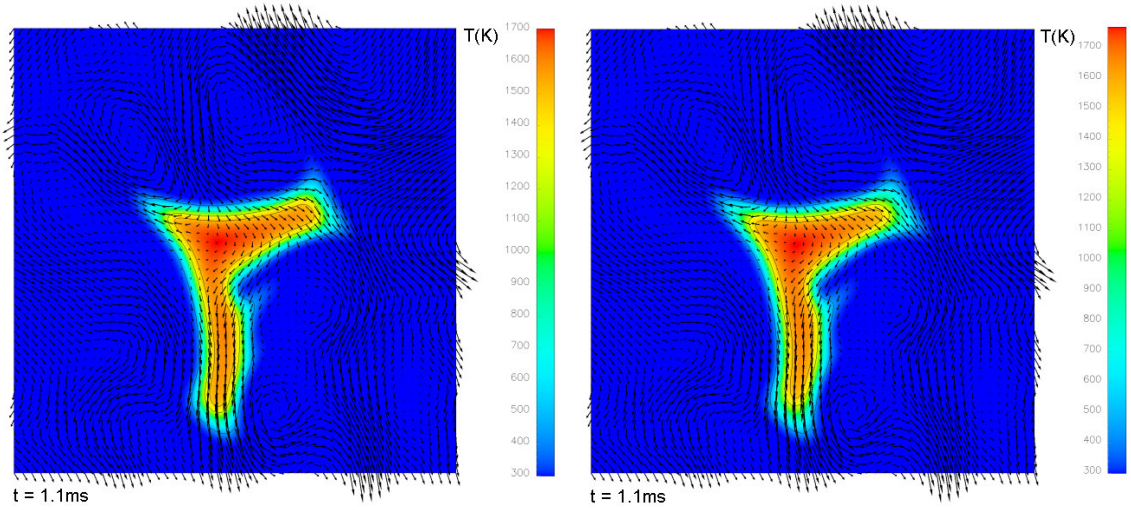

(a) (b)

Figure 6.12a-c. Cases B1 (ϕ = 0.53, α = 0.3, u' = 1.5ms^{-1}) (a), C1 (ϕ = 0.625, α = 0.0, u' = 1.5ms^{-1}) (b), and D1 (ϕ = 0.625, α = 0.3, u' = 1.5ms^{-1}) (c) . Temperature (colour), velocity fields (vector arrows).

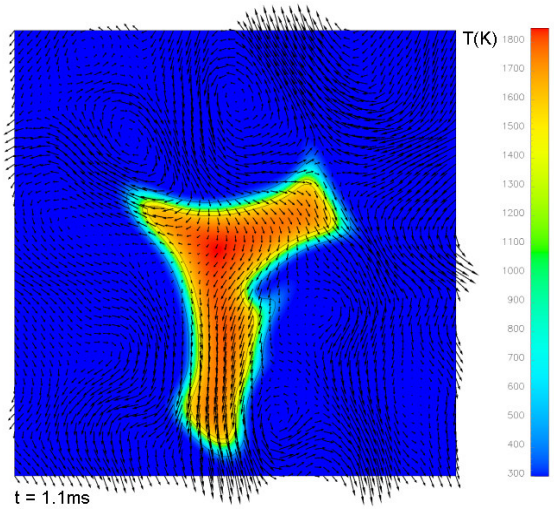

(c)

Figure 6.12 continued.

The reasons for including Case B1 in the comparison can be see from inspection of Figs 6.12a-c. Due to the more rapid growth of the H_2 enriched kernel, the flame surfaces at any instant will be experiencing a different strain field and curvature distribution, and will also have greater mean radius of curvature, and so separating the effects due to laminar flame properties (speed, thickness etc.) from the thermo-diffusive response due to strain and curvature is not possible.

By choosing an equivalence ratio for case C1 so that it more closely matches the physical growth of the H_2 enriched Case B1, it becomes possible to draw conclusions on the relative influence of the two effects. An exact match was not possible of course, but as illustrated in Fig 6.13 the growth of the c = 0.1 isolines for cases B1 and C1 are reasonably close, with a difference of only 2% at t = 1.1ms.

It is perhaps surprising that the growth of B1 actually exceeds that of C1 since, as noted earlier, both the laminar flame speed and the unburnt/burnt gas density ratio across the flames are higher for Case C1, which suggests an important role for the thermo-diffusive effects.

A measure of the differences in global growth rate is found by comparing the global burnt-gas mass fraction, which reaches a value of 1 when all the reactants in the domain

are fully consumed. They are 0.068, 0.065, and 0.1134 for B1, C1 and D1 respectively after 1.1ms. The corresponding global turbulent flame speeds at this instant (defined by Eq. 6.12, §6.3.6) are 1.26ms^{-1}, 1.12ms^{-1}, and 1.81ms^{-1} for B1, C1 and D1.

These figures show that, taking into account the underlying differences in laminar flame speed, the global turbulent flame speed and burnt-gas mass fraction are increased by factors of 1.19 and 1.28 respectively between C1 and D1, and 1.49 and 1.39 between cases C1 and B1. While the differences between C1 and D1 contain the additional effects of differences between the flow fields and mean curvature, the flame speed enhancement of B1 compared to C1 can be ascribed almost exclusively to differences in the thermo-diffusive response to strain and curvature.

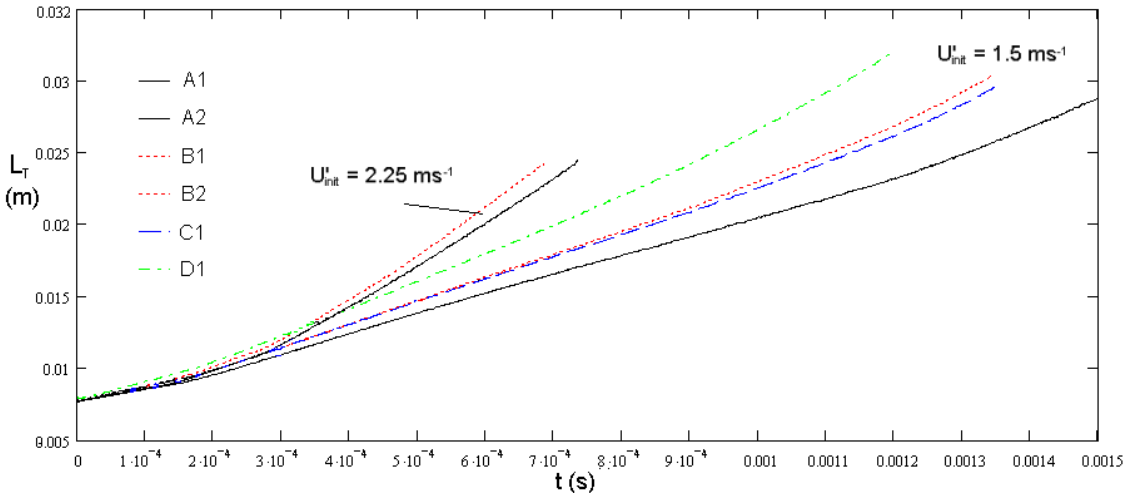

Figure 6.13. Length of the c = 0.1 isoline for all cases. Data ends when isolines reach the boundary or the simulation is terminated.

The underlying causes of the enhanced growth rate due to H_2 addition are revealed by comparing the displacement speed components for cases B1 and C1 against curvature, shown in Fig 6.14. The displacement speed for B1 has both a higher mean value than C1 (10.54cms^{-1} and 9.28cms^{-1} respectively) and is less sensitive to curvature, as indicated by the shallower gradient in Fig 6.14a, which results in a considerable reduction in the frequency and magnitude of flame elements with negative displacement speed. While the tangential diffusion remains similar for both cases due the comparable geometry, a difference can be seen in the balance between the reaction and normal

diffusion components. In the case of the pure methane flame a reduction in the magnitudes of both reaction and normal diffusion can be seen, and this is explained by differences in the laminar flame structure. The pure methane flame C1 has an inherently thinner flame structure compared to the enriched flame, which leads to a higher surface-mean value of SDF, and hence to a reduction in the magnitudes of both s_r and s_n through the relations in Eqs. 6.9 and 6.10.

The distribution of SDF against curvature, as shown in Fig 6.15b, also demonstrates an increased tendency towards flame thickening at positively curved regions for the unenriched flame (indicated by the steeper negative gradient of SDF against curvature), which will tend to increase the reaction component in these regions, and hence explains the 'bending' of s_r evident in Fig 6.14b.

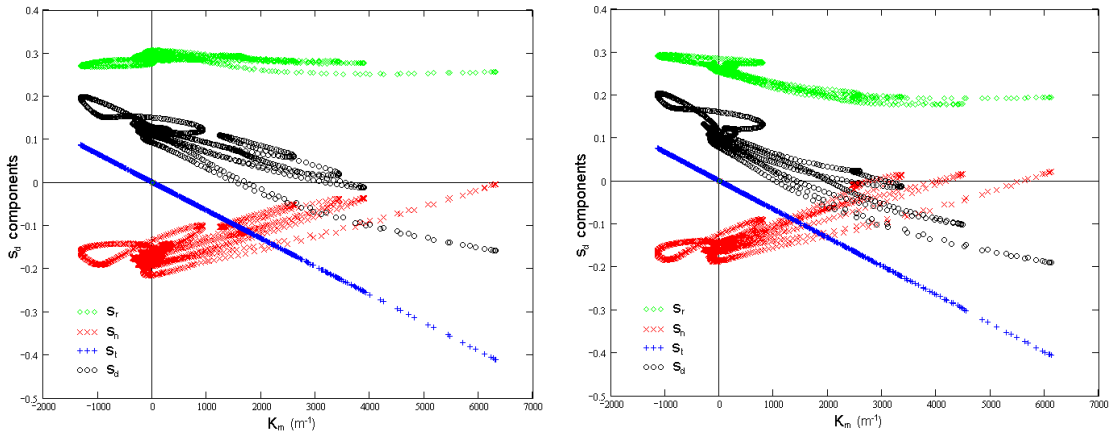

(a) (b)

Figure 6.14 a and b. Displacement speed components vs. curvature K_m, for Cases B1 (a) and C1 (b) on the c = 0.8 isoline at t = 1.1ms.

Since the SDF appears in the expressions for both s_r and s_n its net effect on s_d does not explain the variation between cases B1 and C1, and a second effect is clearly present in the reaction term in C1, causing a reduced sensitivity to curvature.

The reaction rate on an isolevel of CH_4 is a function of both temperature and radical concentration, and in particular on the abundance of the OH radical which is required in the primary breakdown of the CH_4 molecule through the reaction

$$OH + CH_4 \leftrightarrow CH_3 + H_2O \qquad (1)$$

OH is produced in greater quantities in the enriched flame from the chain-branching dissociation reaction of H_2 with the O radical. Figures 6.15a, c, and d show the distributions of temperature and mass fractions of H_2 and the OH radical against curvature for all three flames under consideration.

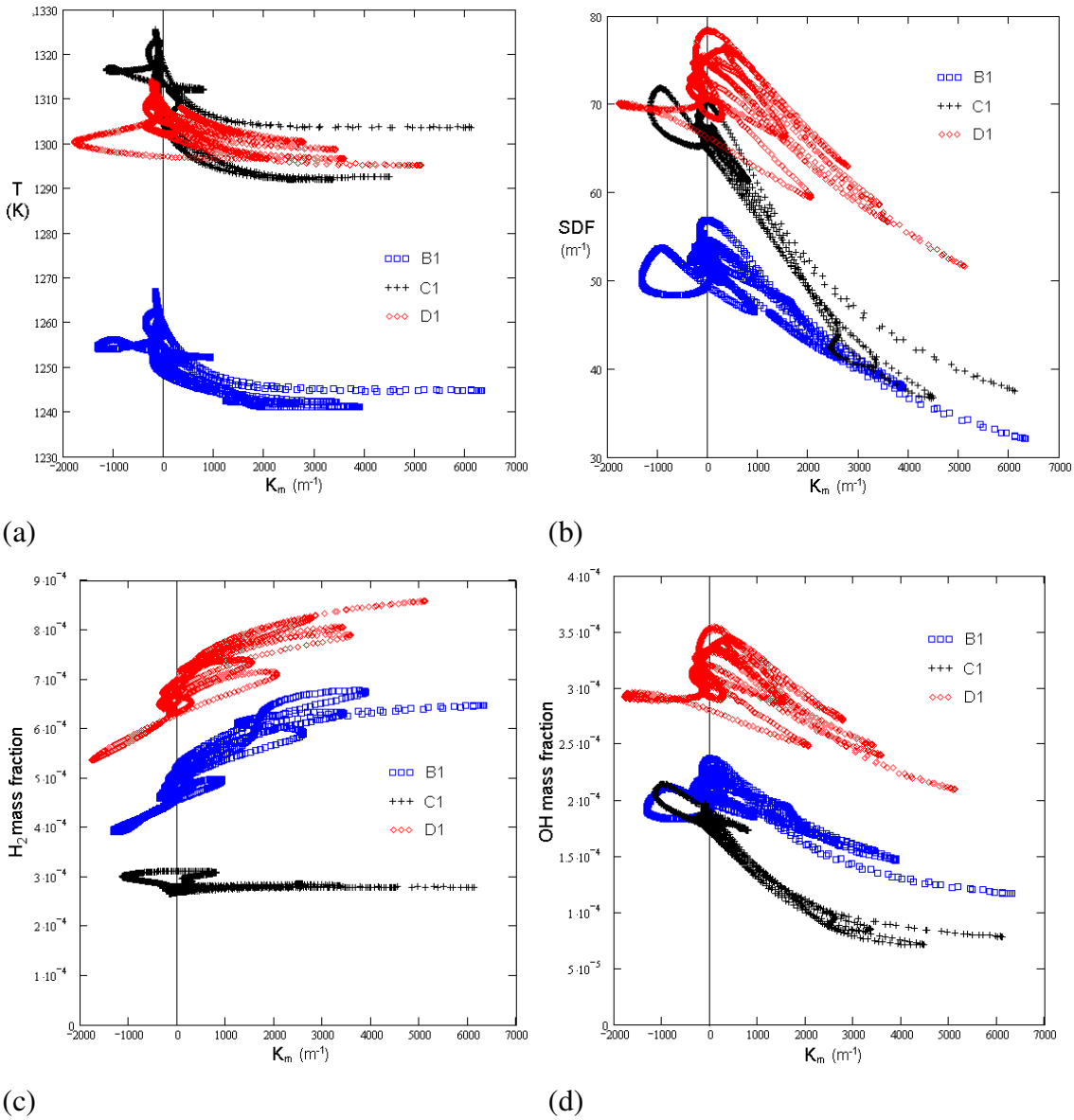

Figure 6.15 a-d. Temperature (a), surface density function (b), H_2 mass fraction (c), and OH mass fraction (d) against curvature for cases B1, C1, and D1 on the c = 0.8 isoline at t = 1.1ms.

The mean temperature on the isoline in D1 (1306K) is only slightly reduced from C1 (1312K), however, the mean temperature in B1 is clearly much lower (1254K). It is also noticeable in Fig 6.15a that for both the enriched flames the variation in temperature along the isolines is less than for the pure methane flame, suggesting an ability to respond more quickly to unsteady effects.

Considering the lower flame temperature of B1, the observed increase in reaction rate compared to C1 can only be a result of the higher concentrations of OH radicals in regions of positive curvature, and this is confirmed by the plots in Figs 6.15 c and d. While OH concentrations are only slightly reduced in the unenriched flame at low curvatures, a greater reduction is seen as curvature increases. The reason for the difference can be seen in the positive correlation of H_2 mass fraction with curvature for the H_2 enriched flames due to preferential diffusion, which through the reactions described above, partially compensates for the loss of OH radicals at higher curvatures.

It is also interesting to note that the reduced thermo-diffusive stability of the H_2 enriched flame B1, as indicated by the slope of s_d in Fig 6.14, does not lead to increased flame wrinkling. In spite of having greater extreme values of both positive and negative curvature, the variance of K_m on the c = 0.8 isoline for B1 is only 1.15×10^6 compared to 1.22×10^6 for C1, with means of 319.3 and 344.6 respectively. This point is discussed further in Section 6.3.7.

6.3.5.1 Flame Extinction

The most marked difference between the enriched and unenriched flames at low equivalence ratios is the quenching observed in Case A1, in contrast to Case B1 which successfully transitioned to a self-sustaining expanding flame. Snapshots of Cases A1 and B1 are compared at time t = 0.8ms in Fig 6.16.

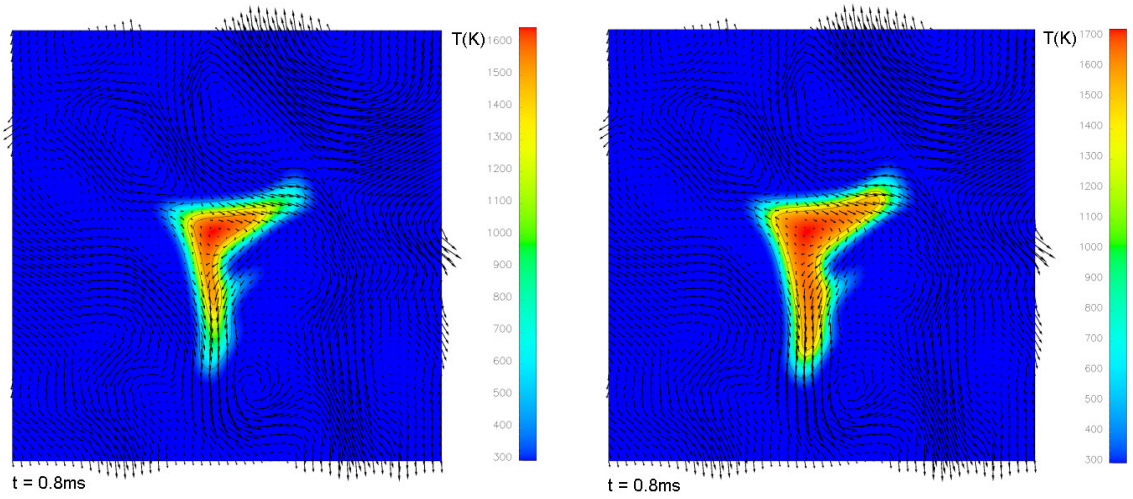

(a) (b)

Figure 6.16 Snapshots of Cases A1 (a) and B1 (b) at t = 0.8ms^{-1}. Temperature (colour), velocity fields (vector arrows).

For sub-unity effective Lewis number flames tangential straining is not, in itself, enough to cause extinction of the flame, since under positive strain rates the burning intensity increases, and at all times in cases A1 and B1 the strain rate is predominantly positive.

The quenching seen in Case A1, as identified by a reduction in the isoline length to below its initial value, is due to a combination of two distinct processes: negative flame speeds produced in regions of high positive curvature, and flame annihilation due to the interaction of flame elements brought into contact by the flow.

Both these processes can be thought of more generally as symptomatic of the longer time scales associated with the pure methane flame ($\tau_f^{A1} \approx 2\tau_f^{B1}$), since they both reflect its relative inability to compensate for the effects of turbulence, which otherwise has a tendency to draw out passive scalars into thin fluid filaments [27].

The curvature distribution and occurrence of negative displacement speeds for cases A1 and B1 are illustrated in Fig 6.17.

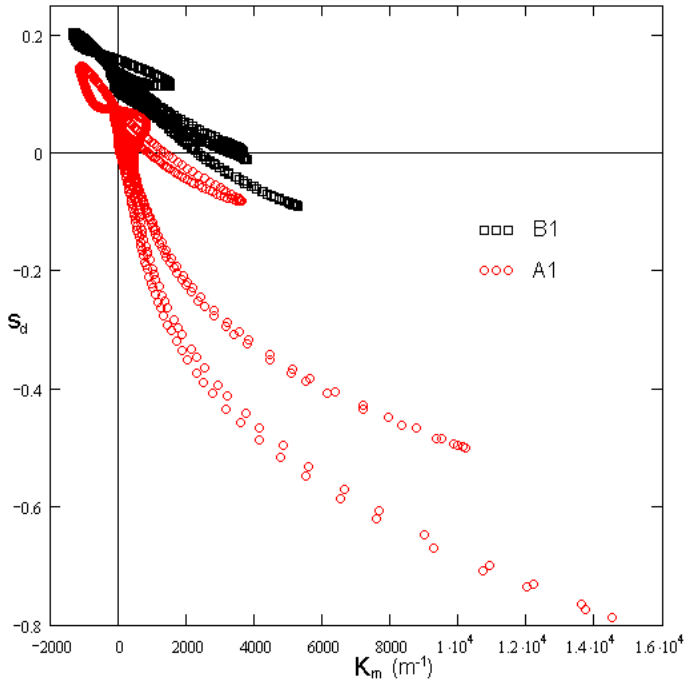

Figure 6.17. s_d against curvature on the c = 0.8 isoline for cases A1 and B1 at t = 0.8ms.

Two effects are immediately apparent from Fig 6.17. The reduction in the mean value of s_d for A1 is simply due to the lower laminar flame speed resulting in a smaller mean kernel radius at this time, and therefore higher mean positive curvature. The second observation is the occurrence of very high local values of positive curvature and associated negative s_d for case A1. While these extreme events undoubtedly contribute to the reduction in flame length, it can also be seen that the large negative displacement speeds occur at quite low values of curvature and appear to 'precede' the onset of high positive curvature. The curvature is not therefore the primary cause of negative s_d in this region, but a secondary effect that is itself the result of a reduction in s_d.

In this case, flame element interaction on the burnt gas side, also known as downstream interaction, is the main mechanism leading to a reduction of the isoline length. More specifically, Hawkes and Chen [9] have identified the onset of extinction through this route with the interaction of the CO oxidation layers.

The importance of this layer can be seen by considering the principal reaction path for the initial breakdown of methane:

$$CO + OH \leftrightarrow CO_2 + H \quad (1)$$

$$H + O_2 \leftrightarrow O + OH \quad (2)$$

$$OH + CH_4 \leftrightarrow CH_3 + H_2O \quad (3)$$

Reactions 1 and 2 are recognised as being crucial for general hydrocarbon-air combustion [10], where the chain-carrying oxidation reaction of CO in (1) produces H radicals for the chain-branching reaction in (2), which in turn supplies the OH radicals required by (3) in sufficient quantities for the rapid breakdown of CH_4. Disruption to this critical pathway by diffusion of the OH radical away from the CO oxidation layer leads ultimately to reduced reaction rates on the methane isoline and hence to the observed negative displacement speeds at low curvatures.

These negative displacement speeds then rapidly decrease further due to the increasing curvature caused by the coming together of isolines undergoing downstream interactions. The result, depending on the local geometry, is either a rapid retraction of the isoline towards the kernel centre, or in addition, the separation of a region of burnt gases, or pinch-off.

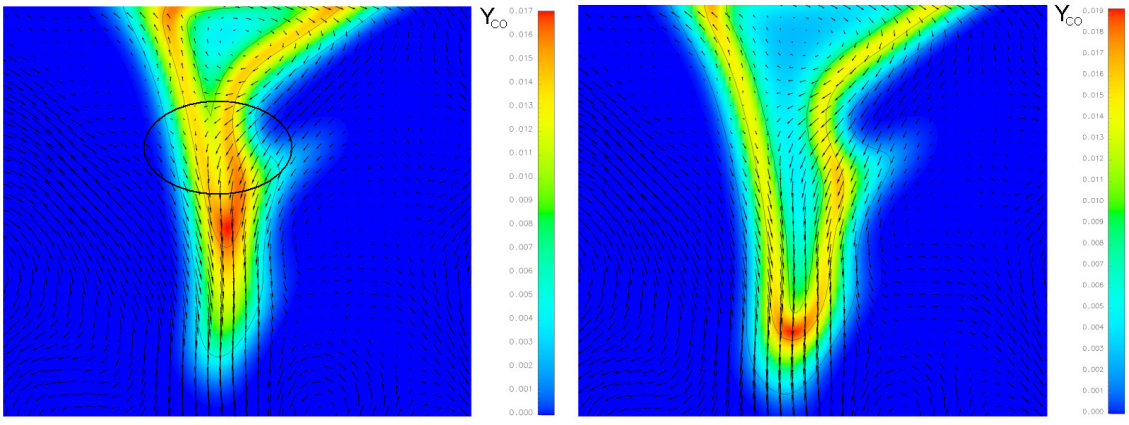

(a) (b)

Figure 6.18a and b. CO mass fraction (colour), velocity (vector arrows) for Cases A1 and B1 at t = 0.8ms.

The Snapshots in Fig 6.18 illustrate the importance of the CO oxidation layer in the extinction process. Taken shortly before the onset of quenching, observed in A1 at t = 0.8ms, the interaction of the downstream CO layers in an area of low curvature can clearly be seen in the highlighted area in Fig 6.18a.

It should be noted here that although global extinction has been assumed, the ultimate fate of the kernel in A1 is not actually known – recovery of the residual kernel is still possible since a region of burnt gases with a temperature exceeding the activation temperature remains. However, such retarded heat release in an IC engine would lead to an unacceptable loss of power and for practical purposes would be considered a misfire.

6.3.6 Comparison with the Statistically Planar Flame

In this section the results of Cases A1 and B1 are compared to the data of Hawkes and Chen [9], who studied statistically planar flames of the same composition and equivalence ratio for a pure CH_4 flame: ϕ = 0.53, α = 0.0 (case A1), and a H_2/CH_4 flame: ϕ = 0.53, α = 0.3 (Case B1) using a 15-step chemical mechanism with 19 species. Similar initial turbulence parameters (u' = 1.5 ms^{-1}, l_0 = 1.5 mm) were used, however, due to the inherently unsteady kernel configuration it was not possible to allow the solution to evolve for the same number of eddy turnover times before statistics were collected ($2\tau_t$ or $2ms^{-1}$), nevertheless, the qualitative differences of interest here are not significantly affected by this. The Hawkes and Chen data will be referred to as HC1 and HC2 for the pure CH_4 and H_2-doped flames respectively.

6.3.6.1 Turbulent Flame Speed

For the HC1 and HC2 flames turbulent flame speeds s_t^p were calculated from the volume integral of the reaction rate normalised by the cross-sectional length L in the mean direction of propagation:

$$s_t = \frac{1}{\rho_0 Y_{0,CH4} L} \int \dot{\omega}_{CH4} dA \qquad \textbf{(6.12)}$$

In the case of a flame kernel, identification of the appropriate reference length is not so obvious since a projection of the mean flame surface in the direction of propagation leads to large differences in length depending on the choice of surface.

Following Lipatnikov and Chomaik [71], the c = 0.1 isoline is therefore used for this purpose here, which has been shown to be close to a theoretical isolevel with which the global turbulent burning velocity should be associated in an expanding spherical flame. The circumference of a circle defined by the mean radius of the c = 0.1 isoline was used together with Eq. 6.12 to produce the equivalent turbulent flame speed for the kernel flames. The results for both planar and kernel flames are summarised in Table 6.5

Case	s_t / s_L^0	L_t / L	s_t^{H2} / s_t^{CH4}	$\frac{L_t^{H2} / L_t^{CH4}}{L^{H2} / L^{CH4}}$	$s_L^{0,H2} / s_L^{0,CH4}$
A1	1.36	1.35	2.04	0.99	1.42
B1	1.95	1.34			
HC1	1.35	1.44	1.72	1.07	1.44
HC2	1.64	1.55			

Table 6.5 Comparison of factors affecting turbulent flame speed for planar and kernel flames. s_t – turbulent flame speed, L_t – turbulent flame length, L – reference flame length. Superscripts H2 and CH4 refer to hydrogen-enriched and pure methane flames respectively. Time t = 0.8ms for both data sets.

Some interesting differences are apparent from the data in Table 6.5. For the unenriched flames a similar increase in s_t / s_L^0 is seen for both data sets, but for the H_2 enriched flames a significantly greater increase is seen for the kernel configuration. In addition a qualitative difference can be seen in the degree of flame wrinkling experienced by the enriched and unenriched kernels, where, in contrast to the planar flame, the enriched

kernel experiences slightly less wrinkling than the pure methane kernel. This difference can be explained by the competition between the effects of reduced thermal-diffusive stability of the enriched flame tending to increase flame wrinkling, and the faster response time of the enriched flame tending to reduce wrinkling. It appears that for the kernels, these effects broadly cancel out, however, a more detailed discussion is provided in Section 6.3.7.

By splitting the turbulent flame speed according to $s_t = I_0 s_L^0 L_t$, where I_0 accounts for the alteration to the laminar flame speed due to unsteady effects, it is found that values of I_0 for the planar and kernel flames are 1.06 and 1.46 respectively. This seems to imply a significant flame speed enhancement due to positive mean curvature for H_2 enriched flames. This enhancement can be ascribed to the preferential diffusion of the highly mobile H_2 atom into the reaction zone in areas of positive curvature causing an increase in the reaction rate of CH_4. This phenomenon has also been noted in the planar flame where a non-linearity is observed in the s_d - K_m relation in going from negative to positive curvature, so that s_d is less sensitive to reduction by positive curvature than negative. For the flame kernel, positive curvature is overwhelmingly more probable, and so the effect of H_2 addition is disproportionately greater. This appears to offer a convenient enhancement to flame stability for the growing kernel compared to the planar flame; in this case by a factor of 1.38.

6.3.6.2 Extinction and Quenching

The most obvious difference between the planar flame and kernel data is that the self sustained combustion exhibited by the planar flame in HC1 was not seen in the equivalent kernel flame A1, with the onset of quenching occurring at t $\approx$ 0.84ms^{-1}. Since all other parameters are similar, the cause of the quenching can be considered in purely geometric terms, i.e. attributable only to the presence of mean curvature.

With respect to extinction mechanisms, the kernel configuration contrasts with the planar flame in the following ways:

- Mean positive curvature reduces the mean displacement speed, thereby reducing the ability of the flame to respond to turbulent straining.
- The occurrence of regions of high positive curvature, associated with negative displacement speeds and radiative losses through flame thickening, becomes more probable due to the presence of the mean curvature.
- The occurrence of downstream interactions also becomes more probable due to the increased proximity of downstream regions under mean positive curvature.
- Thermal expansion due to confinement of the burnt gases will tend to push flame surfaces apart, thereby partially compensating for the mean curvature by reducing the probability of downstream interactions.
- At small kernel radii large eddies convect the entire kernel without causing straining of the flame surface. The effective turbulence intensity is therefore reduced at early times.

These competing, purely geometric, effects appear to have a net negative impact on the development of kernels compared to the equivalent planar flame, but in the case of the H_2 enriched kernel the beneficial thermo-diffusive effects more than compensate for this. Unfortunately it is not possible to draw more general, quantitative conclusions than this from a single simulation.

6.3.7 Effects of Turbulence Intensity

In Section 6.3.6 it was noted that the degree of wrinkling experienced by enriched and unenriched kernels was qualitatively different from the planar flames. In this section this finding is investigated further by considering the effects of the turbulence intensity on turbulent flame speed and wrinkling.

Figure 6.14 shows wrinkling factors L_t/L for all flames in the database. As before, the c = 0.1 isoline is used, but relatively little variation was found when other isolines were chosen.

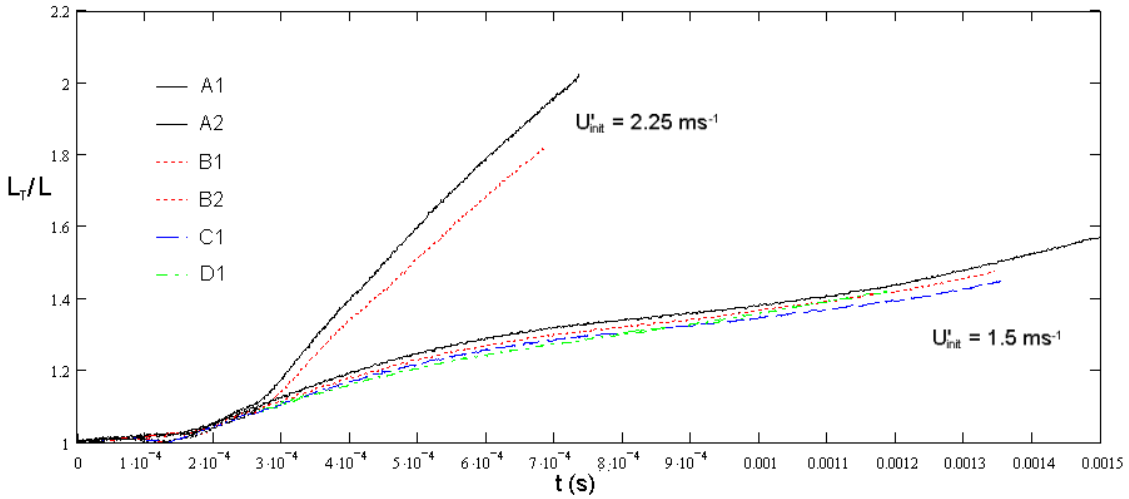

Figure 6.19 Wrinkling factors (L_T/L) for the c = 0.1 isolines. L_T is the total line length and L is the circumference of a circle with radius equal to the mean c = 0.1 isoline radius $R_{0.1}$.

The observation of reduced wrinkling for the enriched kernel is confirmed at the higher turbulence intensity, where the effect is even more pronounced. As discussed previously, for the lower intensity, the tendency towards decreased wrinkling due to shorter flame time scales appears to closely balance with the tendency towards increased wrinkling due to a reduced thermal-diffusive stability for the enriched flame. At higher equivalence ratios (Cases C1 and D1) a cross over is even observed in the wrinkling at t $\approx$ 0.9ms. At higher intensity however, the flame response time appears to be the dominant factor, leading to a greater reduction in wrinkling compared to the pure CH_4 flame.

A comparison of the enhancement of s_t due to turbulence intensity between the enriched and unenriched flames is only possible at relatively early times to avoid the effects of the quenching of the unenriched kernel. However, it is found that despite the lower degree of flame wrinkling for the enriched kernel, an increase in turbulence intensity causes a relatively larger increase in turbulent flame speed for the enriched kernel compared to the unenriched. This increase in turbulent flame speed can be quantified by the ratio s_t^2/s_t^1, where superscripts 1 and 2 refer to the lower and higher intensities respectively. At time t = 0.4ms the values of s_t^2/s_t^1 for the unenriched and enriched kernels are 1.17 and 1.32 respectively.

The reasons for this are, firstly, due to the increased response time of the enriched kernel resulting from the higher flame speed, and secondly, in regions of positive curvature, preferential diffusion of H_2 into the reaction zone enhances the reaction rate compared to the unenriched kernel. In addition to these effects, the faster growth of the enriched kernel means that its global convection by the larger eddies is reduced and it experiences a greater degree of straining. However, the difference due to this last effect, although present, is negligible over these time scales.

In connection to this last point it is also interesting to compare the global stretch rate histories of the kernel flames.

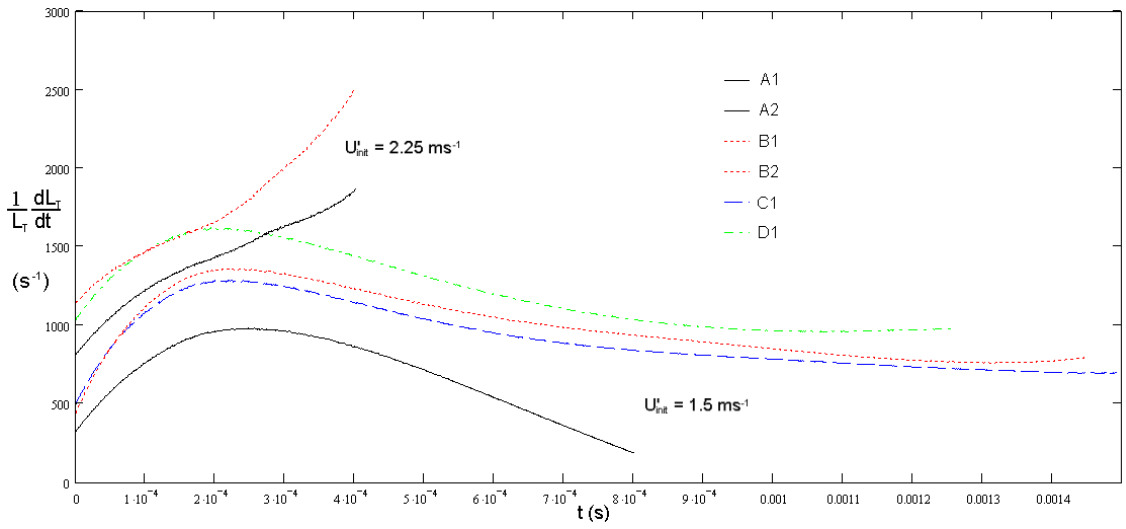

Figure 6.20 Global stretch rates for all cases calculated from the rate of change of isoline length per unit length of the c = 0.8 isoline.

The total stretch rate can be separated into contributions due to heat release, aerodynamic straining, and the combined effects of propagation and curvature.

For flame kernels that are small compared to the integral length scale these last two components are more closely coupled than in a planar flame for the reason described above: as the kernel expands it encounters more of the turbulent spectrum and hence experiences greater aerodynamic straining, but also a simultaneous reduction in the curvature-propagation term due to the lower mean curvature. Additionally, depending

on the effective Lewis number of the mixture, the same strain field will affect the curvature-propagation term in different ways through the response of displacement speed to tangential strain. This effect is also present in planar flames but is exaggerated by the high mean curvatures of kernels, and particularly so for the less thermo-diffusively stable enriched flames.

From inspection of Fig 6.20 it can be seen that during the early stages these two terms are of comparable magnitude. The initial values of cases A1 and B1, are separated only by the curvature-propagation term since the strain fields are essentially the same, and similarly for C1 and D1 which are shifted upwards due to the slightly higher density ratio ρ_u/ρ_b . Conversely, cases A1 compared to A2, and B1 compared to B2 differ only in the strain term at this point. The qualitative trends shown in Fig 6.20 are in agreement with previous DNS of expanding flame kernels [80].

Curvature-propagation terms, at the global level, are at a maximum at t = 0 and decline asymptotically to zero as the kernels expand. The initial rise in stretch for all cases can therefore be attributed to the increasing exposure to the turbulent scales. A maximum is reached when the kernel reaches a comparable size to largest turbulent scales, combined with the continually declining contribution from the curvature-propagation term. This is supported by the observation that the faster expanding kernels reach this turning point earlier in the simulation. For the higher intensity cases A2 and B2 a different turning point is observed due to the onset of quenching (not shown in Fig 6.20), which is marked by a steep decline in stretch rates due to negative net displacement speeds. This can also be seen beginning to occur in Case A1, causing its departure from the trends shown in B1, C1 and D1.

A quantitative comparison to the planar flame results of Hawkes and Chen [9] shows that similar stretch rates are reached after t $\approx$ 0.8ms for case B1, but that before this point the additional stretch due to curvature-propagation and heat release is significant, and so the total stretch reaches a maximum at t $\approx$ 0.2ms which is approximately twice that of the equivalent planar flame. In the planar flame it was also found that the net

contribution from curvature-propagation was negative because of the thermo-diffusively stable behaviour, where higher displacement speeds are associated with areas of negative curvature. In contrast, regions of negative curvature are less likely in the kernel configuration, and so negative curvature-propagation contributions of any significance only occur due to negative displacement speeds in areas of high positive curvature, which have comparatively less impact overall.

6.4 Summary

In this Chapter the flame kernel development of methane and hydrogen-enriched methane-air mixtures was investigated using two-dimensional simulations and a detailed 68-step chemical mechanism. Six cases were considered in total: at equivalence ratios close to the lean limit for methane-air, two turbulence intensities were investigated for kernels with and without the addition of a 30% fuel mole fraction of hydrogen. The substitution of hydrogen was also investigated at a higher equivalence ratio for the lowest turbulence intensity.

Different methods of evaluating the consumption and displacement speeds in multi-fuel flames were assessed. For the consumption speed the approach of Chen and Im [66] based on a weighted sum of all reacting species was found to be most suitable. And a displacement speed based on the methane mass-fraction isosurface was found to give the most consistent results compared to hydrogen.

For the turbulent kernel simulations the regime was identified as close to the Thickened-Wrinkled / Thickened Flame regime boundary according to Peters [3], and the Wrinkled Kernel regime according to Echekki and Kolera-Gokula [36]. However, the onset of quenching was under-predicted in this last case, possibly due to the neglect of the smaller scales of turbulence.

The response of the displacement speed and its reactive, normal and tangential components was examined with respect to strain and curvature for a pure methane-air

kernel. Good qualitative agreement was found with the existing literature. Differences were noted due to the increased likelihood of positive curvature combined with differential diffusion effects, which have not been captured in previous published studies.

The effects of hydrogen addition were examined by comparing H_2-enriched and pure-methane kernels, where the equivalence ratio of the pure methane kernel was chosen to eliminate as far as possible the strain field effects caused by a more rapidly expanding H_2-enriched kernel. An increase in the global turbulent flame speed and burnt gas mass-fraction of approximately 50% was found for H_2-enriched flames, attributable to thermo-diffusive effects alone.

Two mechanisms of flame quenching were identified – one due to negative displacement speeds in areas of high positive curvature, and a second due to interaction of the CO oxidation layers in the downstream flame regions. The second of these was found to be dominant, but with compounding effects due to the first.

A comparison with the planar flame simulations of Hawkes and Chen [9] was made. The turbulent flame speed enhancement in H_2-enriched flames is significantly greater for the kernels – by approximately 38% - while no significant difference between planar / kernel results was found for pure methane. Overall, the purely geometric effects of the kernel configuration had a net negative impact on flame development for non-enriched flames, but a net positive impact for H_2-enriched flames due to their reduced thermal-diffusive stability.

Finally, the effects of turbulence and turbulence intensity were assessed through the wrinkling factor and global stretch rate histories. The wrinkling of the H_2-enriched flames was found to be lower than for pure methane due to the faster flame response of the former. Despite this, the turbulent flame speed is higher for the H_2-enriched flame and a steeper increase in turbulent flame speed with turbulence intensity was also found. Total stretch rates were found to peak at twice the planar flame values due to the additional curvature-propagation contributions, but reached similar values at later times.

7 CONCLUSIONS AND FUTURE WORK

In this thesis the early stages of growth of laminar flame kernels during their transition to fully developed turbulent flames were investigated. The findings presented here offer new insights into the development and behaviour of kernels during these stages, both on a general level relating to the interaction of turbulence with the flame geometry, and more specifically on changes to the local flame response due to fresh gas composition. It is hoped that these findings contribute both to an improved understanding of flame kernels in general, and ultimately to more precise modelling and control of this stage in spark ignition devices.

Many more questions were raised in the course of this work than could be answered in the time available, and this was particularly true for the study into SDF bias presented in Chapter 5. Whilst it is clear that further investigation is required before a definitive analysis can be carried out, it was felt that to do this satisfactorily would have required a more extensive study than would have been possible with the time and resources available. The decision to migrate to the multi-step chemistry code SENGA2, at the expense of some consistency to the work, was therefore made partly for this reason and partly on an assessment of the recent trends in DNS research.

Historically, DNS has been concerned principally with reaching the highest possible Reynolds numbers, whilst assuming that chemical and diffusive processes are secondary to the fluid mechanics of the problem. This assumption is well founded, but has also been necessary simply to make the computations feasible. Despite these simplifications a great deal has been discovered through his approach, however, recent advances in computing power mean that realistic Reynolds numbers, and perhaps more importantly realistic Damkohler and Karlovitz numbers, are now achievable at a relatively low cost. So while higher Reynolds numbers will always be desirable, the emphasis has shifted recently towards incorporating greater chemical complexity and improved molecular transport models into the simulations in a move towards improved quantitative accuracy.

This shift comes from recognising that, at present, the real strength of DNS lies more in its use as a complement to experiment rather than its replacement, and that this might best be done through smaller-scale parametric sweeps rather than a single very large scale simulations. Although it should be noted that this doesn't necessarily alleviate the computational burden, only redistributes it, and so many of the same challenges remain.

The investigation into the turbulence-kernel interaction presented in Chapter 5 is an example of where this small-scale approach can be applied to good effect, although obviously the emphasis here is still on the fluid mechanical aspects.
The period of interest - following ignition and while the mean radius is still small - was realisable on a single-core processor in under a week, and so a form of simple parallelisation could be employed by executing multiple realisations for each parameter set to build ensemble statistics. This has two advantages: not only does it provide more reliable information on the major quantities such as turbulent flame speed and global heat release, but can also potentially reveal otherwise hidden effects. The differential surface velocities and SDF bias described in this study are just such effects, where, had the observations been made only from a single simulation, they would have had negligible statistical significance.

The results described in this part of the study are clearly only the first steps towards understanding these effects, and some uncertainties in the data remain. While every effort was made to reduce unwanted numerical effects in the DNS, it is never possible to eliminate these entirely. Ideally, a comparison with experimental data would provide the most reliable method of checking the validity of the DNS results, assuming, firstly that it is possible to obtain the quantities of interest from the experimental data, and also that a sufficient overlap of scales exists between the two methods to make a meaningful comparison. Recent publications [77,78] have already demonstrated this possibility, however, by extracting statistics of curvature and FSD from experimental flame kernel data and comparing these with the equivalent from DNS.

As suggested in §5.2.2, the connection between the differential isosurface velocity phenomenon and the FSD bias observed in the two-dimensional study is tentative at this

stage, and while experimental comparison might validate the results, it may not necessarily be capable of confirming a causal link. For this, a larger scale DNS study is also required, where the following issues should be considered: Firstly, a three-dimensional domain is essential in order to properly capture the cascade dynamics; energy transfer to the dissipation range sustains the effect over longer time scales and so must be present in the simulation. Secondly, the effects of the initial transients needs to be reduced as much as possible. The two major sources of these are from acoustic waves generated on and near the boundaries at start-up, and from the artificially high initial vorticity in the burnt gas region. The first, but possibly least important of these, is easily eliminated by allowing the initial field to evolve for a short period to allow acoustic activity to decay prior to initialising the flame kernel. The second is not so straightforward. Manipulating the spectral initialisation routine to produce more realistic turbulence in the burnt gas region is one possibility, where a modified energy spectrum – with longer integral length scales and reduced intensity - could be applied over a specified region of the domain corresponding to the burnt gases. However, the exact values for the modified spectrum would be difficult to ascertain, and in addition, the benefits may be lost if the flow is allowed to evolve to remove the acoustic transients as suggested above. A simpler method may be to initialise the turbulence as normal but to then impose a temperature field taken from the initial flame kernel data. With the temperature field fixed the flow could then be allowed to evolve without reaction or heat release until both the acoustic activity has decayed to an acceptable level, and the turbulence has adjusted to the higher kinematic viscosity in the burnt gas region. This evolved velocity field could then be superimposed on the pre-computed kernel data as before to initialise the full reacting flow simulation. While still only an approximation, this should ensure that any further adjustments during the initial stages have only a minimal impact on the results.

A final point to consider with regard to the suggested instability mechanism leading to the FSD bias is the effects of Lewis number variation. Flames with low effective Lewis numbers have a reduced thermo-diffusive stability which tends to lead to higher flame surface densities compared to unity and super-unity Lewis number flames. Their behaviour in relation to the measured surface velocity differentials and subsequent bias

in FSD, as well as being of general interest, would provide useful additional insight into any underlying hydrodynamic instability.

The sensitivity of the mean isosurface velocities to changes in the energy spectrum is highlighted by the results of the phenomenological model described in §5.1.5.1. In order to validate the underlying assumptions on which this model is based and to improve its predictive capacity, it is clearly necessary to obtain better information on the actual energy spectrum experienced by the kernel surfaces. Evaluating the energy spectrum directly from the reacting flow may not provide the relevant information since the effects of thermal expansion will be included in the velocity correlation tensor.
A possible alternative is to extract energy spectra from two separate non-reacting flow simulations with constant temperatures corresponding to the fresh gas and adiabatic flame temperatures respectively. Some linear combination of these two values could then be used in the model to estimate the mean surface velocities. However, a model requiring this level of detail will only ever be of theoretical interest; for practical purposes it would need to be based on more readily available quantities. From the results so far, the turbulent Reynolds number, laminar flame speed, heat release parameter, and possibly Lewis number seem likely candidates with which to search for some form of empirical relation. The ITNFS model of Meneveau and Poinsot [38] may be one possible approach. Although the concern here is the stretch induced on the flame surface by turbulent eddies, some of the same considerations apply such as the intermittency of the turbulence and the effectiveness of the eddies to distort the flame surface.

The implications of a bias in the FSD apply mainly to flame kernel modelling in IC engines. In cycle-resolved IC engine simulations, generally speaking, information on the FSD is passed to a turbulent flame model after a critical kernel size is reached in the preceding sub-model. If the distribution of FSD at this point is assumed to be uniform when in fact it is not, the time taken for the flame to reach important areas, such as the cylinder walls, will be mis-predicted and could potentially lead to errors in the estimated heat release. Even when the direction of the bias is unknown, as would be the case here,

a randomly assigned orientation would still provide a statistical improvement in accuracy.

A final point here is that the existence of a bias is not restricted to flames with spherical symmetry. In principle, the same effect should be seen in any flame configuration in which two conditions are met: 1) that the mean curvature in any direction is sufficiently high to cause a non-negligible difference in area or circumference on each isosurface, and 2) that the turbulence is sufficiently intense to ensure a range of scales of the order of the mean radius of curvature.
What constitutes negligible in the context of (1) is not clear at present, but would hopefully be revealed by larger scale studies or experimental work. An interesting example of a non-kernel flame that fulfils these criteria would be a turbulent Bunsen flame, where the different geometry means that some of specific issues affecting the kernel, such as flame surface expansion due to confinement of the burnt gases, are absent.

In the second part of this study attention was turned to the thermo-chemical behaviour of the kernels during the early stages. A different methodology was required here compared to the first part of the study due to the much more demanding computational requirements of including a detailed chemical mechanism. Each two-dimensional simulation required approximately three days of computation across 64 processors on a dedicated parallel processing cluster. Repeating the simulations was therefore not practical, and so the analysis was focussed mainly on a detailed account of the local flame behaviour, which ultimately determines the overall flame behaviour. While a comparison with planar flame results was made, it is accepted that without considering the possible statistical variation between realisations in either case, the conclusions are more susceptible to anomalous results and so must be interpreted with appropriate caution.

Possible methods of improving the results obtained here, as with DNS in general, fall into three competing categories: three-dimensionality, increased chemical complexity / molecular transport modelling, and statistical repetition.

The 68-step chemical mechanism used was more than adequate for the purposes of this study, and a simpler scheme would have resulted in only a small decrease in accuracy. However, once the reduction to two-dimensions has been accepted, the restrictions on the chemical mechanism are much reduced and some additional complexity may reasonably be retained. It was made clear in the first part of this study, however, that the three-dimensional aspects of the turbulence play an important role in flame kernel development, and that these may become more prominent for flames with a reduced thermo-diffusive stability as studied in Chapter 6. Since the computational overhead of an extra dimension is essentially fixed, the challenge therefore lies in representing the chemistry in sufficient detail but at a minimum computational cost.

Techniques such as ILDM and FGM involve making assumptions about the kinetics and flame structure that restrict their applicability to situations where the regime is not know in advance – in particular where extinction and flame interactions occur and the local chemistry may be far from that expected in a laminar flame. It appears necessary in these situations to retain the full, detailed scheme.

Under the present implementation it is noticeable that a considerable amount of computational effort is used to evaluate the species transport equations and chemical source terms over large parts of the domain where chemical activity is negligible. A strategy involving some form of zoning may therefore be more appropriate, where ILDM or similar could be applied in the low temperature regions of the domain while retaining the full detailed mechanism in areas surrounding the flame front.

In both parts of this study errors were introduced into the DNS solutions from approximation made at the domain boundaries, and this was mainly as a result of deficiencies in the NSCBC implementation. The effects are particularly noticeable in the changes to the turbulence length scales and kinetic energy in the two-dimensional domains as described in Section 6.3.2 which tends to exaggerate the differences between two and three dimensional turbulence. Providing the kernel remains far from the boundaries these errors do not affect the qualitative behaviour of the flame, nevertheless it is clearly desirable to minimise them as much as possible - to provide better quantitative accuracy, or simply to allow longer useful simulation times. Recently, Prosser [130,131] has suggested improvements to the NSCBC conditions

which allows the incoming acoustic wave amplitude variation to be specified directly from the outgoing wave amplitude by filtering out the acoustic component of the flow divergence, thereby preventing the pressure oscillations normally associated with this approach. Additionally, viscous and heat flux terms are included in the characteristic analysis and so may be applied in a more consistent manner than in the current configuration. Incorporating these conditions into the present code may provide some useful improvements to the accuracy and stability of the solutions, although it should be noted that their implementation in a three-dimensional multi-component flow, and their compatibility with the inclusion of source terms as suggested by Sutherland and Kennedy [122], has not yet been established.

The results presented in Chapter 6 demonstrate the importance of the chemistry on the overall behaviour of the kernel during these stages. In particular, the effects of hydrogen addition on the response of the flame to turbulence, both in the increased turbulent flame speed and resistance to local quenching, are not predictable from straightforward extrapolation of planar flame data, or from simplified chemistry simulations. And as the need to reduce emissions and explore a greater range of fuel types continues, understanding the behaviour of these flames at a fundamental level will be crucial in developing accurate models for IC engine simulations. The current simulations were all carried out at atmospheric conditions of pressure and temperature, and an interesting extension to this work would be to repeat the study at conditions more representative of those found in an engine cylinder at the point of ignition. The changes to the length scales and flame speeds found under these conditions are likely to have a considerable quantitative effect on the results.

With respect to hydrogen addition, it has been suggested that to avoid some of the storage issues associated with using twin fuels, the hydrogen may be generated by onboard reforming of methane [132]. The resulting fresh gas mixture contains significant quantities of carbon monoxide, carbon dioxide and water vapour in addition to the methane and hydrogen, and so it would be useful to examine the effect these have on turbulent flame behaviour.

Finally, while the work here has been presented in two largely independent parts, the two aspects are closely related in reality, and so an obvious question remains on the implications that each of the parts have for each other.

The presence of an SDF bias and possible hydrodynamic instability could have very different outcomes depending on the thermo-diffusive behaviour of the kernel. Simply adjusting the effective Lewis number, as suggested above, would not necessarily capture this. For instance, low Lewis numbers are known from theory and experiment to promote wrinkling in turbulent flames under most conditions (moderate intensities), but from the present results it has been found that the wrinkling is actually reduced for hydrogen-enriched flame kernels at the same equivalence ratio due to the increased flame speed. Conversely, the potential existence of an SDF bias in the complex chemistry simulations may have contributed to the enhanced turbulent flame speeds and resistance to quenching observed in the enriched flames, or even reduced these properties in the pure methane flames.

It is in this middle ground that the current limitations of DNS are made clear, but through the development of more efficient implementations combined with the continuing growth in computing power, some of these answers may soon be within reach.

REFERENCES

[1] JB Heywood, Combustion and its Modeling in Spark Ignition Engines, International Conference on Modeling and Diagnostics for Advanced Engine systems (COMODIA) (1994) 1.

[2] A Borghese, M Diana, V Mocia, R Tamai. Early Growth of Flames Ignited by Fast Sparks, Combustion Science. and Technology. 76 (1991) 219-231.

[3] N Peters, Turbulent Combustion, Cambridge University Press, Cambridge, UK, (2000)

[4] J Warnatz, U Maas, RW Dibble, Combustion: Physical and Chemical Fundamentals, Modeling, Simulation, Experiments, Pollutant Formation, 4th ed., Springer (2006).

[5] T Poinsot, D Veynante, Theoretical and Numerical Combustion, 2nd ed. RT Edwards (2005).

[6] A Brandl, M Pfitzner, JD Mooney, B Durst, W Kern. Comparison of Combustion Models and Assessment of Their Applicability to the Simulation of Premixed Turbulent Combustion in IC-Engines. Flow, Turbulence and Combustion 75 (2005) 335-350.

[7] GRI-Mech 3.0, `http://www.me.berkeley.edu/gri_mech/`.

[8] CG Bauer, TW Forest. Effect of hydrogen addition on the performance of methane-fuelled vehicles. Part I: effect on S.I. engine performance. International Journal of Hydrogen Energy. 26 (2001) 55-70.

[9] ER Hawkes, JH Chen. Direct numerical simulation of hydrogen-enriched lean premixed methane–air flames. Combustion and Flame. 138 (2004) 242-258.

[10] CK Law, Combustion Physics. Cambridge University Press, New York, USA, 2006.

[11] FA Williams, Combustion Theory, 2nd ed., The Benjamin/Cummings Publishing Company, Inc, USA, 1985.

[12] CR Wilke. A Viscosity Equation for Gas Mixtures. Journal of Chemical Physics 18 (1950) 517.

[13] A Ern, V Giovangigli. Kinetic Theory of Reactive Gas Mixtures with Application to Combustion. Transport Theory and Statistical Physics. 32 (2003) 657.

[14] A Lipatnikov, J Chomiak. Molecular transport effects on turbulent flame propagation and structure. Progress in Energy and Combustion Science. 31 (2005) 1.

[15] A Ern, V Giovangigli. Impact of Detailed Multicomponent Transport on Planar and Counterflow Hydrogen/Air and Methane/Air Flames. Combustion Science and Technology. 149 (1999) 157.

[16] R Hilbert, F Tap, H El-Rabii, D Thevenin. Impact of detailed chemistry and transport models on turbulent combustion simulations. Progress in Energy and Combustion Science. 30 (2004) 61.

[17] SB Pope, The evolution of surfaces in turbulence. International Journal of Engineering Science. 26 (1988) 445-469.

[18] CK Law, DL Zhu, G Yu, Propagation and Extinction of Stretched Premixed Flames. Proceedings of the Twenty-First Symposium (International) on Combustion. (1986) 1419-1426.

[19] G Yu, CK Law, CK Wu. Laminar Flame Speeds of Hydrocarbon + Air Flames with Hydrogen Addition. Combustion and Flame. 63 (1986) 339-347.

[20] C Mandilas, MP Ormsby, CGW Sheppard, R Woolley. Effects of hydrogen addition on laminar and turbulent premixed methane and iso-octane–air flames, Proceedings of the Combustion Institute 31 (2007) 1443-1450.

[21] GS Jackson, R Sai, JM Plaia, CM Boggs, KT Kiger. Influence of H2 on the response of lean premixed CH4 flames to high strained flows. Combustion and Flame. 132 (2003) 503-511.

[22] R Sankaran, H Im. Effects of hydrogen addition on the Markstein length and flammability limit of stretched methane/air premixed flames. Combustion Science and Technology. 178 (2006) 1585-1611.

[23] FN Egolfopoulos, Dynamics and structure of unsteady, strained, laminar, premixed flames. Proceedings of the Twenty-Fifth Symposium (International) on Combustion. (1994) 1365-1373.

[24] CJ Sung, CK Law. Structural Sensitivity, Response, and Extinction of Diffusion and Premixed Flames in Oscillating Counterflow. Combustion and Flame. 123 (2000) 375-388.

[25] AN Kolmogorov. The local structure of turbulence in incompressible viscous fluid for very large Reynolds numbers, Dokl. Akad. Nauk SSSR. 30(4) (1941). (English translation in Proceedings of the Royal Society London A. 434 (1991) 9-13).

[26] SB Pope, Turbulent Flows. Cambridge University Press, Cambridge, UK, 2003.

[27] PA Davidson, Turbulence. Oxford University Press, Oxford, 2004.

[28] GK Batchelor, AA Townsend, Decay of turbulence in the final period. Proceedings of the Royal Society of London. A194 (1948) 527-543.

[29] U Schumann, GS Patterson. Numerical study of pressure and velocity fluctuations in nearly isotropic turbulence. Journal of Fluid Mechanics. 88 (1978) 685-709.

[30] RS Cant, C Rutland, A Trouve, Statistics for laminar Flame Modelling. Proceedings of the Summer Program 1990, Center for Turbulence Research. (1990) 271-279.

[31] G Damkohler. The effect of turbulence on the flame velocity in gas mixtures. Z. Electrochemie und angewandte Physikalische Chemie. 46 (1940) 601-626.

[32] FA Williams, Recent advances in theoretical descriptions of turbulent diffusion flames. In: S. N. B. Murthy (Ed.) Turbulent mixing in nonreactive and reactive flows, Project Squid Workshop (1975) 202-208.

[33] N Peters, P Terhoeven, JH Chen, T Echekki, Statistics of flame displacement speeds from computations of 2D unsteady methane-air flames, Proceedings of the Twenty-Seventh Symposium (international) on Combustion. (1998) 833.

[34] T Poinsot, S Candel, A Trouve, Applications of direct numerical simulations to premixed turbulent combustion. Progress in Energy and Combustion Science. 21 (1996) 531-576.

[35] PH Renard, D Thevenin, JC Rolon, S Candel, Dynamics of flame / vortex interactions. Progress in Energy and Combustion Science. 26 (2000) 225-282.

[36] T Echekki, H Kolera-Gokula. A regime diagram for premixed flame kernel-vortex interactions. Physics of Fluids. 19 (2007).

[37] DA Eichenberger, WL Roberts. Effect of Unsteady Stretch on Spark-Ignited Flame Kernel Survival. Combustion and Flame. 118 (1999) 469-478.

[38] C Meneveau, T Poinsot. Stretching and Quenching of Flamelets in Premixed Turbulent Combustion. Combustion and Flame. 86 (1991) 311-332.

[39] M Dusing, A Sadiki, J Janika. Towards a classification of models for the numerical simulation of premixed combustion based on a generalized regime diagram. Combustion Theory and Modelling. 10 (2006) 105-132.

[40] T Echekki, JH Chen. Analysis of the Contribution of Curvature to Premixed Flame Propagation. Combustion and Flame. 118 (1999) 308-311.

[41] D Veynante, L Vervisch, Turbulent Combustion Modeling, in: Vervisch L, Veynante D, van Beek JPAJ (Eds.), Turbulent Combustion, von Karman Institute for Fluid Dynamics, Belgium, 2005, pp. 1-175.

[42] O Gulder, Contribution of small scale turbulence to burning velocity of flamelets in the thin reaction zone regime. Proceedings of the Combustion Institute 31. (2007).

[43] O Gulder, GJ Smallwood. Flame surface densities in premixed combustion at medium to high turbulence intensities. Combustion Science and Technology. 179 (2007) 191-206.

[44] H Guo, Y Ju, K Maruta, T Niioka. Radiation Extinction Limit of Counterflow Premixed Lean Methane-Air Flames. Combustion and Flame. 109 (1997) 639-646.

[45] H Guo, GJ Smallwood, F Liu, Y Ju, O Gulder. The effect of hydrogen addition on flammability limit and NOx emission in ultra-lean counterflow CH4/air premixed flames. Proceedings of the Combustion Institute 30 (2005) 303-311.

[46] KNC Bray, JB Moss. A unified statistical model of the premixed turbulent flame. Acta Astronautica. 4 (1977) 291-319.

[47] D Veynante, L Vervisch, Turbulent combustion modeling. Progress in Energy and Combustion Science. 28 (2002) 193-266.

[48] KNC Bray, PA Libby, JB Moss. Flamelet crossing frequencies and mean reaction rates in premixed turbulent combustion. Combustion Science and Technology. 41 (1984) 143-172.

[49] ER Hawkes, JH Chen, Comparison of direct numerical simulation of lean premixed methane-air flames with strained laminar flame calculations. Combustion and Flame. 144 (2006) 112-125.

[50] FC Gouldin, KNC Bray, J Chen. Chemical closure model for fractal flamelets. Combustion and Flame. 77 (1989) 241-259.

[51] E Giacomazzi, C Bruno, B Favini, Fractal modelling of turbulent combustion. Combustion Theory and Modelling. 4 (2000) 391-412.

[52] FE Marble, JE Broadwell, The coherent flame model for turbulent chemical reactions. Project Squid Technical Report TRW-9-PU (1977).

[53] S Candel, T Poinsot . Flame stretch and the balance equation for the flame area. Combustion Science and Technology. 70 (1990) 1-15.

[54] RS Cant, SB Pope, KNC Bray, Modelling of the flamelet surface-to-volume ratio in turbulent premixed combustion. Proceedings of the Twenty-Third Symposium (international) on Combustion. (1990) 809-815.

[55] M Boger, D Veynante, H Boughanem, A Trouve, Direct numerical simulation analysis of flame surface density concept for large eddy simulation of turbulent premixed combustion. Proceedings of the Twenty-Seventh Symposium (international) on Combustion. (1998) 917-925.

[56] JM Duclos, D Veynante, T Poinsot . A Comparison of Flamelet Models for Premixed Turbulent Combustion. Combustion and Flame. 95 (1993) 101-117.

[57] FA Williams, Turbulent Combustion, in: Buckmaster J (Ed.), The mathematics of combustion, SIAM, Philadelphia, 1985, pp. 97-131.

[58] T Echekki, JH Chen. Unsteady Strain Rate and Curvature Effects in Turbulent Premixed Methane-Air Flames. Combustion and Flame. 106 (1996) 184-202.

[59] JH Chen, H Im, Correlation of flame speed with stretch in turbulent premixed methane/air flames. Proceedings of the Twenty-Seventh Symposium (international) on Combustion. (1998) 819-826.

[60] SB Pope. PDF methods for turbulent reactive flows. Progress in Energy Combustion Science 11 (1985) 119-192.

[61] DB Spalding, Mixing and Chemical Reaction in Steady Confined Turbulent Flames, Proceedings of the thirteenth (International) Symposium on Combustion (1971) 649-657.

[62] C Rutland, A Trouve. Direct Simulations of Premixed Turbulent Flames with Nonunity Lewis Numbers. Combustion and Flame. 94 (1993) 41-57.

[63] M Baum, T Poinsot , DC Haworth, N Darabiha. Direct Numerical Simulation of H2/O2/N2 flames with Complex Chemistry in Two-Dimensional Turbulent Flows. Journal of Fluid Mechanics. 281 (1994) 1-32.

[64] DC Haworth, T Poinsot . Numerical Simulations of Lewis Number Effects in Turbulent Premixed Flames. Journal of Fluid Mechanics 244 (1992) 405-436.

[65] N Chakraborty, N Swaminathan. Influence of the Damköhler number on turbulence-scalar interaction in premixed flames. I. Physical insight. Physics of Fluids. 19 (2007).

[66] JH Chen, H Im, Stretch effects on the burning velocity of turbulent premixed hydrogen/air flames. Proceedings of the Twenty-Eighth Symposium (International) on Combustion. (2000) 211-218.

[67] N Chakraborty, RS Cant, Unsteady effects of strain rate and curvature on turbulent premixed flames in an inflow-outflow configuration. Combustion and Flame. 137 (2004) 129-147.

[68] N Chakraborty, RS Cant. Influence of Lewis number on curvature effects in turbulent premixed flame propagation in the thin reaction zones regime. Physics of Fluids. 17 (2005).

[69] ER Hawkes, JH Chen, Evaluation of models for flame stretch due to curvature in the thin reaction zones regime. Proceedings of the Combustion Institute 30 (2005) 647-655.

[70] JB Bell, MS Day, JF Grcar, Numerical Simulation of Turbulent Premixed Methane Combustion. Proceedings of the Combustion Institute 29 (2003) 1987-1993.

[71] A Lipatnikov, J Chomiak. Turbulent Burning Velocity and Speed of Developing, Curved, and Strained Flames. Proceedings of the Combustion Institute 29 (2002) 2113-2121.

[72] KW Jenkins, M Klein, N Chakraborty, RS Cant, Effects of strain rate and curvature on the propagation of a spherical flame kernel in the thin-reaction-zones regime. Combustion and Flame. 145 (2006) 415-434.

[73] N Chakraborty, M Klein, RS Cant. Stretch rate effects on displacement speed in turbulent premixed flame kernels in the thin reaction zones regime. Proceedings of the Combustion Institute 31 (2007) 1385-1392.

[74] M Klein, N Chakraborty, KW Jenkins, RS Cant. Effects of Initial Radius on the Propagation of Premixed Flame Kernels in a Turbulent Environment. Physics of Fluids. 18 (2006).

[75] B Renou, A Boukhalfa, D Puechberty, M Trinite, Effects of stretch on the local structure of freely propagating premixed low-turbulence flames with various Lewis numbers. Proceedings of the Twenty-Seventh Symposium (international) on Combustion. (1998) 841-847.

[76] CF Kaminski, J Hult, M Alden, S Lindenmaier, A Dreizler, U Maas, M Baum, Spark ignition of turbulent methane/air mixtures revealed by time-resolved planar laser-induced fluorescence and direct numerical simulations. Proceedings of the Twenty-Eighth Symposium (international) on Combustion (2000) 399.

[77] S Gashi, J Hult, KW Jenkins, N Chakraborty, S Cant, CF Kaminski, Curvature and wrinkling of premixed flame kernels - comparisons of OH PLIF and DNS data. Proceedings of the Combustion Institute 30 (2005) 809-817.

[78] J Hult, S Gashi, N Chakraborty, M Klein, KW Jenkins, RS Cant, et al. Measurement of flame surface density for turbulent premixed flames using PLIF and DNS. Proceedings of the Combustion Institute 31 (2007) 1319-1326.

[79] JA van Oijen, RJM Bastiaans, GRA Groot, LPH de Goey, Direct numerical simulations of premixed turbulent flames with reduced chemistry: validation and analysis. Flow, Turbulence and Combustion. 75 (2005) 67-84.

[80] D Thevenin, Three-dimensional direct simulations and structure of expanding turbulent methane flames. Proceedings of the Combustion Institute. 30 (2005) 629-637.

[81] K Tanoue, F Shimada, T Ai, H Kido, A Study on Turbulent Combustion Properties of Spherically Propagating Methane Flames, The Fifth International Symposium on Diagnostics and Modeling of Combustion in Internal Combustion Engines (COMODIA) (2001).

[82] RG Abdel-Gayed, KJ Al-Khishali, D Bradley. Turbulent Burning Velocities and Flame Straining in Explosions. Proceedings of the Royal Society London A. 391 (1984) 393-414.

[83] RG Abdel-Gayed, D Bradley, M Lawes. Turbulent burning velocities: a general correlation in terms of straining rates. Proceedings of the Royal Society London A 414 (1987) 389-413.

[84] A Lipatnikov, J Chomiak, Global stretch effects in premixed turbulent combustion. Proceedings of the Combustion Institute 31 (2007).

[85] D Bradley, MZ Haq, RA Hicks, T Kitagawa, M Lawes, CGW Sheppard, et al. Turbulent burning velocity, burned gas distribution, and associated flame surface definition. Combustion and Flame. 133 (2003) 415-430.

[86] SB Pope, WK Cheng, Statistical calculations of spherical turbulent flames. Proceedings of the Twenty-First Symposium (International) on Combustion. (1996) 1473.

[87] GP Beretta, M Rashidi, JC Keck. Turbulent flame propagation and combustion in spark ignition engines. Combustion and Flame. 52 (1983) 217-245.

[88] SB Pope, PK Yeung, SS Girimaji. The Curvature of Material Surfaces in Isotropic Turbulence. Physics of Fluids A. 1 (1989).

[89] M Tanahashi, Y Nada, S Tsukinara, T Saitoh, T Miyauchi. Local flame structure of turbulent premixed flames - DNS and CH/OH PLIF. Proceedings of the Fourth Symposium on Smart Control of Turbulence. (2003).

[90] M Tanahashi, S Kikuta, N Shiwaku, S Kato, S Inoue, S Taka, T Miyauchi, Turbulent combustion controls based on local flame structure. Proceedings of the Sixth Symposium on Smart Control of Turbulence (2005).

[91] D Thevenin, O Gicquel, J de Charentenay, R Hilbert, D Veynante, Two-versus three-dimensional direct simulations of turbulent methane flame kernels using realistic chemistry. Proceedings of the Combustion Institute. 29 (2003) 2031-2039.

[92] RR Maly, M Vogel, Initiation and propagation of flame fronts in lean CH4-air mixtures by the three modes of the ignition spark**.** Proceedings of the Seventeenth Symposium (International) on Combustion. (1978) 821-831.

[93] T Mantel. Three Dimensional Study of Flame Kernel Formation Around a Spark Plug. SAE Transactions 101 (1992) 1087.

[94] L Fan, RD Reitz. Development of an Ignition and Combustion Model for Spark-Ignition Engines. SAE Transactions 109 (2000) 1977.

[95] Z Tan, RD Reitz. Modeling Ignition and Combustion in Spark-ignition Engines Using a Level Set Method. SAE Transactions 112 (2003) 1028.

[96] Z Tan, RD Reitz. An ignition and combustion model based on the level-set method for spark ignition engine multidimensional modeling. Combustion and Flame. 145 (2006) 1-15.

[97] J Duclos, O Colin, Arc and kernel tracking ignition model for 3D spark ignition engine calculations. International Symposium on Diagnostics and Modeling of Combustion in Internal Combustion Engines (COMODIA) (2001).

[98] J Xu, F Behrendt, J Warnatz, 2D-LIF Investigation of the early stages of flame kernel development during spark ignition, International Symposium on Diagnostics and Modeling of Combustion in Internal Combustion Engines (COMODIA) (1994) 69.

[99] R Herweg, RR Maly. A Fundamental Model for Flame Kernel Formation in S.I. Engines. SAE Transactions 101 (1992) 1947.

[100] J Ewald, N Peters, On unsteady premixed turbulent burning velocity prediction in internal combustion engines. Proceedings of the Combustion Institute 31 (2007).

[101] U Maas, SB Pope. Simplifying Chemical Kinetics: Intrinsic Low Dimensional Manifolds in Composition Space. Combustion and Flame. 88 (1992) 239-264.

[102] JA van Oijen, LPH de Goey. Modelling of premixed counterflow flames using the flamelet-generated manifold method. Combustion Theory and Modelling. 6 (2002) 463-478.

[103] JA van Oijen, RJM Bastiaans, LPH de Goey, Low-Dimensional Manifolds in Direct Numerical Simulations of Premixed Turbulent Flames. Proceedings of the Combustion Institute 31 (2007).

[104] B Yang, SB Pope. Treating Chemistry in Combustion with Detailed Mechanisms--In Situ Adaptive Tabulation in Principal Directions--Premixed Combustion. Combustion and Flame. 112 (1998) 85-112.

[105] O Gicquel, N Darabiha, D Thevenin. Laminar premixed hydrogen/air counterflow flame simulations using flame prolongation of ILDM with differential diffusion. Proceedings of the Twenty-Eighth Symposium (international) on Combustion (2000) 1901-1908.

[106] CM White, RR Steeper, AE Lutz. The hydrogen-fuelled internal combustion engine: a technical review. International Journal of Hydrogen Energy 31 (2006) 1292-1305.

[107] C Cohe, F Halter, C Chauveau, I Gokalp, Fractal characterisation of high-pressure and hydrogen-enriched CH4-air turbulent premixed flames. Proceedings of the Combustion Institute 31 (2007).

[108] V Di Sarli, A Di Benedetto. Laminar burning velocity of hydrogen–methane/air premixed flames. International Journal of Hydrogen Energy 32 (2007) 637-646.

[109] JY Ren, W Qin, FN Egolfopoulos, H Mak, TT Tsotsis. Methane reforming and its potential effect on the efficiency and pollutant emissions of lean methane-air combustion. Chemical Engineering Science. 56 (2001) 1541-1549.

[110] F Halter, C Chauveau, I Djebaili-Chaumeix, I Gökalp. Characterization of the effects of pressure and hydrogen concentration on laminar burning velocities of methane–hydrogen–air mixtures. Proceedings of the Combustion Institute 30 (2005) 201-208.

[111] F Halter, C Chauveau, I Gökalp. Characterization of the effects of hydrogen addition in premixed methane/air flames. International Journal of Hydrogen Energy 32 (2007) 2585-2592.

[112] F Ma, Y Wang, L Haiquan, Y Li, J Wang, S Zhao. Experimental study on thermal efficiency and emission characteristics of a lean burn hydrogen enriched natural gas engine. International Journal of Hydrogen Energy 32 (2007) 5067-5075.

[113] AA Wray, Minimal storage time-advancement schemes for spectral methods, Unpublished Report, NASA Ames Research Center, California, USA. (1990).

[114] T Poinsot, SK Lele, Boundary conditions for direct simulations of compressible viscous flows. Journal of Computational Physics. 101 (1992) 104-129.

[115] KW Thompson. Time dependent boundary conditions for hyperbolic systems. Journal of Computational Physics 68 (1987) 1-24.

[116] SA Orszag. Numerical methods for the simulation of turbulence. The Physics of Fluids Supplement II, American Institute of Physics. 12 (1969) 250-257.

[117] RS Rogallo, Numerical experiments in homogeneous turbulence, NASA-TM-81315 (1981).

[118] FN Egolfopoulos. Geometric and Radiation Effects on Steady and Unsteady Strained Laminar Flames. Proceedings of the Twenty-Fifth Symposium (International) on Combustion. 25 (1994) 1375-1381.

[119] Y Ju, H Guo, K Maruta, F Liu. On the extinction limit and flammability limit of non-adiabatic stretched methane-air premixed flames. Journal of Fluid Mechanics 342 (1997) 315-334.

[120] CL Tien, Radiative Properties of Gases, Advances in Heat Transfer, Academic Press, New York, 1968, pp. 253-324.

[121] CA Kennedy, MH Carpenter, RM Lewis. Low-storage, explicit Runge–Kutta schemes for the compressible Navier–Stokes equations. Applied Numerical Mathematics. 35 (2000) 177-219.

[122] JC Sutherland, CA Kennedy. Improved boundary conditions for viscous, reacting, compressible flows. Journal of Computational Physics 191 (2003) 502–524. 191 (2003) 502-524.

[123] IR Gran, T Echekki, JH Chen, negative flame speed in an unsteady 2D premixed flame: a computational study. Proceedings of the Twenty-Sixth Symposium (international) on Combustion. (1996) 323.

[124] Softpredict, COSILAB, 2.1.0 (2007).

[125] A Laverdant, D Thevenin, Direct numerical simulation of a Gaussian a acoustic wave interaction with a turbulent premixed flame. Comptes Rendus Mecanique. 333 (2005) 29-37.

[126] P Boudier, S Henroit, T Poinsot , T Baritaud, A Model for Turbulent Flame Ignition and Propagation in Spark Ignition Engines. Proceedings of the Twenty-Fourth Symposium (International) on Combustion (1992) 503.

[127] C Morley, Gaseq, 0.79.

[128] R Sankaran, ER Hawkes, JH Chen, Structure of a Spatially-Developing Turbulent Lean Methane-Air Bunsen Flame. Proceedings of the Combustion Institute 30 (2007).

[129] KW Jenkins, RS Cant, Curvature effects on flame kernels in a turbulent environment. Proceedings of the Combustion Institute. 29 (2002) 2023-2029.

[130] R Prosser. Improved boundary conditions for the direct numerical simulation of turbulent subsonic flows. I. Inviscid flows. Journal of Computational Physics 207 (2005) 736-768.

[131] R Prosser. Towards improved boundary conditions for the DNS and LES of turbulent subsonic flows. Journal of Computatioanl Physics 222 (2007) 469-474.

[132] P Han, MD Checkel, BA Fleck. Hydrogen from reformer gas a novel fuel and bridging technology: A combustion perspective. International Journal of Hydrogen Energy. 32 (2007) 1416-1420.

APPENDIX 1:

68-STEP METHANE-AIR REACTION MECHANISM

Warnatz (1981) reduced methane-air mechanism incorporating C_1 chemistry. Taken from compiled rate data for hydrocarbon-air flames including C_3 chemistry (available in: Peters, N. & Rogg, B. (eds.); 'Reduced Kinetic Mechanisms for Applications in Combustion Systems'. Springer Verlag, 1993).

Species no.	Species Symbol	Name	Molecular Weight	Lewis Number	Third Body Effieciency
1	CH4	methane	16	0.97	6.50
2	O2	oxygen	32	1.11	0.40
3	CO2	carbon dioxide	44	1.39	1.50
4	H2O	water vapour	18	0.83	6.50
5	H2	hydrogen	2	0.30	1.00
6	O	oxygen atom	16	0.70	1.00
7	OH	hydroxyl radical	17	0.73	1.00
8	H	hydrogen atom	1	0.18	1.00
9	HO2	radical	33	1.10	1.00
10	H2O2	radical	34	1.12	1.00
11	CO	carbon monoxide	28	1.10	0.75
12	CH2O	radical	30	1.28	1.00
13	HCO	radical	29	1.27	1.00
14	CH2OH	radical	31	1.00	1.00
15	CH3OH	radical	32	1.00	1.00
16	CH3	methyle radical	15	1.00	1.00
17	CH3O	methoxy radical	31	1.30	1.00
18	N2	nitrogen	28	1.00	0.40

Table 6 Species list

Step Number	Reaction	A (cm^3/ mole s K^n)	n	E (J/mole)
1	O2 + H == O + OH	2.000E+11	0.00E+00	7.0313E+07
2	H2 + O == OH +H	5.060E+01	2.67E+00	2.6306E+07
3	H2 +OH == H2O +H	1.000E+05	1.60E+00	1.3804E+07
4	OH +OH == H2O +O	1.500E+06	1.14E+00	4.1994E+05
5	H + H + M == H2 +M	1.800E+12	-1.00E+00	0.0000E+00
6	O + O + M == O2 +M	2.900E+11	-1.00E+00	0.0000E+00
7	OH + H + M == H2O +M	2.200E+16	-2.00E+00	0.0000E+00
8	O2 + H + M == HO2 +M	2.300E+12	-8.00E-01	0.0000E+00
9	H + HO2 == 2 OH	1.500E+11	0.00E+00	4.1994E+06
10	H + HO2 == O2 + H2	2.500E+10	0.00E+00	2.9006E+06
11	H + HO2 == H2O + O	3.000E+10	0.00E+00	7.2013E+06
12	O + HO2 == O2 +OH	1.800E+10	0.00E+00	-1.6998E+06
13	OH + HO2 == O2 +H2O	6.000E+10	0.00E+00	0.0000E+00
14	HO2 + HO2 == O2 +H2O2	2.500E+08	0.00E+00	-5.2000E+06
15	OH + OH + M == H2O2 +M	3.250E+16	-2.00E+00	0.0000E+00
16	H + H2O2 == H2 + HO2	1.700E+09	0.00E+00	1.5705E+07
17	H + H2O2 == H2O +OH	1.000E+10	0.00E+00	1.5005E+07
18	O + H2O2 == OH + HO2	2.803E+10	0.00E+00	2.6804E+07
19	OH + H2O2 == H2O + HO2	5.400E+09	0.00E+00	4.1994E+06
20	OH + CO == CO2 +H	6.000E+03	1.50E+00	-3.1024E+06
21	HO2 + CO == CO2 + OH	1.500E+11	0.00E+00	9.8750E+07
22	O +CO + M == CO2 + M	7.100E+07	0.00E+00	-1.9004E+07
23	O2 + CO == CO2 +O	2.500E+09	0.00E+00	2.0004E+08
24	HCO + M == H + CO + M	7.100E+11	0.00E+00	7.0313E+07
25	H + HCO == H2 + CO	9.000E+10	0.00E+00	0.0000E+00
26	O + HCO == OH + CO	3.000E+10	0.00E+00	0.0000E+00
27	O + HCO == CO2 + H	3.000E+10	0.00E+00	0.0000E+00
28	OH + HCO == H2O + CO	1.000E+11	0.00E+00	0.0000E+00
29	O2 + HCO == HO2 + CO	3.000E+09	0.00E+00	0.0000E+00
30	HCO + HCO == CO + CH2O	3.000E+10	0.00E+00	0.0000E+00
31	CH2O + M == H + HCO + M	5.000E+13	0.00E+00	3.2006E+08
32	H + CH2O == H2 + HCO	2.300E+07	1.05E+00	1.3703E+07
33	O + CH2O == OH + HCO	4.150E+08	5.70E-01	1.1602E+07
34	OH + CH2O == H2O + HCO	3.400E+06	1.20E+00	-1.9004E+06
35	HO2 + CH2O == H2O2 + HCO	3.000E+09	0.00E+00	0.0000E+00
36	CH2O + CH3 == CH4 + HCO	1.000E+08	0.00E+00	2.5505E+07
37	O2 + CH2O == HO2 + HCO	6.000E+10	0.00E+00	1.7073E+08
38	H + CH3 == CH4	1.930E+33	-7.00E+00	3.8007E+07
39	O + CH3 == H + CH2O	8.430E+10	0.00E+00	0.0000E+00
40	OH + CH3 => H + CH3O	2.260E+11	0.00E+00	6.4812E+07
41	H + CH3O => OH + CH3	4.750E+13	-1.30E-01	8.8016E+07
42	O2 + CH3 => OH + CH2O	3.300E+08	0.00E+00	3.7409E+07
43	HO2 + CH3 == OH + CH3O	1.800E+10	0.00E+00	0.0000E+00
44	HO2 + CH3 == CH4 + O2	3.600E+09	0.00E+00	0.0000E+00
45	CH3O + M == H + CH2O + M	5.000E+10	0.00E+00	1.0502E+08
46	H + CH3O == H2 + CH2O	1.800E+10	0.00E+00	0.0000E+00
47	O2 + CH3O == HO2 + CH2O	4.000E+07	0.00E+00	8.9011E+06
48	CH2O + CH3O => HCO + CH3OH	6.000E+08	0.00E+00	1.2284E+08
49	O + CH3O == O2 + CH3	1.100E+10	0.00E+00	0.0000E+00
50	O + CH3O == OH + CH2O	1.400E+09	0.00E+00	0.0000E+00
51	CH2OH + M == H + CH2O + M	5.000E+10	0.00E+00	1.0502E+08
52	H + CH2OH == H2 + CH2O	3.000E+10	0.00E+00	0.0000E+00

Step Number	Reaction	A (cm^3/ mole s K^n)	n	E (J/mole)
53	O2 + CH2OH == HO2 + CH2O	1.000E+10	0.00E+00	3.0007E+07
54	CH4 + H == H2 + CH3	1.300E+01	3.00E+00	3.3607E+07
55	CH4 + O == OH + CH3	6.923E+05	1.56E+00	3.5508E+07
56	CH4 + OH == H2O + CH3	1.600E+04	1.83E+00	1.1602E+07
57	CH4 + HO2 == H2O2 + CH3	1.100E+10	0.00E+00	1.0312E+08
58	CH3OH == OH + CH3	9.510E+29	-4.30E+00	4.0405E+08
59	H + CH3OH == H2 + CH2OH	4.000E+10	0.00E+00	2.5506E+07
60	O + CH3OH == OH + CH2OH	1.000E+10	0.00E+00	1.9603E+07
61	OH + CH3OH == H2O + CH2OH	1.000E+10	0.00E+00	7.1008E+06
62	HO2 + CH3OH => H2O2 + CH2OH	6.200E+09	0.00E+00	8.1115E+07
63	H2O2 + CH2OH => HO2 + CH3OH	1.000E+04	1.70E+00	4.7910E+07
64	CH3OH +CH3 == CH4 + CH2OH	9.000E+09	0.00E+00	4.1106E+07
65	CH3OH +CH3O => CH2OH + CH3OH	2.000E+08	0.00E+00	2.9305E+07
66	CH2OH + CH3OH => CH3OH + CH3O	2.200E+01	1.70E+00	4.5408E+07
67	CH2O + CH3OH => 2CH3O	1.530E+09	0.00E+00	3.3326E+08
68	CH3O + CH3O => CH2O +CH3OH	3.000E+10	0.00E+00	0.0000E+00

Table 7 Step list and reaction rate coefficients. M indicates a third body reaction, == indicates forward and reverse reactions, => indicates unidirectional reactions